

**Experimental and Numerical Investigations of Thermal-Fluid
Processes in Oscillatory Flows**

Olusegun Mustapha Ilori

Submitted in accordance with the requirements for the degree of
Doctor of Philosophy

The University of Leeds
School of Chemical and Process Engineering

September, 2016

The candidate confirms that the work submitted is his own, except where work which has formed part of jointly-authored publications has been included. The contribution of the candidate and the other authors to this work has been explicitly indicated below. The candidate confirms that appropriate credit has been given within the theasis where reference has been made to the work of others.

The work in Chapter 3 of the thesis has appeared in the publication as follows:

Design of Thermoacoustic Rig for the Analysis of Thermal and Hydraulic Performance of Heat Exchangers in Oscillatory Flow, 2013, Ilori O.M., Mao X., Jaworski A.J.

I was responsible for the entire work. The contribution of the other authors was support in line of supervision.

The work in Chapters 5 and 6 of the thesis appeared in publications as follows:

CFD Simulation of Oscillatory Flow Around The Heat Exchanger of Thermoacoustic Devices, 2014, Olusegun M. Ilori, Xiaoan Mao, Artur J. Jaworski

I was responsible for the entire work. The contribution of the other authors was support in line of supervision.

The work in Chapters 5 and 6 of the thesis appeared in publications as follows:

Numerical Analysis of the Heat Transfer in an Oscillatory Flow around the Heat Exchangers of Thermoacoustic Systems, 2015, Olusegun M. Ilori, Artur J. Jaworski, Xiaoan Mao

I was responsible for the entire work. The contribution of the other authors was support in line of supervision.

The work in Chapters 5 and 6 of the thesis appeared in publications as follows:

Numerical Simulation of Oscillatory Flow and Heat Transfer in the Heat Exchangers of Thermoacoustic Systems, 2015, Olusegun M. Ilori, Xiaoan Mao, Artur J. Jaworski

I was responsible for the entire work. The contribution of the other authors was support in line of supervision.

This copy has been supplied on the understanding that it is copyright material and that no quotation from the thesis may be published without proper acknowledgement.

The right of Olusegun Mustapha Ilori to be identified as the Author of this work has been asserted by him in accordance with the Copyright, Designs and Patents Act 1988.

© 2016 The University of Leeds and Olusegun Mustapha Ilori

Acknowledgements

It has been an extremely challenging, yet an inspiring and a motivating learning experience for me, most especially here at the University of Leeds. First and foremost, I would like to thank my main supervisor, Professor Artur J. Jaworski for his support, advice, constructive criticism and encouragement throughout the course of this study. His support during the ‘stormy’ and tough period of this project will always be remembered and much appreciated. His expression of confidence (largely non-verbal) in my potential to overcome the tough time was simply motivational.

I would like to thank Dr Xiaoan Mao, who became the second supervisor on this project at a later stage of the work, for his support and useful discussions. Many thanks to my colleagues for the warm interactions. My gratitude goes to the technical support group in the Faculty of Engineering, University of Leeds and the Department of Engineering, University of Leicester, for their technical support.

I would like to thank my wonderful wife, my beloved children and every member of my family for their support, motivation, encouragement, and prayers throughout the period of my study.

Finally, I thank Almighty God for the grace, sustenance, strength, knowledge and the wisdom bestowed on me to successfully complete this study.

This work has been sponsored by the ‘Petroleum Technology Development Fund (PTDF)’, Nigeria. PTDF is a parastatal under the Ministry of Petroleum Resources in Nigeria, dedicated for the development, promotion and implementation of petroleum technology and manpower through research and training of Nigerians.

Abstract

Heat exchangers are critical components of energy systems such as thermoacoustic engines and coolers. In this work, experimental and numerical studies were conducted on the heat transfer and acoustic pressure drop performance of heat exchangers in oscillatory flow. Experimental set-up and measurement techniques were developed to simultaneously measure parameters for the estimation of heat transfer and acoustic pressure drop. Three configurations of heat exchangers – tube-heat-exchanger, finned-heat-exchanger and plate-heat-exchanger were studied. Each configuration consists of three identical sets, arranged in series, to facilitate accurate heat transfer and acoustic pressure drop estimation. The influence of operating and geometric parameters on heat exchanger performance was investigated. The main considerations are to maximise heat transfer and minimise acoustic pressure losses from the heat exchanger, for the improvement of a system's efficiency.

The experimental results show that heat transfer performance, presented as the Nusselt number, strongly depends on drive ratio and mean pressure, especially at the low drive ratios where the gas displacement amplitudes are below, or comparable to, the heat exchanger length. The heat transfer results compared well with results from other studies. A three-dimensional model was developed in ANSYS Fluent, based on the actual experimental set-up. Experimental data was utilised for thermal, acoustic and turbulence boundary conditions and model validation. Good agreement was achieved between the predicted and experimental results. Heat transfer and pressure drop results show dependence on the drive ratio. Ogive edged T-HEX was found to minimise acoustic pressure drop by about 51% at the highest drive ratio in this study. A two-dimensional model was also developed. An appropriate edge shape is found to minimise the acoustic pressure drop and the associated minor losses without significantly affecting the heat transfer performance of the heat exchangers.

Table of Contents

Acknowledgements	iv
Abstract	v
Table of Contents	vi
List of Tables	ix
List of Figures	x
Chapter 1 Introduction	1
1.1 Background	1
1.2 Motivation for the current work.....	3
1.3 Aim and objectives of this work	4
1.4 Significance of the work	5
1.5 Thesis outline	6
Chapter 2 Background and Literature Review	8
2.1 Thermoacoustic effect.....	8
2.1.1 Standing wave thermoacoustic engines and refrigerators	11
2.1.2 Travelling wave thermoacoustic engines and coolers.....	13
2.2 Modelling of thermoacoustic effect	16
2.3 Heat exchangers in oscillatory flow.....	26
2.3.1 Heat transfer in oscillatory flow.....	27
2.3.2 Flow visualisation and flow structures.....	35
2.3.3 Minor losses in oscillatory flow.....	39
2.4 Summary	46
Chapter 3 Design and Development of Experimental set-up	50
3.1 Overview	50
3.2 Experimental set-up	51
3.2.1 Acoustic driver.....	51
3.2.2 Test section.....	55
3.2.3 Heat exchangers (HEX)	59
3.2.4 Edge shapes	65
3.2.5 Fabrication technique.....	67
3.2.6 Heating and Cooling Loops	69
3.2.7 Performing experiments on the test rig	70
3.3 Calibration of the pressure sensors	72

3.4 Resonance frequency determination	75
3.5 Pressure distribution along the test rig	78
3.6 Uncertainties related to the experimental results	80
3.7 Summary	83
Chapter 4 Experimental Analysis of the Tube and Finned Heat Exchangers.....	84
4.1 Experimental conditions.....	84
4.2 Data reduction	86
4.2.1 Heat transfer rates (\dot{Q})	86
4.2.2 Surface temperature (T_s)	89
4.2.3 Nusselt number (Nu)	89
4.2.4 Acoustic Reynolds number (Re_1).....	94
4.3 Heat transfer conditions	94
4.3.1 Temperature measurements	95
4.3.2 Effect of drive ratio (DR) on heat transfer rates (\dot{Q}).....	98
4.3.3 Effect of mean pressure (P_m) on heat transfer rates (\dot{Q})	102
4.3.4 Effect of drive ratio (DR) on Nusselt number (Nu).....	104
4.4 Comparisons of heat transfer results to other models from the literature	107
4.5 Summary	112
Chapter 5 3D Simulation Model for Tube Heat Exchangers.....	113
5.1 Three-dimensional model description.....	113
5.2 Methodology	114
5.2.1 Geometrical model and computational domain	115
5.2.2 Numerical solution procedure	117
5.2.3 Physical model	119
5.2.4 Boundary and initial conditions	120
5.3 Computational conditions	121
5.3.1 Mesh convergence study	121
5.3.2 Investigated conditions	122
5.4 Comparison between experimental and simulation results.....	123
5.4.1 Pressure amplitude profile	123
5.4.2 Velocity amplitude profile	125
5.4.3 Temperature profile.....	127
5.5 Heat transfer	130

5.5.1 Heat flux.....	130
5.5.2 Nusselt number (Nu)	132
5.6 Acoustic pressure drop.....	135
5.7 Summary	138
Chapter 6 2D Simulation Model for Parallel Plate Heat Exchanger	139
6.1 Background	139
6.2 Methodology	140
6.2.1 Geometrical model and Computational Domain.....	140
6.2.2 Physical model	143
6.2.3 Initial and boundary conditions.....	143
6.3 Mesh sensitivity	145
6.4 Model validation against analytical result.....	146
6.5 Validation against experimental results	147
6.6 Effect of edge shape on velocity profile	149
6.7 Effect of edge shape on temperature profile	155
6.8 Effect of edge shape on heat transfer	158
6.8.1 Heat flux calculation	158
6.8.2 Nusselt number calculation	160
6.9 Effect of edge shape on acoustic pressure drop	162
6.10 Summary	165
Chapter 7 Conclusions and Future Work.....	166
7.1 Conclusions	166
7.2 Findings of the study.....	169
7.3 Future works	169
7.3.1 Experimental study.....	169
7.3.2 Numerical study	170
List of References	171
Nomenclatures	179
Appendix A List of Publications	185
Appendix B First version of the test section	186
Appendix C User-Defined-Function (UDF) code	187
Appendix D Calibration of PCB pressure transducers	189
Appendix E Drawing of the experimental set up	192

List of Tables

Table 3.1: Specifications of the acoustic driver (Q-drive1S102D).....	54
Table 3.2: Aluminium 6082-T6 properties for the heat exchangers (Alco Metals, 2016)	60
Table 3.3: Heat exchanger parameters (Dimensioned drawings are given in Appendix – E).....	60
Table 3.4: Aluminium grade 3003-0 properties for the fins (Alco Metals, 2016)	63
Table 3.5: The fin parameter (as supplied by Niagara Thermal).....	63
Table 3.6: Parameters of the edge shapes for the T-HEX and F-HEX	65
Table 4.1: Geometric and operating conditions	85
Table 4.2: Average deviation (%) of the Nusselt number from different models.....	111
Table 5.1: Operating parameters and gas properties	115
Table 5.2: Operating parameters based on the experimental results	122
Table 5.3: Comparison of the simulation results for all edge shapes	127
Table 5.4: Reduction in the acoustic pressure drop on the CHX1	135
Table 6.1: Geometric and operating parameters for the simulation.....	142
Table 6.2: Parameters for the convergence study	145
Table 6.3: Comparison of the simulation results for all the edge shapes at $T_{c1,c2} = 15^{\circ}\text{C}$, $T_h = 50^{\circ}\text{C}$, $P_m = 1$ bar and $\text{Re}_1 = 96 - 672$.....	151

List of Figures

Figure 1.1: Typical thermoacoustic systems (a) standing wave refrigerator/heat pump (b) travelling wave engine driven by a linear alternator	2
Figure 2.1: Heat pumping mechanism in a typical thermoacoustic refrigerator (a) gas parcel undergoing cycle of compression and expansion and the related heat exchange process (the resulting thermodynamic cycle from gas motion is similar to the Sterling cycle) (b) oscillating pressure, p, and velocity, u, distributions in the refrigerator with the possibility of different wavelength configurations.	9
Figure 2.2: Heat pumping mechanism in a traveling-wave engine (a) Stirling cycle travelling wave engine of Figure 1.1b. (b) Gas parcel undergoing a cycle of compression and expansion and the related heat transfer process (Yu and Jaworski, 2010).	11
Figure 2.3: Pressure and velocity versus time in (a) standing wave device (b) travelling wave device. The phase difference of 90° between acoustic pressure and velocity is shown for the standing wave device. The phase difference of 0° is shown for the travelling wave device (Ceperley, 1979).....	12
Figure 2.4: (a) Scale drawing of the torus section (b) scale drawing of the engine, resonator and variable acoustic load (load is not to scale). The pressure antinode is located near the top of the torus section (c) lump-element (impedance model) of the engine (Backhaus and Swift, 2000).	14
Figure 2.5: Spatial average thermoviscous function for different geometries. $r_h / \delta_{k,v}$ is the ratio of hydraulic radius to the penetration depths (δ_k, δ_v - the lengths perpendicular to the gas oscillations). r_h / δ_v yields f_v and r_h / δ_k yields f_k (Swift, 2002).....	19
Figure 2.6: Schematic diagram of two-microphone method in circular duct (Fusco et al., 1992)	20
Figure 2.7: Planar-Laser-Induced-Fluorescence (PLIF) visualised temperature field distribution for 20 phases within an acoustic flow cycle around the parallel plate heat exchanger in oscillatory flow (adapted from Shi et al., 2010).	36
Figure 2.8: Vorticity contour at the end squared edge plate at a flow phase in the acoustic cycle (Mohd-Saat, 2013).	37
Figure 2.9: Evolution of the stream function distribution for eight phases within an acoustic flow cycle (Worlikar and Knio, 1996)	38

Figure 2.10: Measured acoustic resistance per heat exchanger in the 2 – 6 Hz range for a small heat exchanger separation (peak-to-peak displacement amplitude of 5.5 mm). Open circles are the measured resistance divided by two. Closed circles are resistance per heat exchanger minus the linear theory value and minus the boundary-layer value for the duct (Wakeland and Keolian, 2004).	41
Figure 2.11: Definition of suction and ejection stage in a flow cycle of the abrupt change in cross section and time separation between PIV pulses as a function of time (Marx et al., 2008)	43
Figure 2.12: Vortex structure as observed at the end of the plate with various edge shapes (a) rectangular (b) circular (c) 90°C triangle (d) sharp triangular (25°C). Aben et al. (2009).	45
Figure 3.1: Photograph of standing wave experimental set-up (a) overview of the experimental set-up in the laboratory (b) gas charging system (c) test-section (d) heating and cooling water loops (e) measurement devices and data acquisition unit.	52
Figure 3.2: Schematic of the standing wave setup. V1-V10, FS and P are the gas and water control valves, flow sensors and water pump, respectively	53
Figure 3.3: (a) Acoustic driver and (b) displacement sensor as installed in the experimental set-up	53
Figure 3.4: CAD-image of the test section showing the details of the CHX1, HHX and CHX2 arrangement (top) and the drawing of the experimental set-up (bottom).	56
Figure 3.5: Photograph of the test section (a) opening of the test section showing the silicate wool insulation material (b) symmetric arrangement of the heat exchangers	57
Figure 3.6: Arrangement of the thermocouples within the heat exchanger in the gas environment (dimensioned drawing is given in Appendix – E).	58
Figure 3.7: Photograph of the T-HEX. The tube arrangement follows a triangular pitch pattern	61
Figure 3.8: (a) Photograph of the F-HEX (b) fin assembling into the flow channel of the F-HEX	62
Figure 3.9: Photograph of the heat exchangers (a) T-HEX (b) F-HEX.	64
Figure 3.10: Schematic of the uniform-flat-crest for the F-HEX.	64
Figure 3.11: Images of the plate attachments (edge shapes) (a) CAD-images for the T-HEX (left) and the F-HEX (right) (b) photograph of the T-HEX (c) photograph of the F-HEX (d) Schematic of the HEX flow channel for the T-HEX configuration	66
Figure 3.12: Schematic of the T-HEX (left) and the F-HEX (right) and the ogive edge shapes	67
Figure 3.13: Different views of the fabricated tool for producing the T-HEX and the F-HEX edge shapes on the plate attachments.	68

Figure 3.14: Cooling and heating connections for water temperature measurement.....	70
Figure 3.15: DR as a function of the peak-to-peak excitation voltage, for the acoustic driver, at $P_m = 1 - 30$ bar.	72
Figure 3.16: Photograph of the experimental set-up for the calibration of the pressure transducers (a) pressure transducers on a 2-inch flange at the closed end (b) Test-section, showing a 2-inch plastic pipe and the heat exchangers (c) 2-inch plastic pipe in position for the calibration task (d) close-up of the test section.....	73
Figure 3.17: Calibration of the pressure sensor (P_0) at the end of the resonator. The coefficients are the slope and the intercept of the least-squares fit. The transducer's serial number is shown in the legend. Std = standard deviation	74
Figure 3.18: Calibration of the pressure sensor (P_4) at location 2.....	74
Figure 3.19: Determination of the resonance frequency at $P_m = 3$bar, 5bar and 10bar, $T_{room} = 21^\circ C$, and a constant excitation voltage. In the legend, the 'F_max.' indicates the peak frequency in each curve.	76
Figure 3.20: Resonance frequency at various mean pressure for the T-HEX (flat) and the T-HEX (ogive) configurations at $T_{room} = 21^\circ C$.	76
Figure 3.21: Effect of mean pressure on penetration depths at $T_{ref} = 27^\circ C$ and $f = 52$ and 57Hz	77
Figure 3.22: Pressure distribution as a function of various locations in the test rig for the T-HEX (flat) at $0.16 < DR < 1.3\%$, $T_h = 70^\circ C$ and $P_m = 5$bar.....	79
Figure 3.23: Pressure amplitude distribution as a function of various locations in the test rig for the F-HEX (flat) at $0.16 < DR < 0.77\%$, $T_h = 70^\circ C$ and $P_m = 5$bar.....	79
Figure 3.24: Comparison of the pressure amplitude distribution as a function of locations, for the T-HEX and F-HEX configurations at $DR = 0.77\%$, $T_h = 70^\circ C$ and $P_m = 5$ bar. In the legend, Tx1 = T-HEX (flat), Tx2 = T-HEX (ogive), Fx1 = F-HEX (flat), and Fx2 = F-HEX (ogive).	80
Figure 4.1: Measured temperature at various locations versus DR at $T_h = 50^\circ C$, at $P_m = 3$bar, 5bar and 10bar (a) – (c) T-HEX (flat) (d) – (f) T-HEX (ogive).	96
Figure 4.2: Measured temperature at various locations versus DR at $T_h = 50^\circ C$, $P_m = 3$bar, 5bar and 10bar (a) – (c) F-HEX (flat) and (d) – (f) F-HEX (ogive).....	97
Figure 4.3: Effect of DR on \dot{Q} for the CHX1, HHX and CHX2 at various P_m, $T_h = 30^\circ C - 70^\circ C$ and $0.08 < DR < 1.8\%$ (a) – (c) T-HEX (flat) (d) – (f) T-HEX (ogive).....	99

Figure 4.4: Effect of DR on \dot{Q} for the HHX at various P_m, $T_h = 30^\circ\text{C} - 70^\circ\text{C}$ and $0.08 < DR < 0.9\%$ (a) – (c) F-HEX (flat) (d) – (f) F-HEX (ogive).	100
Figure 4.5: Effect of P_m on \dot{Q} for the HHX at $0.08 < DR < 1.52\%$ and $T_h = 70^\circ\text{C}$ (a) T-HEX (flat) (b) T-HEX (ogive).	103
Figure 4.6: Effect of P_m on \dot{Q} for the HHX at $0.08 < DR < 0.64\%$ and $T_h = 70^\circ\text{C}$ (a) F-HEX (flat) (b) F-HEX (ogive).	103
Figure 4.7: Effect of DR on Nu for the HHX at various P_m and $T_h = 30 - 70^\circ\text{C}$ (a) – (c) T-HEX (flat) and (d) – (f) T-HEX (ogive).	105
Figure 4.8: Effect of DR on Nu for the CHX1 at various P_m and $T_h = 70^\circ\text{C}$ (a) T-HEX (flat) (b) T-HEX (ogive).	106
Figure 4.9: Effect of DR on Nu for the CHX2 at various P_m and $T_h = 70^\circ\text{C}$ (a) T-HEX (flat) (b) T-HEX (ogive).	106
Figure 4.10: Effect of DR on Nu for the HHX at $0.08 < DR < 0.9\%$ and $T_h = 30 - 70^\circ\text{C}$ (a) – (c) F-HEX (flat) (d) – (f) F-HEX (ogive).	107
Figure 4.11: Nu versus Re_1 for HHX at $P_m = 5\text{bar}$ and $T_h = 70^\circ\text{C}$ (a) T-HEX (flat), (b) T-HEX (ogive).	108
Figure 4.12: Nu versus acoustic Reynolds number (Re_1) for HHX at $P_m = 10\text{ bar}$ and $T_h = 70^\circ\text{C}$ (a) T-HEX (flat), (b) T-HEX (ogive).	110
Figure 5.1: Adopted approach to integrating experiments with the CFD model	115
Figure 5.2: (a) Sketch of experimental set-up (b) computational domain (c) 3D model of T-HEX showing the mesh.	116
Figure 5.3: Numerical solution procedure for the 3D model	117
Figure 5.4: Definition of flow direction in a flow cycle and the relationship between the velocity, gas displacement and pressure amplitudes	122
Figure 5.5: Comparison between the experimental and the numerical pressure amplitudes in the test section (T-HEX (flat)) at $0.64 < DR < 1.29\%$, $P_m = 5\text{bar}$ and $T_h = 70^\circ\text{C}$.	124
Figure 5.6: Comparison between the experimental and the numerical pressure amplitudes in the test section (T-HEX (ogive)), at $0.64 < DR < 1.29\%$, $P_m = 5\text{bar}$ and $T_h = 70^\circ\text{C}$.	124
Figure 5.7: Effect of edge shape of heat exchanger on pressure amplitude distribution along the test rig, at $0.15 < DR < 1.29\%$, $P_m = 5\text{bar}$ and $T_h = 70^\circ\text{C}$	125
Figure 5.8: Comparison between the predicted velocity amplitude along the test section for the T-HEX (flat) and the T-HEX (ogive), at $0.15 < DR < 1.29\%$, $P_m = 5\text{bar}$ and $T_h = 70^\circ\text{C}$.	126

Figure 5.9: Comparison between the predicted velocity amplitudes for the T-HEX (flat) and the T-HEX (ogive), at $0.15 < DR < 1.29\%$, $P_m = 5\text{bar}$ and $T_h = 70^\circ\text{C}$. The peak velocity amplitude is the maximum velocity amplitude within the flow cycle in a positive direction.....	126
Figure 5.10: Comparison between the experimental and the numerical time-averaged temperatures (T-1, T-2, T-3 and T-4) for the T-HEX (flat), at $0.16 < DR < 1.27\%$, $P_m = 5\text{bar}$ and $T_h = 70^\circ\text{C}$.....	128
Figure 5.11: Comparison between the experimental and the numerical time-averaged temperature (T-1, T-2, T-3 and T-4) for the T-HEX (ogive), at $0.16 < DR < 1.27\%$, $P_m = 5\text{bar}$ and $T_h = 70^\circ\text{C}$.....	128
Figure 5.12: Comparison between the numerical time-averaged temperatures (T-1, T-2, T-3 and T-4) for the T-HEX (flat) and the T-HEX (ogive), at $0.15 < DR < 1.29\%$, $P_m = 5\text{bar}$ and $T_h = 70^\circ\text{C}$.....	129
Figure 5.13: Comparison between the simulation and the experimental heat fluxes for the T-HEX (flat), at $0.16 \leq DR \leq 1.27\%$, $P_m = 5\text{bar}$ and $T_h = 70^\circ\text{C}$.....	131
Figure 5.14: Comparison between the simulation and the experimental heat fluxes for the T-HEX (ogive), at $0.15 \leq DR \leq 1.29\%$, $P_m = 5\text{bar}$ and $T_h = 70^\circ\text{C}$.....	131
Figure 5.15: Comparison between the numerical heat fluxes for the T-HEX (flat) and the T-HEX (ogive), at $0.15 \leq DR \leq 1.29\%$, $P_m = 5\text{bar}$ and $T_h = 70^\circ\text{C}$.....	132
Figure 5.16: Comparison of the experimental and the simulation Nu for the T-HEX (flat), at $0.16 \leq DR \leq 1.27\%$, $P_m = 5\text{bar}$ and $T_h = 70^\circ\text{C}$.....	133
Figure 5.17: Comparison of the experimental and the simulation Nu for the T-HEX (ogive), at $0.16 \leq DR \leq 1.29\%$, $P_m = 5\text{bar}$ and $T_h = 70^\circ\text{C}$.....	134
Figure 5.18: Comparison between the numerical Nu for the T-HEX (flat) and the T-HEX (ogive), at $0.15 \leq DR \leq 1.29\%$, $P_m = 5\text{bar}$ and $T_h = 70^\circ\text{C}$.....	134
Figure 5.19: Acoustic pressure drop as a function of t/T across the T-HEX (flat) and the T-HEX (ogive), at $0.3 \leq DR \leq 1.29\%$, $P_m = 5\text{bar}$ and $T_h = 70^\circ\text{C}$ (a) – (c) CHX1-HHX-CHX2 (flat) (d) – (f) CHX1-HHX-CHX2 (ogive).	136
Figure 5.20: Comparison of the acoustic pressure drop across CHX1 (a) suction stage (b) ejection stage	137
Figure 6.1: Sketch of experimental set-up (b) computational domain (c) aerodynamic edge shapes. Locations 1 ($x = 4244\text{ mm}$), 2 ($x = 4276\text{ mm}$), 3 ($x = 4308\text{ mm}$), 4 ($x = 4340\text{ mm}$), a ($x = 4315\text{ mm}$), b ($x = 4324\text{ mm}$) and c ($x = 4333\text{ mm}$) are used for data sampling.	141
Figure 6.2: Comparison of axial velocity amplitudes as a function of phase angle for various mesh sizes, at $DR = 0.3\%$ ($x = 4324\text{ mm}$).	146
Figure 6.3: Comparison between the analytical and the simulation results for the axial velocity amplitude as a function of phase angle at $DR = 0.3\%$ ($x = 4324\text{ mm}$).	147

Figure 6.4: Comparison between the experimental and the numerical pressure amplitudes blunt edge-shape ($r = 0$) at $DR = 0.3\%$ ($x = 4308$ mm).....	148
Figure 6.5: Comparison between the experimental and the numerical time-averaged temperatures (T-1, T-2, T-3 and T-4), at $0.3 \leq DR \leq 1.5\%$	148
Figure 6.6: Phase-dependent velocity profiles as a function of y at $0.3 \leq DR \leq 2.0\%$ ($x = 4315$ mm).	150
Figure 6.7: Centreline velocity profile at the middle of CHX2 ($x = 4324$ mm) for blunt, cone, ogive and round edge shapes (a) $DR = 0.65\%$ ($\phi 4$) (b) $DR = 1.0\%$ ($\phi 7$).....	152
Figure 6.8: Maximum velocity amplitudes as a function of DR for blunt, cone, ogive and round edge shapes ($x = 4315$ mm)	152
Figure 6.9: Vorticity (1/s) contours for blunt, cone, ogive and round edge shapes, respectively, at $\phi 7$ (a) $DR = 0.3\%$ (b) $DR = 1.0\%$	154
Figure 6.10: Cross-sectional temperature profiles at $0.3 \leq DR \leq 2.0\%$ ($x = 4315$ mm).....	156
Figure 6.11: Time-averaged temperature profile of CHX1, CHX2 and HHX for the blunt, cone, ogive and round edge shapes (a) inlet (b) centreline and (c) outlet. Locations are about a, b, and c (i.e. $x = 4315$ mm, $x = 4324$ mm, and $x = 4333$ mm) in Figure 6.1c. Similar locations are used for the three heat exchangers.....	157
Figure 6.12: Space-cycle averaged heat flux as a function of DR for the CHX1, HHX and CHX2.	159
Figure 6.13: Comparison of Nu from the experiments and space-cycle averaged Nu from the simulation.	161
Figure 6.14: Acoustic pressure drop versus t/T for all the edge shapes (blunt, cone, ogive, and round) at $0.3 \leq DR \leq 2.0\%$ (a) CHX1, (b) HHX, (c) CHX2.	163
Figure 6.15: Comparison of experimental and numerical acoustic pressure drop versus of t/T for blunt edge shape at $P_m = 1$ bar, $DR = 1.4\%$ (Experiment) and $DR = 1.4\%$ (simulation) across (a) HHX (b) CHX2.....	164
Figure A1: CAD-image of the first version of test section of the experimental set-up.....	186
Figure D1: Calibration of pressure sensor P1. The coefficients are the slope and intercept of the least-squares fit.....	189
Figure D2: Calibration of pressure sensor P2.	189
Figure D3: Calibration of pressure sensor (P5) at location 3.....	190
Figure D4: Calibration of pressure sensor (P6) at location 4.....	190
Figure D5: Calibration of pressure sensor P7.	191
Figure D6: Calibration of pressure sensor P8 at the back of linear alternator	191

Figure E1: Overview of the dimensioned drawing of the experimental set up	192
Figure E2: Drawing of the heat exchanger core showing position of the thermocouples (water and gas sides) and pressure transducers.....	193
Figure E3: Drawing of the T-HEX configuration	194
Figure E4: Drawing of a typical edge shape for T-HEX	195
Figure E5: Drawing of the F-HEX configuration	196
Figure E6: Drawing of a typical spacer (end).....	197
Figure E7: Drawing of a pressure sensor holder.....	198
Figure E8: Drawing of a protection-socket for pressure sensor	199

Chapter 1

Introduction

1.1 Background

Thermoacoustic devices are sustainable energy technologies that rely on oscillatory flow principles and thermoacoustic effects. The technology creates acoustic power from heat input (engine or prime mover) or produces a refrigeration effect from acoustic power input (refrigerator or heat pump) and operates either in a standing or travelling wave mode. The basic components of a thermoacoustic device are the resonator, stack (for standing wave device) or regenerator (for the travelling wave device), as well as heat exchangers and acoustic drivers as shown in Figure 1.1. The resonator encloses the internal elements, i.e. the heat exchangers and the stack or regenerator as well as the environmentally friendly inert gas which serves as the working fluid. The resonator is necessary for defining the phase of pressure and velocity of the oscillating gas that interacts with the boundaries of the two heat exchangers and the stack (regenerator) that is placed between them. The heat exchangers act as a heat source and heat sink and by placing hot and cold heat exchangers at the two ends of the stack (regenerator), a temperature gradient is created, and acoustic effects are produced. The stack (regenerator) is a porous material, where the acoustic power is either produced due to the imposed temperature gradient (engine) or consumed for heat pumping up the temperature gradient to occur (refrigerator). The acoustic power generated by the thermoacoustic engine is converted to electricity by the acoustic driver. The acoustic power from the engine can also be used to drive the refrigerator or heat pump directly. An acoustic driver is also used to provide acoustic oscillations for the refrigerator. Such acoustic drivers include a loudspeaker, linear alternator and electrodynamic shakers. Thermoacoustic engines can make use of heat as energy input from different heat sources such as combustion of biomass and gases (e.g. natural gas), waste heat (e.g. industrial waste stream), resistive heating, solar energy and geothermal energy. Thermoacoustic technology has applications in areas such as liquefaction and regasification of natural gas, particularly those found in remote locations, cheap electricity generation, electronic components cooling, industrial waste heat recovery

and utilisation, mixture separation, automotive refrigeration, space and military applications. The possibility of using thermoacoustic systems for the liquefaction of natural gas is an interesting solution to the oil and gas sector in different oil-rich countries including Nigeria. Currently, the associated natural gas from the oil wells is being flared on a large scale in Nigeria. Gas flaring, which causes extreme environmental degradation and community crisis, is being practised primarily because of the huge costs of installing an underwater gas pipeline and the lack of inexpensive and efficient natural gas liquefaction technology that will allow economic recovery of the gas resource.

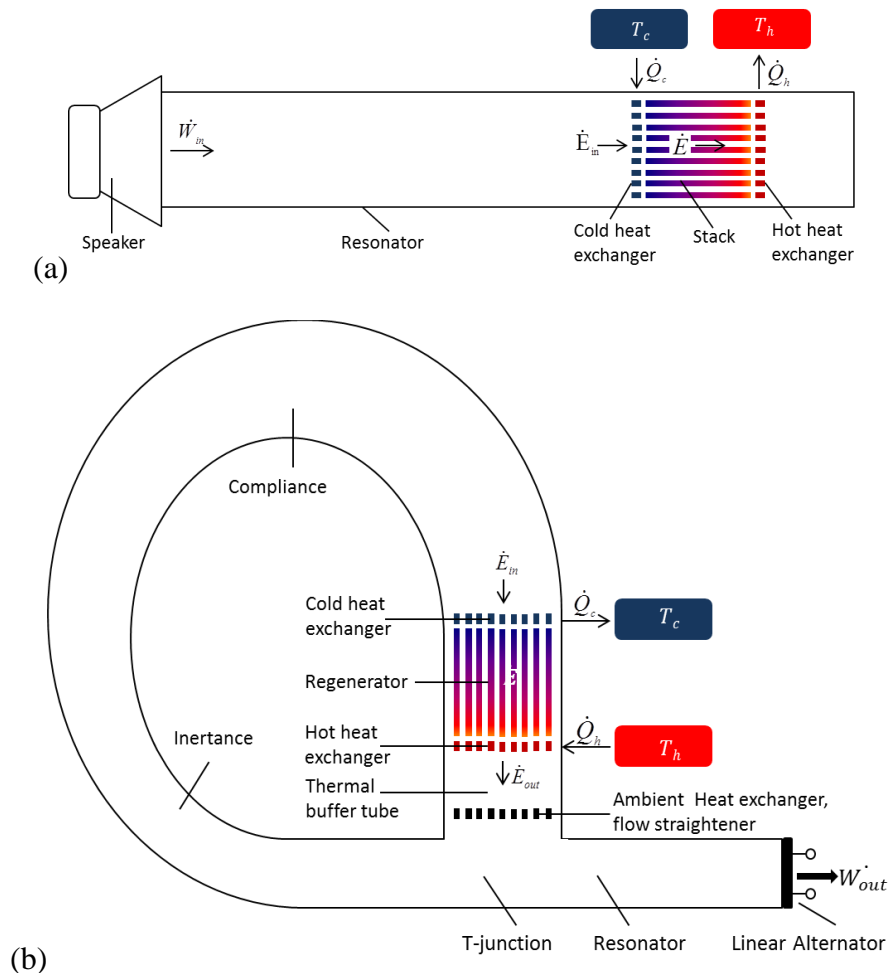


Figure 1.1: Typical thermoacoustic systems (a) standing wave refrigerator/heat pump (b) travelling wave engine driven by a linear alternator

The choice of thermoacoustic technology for the applications above is due to the simplicity of its construction and the high reliability of its operation, which results mainly from a lack of moving parts. Also, the use of environmentally friendly

working fluids such as helium, argon, nitrogen, xenon, air or a mixture of these gases makes thermoacoustic devices an environmental friendly solution. However, despite the attractiveness of thermoacoustic technology due to its wide areas of application and advantages, there are still engineering challenges in the design and development of the technology, especially the heat exchangers, that are yet to be completely understood and solved.

The heat transfer and fluid flow processes in the thermoacoustic technology are quite complex. The complexity is due to the oscillatory nature of the compressible fluid that thermally interacts with the solid boundaries such as heat exchangers. Furthermore, the effect of geometrical discontinuity that the presence of the core introduced to the flow also compounds the problem, this often results in complex flow behaviour such as vortex formation and shedding, turbulence, streaming and complex heat transfer mechanisms that are not yet fully characterised. The non-linear effects are complicated further when the device operates at high amplitude at which a practical thermoacoustic system operates, which has made the design of the heat exchangers a challenging task. The consequence of these challenges is the degradation of the performance of the thermoacoustic system. Presently, the efficiency of a typical thermoacoustic engine is still about 49% of the Carnot efficiency, i.e. 32% thermal efficiency (Tijani and Spoelstra, 2011).

1.2 Motivation for the current work

Heat exchangers are the core energy components of a thermoacoustic system since they act as the heat source and the heat sink. Their thermal and hydraulic performance under oscillatory flow conditions would directly contribute to the overall efficiency of the thermoacoustic engines and coolers. Therefore, the challenges surrounding the oscillating flow and heat transfer in the heat exchangers need to be fully understood and solved.

There are two primary considerations in the study of heat exchangers under oscillatory flow conditions – the first is the maximisation of heat transfer, and the second is the minimisation of acoustic pressure losses. Both effects depend on flow conditions and suggest that the geometry or design of the heat exchanger impacts its performance. The design of a compact heat exchanger that would be efficient in terms of heat transfer and acoustic pressure drop would need to make use of

correlations (Nusselt number and Colburn-j factor, acoustic pressure coefficients) that are reliable, and incorporate non-linear effects (turbulence, vortex, streaming) associated with the presence of temperature, flow channel edge shape, abrupt change in cross-sectional areas and the discontinuity that results from the combination of different dissimilar geometries to form the internal 'core' of a thermoacoustic engine or cooler.

Such correlations are widely available for unidirectional flow but not for oscillatory flow. The researchers within the thermoacoustic community often use data from unidirectional flow for the design and development of heat exchangers for thermoacoustic applications. However, this practice makes the prediction of thermal and hydraulic performance in oscillatory flow open to criticism.

1.3 Aim and objectives of this work

The aim of this work is to study the heat transfer and acoustic pressure drop performance of heat exchangers in oscillatory flow. The specific research objectives are:

1. To develop an experimental set-up and measurement techniques for investigating the heat transfer and acoustic pressure drop in oscillatory flows.
2. To measure the heat transfer performance and the effect of edge shapes of heat exchangers using the experimental set-up and the measurement technique developed. Edge shape is the entrance and exit shape of gas channels of the heat exchanger.
3. To present the heat transfer performance in terms of heat transfer rates and non-dimensional heat transfer coefficient, Nusselt number (Nu), and compare with available existing models from the literature.
4. To develop a three-dimensional numerical model based on the experimental set-up and tube heat exchanger configuration, for the investigation of the effect of gas channel edge shape on heat transfer and acoustic pressure drop, using a commercial CFD Package, ANSYS Fluent 17.0 (2015).
5. To develop a two-dimensional numerical model based on the experimental set-up, for the investigation of heat transfer, acoustic pressure drop and flow behaviour in plate heat exchangers under oscillatory flow conditions, using a commercial CFD Package, ANSYS Fluent 17.0 (2015).

6. To discuss the underlying physical processes of the heat transfer and acoustic pressure drop in the heat exchangers in oscillatory flows.

1.4 Significance of the work

The significance of this study can be summarised as follows:

1. The use of single or a pair of heat exchangers to study heat transfer performance under oscillatory flow for energy devices such as a thermoacoustic device will create an imbalance in the energy balance that will be difficult to capture. Hence the use of two cold heat exchangers on the two sides of the hot heat exchangers will allow a detailed study of the hot heat exchanger (HHX) and improve the estimation of heat transfer. To the author's knowledge of the author, this is the first time that such consideration will be given to the study of heat transfer and acoustic pressure drop in heat exchangers under oscillatory flow conditions.
2. Profiled edge shapes are used on the heat exchangers' gas channels to improve flow conditions associated with an abrupt change in cross section and thus minimise pressure drop on the gas side of the heat exchangers.
3. Simultaneous measurement of the heat transfer and acoustic pressure drop are carried out to determine the relationship between heat transfer and acoustic pressure drop in the heat exchanger under oscillatory flow conditions.
4. The thermal potential for the heat transfer coefficient is defined to reflect the contribution of fluid temperature near the heat exchangers under oscillatory flow. The thermal potential is the temperature difference that appears in the definition of the heat transfer coefficient.
5. The acoustic pressure drop performance of the heat exchanger in oscillatory flow has not been based on resonance frequency before now; this study takes such consideration into account.
6. The experimental result of heat transfer and hydraulic performance of heat exchangers in oscillatory flow are compared with 2D and 3D simulation results obtained by solving Navier-Stokes equations using the commercial CFD package ANSYS Fluent 17.0 (2015). This is a different approach from

the regular practice of comparing experimental results with the one-dimensional (1D) DeltaEC model or at best two-dimensional (2D) simulation results for geometries other than parallel plate heat exchangers.

1.5 Thesis outline

The thesis is organised into seven chapters.

Chapter 1 – provides an overview of the background to thermoacoustics and the motivation for this research study, followed by the aims and objectives of the current study. The significance of the study is highlighted, and the overall thesis layout is described.

Chapter 2 – gives the background of thermoacoustics – including the thermoacoustic effect, classification of thermoacoustic devices, modelling of thermoacoustics and a concise literature review of relevant research work on heat transfer and acoustic pressure drop, comprising numerical and experimental studies.

Chapter 3 – discusses the design, development and testing of a standing wave experimental set-up that is used for the testing of Tube-Heat-Exchanger (T-HEX) and Finned-Heat-Exchangers (F-HEX) including the edge shapes, under oscillatory flow conditions. The description includes the design concepts, measurement capability, fabrication techniques and initial measurements on the experimental set-up. The work described in Chapter 3 covered objective one and part of objective two.

Chapter 4 – describes the heat transfer measurements on T-HEX and F-HEX including their edge shapes. Directly measured parameters are described. The description of the deduced parameters that represent the performance of the tested heat exchangers is given. Analyses of the influence of operating and geometrical parameters on the heat transfer performance are presented. Comparison between the experimental performance results and those available in the literature are made, and conclusions are drawn.

Chapter 5 – discusses the development and experimental validation of a 3D numerical model for the T-HEX utilising the experimental results as thermal and acoustic boundary conditions. Experimental validation of the 3D model results is

discussed, and the analysis of the effect of edge shape on heat transfer and pressure drop from both numerical and experimental viewpoints are described.

Chapter 6 – reports the development of a 2D numerical model based on a parallel plate heat exchanger with a replica arrangement of the experimental set-up described in Chapter 3. Description of the 2D model validation with the experimental results is given. The investigation of heat transfer and pressure drop from both simulation and experiment are described. Four edge shapes are investigated, namely – blunt, cone, ogive, and round. Their impact on heat transfer and acoustic pressure drop across parallel plate heat exchangers is discussed.

Chapter 7 – provides the detailed conclusions that are derived from the study and lists the recommendations for future work.

Appendices – there are four different appendices. Appendix-A gives the list of publications that are produced from this research work. Appendix-B shows the details of the first version of the experimental set-up as designed and fabricated. Appendix-C gives the details of simulation codes used in the numerical work presented in Chapters 5 and 6. Appendix-D describes the concluding part of the results of the calibration of pressure transducers that are used in the study and described in Chapter 3.

Chapter 2

Background and Literature Review

This research focuses on the investigation of heat transfer and oscillating pressure drop in the heat exchangers under oscillatory flow conditions. Thermoacoustic systems operate based on oscillatory flow phenomena; therefore, the basic concepts of a thermoacoustic effect are first discussed in section 2.1, including the general classification of thermoacoustic systems. In section 2.2, the modelling of thermoacoustic effect on the core elements (heat exchangers, stack or regenerator) of thermoacoustic engines and coolers are described in detail. In section 2.3, the review of published work that is relevant to this current study is presented; this includes experimental and numerical studies of heat exchangers covering the heat transfer and acoustic pressure drop performance in oscillatory flow conditions. Section 2.4 gives a summary of the sections of this chapter and direction of the current study in comparison with the existing literature.

2.1 Thermoacoustic effect

The term ‘thermoacoustics’ was first used by Nicholas Rott (1980). It refers to the interactions between heat-transfer processes (thermo-) and pressure oscillations (acoustics) in compressible working fluids. These interactions are quite small and hard to detect within everyday acoustic or sound wave phenomena. However, they can be intensified if an acoustic oscillation of high magnitude (high frequency, mean pressure and drive ratio – the ratio of maximum pressure amplitude to the mean pressure) is present near a solid porous material with an appropriate phase relationship between velocity and pressure oscillations. In such favourable conditions, the “thermoacoustic effect” can be harnessed to enable the conversion between thermal and acoustic energies with relatively high power densities and thermodynamic efficiencies.

The conversion between thermal and acoustic (i.e. mechanical) forms of energy in thermoacoustic systems occurs within its core elements. This energy conversion involves heat transfer and flow processes that are quite complex, partly due to the oscillatory nature of the compressible working fluid, and partly due to geometry

discontinuities that are formed from a combination of heat exchangers and other internal structures in thermoacoustic systems. As mentioned, thermoacoustic systems are usually classified as “engines or prime movers” and “coolers or heat pumps or refrigerators” depending on the practical implementation of the thermoacoustic effect. The working principle of a thermoacoustic refrigerator is described in the following section.

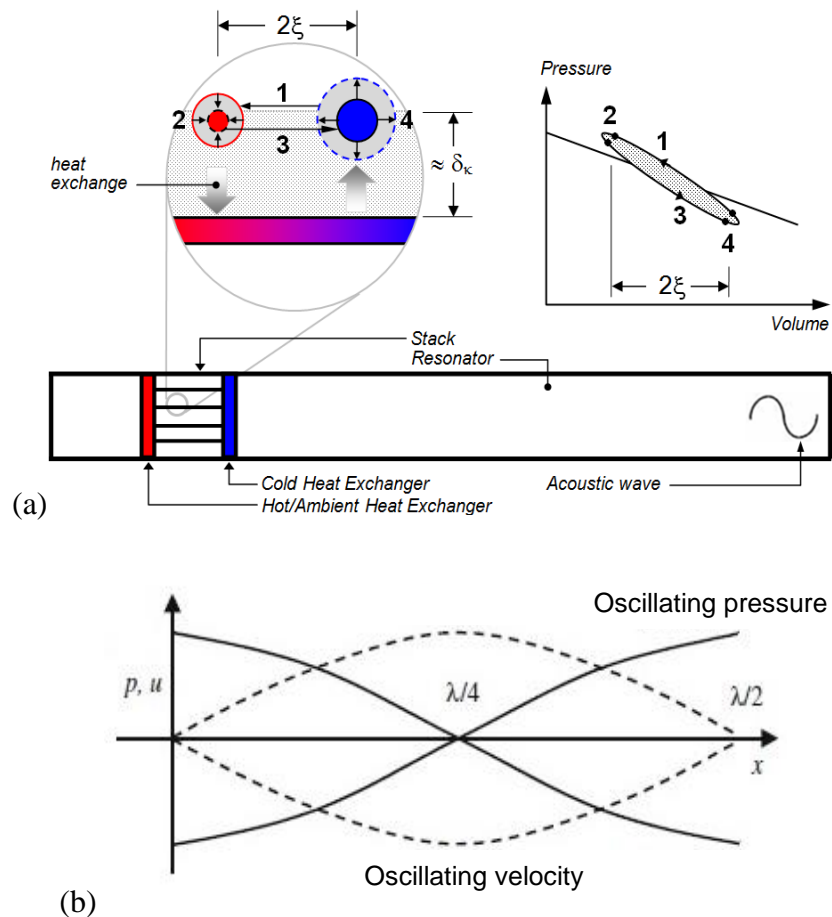


Figure 2.1: Heat pumping mechanism in a typical thermoacoustic refrigerator (a) gas parcel undergoing cycle of compression and expansion and the related heat exchange process (the resulting thermodynamic cycle from gas motion is similar to the Sterling cycle) (b) oscillating pressure, p , and velocity, u , distributions in the refrigerator with the possibility of different wavelength configurations.

In Figure 2.1a, the acoustic driver at the right end of the resonator supplies acoustic power to the working gas inside the resonator. The acoustic power supplied causes the gas parcels to oscillate back and forth. The acoustic wave inside the resonator is described by the distribution of pressure and velocity amplitudes, as shown in Figure

2.1b. Internal structures consisting of heat exchangers, stack or regenerator, is commonly placed together (and often referred to as a ‘core’) at a location where oscillating pressure and velocity are not zero in a thermoacoustic system. A parcel of gas undergoing an acoustic oscillation is shown in the magnified part of the stack on the upper left side of Figure 2.1a. As the fluid oscillates back and forth within the area of the plate by peak-to-peak displacement amplitude, $2|\xi_1|$, the gas parcels supply heat to the solid material at high pressure and remove the heat at low pressure; that is, a change in temperature occurs due to the adiabatic compression and expansion resulting from the pressure variations which accompany the acoustic sound wave. The gas parcel is compressed as it moves to the left and the temperature of the gas parcel increases adiabatically by $2/T_1|$ due to the increased pressure. Therefore, the pressure and temperature of the gas parcel are $P+2|p_1|$ and $T+2|T_1|$. The increase in temperature makes the parcel temperature slightly higher than the plate temperature and, consequently, heat is being transferred from the parcel to the plate. As the flow reverses, the gas parcel expands, and its temperature drops slightly lower than that of the plate by an amount equal to the amount that was initially gained. Thus, heat is being absorbed by the plate, and the parcel returns to its original thermodynamic state, making the process a complete thermodynamic cycle. The acoustic wave provides power that allows the heat to be pumped up the temperature gradient.

Let us now consider the full length of the stack as shown in the lower part on the left side of Figure 2.1a. The overall heat pumping process is like a "bucket brigade" in which each set of gas parcels picks up heat from the “neighbour” to the right at a lower temperature and hands it over to its “neighbour” to the left at a higher temperature. Two heat exchangers are placed at the ends of the stack, cold and hot. Heat is withdrawn from a load at low temperatures through the cold heat exchanger, and the waste heat is rejected to an ambient temperature through the hot heat exchanger (left-end of the stack). If a large temperature gradient is imposed across the stack/regenerator, intensification will occur, and acoustic power will be self-excited leading to the production of useful energy (Swift, 2002). As remarked, the acoustic power that is produced could be extracted using a linear alternator to generate electricity or use to drive a cooler/heat pump.

The P-V diagram on the upper right side of Figure 2.1a and the left side of Figure 2.2 show the corresponding Stirling thermodynamic cycle that is formed from a

series of processes occurring between solid wall and gas medium in the thermoacoustic system. In an ideal Stirling cycle, the compression and expansion of the working medium occur at the adiabatic condition. Furthermore, the heat transfer is ideally an isochoric process. In real thermoacoustics application, compression, expansion and heat transfer occurs simultaneously; hence creating irreversibility to the system. Therefore, the actual cycle for thermoacoustic systems resembles an elliptical shape as shown in Figures 2.1a and 2.2a. The work required by the cycle to produce the necessary cooling effect is represented by the shaded area inside the “loop” representing the cycle (Figure 2.1a). A similar process will be followed in the thermoacoustic system that is working as an engine but in a reverse way as shown in Figure 2.2a. Furthermore, the magnitude of the temperature gradient along the stack is different in the engine and the refrigerator. The steepness of the temperature gradient in a stack of the thermoacoustic refrigeration is much lower than that of the engine.

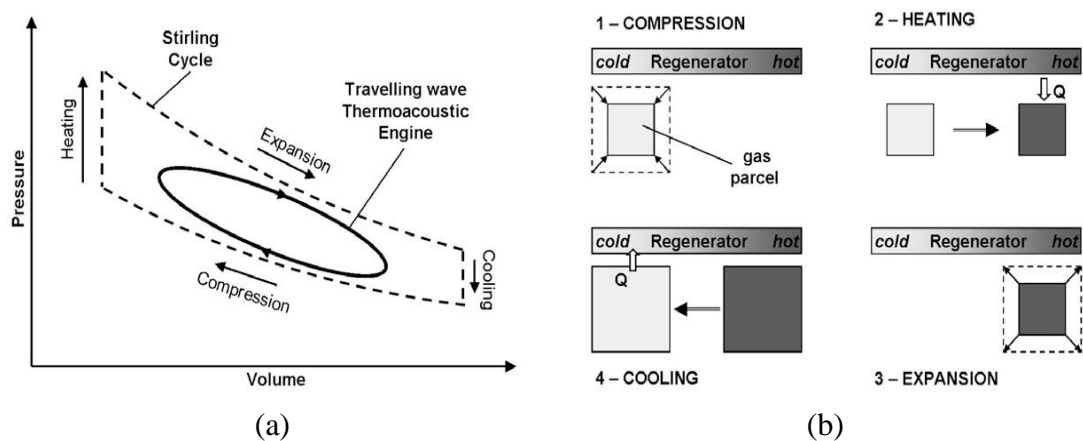


Figure 2.2: Heat pumping mechanism in a traveling-wave engine (a) Stirling cycle travelling wave engine of Figure 1.1b. (b) Gas parcel undergoing a cycle of compression and expansion and the related heat transfer process (Yu and Jaworski, 2010).

2.1.1 Standing wave thermoacoustic engines and refrigerators

Many thermoacoustic engines and coolers use standing waves. A standing wave – is a waveform phenomenon exhibited by waves of different nature such as sound, light, or even water waves. These waves in a gas are pressure waves. Standing waves seem to vibrate in fixed position around stationary nodes, and the location of maximum displacement is the antinode (Figure 2.3a).

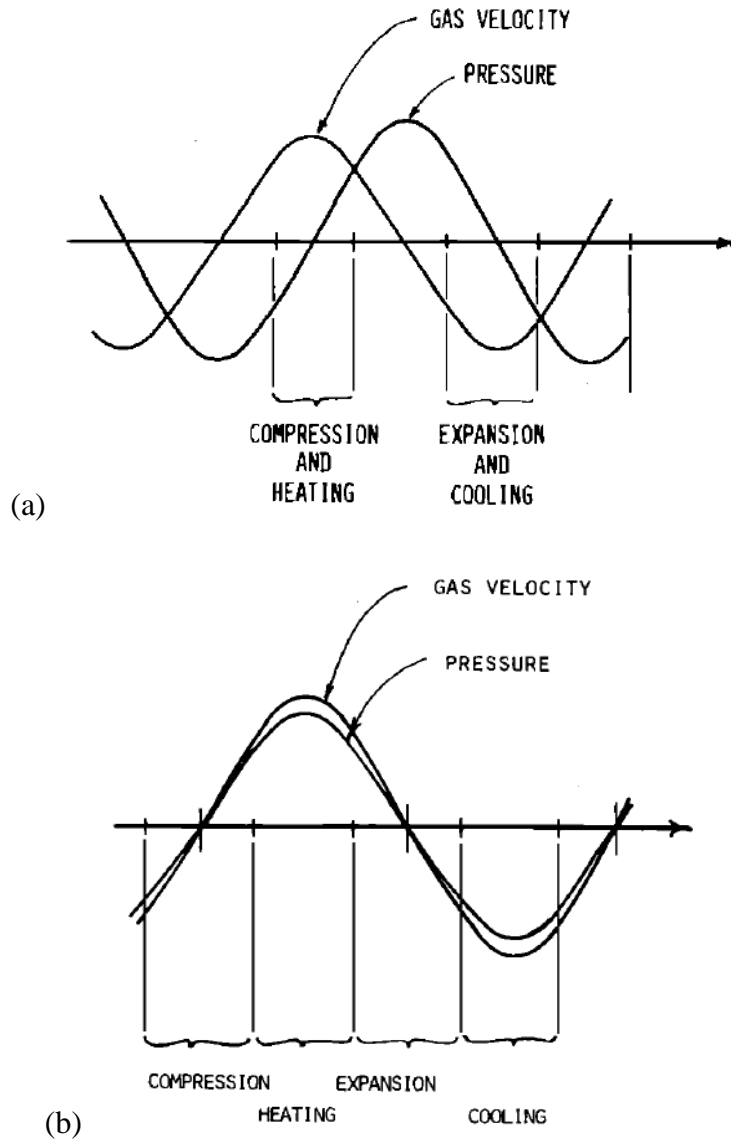


Figure 2.3: Pressure and velocity versus time in (a) standing wave device (b) travelling wave device. The phase difference of 90° between acoustic pressure and velocity is shown for the standing wave device. The phase difference of 0° is shown for the travelling wave device (Ceperley, 1979).

The maximum compression of the gas also occurs at the pressure antinodes. In a standing wave thermoacoustic system, the thermal energy is converted to mechanical energy and vice versa using the thermoacoustic effect that takes place in the stack placed between hot and cold heat exchangers (cf. Figure 1.1a). The stack can have different geometries such as a parallel plate, a pin array, circular pore, ceramic pore encased in a stainless-steel cylinder and honeycomb. The stack can be imagined as a series of plates forming a set of parallel channels through which

acoustic oscillations with standing wave phasing occurs. The time phasing between pressure and velocity amplitudes in a pure standing wave is 90° (Figure 2.3a) but slightly less than 90° for a practical thermoacoustic device. The phase delay is caused by an ‘imperfect’ thermal contact between the stack and the working gas, and is required for heat pumping in the standing wave thermoacoustic device, but it also gives rise to irreversible heat transfer and friction, which has an adverse effect on the efficiency (Yu and Jaworski, 2010).

A standing wave device can operate as an engine or a refrigerator. The regime between standing wave engine and refrigerator is defined by the critical temperature in the stack (Swift, 2002):

$$\nabla T_{crit} = \frac{\omega A |p_1|}{\rho_m c_p |U_1|} \quad (2.1)$$

where ω , A , p_1 , U_1 , ρ_m and c_p are angular frequency, the area of the stack, oscillating pressure, oscillating volume flow rate, mean density and specific heat capacity of the working gas. When the temperature gradient in the stack is lower than the critical temperature, the device operates as a thermoacoustic refrigerator. If the temperature gradient in the stack is greater than the critical temperature, the device works as a thermoacoustic engine. The simplicity offered by the standing wave device still makes it an attractive option, and detailed investigation of specific thermoacoustic system components is often carried in a rig that operates in a standing wave mode due to this simplicity.

2.1.2 Travelling wave thermoacoustic engines and coolers

The idea of using a travelling wave in the thermoacoustic device was first demonstrated by Cerperley, 1979, who observed that sound waves could replace pistons (used in conventional Sterling engines) for gas compression and displacement. The thermoacoustic effect in a travelling wave device occurs in the regenerator placed between two heat exchangers of a travelling wave device (cf. Figure 1.1b). A regenerator is a porous media which acts as an acoustic wave ‘amplifier’ (Yazaki et.al, 1998). It can have different geometries such as a parallel plate, wire screen mesh, etched stainless steel foil, pin-array, and circular pores regenerators (Gardner and Swift, 2003; Mozurkewich, 2001). For a pure travelling wave, the pressure is in phase with the velocity, as shown in Figure 2.3b, but for a

practical traveling-wave engine or cooler, there is a slight phase difference. In a travelling wave device, the working gas undergoes a thermodynamic cycle that is similar to the Sterling cycle due to the excellent thermal contact within the regenerator. The pore size of the regenerator in the travelling wave devices is much smaller than the thermal penetration depth, so the thermal contact between the gas and solid material is excellent. The excellent and reversible heat transfer in the regenerator of the travelling wave system makes it possible for the travelling wave device to be thermally more efficient than the standing wave device but the challenge lies in reducing losses primarily within the core (heat exchangers and regenerator arrangement) of the travelling wave system. The pressure loss imposed by the tightly packed porous material may degrade the acoustic power produced or consumed (depending on engine or heat pump) within the regenerator and possibly affects the overall efficiency of the system (Swift, 2002).

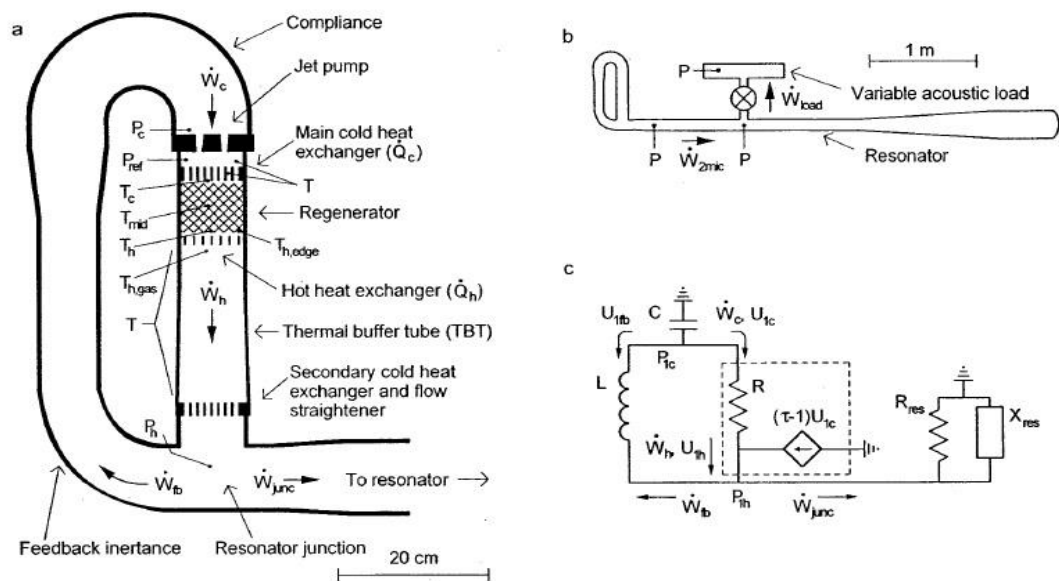


Figure 2.4: (a) Scale drawing of the torus section (b) scale drawing of the engine, resonator and variable acoustic load (load is not to scale). The pressure antinode is located near the top of the torus section (c) lump-element (impedance model) of the engine (Backhaus and Swift, 2000).

The performance of thermoacoustic systems (engine and refrigerator) is usually measured by using the principles of first and second law of thermodynamics. For the engine, the performance is given by:

$$\eta = \frac{\dot{W}}{\dot{Q}_H} \leq \frac{(T_H - T_C)}{T_H} \quad (2.2)$$

The Coefficient of Performance (COP) of the refrigerator is defined by:

$$COP = \frac{\dot{Q}_C}{\dot{W}} \leq \frac{T_C}{(T_H - T_C)} \quad (2.3)$$

where \dot{W} , \dot{Q}_H , \dot{Q}_C , T_H , T_C are the acoustic power, heat fluxes and temperatures at hot and cold thermal reservoirs respectively. The performance of the engine and the COP of the refrigerators are limited by the Carnot's efficiency i.e. the temperature ratio on the right side of both the efficiency and COP expressions (Swift, 1988).

In their work, Backhaus and Swift (2000) described a thermoacoustic-Stirling (Figure 2.4) heat engine that achieved 42% of the Carnot efficiency (30% thermal efficiency). The engine consists of a torus shaped section of variable cross-sectional area attached to a 1/4 wavelength resonator. The engine uses helium at 30bar as working gas and operates at the 80Hz resonance frequency (the frequency at which the maximum pressure amplitude is achieved for a given gas displacement). The highest thermal efficiency is obtained at the drive ratio (maximum pressure amplitude to the mean pressure in the system) of 6% at a temperature of 725°C. Also, the engine is modelled as a lumped-element (cf. Figure 2.4c), an electrical analogy of the thermoacoustics. Tijani and Spoelstra, (2011) further gained more efficiency by achieving 49% of the Carnot engine, i.e. 32% thermal efficiency, in a similar engine by allowing velocity to lag pressure by 30° at the ambient side of regenerator and lead pressure by 30° at the hot side, in addition to minimisation of the acoustic streaming – a steady flow of a fluid driven by the absorption of high amplitude acoustic oscillations. The efficiency of that engine is defined as the ratio of the acoustic power produced by the engine to the heat input into the engine, as given in equation 2.2.

The choice of working gas in thermoacoustic engines and refrigerators is important to the acoustic power output and to the efficiency of the system. Belcher et al. (1999) theoretically and experimentally demonstrated the effects of gas properties on the onset temperature in thermoacoustic systems. Onset temperature was determined by measuring the temperatures in the heat exchangers of a heat driven prime mover. The measured onset temperature against frequency is reported for

different percentages of binary mixtures of He-Ar and He-SF₆. Good agreements between theoretical and experimental results were reported for all percentages of He-Ar. Similar results were also reported for low percentages of He-SF₆. A working gas with a high ratio of specific heat capacities and low Prandtl number is proposed for thermoacoustic refrigeration. On the other hand, a working gas with a low ratio of specific heat capacities and high Prandtl number is proposed for the thermoacoustic engine.

2.2 Modelling of thermoacoustic effect

Modelling, design and development of thermoacoustic systems and their components are widely based on Rott (1980) acoustic approximation to thermoacoustics, as detailed by Swift (1988, 2002). This approximation is commonly referred to as linear theory within the thermoacoustic community. In linear theory, a plane wave is assumed, and all terms higher than the first order in the thermoacoustic continuity and momentum equations are considered negligible compared to the mean terms, except in the energy equations. The oscillating variables in thermoacoustic systems are approximated as:

$$P = P_m + \text{Re}[p_1(x)e^{i\omega t}] \quad (2.4)$$

$$U = \text{Re}[U_1(x)e^{i\omega t}] \quad (2.5)$$

$$u = \text{Re}[u_1(x, y, z)e^{i\omega t}] \quad (2.6)$$

$$T = T_m(x) + \text{Re}[T_1(x, y, z)e^{i\omega t}] \quad (2.7)$$

$$\rho = \rho_m(x) + \text{Re}[\rho_1(x, y, z)e^{i\omega t}] \quad (2.8)$$

$$\mu = \mu(x) \quad (2.9)$$

$$k = k(x) \quad (2.10)$$

where, P , U , u , T , ρ , μ , and k are the pressure, volume flow rate, velocity, temperature, density, viscosity and thermal conductivity, respectively. $\text{Re} []$, subscript m and subscript 1 denote real part, mean variables and first harmonic oscillation of the time-dependent variable, respectively. The complex notation makes use of $i = \sqrt{-1}$ and the identity $e^{i\omega t} = \cos(\omega t) + i\sin(\omega t)$. The linear theory

neglects terms higher than the first order. Additionally, the gradients of pressure in the y and z directions are small and assumed to be negligible. Therefore, the oscillating pressure is always written as a function of x (axial dimension in the direction of wave propagation) only. The mean pressure, P_m , is a constant and is independent of locations x , y or z , since the gradient in the mean pressure would cause gas to accelerate. Other flow variables have the same form as ρ and T . The oscillating variables are assumed to be small in comparison to the mean value (i.e. $\rho_1 \ll \rho_m, T_1 \ll T_m$). The product of two oscillating variables is very small and therefore negligible. The mean values of T and ρ depend only on the flow direction, x , which means that only the oscillation can cause gradients perpendicular to the direction of flow. The velocity in the direction of flow, u , is larger compared to the other components, v and w . Therefore, the flow is assumed to be one-dimensional (1D), mono-frequency and the oscillating flow is also assumed to be steady according to Rott's assumptions.

The thermoacoustic approximations to momentum, continuity and energy equations are defined by (Swift, 2002):

$$i\omega\rho_1 + \rho_m \frac{\partial u_1}{\partial x} = 0 \quad (2.11)$$

$$i\omega\rho_m u_1 = -\frac{\partial p_1}{\partial x} + \mu \left(\frac{\partial^2 u_1}{\partial y^2} + \frac{\partial^2 u_1}{\partial z^2} \right) \quad (2.12)$$

$$\rho_m c_p \left(i\omega T_1 + u_1 \frac{dT_m}{dx} \right) - i\omega p_1 = k \left[\frac{\partial^2 T_1}{\partial y^2} + \frac{\partial^2 T_1}{\partial z^2} \right] \quad (2.13)$$

The general solution of equations (2.11), (2.12) and (2.13) can be obtained as given by Swift (2002) and they the basic thermoacoustic equations used to calculate the pressure, velocity and temperature of the flow for further analysis such as the acoustic losses, acoustic power and total power produced within the selected area of interest. Equation (2.12) represents the differential equation for $u_1(y, z)$. When boundary condition $u_1 = 0$ at the solid surface, the solution for the equation can be written as:

$$u_1 = \frac{i}{\omega\rho_m} [1 - h_v(y, z)] \frac{dp_1}{dx} \quad (2.14)$$

between the wall and the fluid (i.e. spatial-average thermal function (f_k)). The shape factor of other geometries that are also commonly used in thermoacoustics are given in Arnott et al. (1991) and Swift and Keolian (1993). In the thermoacoustic approximation to momentum and energy equations, the attenuation in thermal relaxation and viscous shear are considered, but the attenuation in the acoustic wave is neglected. The relationship between the real and imaginary parts of $f_{k,v}$ and the ratio of hydraulic radius to the penetration depth is shown in Figure 2.5 for different geometries. For the large channel size compared to the penetration depth ($r_h \gg \delta_{k,v}$), most of the fluid experiences virtually no viscous shear force and has a uniform velocity profile. Therefore, both f_k and f_v functions approach zero. The fluid expands and compresses adiabatically inside the channel. For a small channel ($r_h/\delta_{k,v} \approx 0$), the fluid has perfect thermal contact with the solid structure as it expands and compresses.

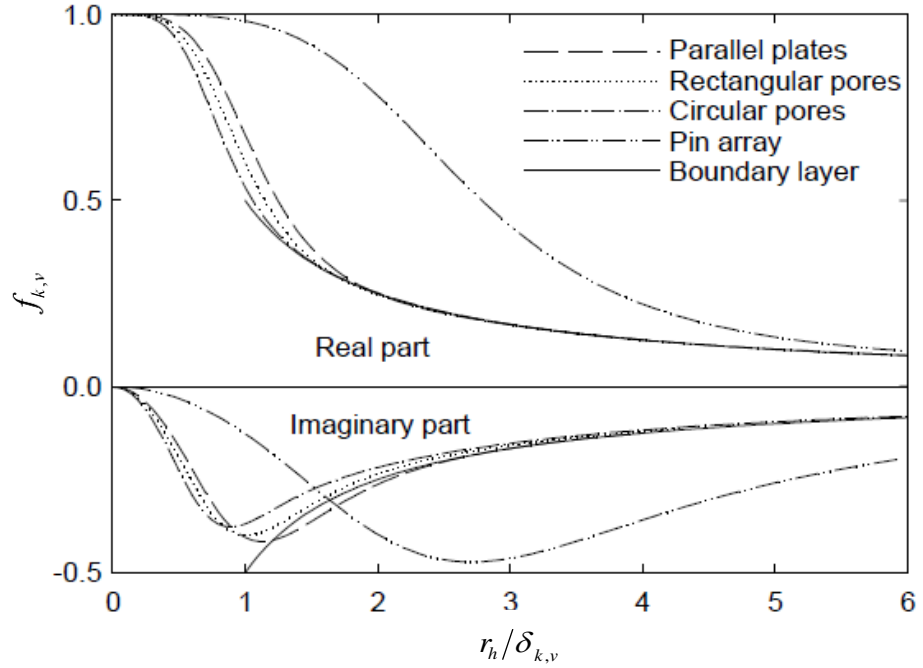


Figure 2.5: Spatial average thermoviscous function for different geometries.

$r_h/\delta_{k,v}$ is the ratio of hydraulic radius to the penetration depths (δ_k, δ_v - the lengths perpendicular to the gas oscillations). r_h/δ_v yields f_v and r_h/δ_k yields f_k (Swift, 2002).

The simplest form of thermoacoustic theory is the lossless model. The lossless model neglects the effect of viscosity. The analytical solution of pressure and velocity amplitudes is given as (Swift, 2002):

$$p_1(x) = p_o \cos(k'x) \quad (2.20)$$

$$u_1(x) = \frac{P_o}{i\rho_m a} \sin(k'x) \quad (2.21)$$

where p_o and a refer to the pressure amplitude at the pressure antinode (reference point) and the speed of sound, respectively. The term $k' = 2\pi/\lambda$ is the wave number. In a location where viscous effects are minimum and negligible, the lossless model provides a solution that is useful, especially at the locations where the flow is not disturbed by the presence of any physical elements. In real situations for the thermoacoustic devices, the viscous effect will be present. This is because most of the noble gases commonly used in thermoacoustics have almost the same size of viscous and thermal penetration depths. Therefore, viscous and thermal effects are both significant in the development of the thermoacoustic effect. This is an important reality that needs to be considered carefully, especially within the area of the internal core of the thermoacoustic devices (stack/regenerator and heat exchangers) where the viscous effect can become important and significant.

In thermoacoustics, the acoustic power measurement in the thermoacoustic engine and cooler is required for the analysis of performance of the whole system or often the individual components such as heat exchangers and stack/regenerators. The measurement of the pressure amplitude, the volumetric velocity amplitude, and the phase between these variables is required for obtaining the acoustic power.

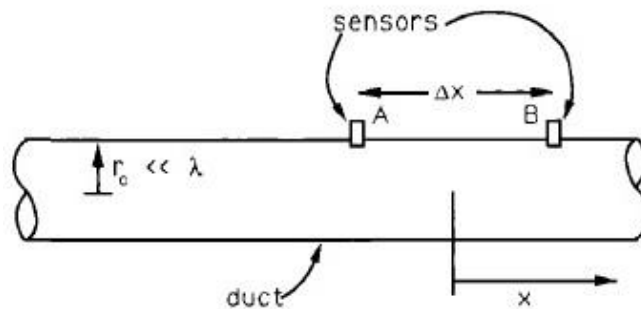


Figure 2.6: Schematic diagram of two-microphone method in circular duct (Fusco et al., 1992)

The pressure amplitude can be measured directly by using pressure sensors. However, the measurement of volumetric velocity is more challenging. One of the common methods for acoustic power measurement within the thermoacoustic community is based on the work of Fusco et al. (1991) who measured the acoustic power flowing through a duct, Figure 2.6, using two pressure sensors. The method is commonly referred to as ‘two-microphone method’ and has been experimentally validated (Swift et al., 1999; Tijani and Spoelstra, 2008; Biwa et al., 2008; Abduljalil et al., 2011).

In the two-microphone method, the velocity is related to pressure gradient by $i\omega\rho_m u_1 = -dp_1/dx$ if attenuation is neglected and $\Delta x \ll \lambda$ so that the approximate volume flow rate midway the two sensors is:

$$U_1 \cong \frac{i\pi r_o^2}{\omega\rho} \frac{P_A - P_B}{\Delta x} \quad (2.22)$$

The midway pressure is:

$$p_1 \cong \frac{P_A - P_B}{2} \quad (2.23)$$

The acoustic power is therefore given as:

$$\dot{W} = \frac{\pi r_o^2}{2\omega\rho\Delta x} |p_A||p_B| \sin \theta_{AB} \quad (2.24)$$

By taking into account an attenuation, a boundary layer approximation and an arbitrarily large Δx , a relation by which a higher accuracy can be achieved is given by (Fusco et al., 2002):

$$\begin{aligned} \dot{W} = & \frac{\pi r_o^2}{2\rho a \sin\left(\frac{\omega\Delta x}{a}\right)} \left(\text{Im}(p_A \tilde{p}_B) \left\{ 1 - \frac{\delta_v}{2r_o} \left[1 - \frac{\gamma-1}{\sqrt{\sigma}} + \left(1 + \frac{\gamma-1}{\sqrt{\sigma}} \right) \frac{\omega\Delta x}{a} \cot \frac{\omega\Delta x}{a} \right] \right\} \right. \\ & \left. + \frac{\delta_v}{4r_o} (|p_A|^2 - |p_B|^2) \left[1 - \frac{\gamma-1}{\sqrt{\sigma}} + \left(1 + \frac{\gamma-1}{\sqrt{\sigma}} \right) \frac{\omega\Delta x}{a} \csc\left(\frac{\omega\Delta x}{a}\right) \right] \right) \end{aligned} \quad (2.25)$$

Where p_A , and \tilde{p}_B are the pressure amplitude at locations A and B. λ , θ , a and ‘ \sim ’ are wavelength, phase angle, sound speed and complex conjugate. The two-microphone method is sensitive to the location of the two sensors, the phase

difference between the two sensors, a sufficient accuracy of the sensor (better than 0.01°) and the flow conditions (Swift, 2002; De Blok, 2013).

There are many performance parameters and length scales that are used in the design and analysis of thermoacoustic systems. These key parameters which are usually combined in different ways to achieve the desired design and operating performance include:

The wavelength of sound, defined along the wave propagation direction x (the direction of motion of gas) as:

$$\lambda = \frac{a}{f} \quad (2.26)$$

where f is the frequency. When gas inertia contributes to the resonance behaviour, the whole length of thermoacoustic engine or refrigerator may typically be a half wavelength or a quarter wavelength (cf. Figure 2.1b). The standing wave test rig in this study is a half-wavelength ($\frac{\lambda}{2}$). The speed of sound for ideal gases can be expressed as:

$$a = \sqrt{\frac{\gamma P_m}{\rho_m}} = \sqrt{\gamma R_{sp} T} \quad (2.27)$$

where R_{sp} is a specific gas constant. The speed of sound is dependent on the temperature and the working fluid. This relation assumes that the sound propagation process is adiabatic. The mean density of the working fluid is related to its mean pressure through the ideal gas law, defined as:

$$P_m = \rho_m \gamma R_{sp} T \quad (2.28)$$

Of equal high importance are the thermal and viscous penetration depths (δ_k and δ_v). They are the lengths perpendicular to the gas oscillations. At distances that are much greater than these depths, the gas feels no thermal or viscous contact with the solid boundaries. When the components (e.g. heat exchangers) where the lateral dimensions are of the order of the thermal or viscous depths, the gas does feel thermal or viscous effects from the solid boundaries. The thermal penetration depth is defined as:

$$\delta_k = \sqrt{\frac{2k}{\omega\rho c_p}} = \sqrt{\frac{2\kappa}{\omega}} \quad (2.29)$$

The viscous penetration depth is defined as:

$$\delta_v = \sqrt{\frac{2\mu}{\omega\rho}} = \sqrt{\frac{2\nu}{\omega}} \quad (2.30)$$

where κ (k/ρ) is the diffusivity of the gas, μ and ν are the dynamic and kinematic viscosities, ρ and c_p are the density and specific heat capacity of the working gas. $\omega = 2\pi f$ is the angular frequency of oscillation (f is the frequency). It is within these layers that heat exchange with the working gas and viscous shear forces occur. Turbulence can promote heat exchange with the working gas rapidly within and outside the thermal penetration depth, while the viscous shear forces can result in the dissipation of acoustic power.

The square of the ratio between the thermal and viscous penetration depths can be written in terms of Prandtl number (Pr) which is the ratio of kinematic viscosity to thermal diffusivity. It can be applied to characterise the relative magnitude of the viscous and thermal effects in the thermoacoustic study as previously remarked and is written as:

$$\text{Pr} = \left(\frac{\delta_v}{\delta_k} \right)^2 = \frac{\mu c_p}{k} \quad (2.31)$$

The displacement amplitude is also another important parameter (ξ_1), which represents half of the total excursion of the gas parcel during one acoustic cycle as shown in Figure 2.1a on the upper left. It expresses the ratio of velocity amplitude, u_1 , and angular frequency of the acoustic wave. Its value can be found at any distance in the thermoacoustic system using the linear theory approximation:

$$\xi_1 = \frac{|u_1|}{\omega} = \frac{p_o}{\omega\rho_m a} \sin(k'x) \quad (2.32)$$

where k' and x are the angular wavenumber which is defined as the ratio of angular frequency to the speed of sound in the air ($k' = \omega/a$), and the axial location in the direction of wave propagation.

This value is employed to be an appropriate length of heat exchangers in the thermoacoustic systems (Swift, 1988). In thermoacoustic engines and refrigerators typically the gas displacement amplitude $|\xi_1|$ is much larger than the penetration depths, but still much smaller than the acoustic wavelengths, i.e. $\delta_v, \delta_k \ll |\xi_1| \ll \lambda$.

The drive ratio constitutes a parameter which is used to evaluate the intensity of thermoacoustic oscillations (Swift, 2002) and it is defined as the ratio of the pressure amplitude at the pressure antinode to the mean pressure.

$$DR = \frac{|P_o|}{P_m} \times 100\% \quad (2.33)$$

Other dimensionless numbers of high relevance in the current study are briefly reviewed here. The Reynolds number (Re) is the ratio of the inertial to viscous forces within a fluid flow and is often used as an indicator of flow conditions, for example, laminar against the turbulent flow.

$$Re = \frac{\rho u D_h}{\mu} \quad (2.34)$$

where u is the fluid velocity. For a heat exchanger with simple geometry, the hydraulic diameter is defined as the ratio of four times the cross-sectional area, A_c , to the perimeter of the channel, Π :

$$D_h = \frac{4A_c}{\Pi} \quad (2.35)$$

The porosity of the heat exchanger is also an important parameter. For regular geometry, it can be defined as the ratio of the minimum free-flow area for gas (cross-sectional area), A_c , to the total frontal core area of the heat exchanger, A_f :

$$\sigma = \frac{A_c}{A_f} \quad (2.36)$$

For a parallel plate heat exchanger with a thickness of t_p and plate spacing of d , the volumetric porosity is:

$$\sigma = \frac{d}{d + t_p} \quad (2.37)$$

In the characterisation of heat transfer performance of heat exchangers, the Nusselt number is an important parameter. The Nusselt number (Nu) is a dimensionless form of the heat transfer coefficient (h), which relates the heat transfer coefficient of the working medium and the characteristic length – hydraulic diameter, to its thermal conductivity, k :

$$Nu = \frac{hD_h}{k} \quad (2.38)$$

Heat transfer coefficient (h) as it appears in the definition of Nu , is defined as:

$$h = \frac{q}{\Delta T} \quad (2.39)$$

where, q is the heat flux. ΔT is the temperature difference between the solid medium and the fluid temperature, being referred to as the thermal potential for heat transfer coefficient. In oscillatory flow, the fluid temperature changes in time and location due to the forward and backwards movement of the gas particles. Heat transfer coefficients as typically defined for the steady flow may not strictly be appropriate for oscillating flow. Until now, it appears that there is no general guideline for articulating the way by which the heat transfer coefficient can best represent the oscillatory nature of the reciprocating flow. This question of how to define the thermal potential for heat transfer coefficient to accurately reflect the performance of heat exchanger in oscillatory flow will be addressed in the current work.

The Colburn-J factor is often used in steady-flow applications. Its usefulness comes from the Chilton and Colburn-J Factor analogy. This analogy states that heat, mass, and momentum transfer in thermally and viscously fully-developed steady flows are all related to each other by constant conversion factors. The Colburn-J factor can be defined as:

$$j_c = \frac{Nu}{RePr^{1/3}} \quad (2.40)$$

Beyond the linear theory, three-dimensional fluid flow and heat transfer conditions in thermoacoustic engines and refrigerators can be physically modelled by Navier-Stokes equations, given as (Versteeg and Malalasekera, 2007):

$$\frac{\partial \rho}{\partial t} + \nabla \cdot (\rho \vec{v}) = S_C \quad (2.41)$$

$$\frac{\partial}{\partial t} (\rho \vec{v}) + \nabla \cdot (\rho \vec{v} \vec{v}) + \nabla p = \nabla \cdot (\vec{\tau}) + S_M \quad (2.42)$$

$$\frac{\partial}{\partial t} (\rho E) + \nabla \cdot (\vec{v} (\rho E + p)) = \nabla \cdot (k \nabla T + (\vec{\tau} \cdot \vec{v})) + S_E \quad (2.43)$$

where

$$\begin{aligned} \tau_{xx} &= -\frac{2}{3} \mu \frac{\partial v}{\partial y} + 2\mu \frac{\partial u}{\partial x}; \quad \tau_{xy} = \tau_{yx} = \mu \left(\frac{\partial u}{\partial y} + \mu \frac{\partial v}{\partial x} \right); \\ \tau_{yy} &= -\frac{2}{3} \mu \frac{\partial u}{\partial x} + 2\mu \frac{\partial v}{\partial y}; \quad \tau_{zz} = -\frac{2}{3} \mu (\nabla \cdot \vec{v}) + 2\mu \frac{\partial w}{\partial z}; \\ \tau_{zx} = \tau_{xz} &= \mu \left(\frac{\partial u}{\partial z} + \mu \frac{\partial w}{\partial x} \right); \quad \tau_{yz} = \tau_{zy} = \mu \left(\frac{\partial w}{\partial y} + \mu \frac{\partial v}{\partial z} \right) \end{aligned} \quad (2.44)$$

Equations (2.41), (2.42), (2.43) and (2.44) are the mass conservation, momentum and energy equations, and the viscous stress tensor, respectively. \vec{v} is the velocity vector, S_C , S_M and S_E are the source terms which represent user-defined features as commonly available in commercial software such as ANSYS Fluent. For compressible flows, such as those present in thermoacoustic devices, the stress tensor takes a slightly different form and is written as:

$$\tau_{ij} = -p \delta_{ij} + \mu \left(\frac{\partial u_i}{\partial x_j} + \frac{\partial u_j}{\partial x_i} - \frac{2}{3} \delta_{ij} \vec{\nabla} \cdot \vec{v} \right) \quad (2.45)$$

where δ_{ij} is the Kronecker delta.

2.3 Heat exchangers in oscillatory flow

Appropriately designed heat exchangers are critical to the overall efficiency of energy systems such as thermoacoustic engines and pulse tube coolers in cryogenics. This is due to the possible potential gain in the efficiency of the system which could result from an improved heat exchanger design. However, the presence of acoustically induced flow and cyclic flow reversal at certain distances in the thermoacoustic system makes the design of heat exchangers a challenging task. Additionally, the use of the data from unidirectional flow for the prediction of heat

transfer performance of heat exchanger under oscillatory is still open to criticism, due to simultaneous spatial and temporal variations of the oscillating variables. In this section, the review of numerical and experimental studies on heat exchangers will be given.

Garret et al. (1994) observed that the design and analysis of heat exchangers in oscillatory flow are fundamentally different from that of unidirectional flow. The most significant difference is the fact that in oscillating flow, the oscillating gas parcels only move a limited distance before reversing their direction, which implies that the heat transfer in oscillatory flow cannot arbitrarily be increased by increasing the heat transfer area of the heat exchanger. Therefore, the authors designed and built a finned-tube heat exchanger that was incorporated into their thermoacoustic device. However, the authors did not discuss the effect of operating conditions on the performance of their heat exchanger and no performance correlation for the general use was given.

2.3.1 Heat transfer in oscillatory flow

Heat transfer and flow structures in the heat exchangers under oscillating flow conditions have been studied theoretically, numerically, experimentally or through the combination of different methods by the researchers within the thermoacoustic community. To find the optimal length of the heat exchanger in oscillatory flow and quantify the magnitude of heat transfer between the gas and solid wall of thermoacoustic systems, Piccolo and Pistone (2006) integrated linear acoustic theory through numerical calculus with a simple energy conservation model. The investigation was based on the simple geometry of parallel plate heat exchangers and the assumption that the flow is laminar, which made it possible to omit the effect of non-linearity and turbulence within the range that their operating conditions covered. The effects of acoustic amplitude, plate spacing, plate thickness and Reynolds number on the heat transfer characteristics were examined. They demonstrated, in their results, that the optimal length of the heat exchanger is a function of plate spacing, and concluded that the length of the heat exchanger should match the peak-to-peak particle displacement amplitude when the plates are separated by one or two thermal penetration depths. They compared their results with the Time-Average Steady-Flow Equivalent (TASFE) and Root Mean Square Reynolds Number (RMSRe). The authors also compared their results with

experimental results of Brewster et al. (1997). Their results correlated well with the TASFE model at Reynolds numbers below 700 (based on velocity amplitude and heat exchanger length). At a Reynolds number of 2000, however, the TASFE approximation and RMSRe-modified Hausen correlation overestimated heat transfer by about 40%. They pointed out that the TASFE and other quasi-steady models should not work well at plate spacing less than a couple of thermal penetration depths because steady flow correlations are not developed based on internal flow, rather they are based on external flow. Their proposed model, the TASFE and the RMSRe models predicted higher Nusselt numbers compared with the experimental data of Brewster et al. (1997), by 20% 32%, and 39%, respectively. The observed discrepancies in their results are attributed to the type of geometries since a parallel-plate structure was utilised in the numerical model, while a ceramic lattice of parallel square ducts was used in the experiment of Brewster et al. (1997). Differences in the methods of evaluation were also cited as a possible cause of the discrepancy.

A recent extension of the work reviewed above is the time-averaged numerical method of temperature and heat flux for parallel plate thermoacoustic heat exchangers, which is presented by Piccolo (2011). The new model was developed based on one-dimensional linear thermoacoustic theory incorporating the two-dimensional energy balance. The physical domain involves a pair of heat exchangers and a stack. The numerical work involves various parametric investigations at different sizes of the heat exchanger plate and the effect of several flow conditions on heat transfer performance. These studies include the effects of temperature difference, drive ratio, heat exchanger length and fin interspacing, and blockage ratio on heat transfer performance. The author reported heat transfer coefficient predictions with errors in the range between 36% and 56% when compared to the experimental results of Nsofor et al. (2005), Mozurkewich (2001), Brewster et al. (1997), and Paek et al. (2005), at moderate and high acoustic Reynolds number. Several important characteristics that influence the performance of the parallel-plate heat exchanger are discussed. Assuming symmetry for flow and geometry, the computational domain selected for the study is simplified considerably into half of the plate thickness and half of the gap between the plates. The simplified domain together with the time-averaged approach is computationally efficient in solving the problem and results in delivery. However, simplification could overlook the details

which might influence the performance of real systems when put into practice. In addition, the model suffers quite a few limitations of which the most important is that the model does not account for the entrance and exit effects which become relevant near the sudden change of cross section as can be found at the ends of heat exchangers. One of the final conclusions of the study is that the fin length along the axial direction of particle oscillation can be chosen considerably lower than the peak-to-peak displacement amplitude without compromising the heat exchanger performance. This has the benefit of reducing the viscous losses.

Mozurkewich (1998) developed an analytical model based on the parallel geometry of both the stack and heat exchanger. The author described the model as one-dimensional, and they first applied it to the thermally insulated stack and then extended it to the heat exchanger adjacent to the stack. The assumptions of laminar flow and an additional assumption that the variation in gas temperature occurred only along the length of the heat exchanger or stack were imposed. The author observed that the gas temperature within the heat exchanger could be quite non-uniform, rather than being anchored to the wall temperature. A plot to assist in sizing of heat exchangers for practical thermoacoustic devices was proposed. However, the complex flow conditions between the stack and heat exchanger were not considered. Therefore, the model was subjected to experimental tests, since it is likely that it may introduce significant inaccuracies when compared with experimental results. The model provided several interesting results. Also, a temperature difference between the heat exchanger and the adjacent stack end increases the net heat transfer between the gas and heat exchanger. The optimal heat exchanger length given by the model was about equal to the peak-to-peak acoustic displacement, and optimal plate spacing was shown to be equivalent to a few thermal penetration depths in the gas.

Herman and Chen (2006) studied the performance of parallel-plate heat exchangers and stacks via numerical modelling. Their model assumed that the exchanger and stack plates were of the same thickness, width, and spacing, with either no gap or a small gap between them. The flow was assumed to be laminar, and constant temperature and constant heat flux along the heat exchanger tubes were considered as boundary conditions. In their results, they noted that the thermal performance of one heat exchanger had a negligible impact on the performance of the heat exchanger at the other ends of the stack, the condition suggested that the

performance of two exchangers could be considered independently during the design process. They also found that the temperature of the stack plates was one-dimensional and linear along the stack, except at the edges near the heat exchangers where the temperature distribution became two-dimensional and very nonlinear. High heat fluxes occurred near the edges as well, with zero net heat flux elsewhere along the stack. Although not clearly mentioned by the authors, these results suggest that the edge shape of a heat exchanger or stack could have a considerable impact on heat transfer between heat exchanger and stack.

Brewster et al., (1997) studied the temperature discontinuities between heat exchangers and stacks in thermoacoustic devices. They derived an analytical expression for the heat transfer coefficient based on the assumption of perfect heat transfer within the heat exchanger, and the assumption of laminar flow and same parallel-plate geometry in both the heat exchangers and the stack. They calculated their heat transfer coefficient based on the heat flux at the hot heat exchanger and the difference in temperature between the hot heat exchanger and that of the hot end of the stack and predicted it to be linearly dependent on the amplitude of oscillation. They focused on energy flow in the heat exchanger and stack rather than the mechanism for heat flow between them. The authors found significant differences in temperatures between adjoining heat exchanger and stack of thermoacoustic prime movers. They compared their expression against experimental results obtained from a controlled experiment that was designed to measure the heat transfer coefficient between stack and heat exchanger inside a longitudinal resonator. They found that the analytical expression overestimated the stack/heat exchanger heat transfer coefficient by about 20% when the experiment was run at low to moderate acoustic amplitudes. At higher amplitudes, however, the predicted results were too low, and no explanation was given for this effect. However, it is important to note that gaps existed between the heat exchangers and stack in the experimental device and that their model did not consider the potential impact of these gaps. No heat transfer correlation is proposed from their results, but a useful insight into the temperature discontinuities between the stack and the heat exchanger can be inferred from the findings. Also, convection was identified as the dominant heat exchange mechanism within the thermoacoustic core elements forced by the action of oscillation.

Zhao and Cheng (1995) conducted a numerical study of convective heat transfer in periodically reversing flow. Their geometry is a single pipe of finite length with an

indication of the rounded entrance and exit edge shape. Their pipe is uniformly heated, and the imposed boundary conditions consist of a forced laminar, incompressible, and fully developed flow with a developing thermodynamic layer. The numerical model is a two-dimensional solution. The thermal potential for their heat transfer coefficient was obtained from the difference of wall temperature and the fluid temperature at the inlet or exit of the pipe. Their results showed that four parameters govern heat transfer between the gas and tube – the Prandtl number, the ratio of gas displacement to tube diameter, the ratio of tube length to diameter, and the oscillating Reynolds number (the product of the square of diameter and the angular frequency, divided by the gas viscosity). For a fixed ratio of length to diameter (L/D), they found that heat transfer increases with either increasing displacement or Reynolds number. They also found that the ratio of length to diameter significantly impacts heat transfer. The results further reveal that “annular” effects also exist in the temperature profiles of an oscillatory flow at high kinetic Reynolds number near the entrance and exit locations of the tube. The annular effect is a phenomenon where maximum velocity or temperature occurs at a location near the wall rather than at the core (Zhao and Cheng, 1995). From the results, the authors derived correlation for temporally and spatially averaged Nusselt number $Nu = 0.00495(x/D)^{0.9} Re_{\omega}^{0.656}(43.74(D/L)^{1.18} + 0.06)$. Their correlation implies that two tubes of the same diameter but different lengths will produce different amounts of heat transfer – even for the same absolute gas displacement and frequency of oscillation. The author, however, did not give any explanation for this effect. Also, an effect that was present but not mentioned by the author was the role of entrance and exit shape of their geometry on the heat transfer solution from their model.

Mozurkewich (2001) tested the predictive power of TASFE using the result of experiments on parallel tube heat exchangers in a modular thermoacoustic refrigerator that is vertically oriented. Three different configurations of heat exchangers were employed in the study. The first one consisted of a configuration with 12 parallel water-carrying tubes with a 5mm gap from one to another. The second one consisted of seven tubes with bigger diameters in comparison to the first one. The third one was a copper screen soldered to transverse four parallel tubes. All the heat exchangers were arranged transversely to the oscillating gas and placed next to a stack. The heat transfer rate was found from the temperature difference measurement between the hot heat exchanger and the adjacent hot end of the stack.

The author reported quantitative agreement between TASFE prediction (based on Zukauska's correlations), and found that TASFE predicted heat transfer well when the acoustic Reynolds number was less than 1000 (Reynolds number based on the peak acoustic velocity between tubes), and noted that this was likely due to the relatively wide spacing of the tubes. Above this Reynolds number, a qualitative agreement was reported. The experimental values were lower than the TASFE estimation by about 20% - 30%. Mozurkewich theorised that this result would likely be true for other geometries as well if the flow could be approximated as external rather than internal flow.

Paek et al. (2005) also investigated the accuracy of the quasi-steady assumption by carrying out an experimental investigation into heat transfer coefficient for a micro-channel heat exchanger in a thermoacoustic cooler. They measured the time-averaged heat transfer in both steady and oscillating flows as functions of Reynolds numbers and compared the results to both TASFE approximation previously investigated and as well as a boundary-layer approximation proposed by Zukauskas (1972) for tubes in cross-flow, which is usually adopted for the thermoacoustic application. Their results showed that the TASFE approximation over-predicted heat transfer by as much as 36% at Reynolds numbers less than 1000 (the Reynolds number is based on acoustic particle velocity). At higher Reynolds numbers the approximation significantly underpredicted the heat transfer. By comparison, the boundary-layer approximation was off by as much as 114% at the same lower Reynolds numbers and under-predicted the heat transfer at higher Reynolds numbers. The authors, therefore, suggested a modification by introducing a correction factor that correlates with the oscillatory flow Reynolds number and the steady flow Reynolds number, considering the difference of particle velocity between the suction and ejection flow direction. The modified Reynolds number is applied to a steady flow correlation and the resulting Colburn j-factor, $j_c = Nu / Re Pr^{1/3}$, was compared to the experimental result. A good agreement was achieved. Based on the experimental results, it is concluded that the heat transfer prediction from DeltaEC (one-dimensional modelling software is commonly used for design purposes in thermoacoustics) may give an error as much as twice the real value.

Nsofor et al. (2007) experimentally investigated the heat transfer performance of a finned tube type heat exchanger of a thermoacoustic refrigeration system. Heat

balance model on a single fin of the heat exchanger was derived, and the heat transfer coefficient was found from the measurement of temperature distribution on the fins using several thermocouples. This method allows the author to obtain the heat transfer coefficient directly from the gas side in their experiment. The effect of the operating frequency and mean pressure on the heat transfer performance of the heat exchanger was studied. They correlated the results from their experiment with a Nusselt number defined in terms of the Prandtl and Reynolds number ($Nu = 0.61Re_{rms}^{0.31}Pr^{0.11}$). Within the Reynolds number investigated, the oscillatory Nusselt number obtained is reported to be lower in comparison to the published data for a steady case. The Reynolds number investigated (calculated using root-mean-square velocity) is reported to be within the range of 15 to 55. The author estimated the deviation in their experimental results to be within 18%. Also, they showed that there is a possible degradation of heat transfer when the frequency increases above the resonance frequency of the system.

Because of the need for accurate heat balance measurement on heat exchanger of thermoacoustic devices, a pair of heat exchangers, usually hot and cold, is often used in an experimental investigation of the thermoacoustic heat exchanger. Researchers within the thermoacoustic community had thought this would provide a solution to the imbalanced heat transfer problem that may be associated with using a single heat exchanger (Nsofor et al., 2007; Tang et al., 2013, 2014), when used for heat exchangers characterisation. An experimental study on heat transfer in oscillatory flows between two identical parallel plate heat exchangers – one hot and one cold, over a range of frequencies and displacement amplitudes, was carried out by Wakeland and Keolian (2004). The two heat exchangers used in the test were constructed as parallel (hollow) flat tubes (used to the approximate parallel plate) made from aluminium material and placed adjacent to each other in the oscillating air. As a form of insulation, a spacer made from a piece of foam was inserted between the heat exchangers to minimise heat conduction from each other and the test apparatus. Acoustic excitation was initiated and sustained within the apparatus filled with air by using an electrodynamic shaker installed at the bottom of the device. Their results are analysed and summarised in terms of heat-exchanger effectiveness, defined as the ratio of the actual heat transfer rate to the amount of heat transfer that would have occurred if the fluid and heat exchanger was in perfect thermal contact ($\varepsilon = \dot{Q} / \dot{Q}_{perfect}$). They compared their measured results to the DELTAE model. The

comparison of measured heat transfer rates in the experiment with the predicted results using the proposed correlations was reported with a deviation of within 10% for high amplitudes. No percentage error was reported for the low amplitude. Based on this comparison, the authors argued that heat exchanger effectiveness should be used to characterise exchanger performance rather than a heat transfer coefficient because the effectiveness method predicted heat transfer at narrow plate spacing far better than the boundary-layer model. However, the author reported an incident when heat transfer rate was observed in their experiments at peak-to-peak displacement amplitude that was smaller than the gap between the two heat exchangers. They termed the situation as ‘low-amplitude enhancement effect’. This occurrence made the heat transfer effectiveness exceed 1.0 when the gap was small.

The work of Kamsanam et al. (2015, 2016) is also based on the investigation of heat transfer in oscillatory flow using a pair of heat exchangers – one hot and one cold. Their heat exchangers are the finned-tube type and fabricated from copper material. The authors considered the effect of fin spacing, fin length and gas displacement amplitude on heat transfer performance. Like Paek et al. (2005), they obtained their water side heat transfer coefficient from a steady flow experiment and subsequently used the result to get the heat transfer coefficient for oscillatory flow. They presented their results in terms of Colbourn-j and later in terms of “effectiveness” proposed by Wakeland and Keolian (2004). The authors also compared their results with models and experimental results from the literature and reported agreement to be generally good. A correlation that is specific to the tube-finned heat exchanger configuration was proposed.

Tang et al. (2014) characterised the heat transfer performance of heat exchangers employed by pulse tube refrigerators in a custom-built experimental apparatus. Their heat exchanger, like that of Nsofor et al. (2007), is fabricated from copper fins and is a water-cooled finned type. They tested its performance in a laminar oscillating flow. They correlated their experimental results in terms of the Nusselt number derived as a function of the maximum Reynolds number (Re_{max}) and the Valensi number (Va), $Nu = b Re_{max}^m Va^n$. The maximum Reynolds number was based on the velocity amplitude of oscillating gas in the channel of the heat exchanger and the hydraulic diameter of fin spacing as a characteristic length. The results indicated that a maximum Reynolds number in the range of 200 – 1,200 and Valensi number in the

range of 150 – 350 could lead to a rise in the Nusselt number. The authors further compared the Nusselt number from their experiment with other existing approaches, including TASFE, RMSRe, boundary layer conduction, the correlations proposed by Zhao and Cheng (1996), and Nsofor et al. (2007). The comparison shows that the boundary layer conduction model achieves a relatively better agreement with their experimental results (with a maximum deviation of 21.5%). They reported their proposed correlation achieved a maximum deviation of 6.3% compared to the experimental data. However, no discrepancies from experimental results from the correlation of Zhao and Cheng (1996), and Nsofor et al. (2007) were reported. The authors theorised that their proposed correlation would better aid the design of the heat exchangers that are commonly used in pulse tube refrigerators.

2.3.2 Flow visualisation and flow structures

Researchers in thermoacoustics often use visualisation techniques to understand different heat transfer and fluid flow phenomena association with the internal core of thermoacoustic devices, specifically the heat exchangers. Lei Shi et al. (2010) demonstrated the use of the acetone-based PLIF measurement technique to study unsteady characteristics of heat transfer processes in a parallel heat exchanger. Two-dimensional temperature distributions of gas around a pair of parallel plate heat exchangers, arranged side-by-side, was obtained as a function of phase angle in the acoustic flow cycle. The investigation covers the drive ratio range of 0.3 – 0.83%. The authors proceeded to obtain a space-averaged Nusselt number with respect to the Reynolds number (defined based on acoustic velocity amplitude and plate separation distance). The thermal potential in their heat transfer coefficient definition was obtained from the difference between the wall temperature of the parallel plate and midpoint temperature on the centre line of the channel over the joining point of their cold and hot heat exchangers.

The authors (Lei Shi et al., 2010) observed heat transfer variations as a function of phase within the flow cycle as shown in Figure 2.7. In addition, the velocity profiles are shown to be affected by temperature. However, the authors concluded that their study was primarily a test-bed for developing a more accurate PLIF method for obtaining time-dependent temperature distributions in an acoustic cycle in thermoacoustic systems, which they hope will further lead to obtaining better temperature gradients and the corresponding heat fluxes.

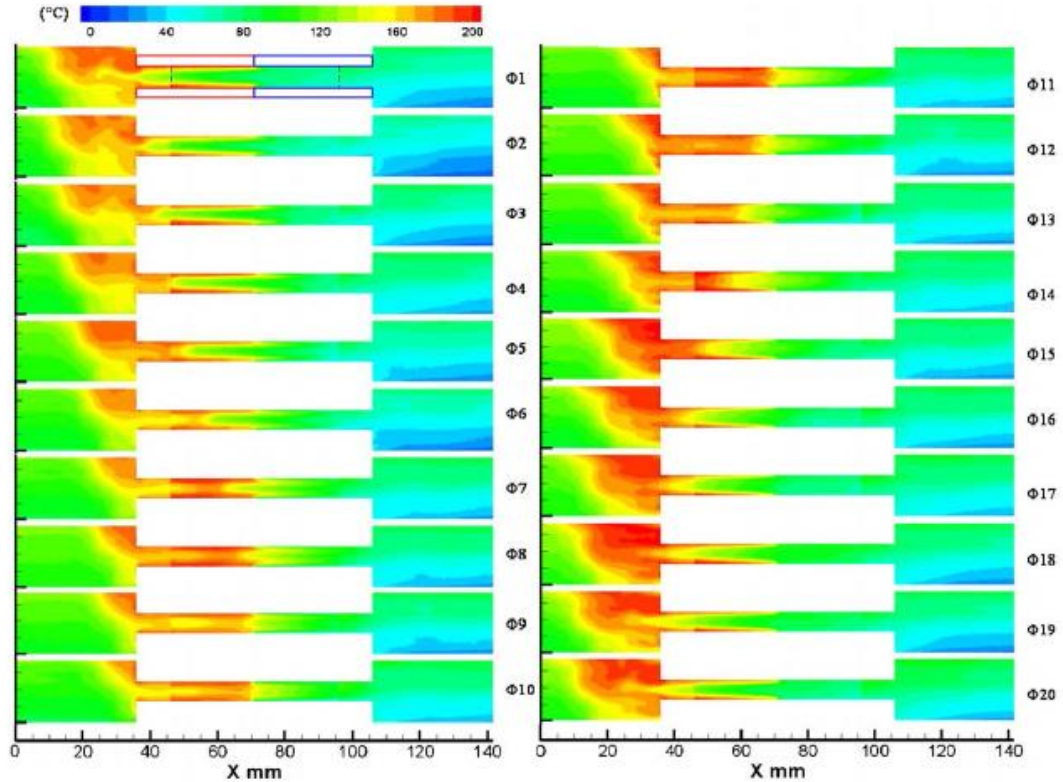


Figure 2.7: Planar-Laser-Induced-Fluorescence (PLIF) visualised temperature field distribution for 20 phases within an acoustic flow cycle around the parallel plate heat exchanger in oscillatory flow (adapted from Shi et al., 2010).

Computational fluid dynamics (CFD) offers the possibility of studying the heat transfer and flow behaviour in the internal core of thermoacoustic technology, for understanding the complexity associated with the presence of the internal core in thermoacoustic devices. The benefit of using CFD simulation includes the possibility of visualising the physics behind different phenomena occurring within the core, coupled with the benefit of investigating a large variety of operating and geometrical effects on the phenomena. Notable research on the CFD approach to modelling of thermoacoustics includes the work of Nijeholt et al. (2005) in which a travelling wave thermoacoustic engine using 2D CFD was modelled. The study, however, omitted the modelling of geometrical details of the heat exchanger.

Mohd-Saat et al. (2013) carried out a 2D CFD study of heat transfer and flow structure inside parallel plate heat exchangers of thermoacoustic devices. The computational domain in the CFD was defined to match the experimental set-up in the work of Shi et al. (2010). The simulation results were also validated based on the experimental data from the same source. The influence of drive ratio (defined as the

ratio of the peak pressure amplitude to the mean pressure in the system) on the fluid mechanics and heat transfer condition was investigated. The Reynolds Averaged Navier-Stokes (RANS) equation was used to model the turbulence flow in author's fluid domain.

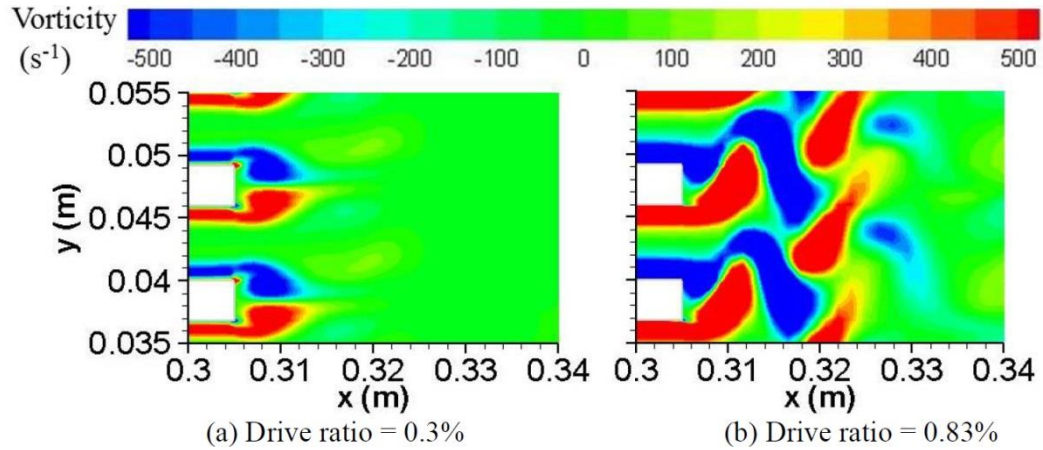


Figure 2.8: Vorticity contour at the end squared edge plate at a flow phase in the acoustic cycle (Mohd-Saat, 2013).

Their simulation results (Mohd-Saat, 2013) show that heat transfer influences a change in flow structure. Hence, the presence of imposed temperature field led to a broken symmetry of time-dependent velocity profiles over one full acoustic cycle. They added that a buoyancy effect could also contribute to the asymmetric velocity profile in their results. The authors reported good agreement between their predicted temperature result and that of the experiment when SST $k-\omega$ turbulent model was used. The formation of vortex structure at the end of squared edge plate at a selected phase in the flow cycle, as observed in their study, is shown in Figure 2.8. They found that the vortex strength increased as the drive ratio increases and concluded that if a high strength vortex gets pushed back into the channel, it will create a strong disturbance which would lead to power dissipation and losses.

In the numerical study of Worlikar and Knio (1996), the effect of vortex structures on the flow characteristics within the locality of the parallel plate stack was investigated. The authors investigated the streamlines (Figure 2.9) and viscous dissipation within the plates in comparison to the open area next to the plates. The numerical study utilises a simplified periodic computational domain covering some length of the open area next to the plates. Streamlines and viscous dissipation

discussion are related to the mechanical energy losses within the model. The author focused mainly on the effects of the drive ratio, stack blockage ratio and stack position in the resonator, boundary layer thickness and the plate aspect length, respectively. It was shown that the dissipation increases with an increase of Stokes layer thickness and length but has not been affected by blockage ratio.

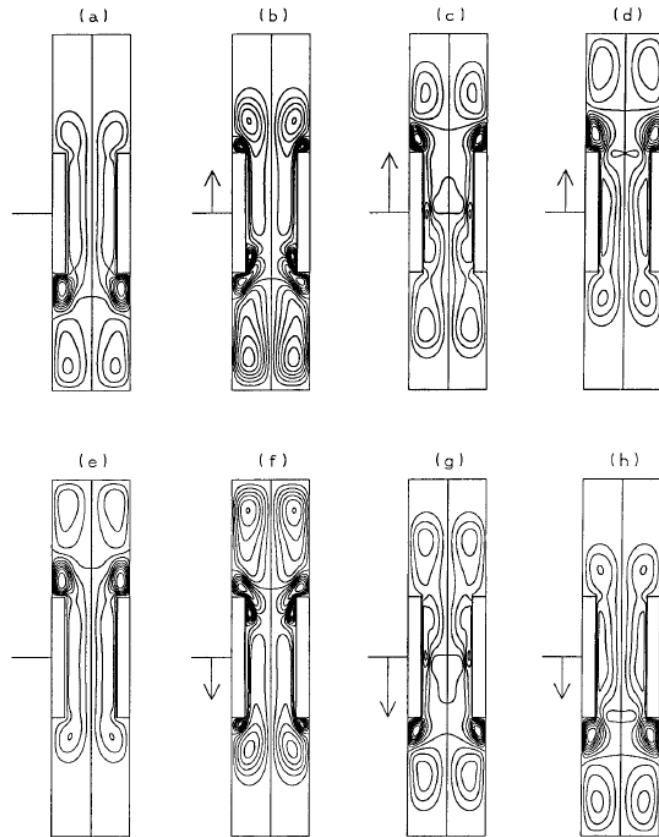


Figure 2.9: Evolution of the stream function distribution for eight phases within an acoustic flow cycle (Worlikar and Knio, 1996)

The study (Worlikar and Knio, 1996) suggests that the dissipation would be higher when the structure is located at the velocity antinode and reduced as it moves further from the antinode, a condition that is related to the difference in the magnitude of velocity at different locations. It is further reported that selection of a suitable length between the end of the plates and the boundary of the computational domain is important so that the vortex shedding that is developed at the end of plates does not interfere with the imposed boundary conditions. A length that is too short can lead to computational error due to the travel of vortex structure across the boundary. In later studies, the authors and their co-investigators made a series of improvements to the model they developed (Worlikar and Knio, 1998; Besnoin and Knio, 2001; Besnoin

and Knio, 2004), which made use of adiabatic stacks and heat exchangers, all working in a thermoacoustic standing wave environment.

2.3.3 Minor losses in oscillatory flow

In a flow at high Reynolds number, additional pressure drops are associated with the transitions between channels, and with changes in the direction of a channel. These effects are known as ‘minor losses’ because in long piping systems such transitions are indeed minor contributors to the overall pressure drop. However, in thermoacoustic devices operating at high amplitudes, the so-called minor losses can be major. A thermoacoustic system relies on oscillatory flow through its internal elements to pump heat over stacks or regenerators to create an acoustic power or cooling effect. The geometrical discontinuity that results from the combination of heat exchangers and other internal elements of a thermoacoustic device also causes flow resistance and non-linear effects (e.g. turbulence, vortex shedding, streaming, etc. (Swift, 2002). The resulting flow resistance and non-linear effect can adversely affect the efficiency of the thermoacoustic system especially when the system operates at high amplitudes (Olstron and Swift, 1997; Gardner and Swift, 2003). Again, the use of the data from unidirectional flow for the prediction of hydraulic performance of heat exchanger under oscillatory flow condition is questionable due to concurrent temporal and spatial fluctuations of the time-dependent variables.

One of the early works that focus on an attempt to understand minor losses in oscillatory flow using numerical approach was conducted by Morris et al. (2004), who studied the minor losses that are associated with an abrupt change in a resonator’s cross-sectional area, using time-accurate high-order numerical modelling. Their sudden change cross section has a 90° sharp edge. The author showed that in oscillating flow, a net pressure drop is established with the pressure in the smaller channel being greater than that in the larger one. They observed that this pressure drop is caused by the difference in the minor losses between the parts of the flow cycle where the sudden change in area is associated with an expansion or a contraction. They also showed that this pressure build up is almost constant along their smaller channel length and that it provides a means by which the minor losses due to the sudden change in the cross-sectional area can be easily measured. The author compared their results to the quasi-steady (Iguchi) hypothesis (the hypothesis assumes that for low-frequency oscillatory flows, the same relation that is used for

steady state flow may be utilised) and found that ‘Iguchi-hypothesis’ under predicts the minor losses by a factor of three. They also compared their results with the experimental results and reported excellent agreements between the results but no information about the percentage of discrepancy was given. The effect of heat transfer on the minor losses caused by the expansion, however, was not considered.

Wakeland and Keolian (2002) analytically demonstrated that the nonlinear resistance of a sudden, square-edged expansion could be significantly different for fully developed laminar flow (Poiseuille flow) as compared to fully turbulent flow (uniform flow profile). This difference can be as high as 3.9 (Poiseuille > uniform flow) for the same plate spacing of a parallel plate heat exchanger. The authors used the well-established laminar oscillating boundary layer theory and developed equations for calculating effective exit-flow minor loss coefficients for time varying, oscillating flows based on frequency, velocity, and porosity of the expansion. They applied their results to velocity profiles found between parallel plates and circular tube heat exchanger geometries and showed that the value of their minor loss coefficient is in the range from 0.6 to 1.1 for uniform and Poiseuille flow, respectively. They argued that the results could represent an improvement over the Borda-Carnot formula for calculating flow losses at the exit from heat exchangers in thermoacoustic devices.

In another study on flow resistance in oscillatory flow, Wakeland and Keolian (2004) experimentally investigated the pressure drop across parallel plate heat exchangers in an acoustic environment to estimate deviation of linear theory from high amplitude measurements, regarding a minor loss coefficient. Their pressure data was collected in the experiments by the same authors (Wakeland and Keolian, 2004) where a pair of two identical parallel plate heat exchangers was studied for performance in terms of “effectiveness”. Resistance was defined as the ratio of the resistive component of the pressure drop across the test section, i.e., the component of the total pressure drop that is in phase with velocity, to the volumetric velocity and it was measured with respect to the heat exchangers’ separation gaps given as:

$$R = \frac{\Delta P}{U_1} = \frac{\Delta P}{A_f u_1} = \frac{\Delta P}{\sigma A_f u_1} \quad (2.46)$$

where A_f is the open cross-sectional flow area. $u_{hx} = u_1 / \sigma$ is the velocity amplitude in the heat exchanger.

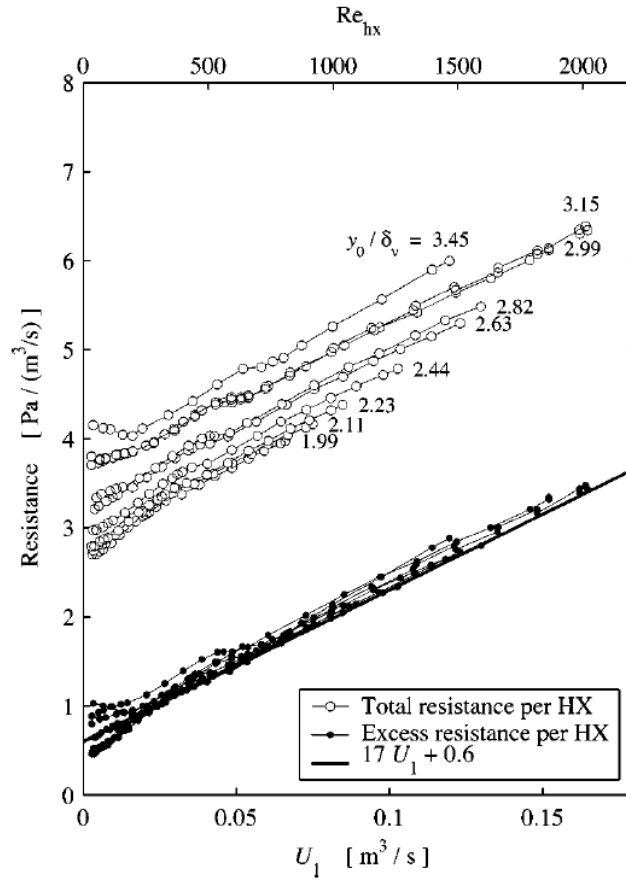


Figure 2.10: Measured acoustic resistance per heat exchanger in the 2 – 6 Hz range for a small heat exchanger separation (peak-to-peak displacement amplitude of 5.5 mm). Open circles are the measured resistance divided by two. Closed circles are resistance per heat exchanger minus the linear theory value and minus the boundary-layer value for the duct (Wakeland and Keolian, 2004).

The pressure drop across the heat exchanger is related to the “effective” minor loss coefficient as:

$$\Delta P = K \frac{1}{2} \rho_m u_{hx}^2 \quad (2.47)$$

They found this minor loss coefficient by subtracting the acoustic resistance predicted by the established linear theory from that measured in their experiment.

The result was plotted as a function of volumetric velocity (an example is shown in Figure 2.10), and the slope of this difference was then used to calculate the minor loss coefficient as follows:

$$K = \frac{2\sigma^2 A_f^2}{\rho_m} \frac{dR}{dU_1} \quad (2.48)$$

The authors referred to expression (2.48) as the effective minor loss coefficient because it presumably includes “entrance effect”, since the hydrodynamic boundary layer is almost certainly thinner near the leading edge of the heat exchanger. They concluded that minor loss coefficient might be less than that predicted in their previous study (Wakeland and Keolian, 2002) for heat exchanger due to non-occurrence of fully developed oscillating velocity profile at high amplitude.

The effect of sudden expansion on heat transfer would be a major consideration for thermoacoustic devices as heat transfer, and temperature differences appear to be concentrated at the ends of the exchanger plates as reported by Brewster et al. (1997) and Herman and Chen (2006). It would seem reasonable that any turbulence or disturbance generated by those ends could impact heat transfer. Ibrahim and Hashim (1992) conducted a computational investigation to study the heat transfer in oscillating flow between two parallel plates with a sudden change in cross section. Their numerical model assumed laminar, incompressible flow with inflow velocity uniform over the channel cross section but varying sinusoidally with time. Their results showed that the instantaneous heat transfer coefficient near the expansion is affected by maximum Reynolds number and Valensi number. They found that instantaneous heat transfer further increased when the thermal expansion of the gas was taken into consideration. The authors reported that this was due to an increase in turbulence at the expansion caused by the additional gas velocity.

To improve the flow condition around the extremity of the internal core of the thermoacoustic system, specifically the heat exchangers, the use of profiled edge shape to minimise minor losses at the entrance and exit of heat exchangers could be useful. The studies above were performed using geometries with square edges (flat edges or zero radius), and simultaneous consideration of heat transfer and acoustic pressure drop was only carried in the study of Wakeland and Keolian (2004).

Marx et al. (2008) experimentally studied the unsteady effects in acoustic waves at geometrical discontinuities in acoustic ducts. The velocity fields in the abrupt change location were measured using PIV and analysed using Proper Orthogonal Decomposition (POD) methods. The abrupt change was created by placing a small step in an acoustic duct, and the suction and ejection stages are defined relative to the acoustic flow direction (Figure 2.11). Effects of displacement amplitude and three different radii (0 - 5mm) of curvature of the rounded edge are considered on

the pressure and energy losses. These effects are considered as a function of Strouhal number (defined in terms of the radius of curvature to the particle displacement amplitude).

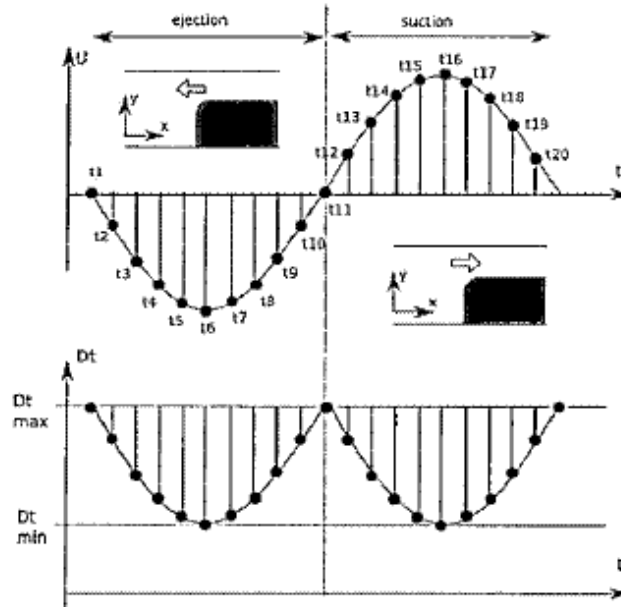


Figure 2.11: Definition of suction and ejection stage in a flow cycle of the abrupt change in cross section and time separation between PIV pulses as a function of time (Marx et al., 2008)

The result showed that an acoustic wave generates a nonlinear flow near the abrupt change in the cross section. The dependency of energy flowing from the first acoustic to nonlinear mode was shown to be largely governed by the Strouhal number. At sufficiently high acoustic levels, and past a value of 0.5 for Strouhal number, the flow separates, and a vortex was formed in the large acoustic duct noticeably during the ejection stage. At large curvature radius of the step, the authors also reported the formation of a vorticity structure in the small channel during the suction phase. The evolution and reproduction of the vortex structure were studied by detecting their centres. The author further reported that the vortex structure at the suction stage has a shorter spatial range than that of the ejection stage and a shorter time of existence.

Smith and Swift (2003) explored the use of a rounded edge shape at the entrance and exit of flow channels in their experiments on the oscillating flow at the abrupt transition between a two-dimensional channel and an essentially infinite space. The effect of minor losses on the time-averaged pressure and acoustic power dissipation

generated by oscillating flow in the rounded entrance and exit rectangular were considered. The authors presented both the acoustic pressure and power dissipated as functions of three different dimensionless parameters. These include the ratio of the radius of the rounded edge to the height of the channel, the ratio of peak-to-peak displacement amplitude to the channel height and the Reynolds number (based on maximum velocity amplitude and the viscous penetration depth). They noted that the first dimensionless ratio governs the severity of the adverse pressure gradient experienced by the exiting flow, which in turn affects the tendency for the boundary layer to separate. The second dimensionless parameter affects the turbulent transition and boundary layer thickness while the third one governs the vortex pair dynamics and steady jet tendencies. They derived an expression for minor loss coefficients at both the ejection and suction stage in the flow cycle in terms of the pressure drop across their geometry, based on the assumption that velocity amplitude is independent of the coordinate perpendicular to the streamwise direction. Pressure measurements are made simultaneously with the velocity measurements using a series of piezo-resistive pressure transducers mounted directly into the channel walls at seven different streamwise positions. It was observed that nonlinear effects result in some distortion of the average velocity waveform. Because of the distortion, the maximum pressure during the ejection does not equal the maximum pressure during the suction. They found that the rounded edge radius reduces the adverse pressure gradient experienced by the flow at the abrupt change in the cross section. They reported that increasing the exit radius minimises minor losses by allowing the flow to expand more in the cross-stream direction near the exit of the profiled channel and that the effect can be enhanced by increasing the Reynolds number. The authors, however, did not consider the effect of profiled edge on heat transfer, and the effect of heat transfer on minor losses. The author concluded that the best hope for understanding the minor losses in oscillatory flow might lie with extensive numerical studies benchmarked against a few limited experimental studies.

Another related work on the use of edge shape on flow behaviour includes that of Petculescu and Wilen (2002) who used a non-resonant, lumped-element technique to experimentally investigate the behaviour of tapered cylindrical flow constrictions (jet pump) in the nonlinear oscillatory flow regime. Their study included the use of a wide range of inlet curvature radii and taper angles in order to determine the minor

loss coefficients for flow at the location of abrupt changes in the cross section. They found that minor loss coefficients are relatively insensitive to all but the smallest curvature radii (sharp edges) and that for fixed radius of curvature, the inflow minor loss coefficient increases with increasing taper angle while the outflow coefficient remains relatively constant. The author compared their oscillatory flow minor loss coefficient to that of steady flow which they equally measured and found that there is good agreement between the two results. They concluded that their results confirmed the Iguchi's hypothesis but would require further confirmatory studies.

Aben et al. (2009) conducted a two-dimensional PIV experiment to study the vortex formation at the transition from the end of a parallel-plate stack to open area. Effect of velocity amplitude, frequency, porosity (plate thickness and spacing), and plate edge shape on vortex formation was investigated. Vorticity pattern at the end of the plate was plotted for different plate edge shapes consisting of rectangular, circular, triangular (90°) and sharp triangular (25°) end shapes as shown in Figure 2.12. It is very interesting to see how the plate-end shape can influence flow behaviour in these plots. The author reported that when the flow is directed outwards of the stack, vortices originate behind the stack plates.

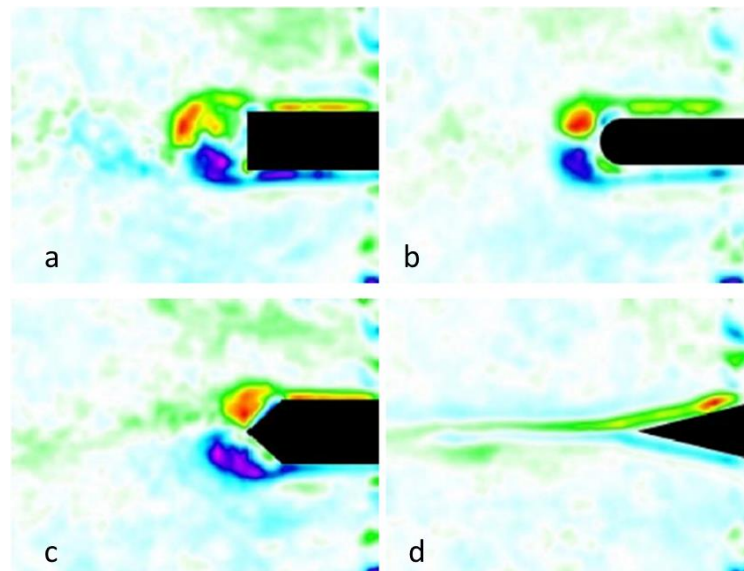


Figure 2.12: Vortex structure as observed at the end of the plate with various edge shapes (a) rectangular (b) circular (c) 90° triangle (d) sharp triangular (25°). Aben et al. (2009).

They (Aben et al., 2009) found that the ratio of Strouhal (defined as the ratio of product of frequency and plate spacing to the velocity amplitude) to the Reynolds

number (defined in the terms of velocity amplitude and the plate spacing) determines the vortex pattern behind the stack plates, varying from a single vortex pair to a complete vortex street, for a squared edge plate. It was shown that different vortex patterns (one vortex pair, two vortex pairs, Vortex Street) could originate behind a parallel plate. In Figure 2.12, the authors observed that due to the absence of sharp corners for the circular edge shape the vorticity plot is smoother compared to the rectangular shape and the two vortices are almost circles. The 90° triangle does have sharp corners and behaves similarly to the rectangular edge shape. The vorticity pattern behind the sharp triangular-edged plate (25° or smaller) differs from rectangular or circular plate edge shape. Instead of a vortex pair or a vortex street, two thin layers of vorticity that do not roll up are formed. Based on these results, they concluded that the choice of a shape could significantly influence the dissipation due to the vortices that are shed off and the heat transfer in the heat exchanger. The author, however, did not consider the effect of temperature on the disturbances generated by different plate edge shapes. Their results showed that streamlined edges could be explored to improve the nonlinear effects such as vortex formation at the extremity of the heat exchangers, for the improvement of efficiency of thermoacoustic engines and refrigerator.

2.4 Summary

The study of heat transfer and acoustic pressure drop in the heat exchanger under oscillatory flow conditions is an important research area in thermoacoustics because it is directly related to the overall efficiency of thermoacoustic engines and coolers. There are two main considerations in the study of heat exchangers in oscillatory flow. The first one is the maximisation of heat transfer, and the second one is the minimisation of acoustic pressure losses. Both effects depend on flow conditions and suggest that the geometry or design of the heat exchanger impacts its performance. The current study focuses on the experimental and numerical investigations of heat transfer and acoustic pressure drop in the heat exchanger configurations that include – T-HEX, F-HEX and parallel-plate heat exchangers, for the application of the thermoacoustic engines and coolers.

Research studies, both numerical and experimental that are relevant to the current work have been reviewed in the sections of this chapter. In the reviewed numerical

studies, the flow and heat transfer through simple geometries have been considered, coupled with the use of a different set of assumptions and boundary conditions to simplify the studies of heat transfer in heat exchangers for thermoacoustic applications (Piccolo and Pistone, 2006 and 2011; Mozurkewich, 1998). In addition to the geometries been simple, there have been no changes in their cross-sections. Heat transfer and temperature differences appear to be concentrated at the ends of the exchanger plates (Brewster et al., 1997; Herman and Chen, 2006), and it would seem reasonable that any turbulence, vortices or disturbances generated by those un-profiled ends could impact heat transfer. The conditions of flow and heat transfer in real thermoacoustic devices are complex and occur within physical structures that are near each other. Therefore, the use of simple geometry to derive a correlation which will be utilised for the design of a practical compact heat exchanger would be questionable. Studies of the influence of cross-sectional changes on heat transfer and acoustic pressure drop as related to oscillatory flow are still scarce.

Quasi-steady approximations are often used for the design of heat exchangers in oscillatory flow. The reviewed literature here shows that quasi-steady approximations failed at higher oscillating velocities (Mozurkewich, 2001; Piccolo and Pistone, 2006). The heat transfer model based on boundary layer conduction also over-predicts heat transfer in oscillatory flow (Paek et al., 2005). Therefore, the design and development of heat exchangers for the thermoacoustic application would need more reliable performance data.

Besides the simplified geometry in the numerical study of heat transfer, the experimental study of heat transfer in the heat exchanger under oscillatory flow include the use of a single heat exchanger (Nsofor et al., 2007; Tang et al., 2013 and 2014) or a pair of heat exchangers (Wakeland and Keolian, 2004; Kamsanam et al., 2014 and 2016). However, even with the use of a pair of heat exchangers for heat transfer study, the issues with heat loss was not resolved or accurately accounted for because of lack of symmetry in the heat exchanger arrangement, therefore, the heat balance measurement from these studies only relies on a heat transfer rate that can further be improved.

The edge shape in the heat exchanger is of high importance in thermoacoustics since it could be used to minimise pressure losses, which can lead to increased efficiency of the system. The reviewed studies considered heat transfer and flow conditions

through a square-edged and abrupt change in the cross section. In thermoacoustic engines and coolers; however, heat exchangers are placed near stacks/regenerators. It would appear reasonable that the vicinity of the regenerator/stack may alter the nonlinear impedances of the heat exchanger by reducing jetting and vortex shedding. Likewise, if the flow is modified in such a way as to mitigate these effects, there may be a corresponding effect on heat transfer. Disturbances produced by the edge shape of the heat exchanger may impact heat transfer as well as generate minor losses. Reducing heat transfer and increasing acoustic pressure losses are both detriments to the overall efficiency of the thermoacoustic system. These effects are considered in the current study, experimentally and numerically.

Another important area in the study of heat exchangers within the thermoacoustic community is the determination of heat transfer coefficients on the process side (gas side) of thermoacoustic engine and refrigerator. The thermal potential for heat transfer coefficients are usually calculated differently in the literature, and most often it is application dependent (Shi et al., 2010; Zhao and Cheng, 1995). In oscillatory flow, the fluid temperature changes in time and location due to the forward and backwards movement of the gas particles, which in turn dictate different heat transfer behaviour compared to that of steady flow. There appears to be no consensus in the literature over the definition of the heat transfer coefficients in the oscillatory flow. The question of how to define the thermal potential in the heat transfer coefficient to reflect the contribution of gas temperatures around the heat exchangers will be addressed in the current work.

The changes of flow variables, for example, velocity in oscillating flow patterns result in a special flow characteristic, and its corresponding heat transfer performance is yet unpredictable. Hence, to understand the heat transfer phenomenon, it is always useful to investigate the fundamental features of the velocity and temperature that shows the behaviour of flow and how it changes the heat transfer across the solid structure. The PIV (Aben et al. 2009) and PLIF measurements (Shi et al. 2010) and numerical simulations (Mohd Saat, 2013) provide important information for the understanding of the fluid flow in parallel plate stacks and heat exchangers, but only in two-dimensional form. The information about the three-dimensional effects that are present for the real heat exchangers in oscillatory flow conditions is still missing. In general, a study on heat transfer and pressure losses in different geometries of heat exchangers are still very

limited. The current study considers three-dimensional effects on heat transfer and acoustic pressure drop of compact heat exchangers from experimental and simulation perspectives.

In summary, the current study would contribute to the improvement of the knowledge of heat transfer and acoustic pressure drop in the heat exchangers under oscillatory flow conditions by:

1. Using symmetrical arrangement of heat exchangers to improve heat balance measurement and the estimation of heat transfer.
2. Using edge shapes at the entrance and exit of the heat exchanger to improve flow condition associated with an abrupt change in cross section and thus minimise acoustic pressure drop, and quantify the effect of the edge shape of heat transfer performance.
3. Simultaneously measuring the heat transfer and acoustic pressure drop to determine the relationship between heat transfer and acoustic pressure drop in the heat exchanger under oscillatory flow conditions.
4. Comparing the experimental results of finding for heat transfer and acoustic pressure drop performance of heat exchangers to the 2D and 3D simulation results obtained by solving full Navier-Stokes equations in the commercial CFD package ANSYS Fluent 17.0 (2015).

Chapter 3

Design and Development of Experimental set-up

This chapter describes the design, the development and the testing of $\frac{1}{2}$ wavelength standing wave experimental set-up driven by a ‘Q-drive (1S102D Acoustic Driver)’ linear alternator. The overview of the experimental set-up is outlined in section 3.1. The descriptions of different parts of the standing wave experimental set-up including the test object (heat exchangers and plate attachments) and the measurement capability of the system are described in section 3.2. Section 3.3 focuses on the instrumentation. The first phase of experimental results is outlined in section 3.4. Measurement uncertainties related to the experimental data are discussed in section 3.5. The summary for the chapter is given in section 3.6.

3.1 Overview

The main aim of this work is to investigate heat transfer and hydraulic performance of cross-flow heat exchangers in a pressurised helium gas environment subjected to acoustic excitation. In this regard, the design of experimental set-up and measurement techniques is considered as one of the primary objectives. Hence, special attention is given to the design stage to enable development of a system that has the required capability of testing the effects of relevant operating conditions (drive ratio, gas displacement amplitude, mean pressure, and temperature) and geometrical parameters (different configurations of heat exchangers and edge shapes) on the heat transfer and acoustic losses in oscillatory flows. The design and development of the set-up involve several considerations that include the capability of the set-up to fulfil the research objectives, the cost and, most importantly, Health and Safety (H&S) requirements because of the high pressure ($\leq 30\text{bar}$) that is involved. The greatest challenge of this research work emerged through the fulfilment of the H&S requirements at the University of Leeds. The design and fabrication of the experimental set-up began at the University of Leicester where the author first enrolled for his PhD before transferring to the University of Leeds for completion. The complication arose from the significant difference in the H&S regulations for ‘high’ pressure equipment in both universities. Meeting and

inspection sessions were held by the team of technicians, H&S officers and the academics at the University of Leeds to decide on how to proceed with the project safely and cost effectively. Unfortunately, the need to fulfil the requirements of high-pressure vessels at the University of Leeds led to the design and development of a second version of the experimental set-up while the first version that was to be assembled and tested was discarded. The first version of the set-up (cf. Ilori et al. 2013) as it was initially designed and fabricated is given in (Appendix – B). The second version is used for experimental work described in this thesis, therefore, the description of the design, fabrication and testing is given in the subsequent sections of this chapter. The main difference between the two versions is the mode of opening of the test section. The first version had a ‘side-entry’ test section while the second version has ‘top-entry’ housing for installing the heat exchangers, supporting spacers and fittings.

3.2 Experimental set-up

The experimental set-up in this study consists of the acoustic driver (Q-drive - 1S102D), test section and three symmetrically arranged heat exchangers (two cold heat exchangers and a hot heat exchanger), gas-charging unit, the hot and cold water circulating loops, 2” pipes, measurement devices and data acquisition system, and the rigid supporting structure. The photograph in Figure 3.1 and the schematic diagram in Figure 3.2 show the overview of the set-up layout. Helium gas is used as working fluid in the experimental set-up at a mean pressure up to 30bar. The total volume of the set-up is 21liters (at 1bar mean pressure). The safety aspect of the rig was quite rigorous. A complete pressure testing in the company and in-house was carried out on the complete experimental set-up before the commencement of the debugging, initial testing and the actual experiment, to guarantee the safety of the author and the people in the thermoacoustic laboratory, where the test rig is located.

3.2.1 Acoustic driver

The key requirement in the study is to test the heat exchangers in an oscillatory flow. The oscillatory flow is generated and sustained in the system of pressurised helium gas using commercially available Q-drive (1S102D Acoustic Driver) as shown in Figure 3.3a. The Q-drive and its housing were taken from the previous configuration of an experimental rig tested in the Thermoacoustic Laboratory.



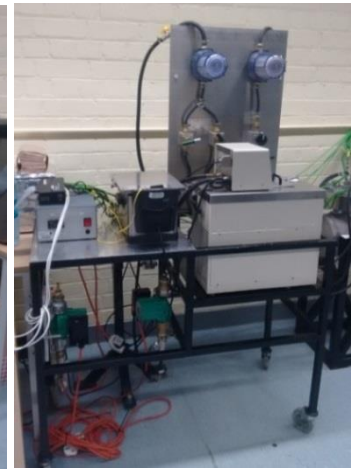
(a)



(b)



(c)



(d)



(e)

Figure 3.1: Photograph of standing wave experimental set-up (a) overview of the experimental set-up in the laboratory (b) gas charging system (c) test-section (d) heating and cooling water loops (e) measurement devices and data acquisition unit.

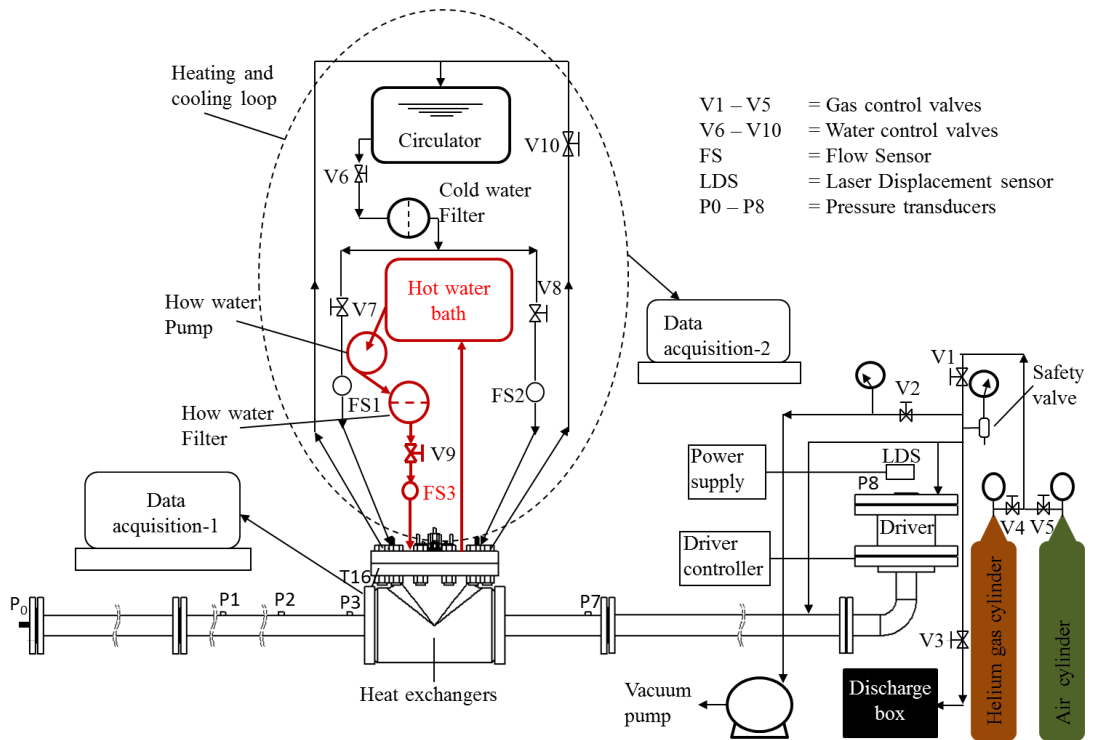


Figure 3.2: Schematic of the standing wave setup. V1-V10, FS and P are the gas and water control valves, flow sensors and water pump, respectively.

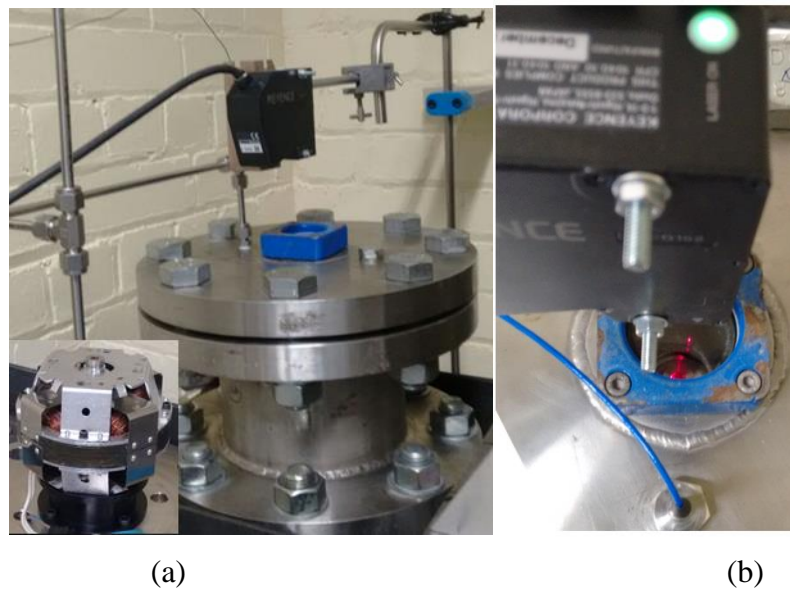


Figure 3.3: (a) Acoustic driver and (b) displacement sensor as installed in the experimental set-up.

Table 3.1 gives the specifications and the maximum operating conditions of the acoustic driver. Since both low and high amplitude investigations on heat exchangers were going to be conducted, a high-impedance transducer is used and

located at a high acoustic impedance point in the standing wave (Swift, 2002). Acoustic impedance is the ratio of acoustic pressure p_1 to acoustic volume flow U_1 . The beginning and the end of the current $\frac{1}{2}$ wavelength rig are the locations of highest acoustic impedance. The high power of the driver facilitated the testing of T-HEX and F-HEX at different drive ratios up to 3.0%. The driver is installed in a high-pressure housing and bolted to a rigid support to prevent vibration during operation. The high-pressure housing allows easy coupling of the driver to the rest of the set-up. The driver is powered by a power supply, Allen-Bradley model PowerFlex700, from Rockwell Automation. The operation of the driver can be controlled through the power supply by setting parameters such as frequency and driving voltage. Further details of different setting range in this study will be discussed in the later section. The piston displacement (stroke) of the driver was monitored through an optical window installed in the driver housing. The peak to peak stroke of the piston was monitored using LK G152 displacement sensor (0.25 V/mm (4mm/V)) with a measurement range of $\pm 10.8V$, positioned directly above the optical window as shown in Figure 3.3b. The LK G152 is mounted such that its laser light beams directly on the moving piston of the driver and there was no transmission of vibration from the set-up to the sensor when the acoustic driver is working. The output signal in rms Volt is displayed on the multimeter (1.06 V for maximum driver piston displacement of 6mm (0 – peak)) and as well recorded on the PC.

Table 3.1: Specifications of the acoustic driver (Q-drive1S102D)

Parameter	Magnitude	Unit
Operating current	3.5	Amp
Input electric power	350	Watt
Acoustic power output (pv)	225	Watt
Operating frequency	60	Hz
Peak-to-peak piston displacement	12	mm
Maximum operating temperature	30	°C

The acoustic driver is connected to the rest of the test rig via a 2-inch stainless steel resonator. The resonator as used here is necessary for defining the phase of pressure and velocity of the oscillating helium gas that interacts with the boundaries of the

three heat exchangers in the test section of the set-up. It has a constant cross section with a smooth internal surface of 52.5 mm in diameter. It has joints that can be used to redefine the resonance frequency of the set-up, but the joints are few enough to keep the pressure leaks in the system to a minimum. O-rings of ferrule types are used at all joints to prevent pressure losses.

3.2.2 Test section

Figure 3.4 shows the test section of the experimental set-up as used for measurement in the current study. The main components of the test section consist of top-entry housing with lid, M27 clamping bolts and nuts, heat exchangers, spacers, feed-through assemblies for temperature probes, in-house made fittings for the dynamic pressure transducers installed between the heat exchangers, standard Swagelok fittings for water tubes, feedthrough for pressure transducer cable and 2-inch weld pipe and flanges that connect to the rest of the resonator. The mid-point of the test section is located at approximately 4.29 m from the closed end of the experimental set-up as shown in Figure 3.4 (bottom), which is equivalent to 0.241λ near the velocity antinode. The choice of this position is to ensure a large range of gas displacement amplitude. The test section is 1.6 m long, fabricated from stainless steel 316L materials and weighs about 180 kg. The housing and its lid enclose the heat exchangers, spacers and the silicate wool insulation materials, dynamic pressure transducers and the thermocouples. It is made from an 8-inch weld equal-tee sch-40 316SS. It was sized such that it conveniently accommodates compact heat exchangers of different sizes, the spacers and the fittings for inflow and outflow of hot and cold water through the heat exchangers, and is designed to allow installation of pressure and temperature measurement instrumentations, for simultaneous temperature and pressure data collection. Grooves of 9 x 4.5 mm (W x D) are made on the flat circular edges for a 240 mm (ID) O-ring of 7 mm cross section for the pressure sealing. The key features of the test section can be summarised as follows:

- Symmetrical arrangement of heat exchangers for enhanced heat balance measurement and heat leak minimisation
- The heat exchangers are submerged in the acoustic environment
- Simultaneous measurement of pressure amplitude and mean temperature
- Built-in flexibility to allow different configurations of heat exchangers

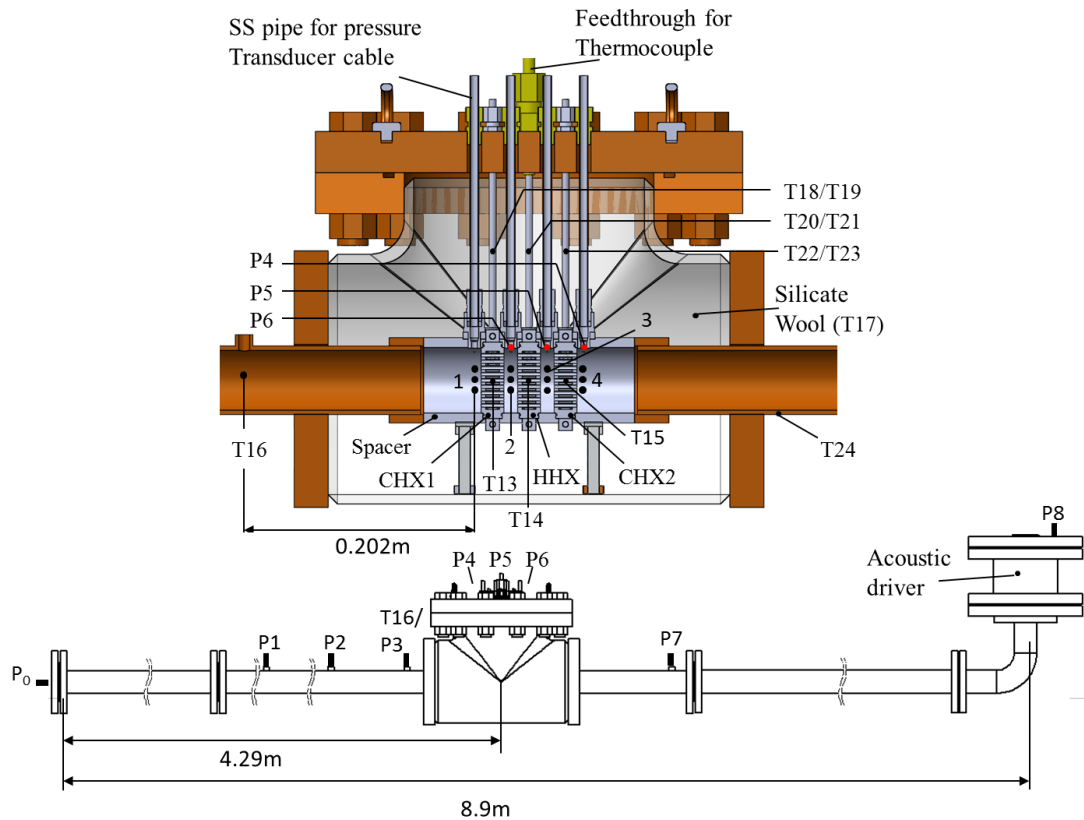


Figure 3.4: CAD-image of the test section showing the details of the CHX1, HHX and CHX2 arrangement (top) and the drawing of the experimental set-up (bottom).

The arrangement of heat exchangers in the test section consists of three identical types of heat exchangers arranged in series with a hot heat exchanger (HHX) placed centrally between two cold heat exchangers (CHX1 and CHX2). The main advantage of this heat exchanger arrangement is that it enables an improved heat balance measurement on the HHX in the middle which creates a dedicated environment for studying the performance of heat exchange components of thermoacoustic coolers and engines. Furthermore, identical sets of heat exchangers (CHX1-HHX-CHX2) are chosen for the symmetry to minimise the nonlinear effect associated with geometrical discontinuity (Jaworski et al., 2009). The separation gap between two adjacent heat exchangers is 12 mm, which is the smallest gap that can be achieved (without the plate attachment), due to the space requirement for the pressure transducer in the spacers. In addition to heat leak prevention, symmetrical arrangement of heat exchangers will also protect the acoustic driver from overheating. The test section allows both internal and external insulation, but internal insulation was found to be sufficient during the experiments as shown in

Figure 3.5. Silicate wool insulation blanket (Insulfrax S) with a thermal conductivity of 0.1 W/mK (25°C) was used for the internal insulation.

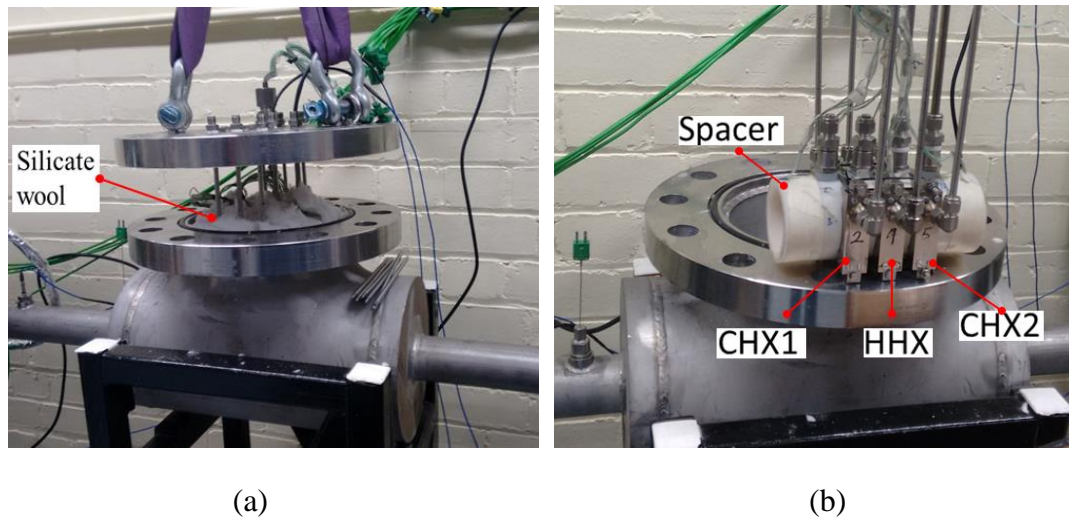


Figure 3.5: Photograph of the test section (a) opening of the test section showing the silicate wool insulation material (b) symmetric arrangement of the heat exchangers

On the gas side, thermocouple probes are installed within the high-pressure acoustic environment with the use of high-density feed-through assembly for thermocouples, from TC direct. The feed-through has 20-pair of 0.5 mm diameter type-K thermocouples and is installed in the test section (on the lid) as shown in Figure 3.5. The use of feedthrough offers the advantage of minimising the pressure leak and the heat leak by heat conduction through metal fittings. Three different 0.5 mm type-K thermocouples are located between the heat exchangers to allow temperature measurement at locations 1, 2, 3, and 4 (cf. Figure 3.4). This implies that 12 thermocouples (T1 –T12) are used for the gas temperature measurement near the heat exchangers, and an average of three temperature readings at each location 1, 2, 3, and 4 are used in the calculation of heat transfer rates, as shown in Figure 3.6. Detailed drawings that show the exact location of the thermocouple (water and gas sides) and pressure transducer measurement points are given in Appendix – E. Thermocouples T13, T14 and T15 are installed in the gas flow channels of the heat exchangers. These thermocouples (T13, T14 and T15) are used in two ways – they are either attached (using silicone gel) to the wall for wall temperature measurement or positioned in the gas flow path within the gas channel for gas temperature measurement. Additional thermocouples, T16 and T17, are used to monitor the gas temperature at 202 mm from the CHX1 side and inside the insulation material,

respectively, to observe the heat transfer by conduction through helium gas and insulation material. This number of temperature measurement points allowed accurate account for the magnitude of heat transfer rates during the experiments. On the water side, the inlet and outlet water temperatures are measured with 1.0 mm type-K thermocouples T18 – T23. Additionally, T24 is used to monitor the temperature of the resonator to determine heat loss through the resonator wall. All temperature readings from the gas side, water side and solid pipe are transferred to the PC via the OMB-Daq Temp device from Omega.



Figure 3.6: Arrangement of the thermocouples within the heat exchanger in the gas environment (dimensioned drawing is given in Appendix – E).

A challenging but unique and exciting feature of the test section is the design of pressure transducer holder for the installation of pressure transducers within the pressurised helium gas environment. In order to directly measure the pressure amplitudes for the determination of acoustic pressure drop across each of the heat exchangers, simultaneously with the temperature measurement, the test-section is designed so the pressure sensors were installed within the high-pressure environment without exposing the sensors to the pressurised helium gas in the test section. The sensor cables run from the process side through an 8 mm stainless tube and Swagelok standard feedthrough fittings to connect the signal conditional and data acquisition card outside the test section. Four sensors (P3, P4, P5 and P6) are in the test section, and the distance between two adjacent pressure sensors is 32 mm. Only P4, P5 and P6 pressure transducers are installed for the actual measurement. An additional four pressure ports are in the resonator. Pressure ports P1 and P2 are separated by a 300 mm gap, P7 and P8 are 700mm away from each other. Pressure amplitudes are measured using PCB PIEZOTRONICS pressure transducers. The

signal outputs (Volt) were amplified using Integrated Circuit Piezoelectric (ICP) sensor signal-conditional (model 482C16, version 1.19). At some points, not all the pressure transducer ports are used at the same time; for example, port P3/T16 is used interchangeably for pressure transducer and thermocouple. The ports allow putting the sensors at different locations of interest on the test rig while blanking off the remaining ports by M12 screws of appropriate length.

Four spacers are designed and used in the test section (two middle-spacers and two end spacers), to separate the symmetrically arranged heat exchangers with equal gaps and minimise heat conduction between them. The middle spacers separate the CHX1, HHX, and CHX2 from each other and the end spacers separate the CHX1 and CHX2 from the inner wall of the test section housing. In addition to minimising heat conduction, spacers provide a continuation of the resonator through which the helium gas oscillates. Each spacer is fabricated from Nylon 6 material (0.88 W/mK at 25 °C) and has an inner diameter of 57.4 mm and thickness of approximately 8.8 mm. An interesting feature of the spacers is the pressure sensor holder, through which the dynamic pressure sensors are mounted. The design is such that the pressure sensors were flush mounted (cf. Figures 3.4 and 3.5) at 6.5 mm from the nearest heat exchanger. The choice of this location is to enable pressure amplitude and temperature measurement as close as possible to the heat exchanger inlet and outlet.

3.2.3 Heat exchangers (HEX)

As remarked in the introductory section, the design of heat exchangers is a challenging task. Due to the oscillatory nature of flow in the thermoacoustic engines and coolers, standard steady flow design methodology for compact heat exchangers cannot be applied directly (Garret, 1994). Performance data that take into account nonlinearity caused by abrupt change, discontinuity of geometry, entrance effects, turbulence and streaming (Swift, 2002) is still lacking. Few types of heat exchangers have been studied as reviewed in Section 2.3. In this study, two different heat exchangers – Tube-Heat-Exchanger (T-HEX) and Finned-Heat-Exchanger (F-HEX) have been selected, designed, fabricated and tested. Dimensioned drawings of the HEX are given in Appendix – E. The activities that preceded the selection of the heat exchanger for this study are not described here for brevity.

Table 3.2: Aluminium 6082-T6 properties for the heat exchangers (Alco Metals, 2016)

Properties	Values
Chemical Composition (%)	Aluminium: min 96.15% Others (Mn, Fe, Mg, Si, Cu, Zn, Ti, Cr): max 3.85%
Density	2700 kg/m ³
Melting point	555°C
Thermal expansion coefficient	24 x 10 ⁻⁶ /K
Modulus of elasticity	70GPa
Thermal conductivity	180 W/m.K(25 °C)
Electrical resistivity	0.038 x 10 ⁻⁶ Ω.m

Table 3.3: Heat exchanger parameters (Dimensioned drawings are given in Appendix – E)

Helium gas side	T-HEX	F-HEX
Flow length (<i>l</i>), mm	20	20
Number circular tubes	89	-
Tube diameter, mm	3	-
Hydraulic diameter, mm	3	0.715
Slot height for fins, mm	-	3
Number of slots for fins	-	9
Frontal core diameter, mm	57.4	57.4
Porosity, %	24.31	32.5
Separation wall thickness, mm	0.5	0.5
Total surf. Area (lateral i.e. gas side), mm ² (For basic heat exchangers without attachment)	16,780	36,467
Water side		
Channel width, mm	12	
Channel height, mm	1.5	
Channel length, mm	67	
Number of channels	10	
Hydraulic diameter (all), mm	26.67	
Total area of water channel, mm ²	18,090	

However, to reach a conclusion on the choice of the heat exchanger, the following factors were rigorously considered:

- Possibility of achieving excellent thermal contact between oscillating helium and thermal reservoir (water) – for this reason, the separation wall between the gas and the water side in the heat exchanger was made to be 0.5 mm
- Operating conditions (mean pressure, temperature, and oscillating gas displacement) – for this reason, the designed heat exchangers were pressure tested with a safety factor of 1.5 of the targeted mean pressure in the experiment.
- Time, technique and cost of fabrication
- Thermal and acoustic pressure drop considerations on the helium side

The T-HEX and F-HEX as tested for the investigation of heat transfer and acoustic pressure drop study are shown in Figures 3.7 and 3.8, respectively. The material and geometric properties for the heat exchangers are shown in Tables 3.2 and 3.3, respectively. Both types are water heated and water cooled cross flow heat exchangers when they are installed in the test section. Both heat exchangers have their ten rectangular water channels made in an aluminium block and covered with custom designed end-caps that incorporate standard fittings from Swagelok to connect the heating and cooling water loops outside the test section.

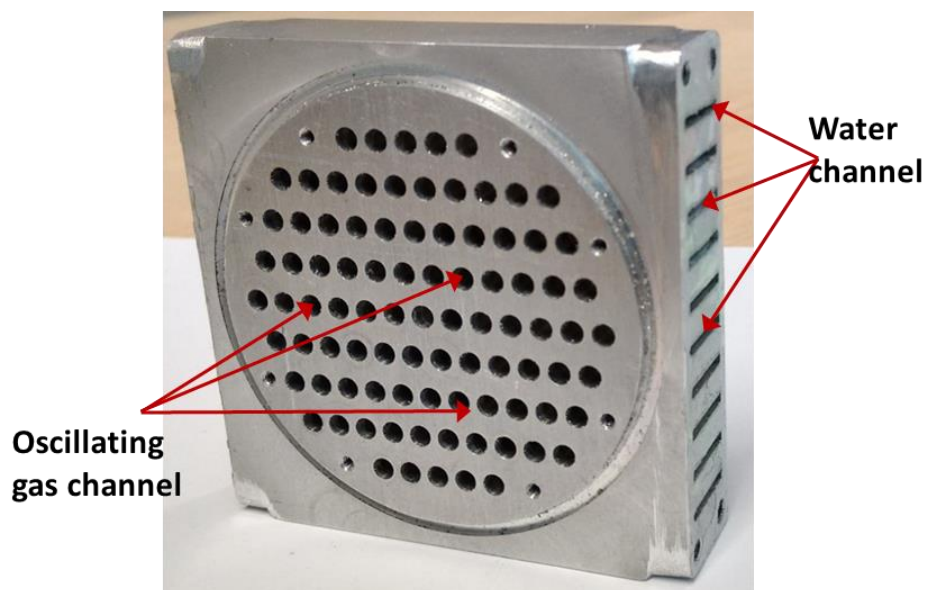
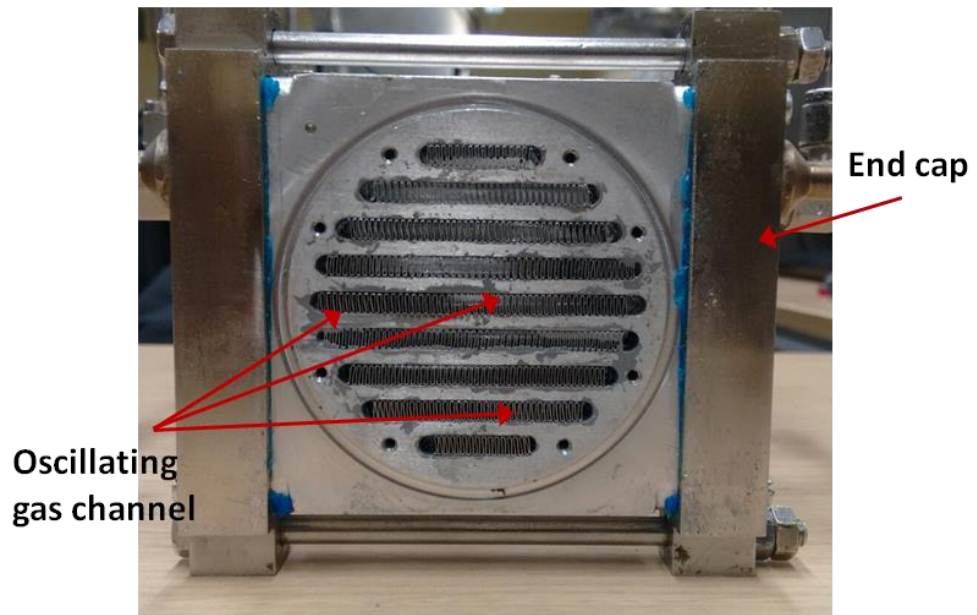


Figure 3.7: Photograph of the T-HEX. The tube arrangement follows a triangular pitch pattern



(a)



(b)

Figure 3.8: (a) Photograph of the F-HEX (b) fin assembling into the flow channel of the F-HEX

The main difference in the two configurations comes from the gas channels as can be seen in Figures 3.7 and 3.8. The T-HEX has 89 circular tubes of 3 mm diameter each, arranged in a triangular pitch pattern (Isosceles triangle) with 4 mm and 5.5 mm horizontal and vertical distances, respectively, as shown in Figure 3.7.

Pressurised helium oscillates through the tubes and water flows unidirectionally through the ten rectangular channels in a cross flow pattern.

Table 3.4: Aluminium grade 3003-0 properties for the fins (Alco Metals, 2016)

Properties	Values
Chemical Composition (%)	Aluminium: min 97.025% Others (Co, H, Mg, Si+Fe, Zr): max 2.975%
Density	2730 kg/m ³
Melting point	655 °C
Thermal expansion	23.1 x 10 ⁻⁶ /K
Modulus of elasticity	96.5 GPa
Thermal conductivity	190 W/m.K (at 25 °C)
Electrical resistivity	0.034 x 10 ⁻⁶ Ω.m
Tensile strength	95 – 135 MPa

Table 3.5: The fin parameter (as supplied by Niagara Thermal)

Geometry	Plain flat-crest (rectangular cross section)
Material	Aluminium
Thickness (f_t), mm	0.1
Height (f_h), mm	3.0
Flow Length (f_l), mm	20.0
Fin pitch (N_f), FPI	50.0
Fin spacing (f_s), mm	0.4
Cut-off length (f_w), mm	As per each slot in the F-HEX

The F-HEX has nine straight slots filled with flat crest fins to extend the heat exchange area for oscillating helium gas, as shown in Figure 3.8. The material and geometric properties of the flat crest fins installed in F-HEX are shown in Tables 3.4 and 3.5, respectively. The fin density is chosen to allow a significant level of porosity without resulting to a significant pressure drop. However, the porosity

turned out to cause a high flow resistance and a significant drop in the range of drive ratio, as will be discussed in the result section.

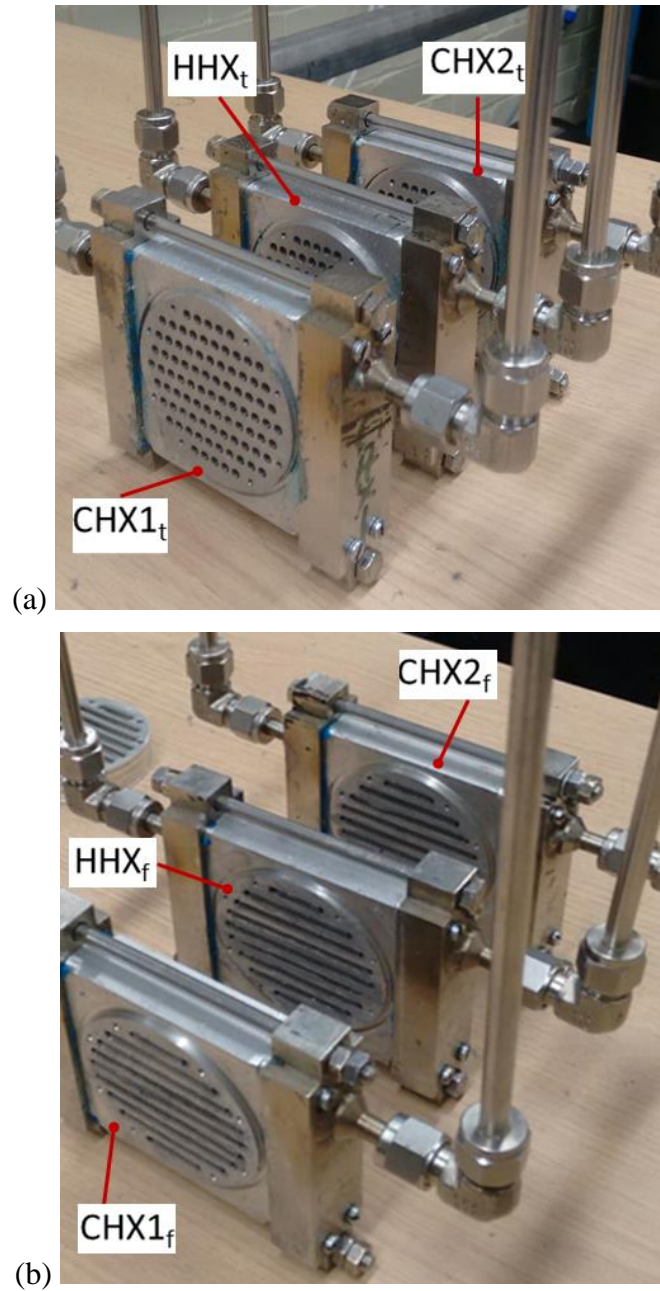


Figure 3.9: Photograph of the heat exchangers (a) T-HEX (b) F-HEX.

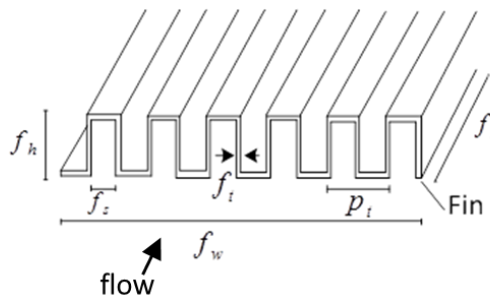


Figure 3.10: Schematic of the uniform-flat-crest for the F-HEX.

The fins are inserted into their respective slots as shown in Figure 3.8b, and ‘brazed’ to the aluminium block using thermally conductive epoxy adhesive (3M TC-2707) with a thermal conductivity of 0.72 W/m-K.

For every experiment, an identical set of heat exchanger type is used in the symmetric arrangement as shown in Figure 3.9. A typical arrangement of heat exchangers in an experiment will consist of CHX1_t-HHX_t-CHX2_t or CHX1_f-HHX_f-CHX2_f for the T-HEX or F-HEX, respectively. The fin parameters as defined in Table 3.6 are shown in Figure 3.10.

3.2.4 Edge shapes

An important aspect of the current study is the use of edge shape at the entrance and exit of each heat exchanger geometry, which is considered as a method of optimising the performance of heat exchangers in oscillatory flow. The parameters of edge shapes as designed, fabricated and tested for T-HEX and F-HEX are shown in Table 3.6. Curvatures of the edge shapes as given in Table 3.6 are shown in Figure 3.11.

Table 3.6: Parameters of the edge shapes for the T-HEX and F-HEX

Heat Exchanger (HEX)	Radius of Curvature (RC), mm	Plate thickness (T_p), mm
T-HEX (flat)	0	4
T-HEX (ogive)	7	4
F-HEX (flat)	0	2
F-HEX (ogive)	2	2

The effect of edge shapes at the entrance and exit of the heat exchanger are considered to improve flow conditions associated with an abrupt change in the cross section in order to minimise the acoustic pressure drop. As previously remarked in the introductory chapter, minimising the acoustic pressure drop in the heat exchangers will contribute to the overall efficiency of the thermoacoustic engines and coolers. The use of profile edge shapes for improving the flow conditions in and around the heat exchangers in oscillatory flow has not been studied experimentally and numerically before now.

An ‘ogive’ edge shape was selected for use based on the knowledge of using a streamlined shape to reduce drag at the boundary layer pressure drop minimisation.

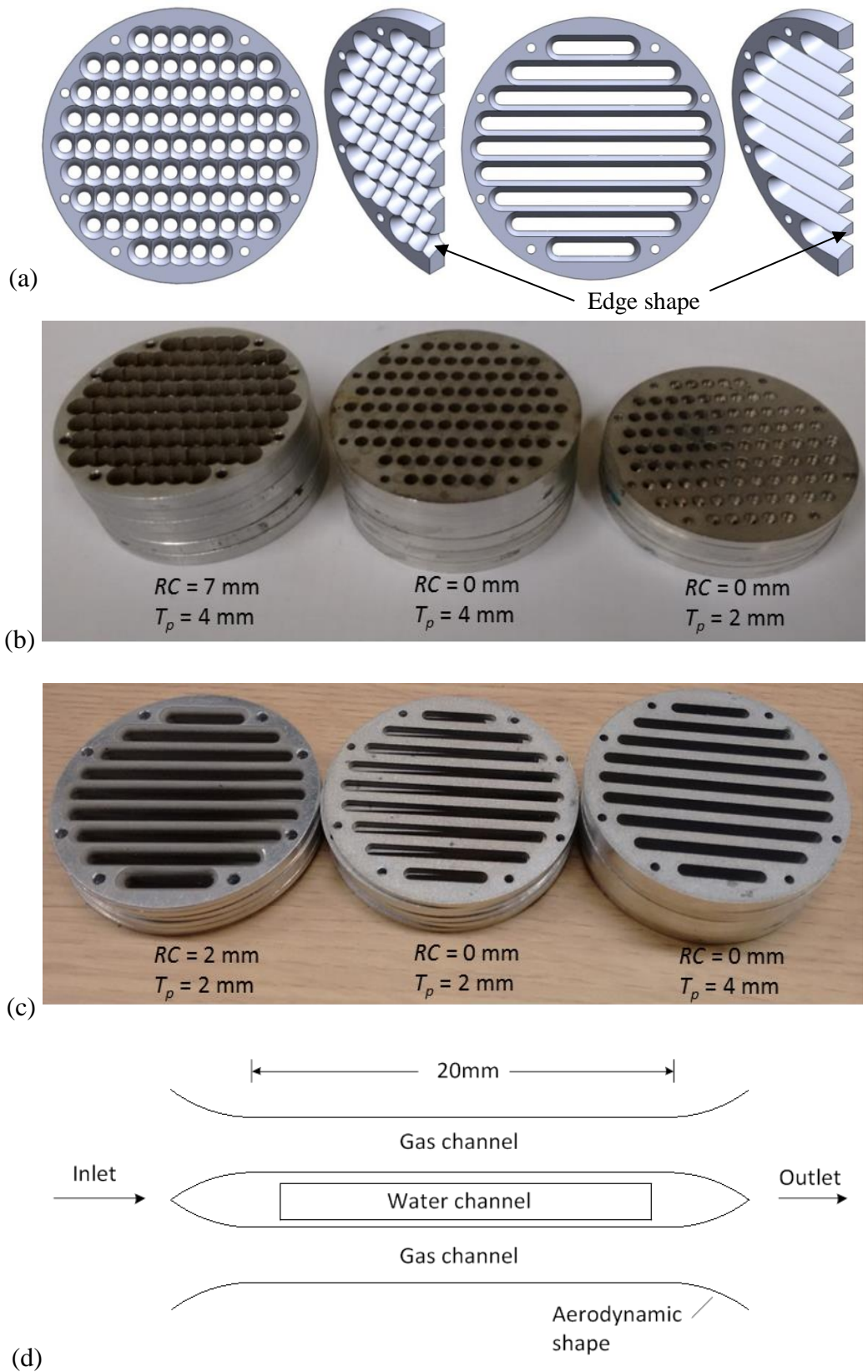


Figure 3.11: Images of the plate attachments (edge shapes) (a) CAD-images for the T-HEX (left) and the F-HEX (right) (b) photograph of the T-HEX (c) photograph of the F-HEX (d) Schematic of the HEX flow channel for the T-HEX configuration

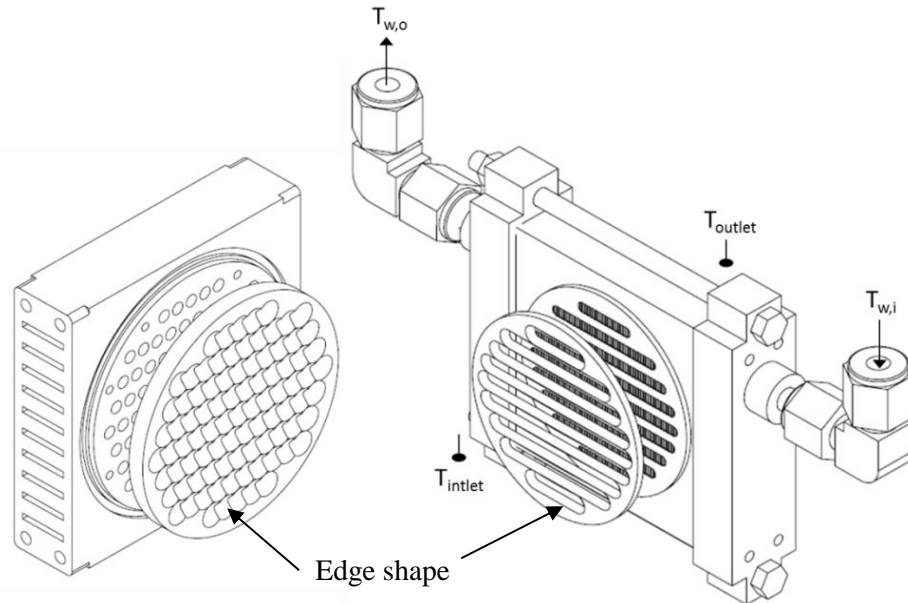


Figure 3.12: Schematic of the T-HEX (left) and the F-HEX (right) and the ogive edge shapes

Having different heat exchangers with different edge shapes was considered impractical. Therefore, the ogive shapes with known radii of curvature were designed on separate plates which were then attached to the entrance and exit of T-HEX and F-HEX to provide the necessary edge shape effects. This provides the flexibility that allowed the fabrication of just the basic heat exchangers and multiple edge shape designs. As can be seen in Figure 3.11 (b and c), besides the patterned plates, blank plate attachments (i.e. 0 mm radius) of same thickness are fabricated to provide a benchmark for comparing the influence of the ogive edge shape. The ogive shapes are manufactured on 4 mm and 2 mm plate thicknesses for T-HEX and F-HEX, respectively. All plates have the same material properties as the heat exchanger body. Identical edge shapes are used at the entrance and exit of a regular set of heat exchangers, in a single experiment. The plate attachment resulted in an increase in the heat exchanger length as shown in Figure 3.11d. The length will increase to 28 mm and 24 mm from 20 mm for T-HEX and F-HEX, respectively, based on the plate thickness given in Table 3.6. Figure 3.12 shows a typical arrangement of T-HEX and F-HEX and their respective ogive edge shapes.

3.2.5 Fabrication technique

For the heat exchangers, the gas channels are fabricated using CNC machine, for both T-HEX and F-HEX. The water channels, which are similar for the two heat

exchanger configurations, are fabricated using a spark-erosion machining technique. This is a machining technique whereby the desired shape is obtained using electrical discharges (sparks) to remove material from the workpiece by a series of rapidly recurring current discharges between two electrodes, separated by a dielectric liquid and subject to an electric voltage. The choice of this technique is because of the length of the rectangular channel (67 mm) and the channel height (1.5 mm) coupled with the thin separation wall (0.5 mm) requirement between the water and the gas channels.



Figure 3.13: Different views of the fabricated tool for producing the T-HEX and the F-HEX edge shapes on the plate attachments.

A typical ogive shape is obtained by pre-fabricating the required profile with desired aspect ratio as a tool, as shown in Figure 3.13. The tool is fabricated to account for the accuracy of the final profile dimensions in the ogive edge shape. The patterned tool is attached to a Joemars JM32NZ (with fuzzy control) spark eroding machine and the profile on it is machined on a plate of appropriate thickness using a spark erosion technique to achieve the production. The production begins with an operating current of 21 Amps which gives a coarse surface finish. The profile is further smoothed to achieve precise profile dimensions and quality surface finish

by decreasing the operating current to 4 Amps which gives an acceptable level of surface finish. Decreasing the operating current further is possible but with huge 'cost' of fabrication time. This method of manufacturing is adopted, as the conventional milling method could not be used to achieve the required profile of the edge shapes.

3.2.6 Heating and Cooling Loops

The heating and cooling loops (cf. Figure 3.1d and 3.2) consist of a hot water bath, refrigerated circulator (KTB-30), pumps (Wilo-Smart 25/6), water filters, flow sensor, control valves, and data acquisition system. In the loops (cold and hot), water at the required temperature gets pumped continuously through the heat exchangers. The purpose of the hot water flow loop is to transport heat from a hot water bath to the heat exchanger by using hot water as a carrier.

The hot water that is used as a heat carrier is produced from a hot water bath with a heating power of 1500 W and pumped through the hot heat exchanger. The temperature at the inlet of the hot heat exchanger is maintained at the desired level by using a PID temperature controller (Omega Engineering, model SSRL240DC10).

The temperatures at the inlet and outlet of all heat exchangers are monitored with thermocouple Type K-310 stainless steel sheath of 1.0 mm diameter and 150 mm in length and installed at the inlet and outlet of each heat exchanger as shown in Figure 3.14. The circulating hot water flowing through the loop returns to the hot water bath before being pumped through the loop again. The maximum working temperature for this water pump (Wilo-Smart 25/6) is 95°C, and this was considered in the design of the experimental conditions as will be discussed in section 4.1. For the two cold heat exchangers, cold water at the required temperature is produced, sustained and pumped through the cold heat exchangers by the refrigerated circulator with a cooling capacity of 500 W (at 20°C). The temperature set point is controlled in the LabVIEW computer program on the PC, and both the inlet and the outlet temperatures are monitored, like the hot water loop. The cold water at 10°C is maintained at the inlet of the cold heat exchangers in all experiments.

Thermocouple probes T18 – T23 (cf. Figure 3.4) are installed to obtain temperature data from the water side for heat transfer analysis. Control of the water flow rate was achieved by the Swagelok needle valves (V6-V10) and monitored by mini turbine flow meters with an accuracy of 0.005l/min installed in the flow loops for each heat

exchanger (cf. Figure 3.2). These flow turbines also serve as safety devices, given the heat exchangers are completely submerged in the high-pressure environment. Any fluctuations in the output readings could signify a potential pressure leak into the water loops. The flow rate data was acquired through the OMB-Daq Temp and the LabVIEW program. The accuracy of these flow sensors was double checked with a conventional method of mass flow rate measurement by weighing of water against time using a stopwatch.



Figure 3.14: Cooling and heating connections for water temperature measurement

3.2.7 Performing experiments on the test rig

The working fluid in the experimental set-up is pure helium gas. The gas charging system consisted of vacuum pump, valves, pressure gauges, vacuum gauge, safety release valve (pressure relieve valve) and cylinders of pressurised helium gas and compressed air (cf. Figures 3.1b and 3.2). The choice of working gas for thermoacoustic engine and cooler has already been discussed in detail in the literature review section of Chapter 2. Helium gas in its pure form is chosen here due to the parametric nature of the current study which requires the test section of the experimental set up to be dismounted and reassembled for every new combination of heat exchanger set and the edge shapes. Using pure helium gas offers the advantage of higher thermal conductivity and lower viscosity in comparison with other noble gases. A typical procedure for charging the experimental set up with helium gas and making it ready for experiments when a change is made to the heat exchangers in the test section, involves the steps that can

be summarised as: pre-check for leakage, vacuuming, charging with helium gas, heating and cooling of the heat exchangers, and performing measurements.

The pre-check for leakage involves charging of the set-up with compressed air to a maximum mean pressure at which the actual experiments will be performed and applying a leak detecting fluid to all joints to determine if there is leakage anywhere in the test section. When no leakage is found, the air in the test rig is discharged safely and is ready for vacuuming. For the vacuuming, a vacuum pump was used to draw out the air in the set-up at -0.8 bar pressure (below atmospheric pressure) to avoid contamination of the helium gas. The vacuuming step was repeated the second time by first introducing a small amount of helium to bring the pressure to 1.0bar and then vacuum again to ensure all air in the test has been removed. After that, the set-up was charged with helium gas to the maximum desired mean pressure for the experiment. At this stage, the hot and cold heat exchangers need to be brought to the required temperature for the experiments by pumping hot and cold water from the hot water bath and the chiller, respectively, through the loops. It takes about 45 minutes of simultaneous heating and cooling of the hot and cold heat exchanger set to bring the system to a thermal equilibrium state where the experiment can be performed. When the system is in a thermal equilibrium condition, the next step before exiting the flow was to collect 'static measurement data' for the determination of the magnitude of heat conduction through the helium gas and insulation material. This step is done for every single experiment, and the results are used in the heat transfer analysis as will be discussed in Chapter 4 (section 4.3).

As already described in section 3.2.1, the oscillation of helium gas was generated by the acoustic driver (1S102D Acoustic Driver). Operating parameters for controlling the linear driver, such as excitation voltage (VAC) and operating frequency are selectable from the controller. The peak-to-peak excitation voltage for the acoustic driver at a mean pressure of 1 – 30 bar and drive ratio 0.15 – 2.0%, is shown in Figure 3.15. After reaching an acoustic equilibrium state, acoustic pressure amplitude was measured by a PCB PIEZOTRONICS pressure transducer model 112A21, attached to the end of the set-up, at the pressure antinode (cf. Figure 3.2). The ratio of the output signal from this pressure transducer (when converted to Pa) to the mean pressure in the set-up (drive ratio) is used as a controlling parameter in all the experiments.

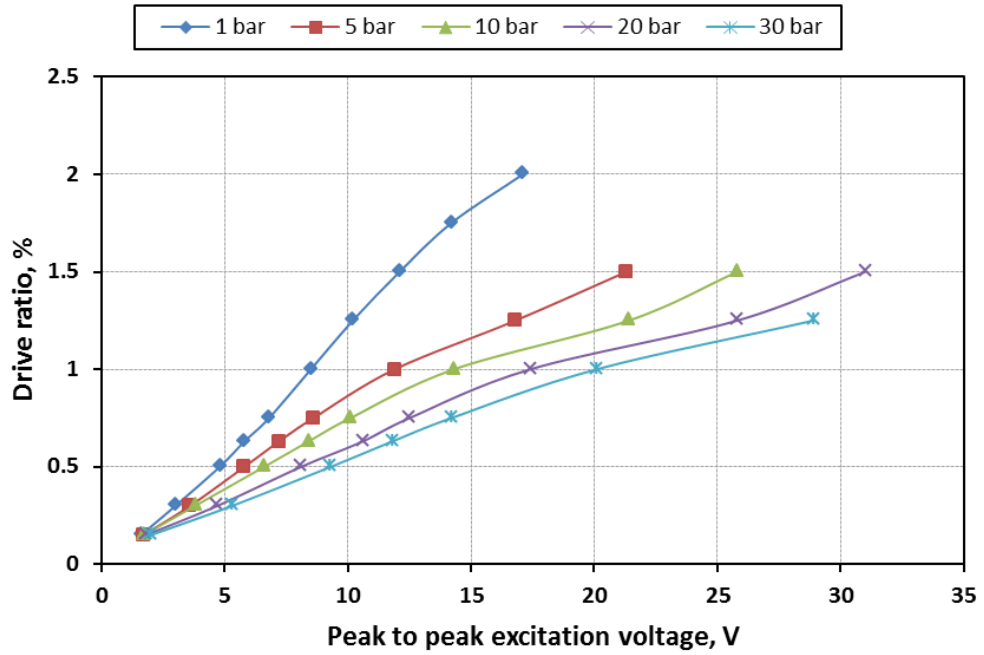


Figure 3.15: *DR* as a function of the peak-to-peak excitation voltage, for the acoustic driver, at $P_m = 1 - 30$ bar.

3.3 Calibration of the pressure sensors

The measurement sensors that are used in the experiments for the temperature and the water flow rate were all new and factory calibrated. Although some of the pressure transducers (PCB PIEZOTRONICS) are also new, few of them have been in service in the thermoacoustic laboratory before the current study. Therefore, all the pressure transducers were calibrated.

Figure 3.16 shows the details of the test rig arrangement for the calibration task. This is essential given the significance of the pressure amplitude measurement in the test section. For the calibration task, the heat exchangers in the test section are replaced with a tube of a uniform internal diameter that is of equal length to the ‘core’ formed by the heat exchangers in the test section. The purpose of the tube is to minimise flow restriction that will be caused by the porosity of the heat exchanger. Drive ratio of 3.0% was achieved for the calibration, thus covering the range in the experiments. To achieve the calibration goal, a 2-inch flange was designed to have multiple transducer ports with the reference transducer sitting in the middle of other transducers as shown in Figure 3.16 (upper left).

The reference transducer is new and factory calibrated. The 2-inch flange is fitted to the end of the set-up at the location of pressure antinode. All the settings in the experimental set-up remain as previously described. Figures 3.17 – 3.18 show the signal output from the PCB pressure transducer in rms volt (V) against the mean pressure at $DR = 1.25\%$.

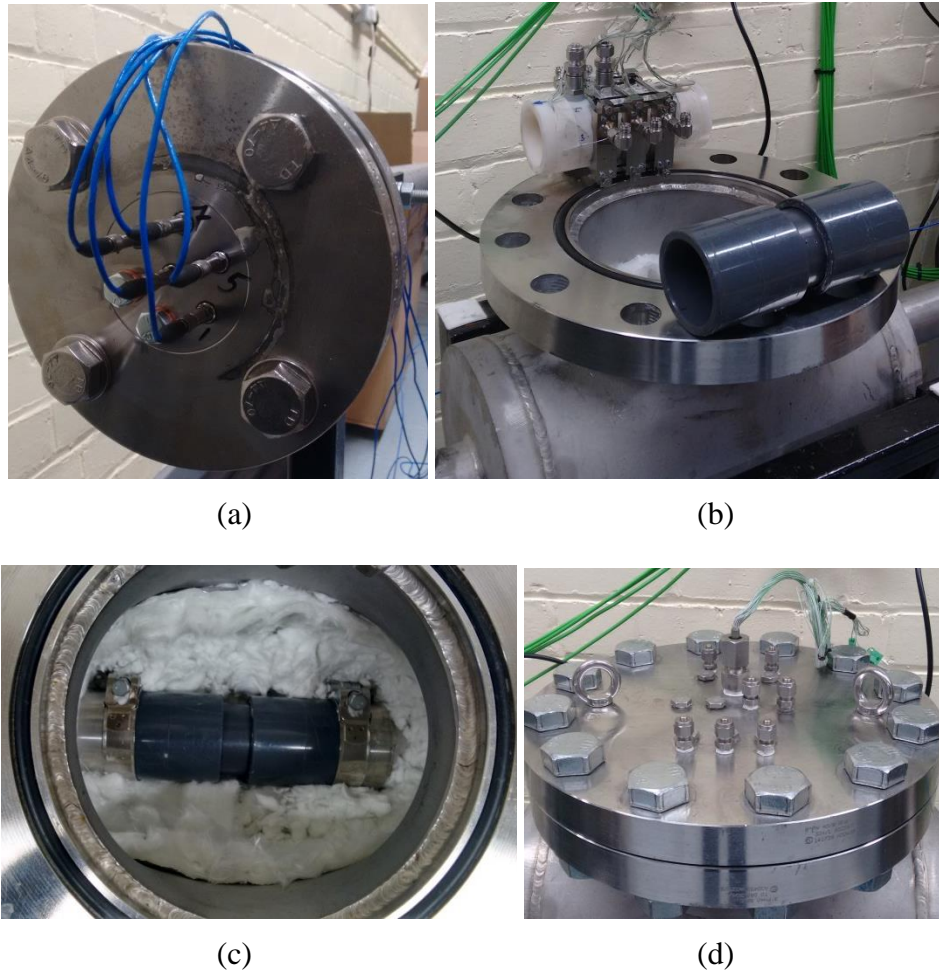


Figure 3.16: Photograph of the experimental set-up for the calibration of the pressure transducers (a) pressure transducers on a 2-inch flange at the closed end (b) Test-section, showing a 2-inch plastic pipe and the heat exchangers (c) 2-inch plastic pipe in position for the calibration task (d) close-up of the test section.

The standard deviation in the slope and intercept are displayed on each of the plots. The average of standard error in the calibration results shown in Figures 3.17 – 3.18 is 0.21%. During the calibration, the mean pressure was stepped through a range of pressure at 0.5bar at a constant $DR = 1.25\%$. The calibrated sensitivities in mV/kPa for each of the pressure transducers P_0 and P_4 are 7.10646 and 14.7028 mV/kPa, respectively. The calibration results (plots and sensitivities) for the pressure

transducers at other locations on the test rig (cf. Figures 3.2 and 3.4) at $DR = 1.25\%$ are given in appendix-D.

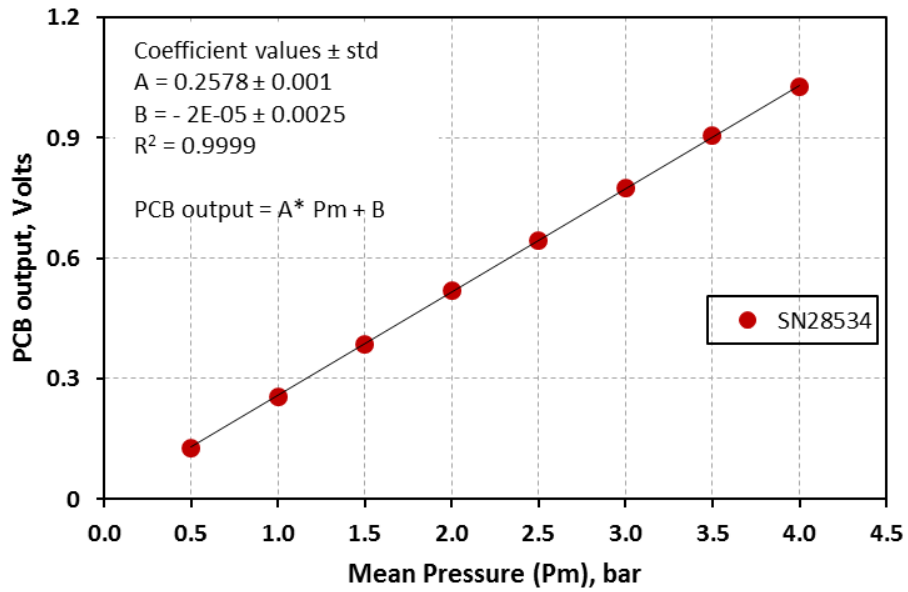


Figure 3.17: Calibration of the pressure sensor (P_0) at the end of the resonator. The coefficients are the slope and the intercept of the least-squares fit. The transducer's serial number is shown in the legend. Std = standard deviation

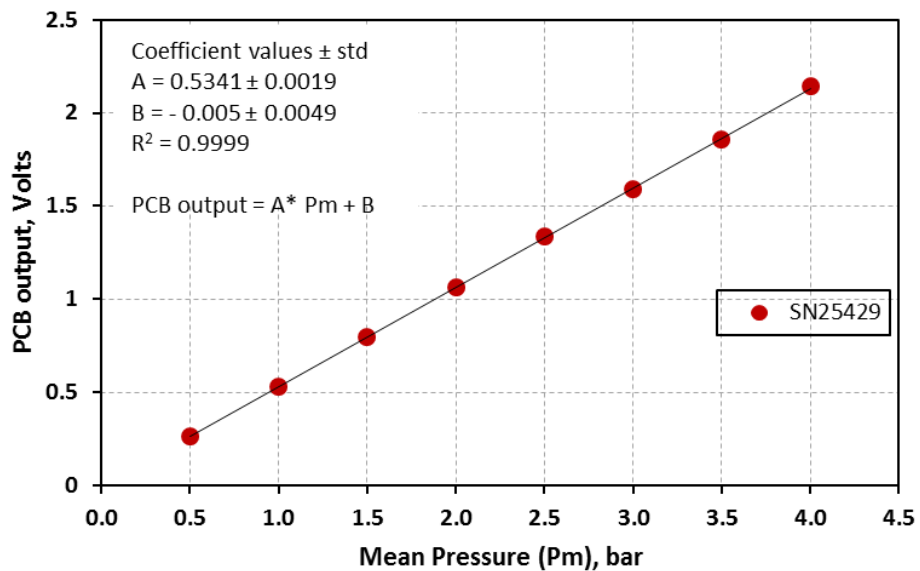


Figure 3.18: Calibration of the pressure sensor (P_4) at location 2

The conversion of the output signal (rms volt) to the pressure amplitude (in Pascal) is done using the following expression:

$$p_a(Pa) = \frac{V(rms) \times \sqrt{2} \times 1000^2}{Gain \times Sensitivity} \quad (3.1)$$

The $V(rms)$ is the output signal from the pressure transducer. Gain is the amplification factor setting in the ICP-signal conditional (model 482C16, version 1.19). The sensitivity is the calibrated sensitivity of each pressure transducer. The phase differences between the oscillating pressures signals are obtained from LABVIEW programme with an accuracy of 0.01° .

3.4 Resonance frequency determination

Before the actual experiments were performed, the resonance frequency in the experimental set-up was first determined at various mean pressures covered in the experiments. This is considered important because the displacement amplitude of gas as defined in equation (2.32) depends on mean pressure, frequency, and the penetration depths as shown in equations (2.29) and (2.30). The heat transfer condition in oscillatory flow, in turn, depends on the gas displacements amplitude. The standing wave mode of the gas displacement amplitude in the experimental set-up can be deduced at the resonance frequency. The resonance frequency is the operating frequency at which the highest acoustic pressure amplitude was achieved. Since the acoustic pressure drop across the heat exchanger would be derived from the pressure amplitude to determine the influence of the edge shape, it is important that each edge shape is evaluated with its peak pressure amplitude to enable same platforms for the comparison. Studies on experimental investigation of the heat exchanger in oscillatory flow in the literature are often conducted without the operating frequency being at resonance. For example, in the experiments of Wakeland and Keolian (2004), Nsofor et al. (2007) and Zhao and Cheng (1996), their results described heat transfer performance at varying frequency without identifying the resonance frequency or the wave mode of their systems. Performing heat transfer study at operating frequency other than resonance frequency may make it difficult for making a comparison between the performances of two modes of thermoacoustic systems working at resonance frequencies.

To determine the resonance frequency at each mean pressure in the current study, the operating frequency of the acoustic driver was stepped through a range of 5 Hz frequency starting from 50 Hz at 0.1 Hz intervals by keeping the excitation voltage

constant. The pressure transducer (P0) at the end of the resonator was used for the detection of the acoustic pressure that is used for determining the resonance frequency. The results for T-HEX (ogive) at three mean pressures, 3bar, 5bar and 10bar are shown in Figure 3.19.

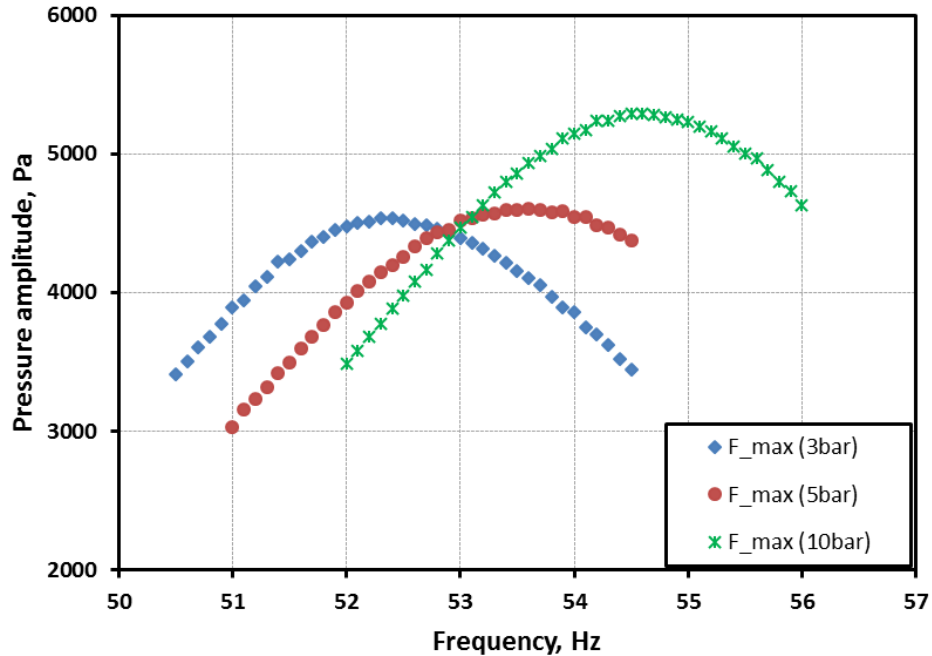


Figure 3.19: Determination of the resonance frequency at $P_m = 3\text{bar}$, 5bar and 10bar , $T_{\text{room}} = 21^\circ\text{C}$, and a constant excitation voltage. In the legend, the ‘F_max.’ indicates the peak frequency in each curve.

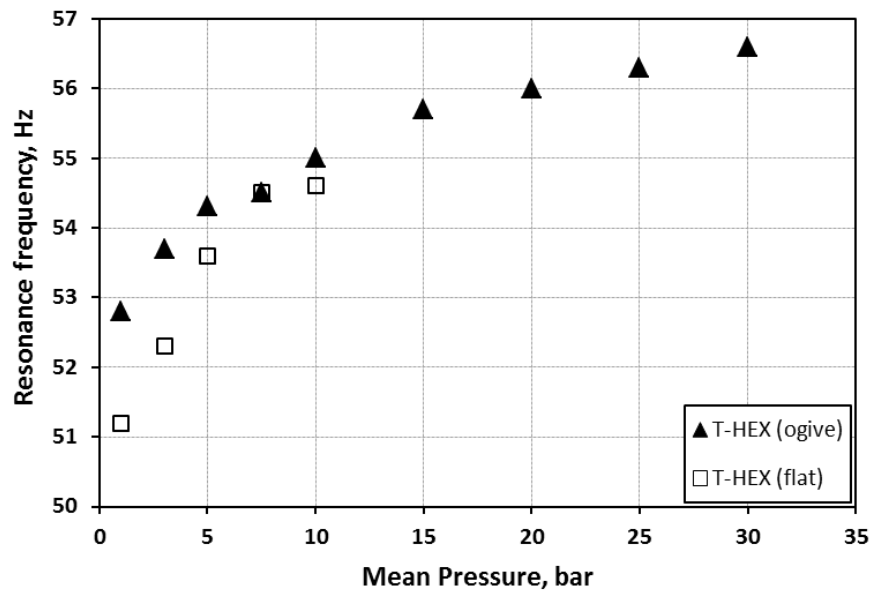


Figure 3.20: Resonance frequency at various mean pressure for the T-HEX (flat) and the T-HEX (ogive) configurations at $T_{\text{room}} = 21^\circ\text{C}$.

The peaks of acoustic pressures were found at frequencies 52.3 Hz, 53.6 Hz and 54.6 Hz for the mean pressure of 3bar, 5bar and 10 bar, respectively. The resulting resonance frequency at different mean pressure for the T-HEX (flat) and T-HEX (ogive) is shown in Figure 3.20. The dependence of resonance frequency on the mean pressure and edge shape of the heat exchanger can be seen in the plot. The resonance frequency increases as the mean pressure is increasing. This is because the compliance of helium gas decreases as the mean pressure increases at constant volume ($C = V / \gamma P_m$), thereby leading to an increase in the resonance frequency (cf. equation (4.9) by Swift, 2001). The influence of the edge shape can be seen at low mean pressure. It appears that the ogive edge shape caused an increase in the resonance frequency, but the influence became weak as the mean pressure increases.

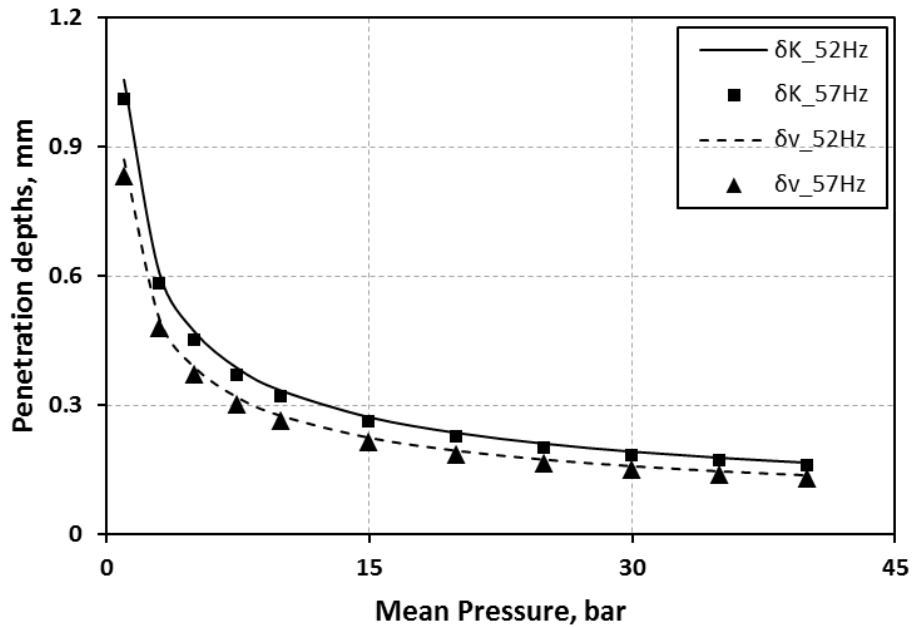


Figure 3.21: Effect of mean pressure on penetration depths at $T_{ref} = 27^\circ\text{C}$ and $f = 52$ and 57Hz

The influence of mean pressure on the thermal and viscous penetration depths at the frequency range in this study is shown in Figure 3.21. The penetration depths defined by equations (2.29) and (2.30) show a strong dependence on the mean pressure. They decrease rapidly as the pressure increases until about 15bar. The decrease becomes less pronounced as the pressure increases further than this point.

3.5 Pressure distribution along the test rig

The distribution of the pressure amplitudes at different locations along the test apparatus is discussed in this section. Figure 3.22 shows the pressure amplitude distribution for the T-HEX (flat) at a mean pressure of 5 bar, $0.16 < DR < 1.36\%$, frequency of 53.6 Hz and 70°C on HHX_t . The maximum drive ratio obtainable due to the limitation of the acoustic driver's excursion is 1.36% for the T-HEX configuration. This gives a maximum pressure amplitude of 6.3 kPa at the pressure antinode ($x = 0$). Ideally, two pressure antinodes are expected for a $\frac{1}{2}$ wavelength rig (cf. Figure 2.1b). These locations are at $x = 0$ and $x = 8.9$ m (location in front of the piston of the acoustic driver). Pressure amplitudes at the pressure antinodes are expected to be higher than all other locations. However, pressure amplitude at $x = 8.9$ m could not be measured directly. For this reason, the pressure amplitude profiles in Figures 3.22 – 3.24 exclude the pressure amplitude at $x = 8.9$ m. Location $x = 9.09$ m corresponds to the pressure amplitude at the back of the acoustic driver, measured by the pressure transducer P8.

In Figure 3.22, the centre of the heat exchanger (HEX) core is at $x = 4.29$ m and the pressure transducers P4, P5 and P6 are positioned within a high-pressure environment in the test-section, at $x = 4.276$, 4.308 and 4.340 m, respectively. The centre of the test rig is at $x = 4.45$ m. The pressure amplitude profile is distorted at the vicinity of the heat exchanger core due to the flow resistance caused by the presence of this HEX. Asymmetric pressure profile around the centre of HHX ($x = 4.29$) can be observed, which is partly because the centre of HHX is located along the rising part of the standing wave in the test rig (cf. Figure 2.1 b). Therefore, pressure amplitude on the position $0 < x < 4.29$ m is expected to be higher than $4.29 > x > 4.45$ m. Also, the pressure transducer (P8) at location 9.09 m is at the back of acoustic driver (cf. Figure 3.4). As previously mentioned, the setup is designed for standing wave profile of $0 \leq x \leq 8.9$ m, but there is no pressure transducer located at $x = 8.9$ m. Therefore, the pressure amplitude at that point was not measured and not included in the plots, which made Figures 3.22 – 3.24 appear slightly different than they would be if the pressure amplitude at $x = 8.9$ m were included. In Figure 3.23, the pressure amplitude profile for F-HEX (flat) at the same testing condition as T-HEX (flat) is shown. From the plot, the presence of F-HEX in the test section also resulted in distortion to the pressure amplitude profile around the HEX core.

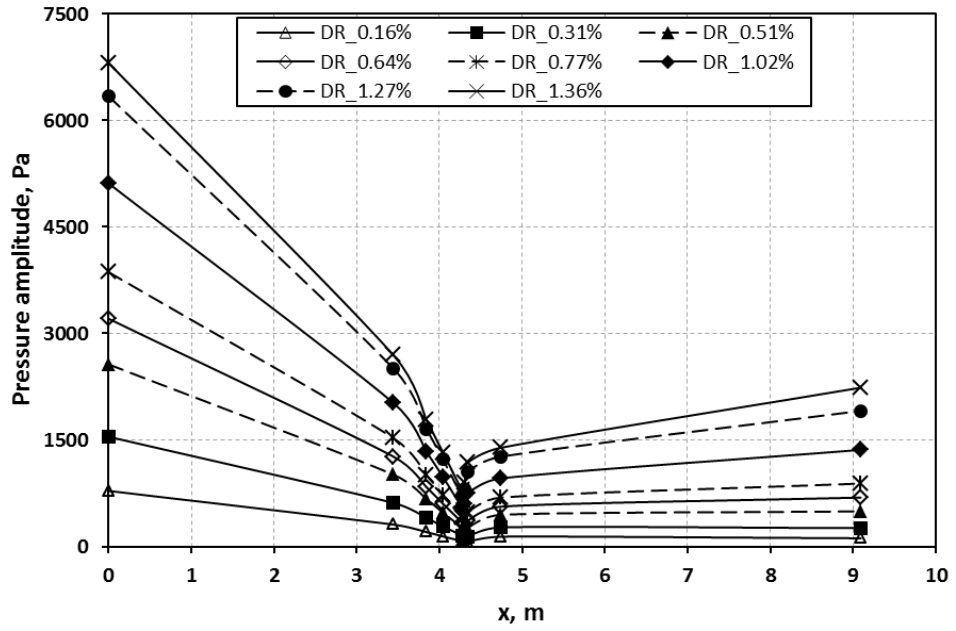


Figure 3.22: Pressure distribution as a function of various locations in the test rig for the T-HEX (flat) at $0.16 < DR < 1.3\%$, $T_h = 70^\circ\text{C}$ and $P_m = 5\text{bar}$.

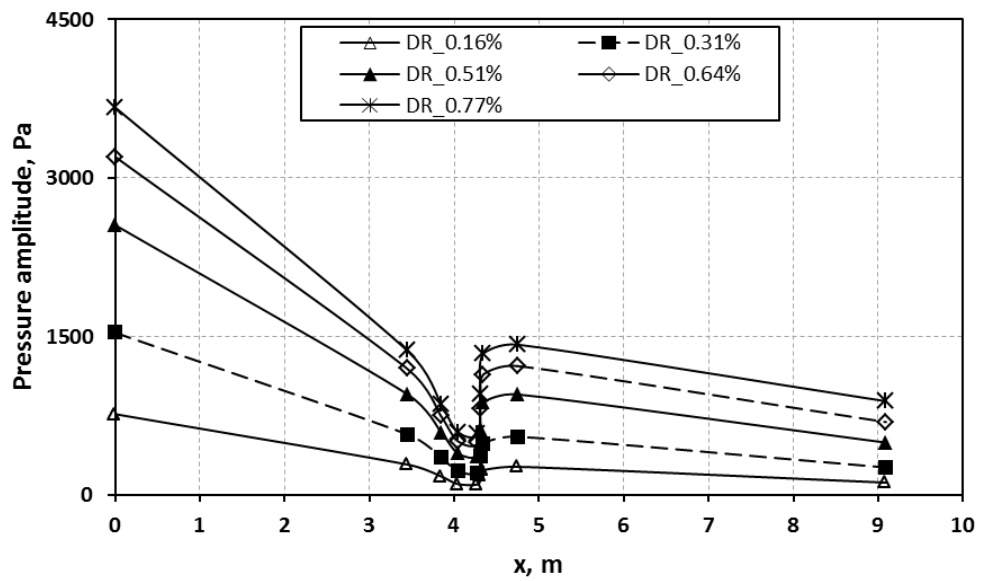


Figure 3.23: Pressure amplitude distribution as a function of various locations in the test rig for the F-HEX (flat) at $0.16 < DR < 0.77\%$, $T_h = 70^\circ\text{C}$ and $P_m = 5\text{bar}$

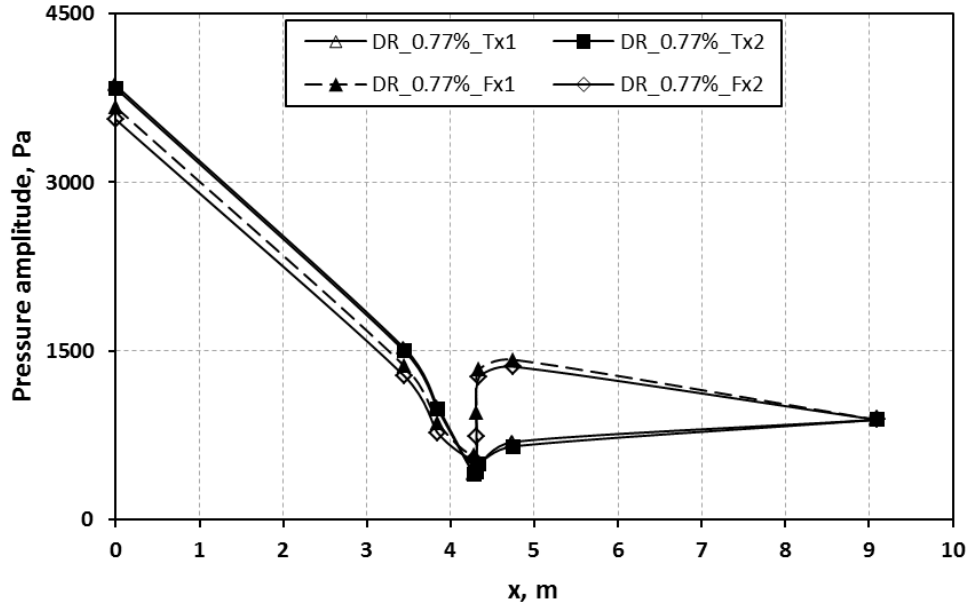


Figure 3.24: Comparison of the pressure amplitude distribution as a function of locations, for the T-HEX and F-HEX configurations at $DR = 0.77\%$, $T_h = 70^\circ\text{C}$ and $P_m = 5$ bar. In the legend, Tx1 = T-HEX (flat), Tx2 = T-HEX (ogive), Fx1 = F-HEX (flat), and Fx2 = F-HEX (ogive).

A higher magnitude of pressure amplitude can be seen at $x = 4.34$ m (P6) and $x = 4.74$ m (P7) in comparison to the profile for T-HEX (flat). The difference can be attributed to the difference in porosities for the two HEXs. Figure 3.24 shows the comparison of pressure profile distribution for T-HEX (flat), T-HEX (ogive), F-HEX (flat) and F-HEX (ogive) on a single plot. In addition to the effect of porosity as the likely reason for the difference in the pressure amplitude profiles between T-HEX and F-HEX configurations, the separation gaps between two adjacent heat exchangers could also contribute to the observed difference. However, the influence of edge shapes is less pronounced for both T-HEX and F-HEX types.

3.6 Uncertainties related to the experimental results

The heat transfer and acoustic pressure drop performance in oscillatory flow are derived from the measured variables such as the temperatures, fluid property, flow rates, frequency, gas displacement amplitude, etc., regardless of how it is represented, for example, heat transfer rates, heat transfer coefficient or its dimensionless form, the Nusselt Number, and minor loss coefficient. As with every experiment, it is inevitable that uncertainty will be present in the experimental

results. These uncertainties were evaluated at 95% confidence level using the method described by Moffat (1988), Coleman and Steele (2009). In this approach, for a value of R, whose results depend on uncorrelated input estimates X_1, X_2, \dots, X_N , the standard uncertainty of the measurement was obtained by appropriately combining the standard uncertainties of these input estimates. The uncertainty of the value R was calculated from the following equations:

$$R = R(X_1, X_2, \dots, X_N) \quad (3.2)$$

$$\delta R = \left\{ \sum_{i=1}^N \left(\frac{\partial R}{\partial X_i} \delta X_i \right)^2 \right\}^{1/2} \quad (3.3)$$

Considering the propagation of errors, the errors of each measured variable include the systematic and random errors, as presented in equation (3.4). The systematic errors is defined in equation 3.5 and depend on the sensors and the corresponding data acquisition devices. The random errors are presented in equation (3.6).

$$\delta X_i = (s_R^2 + r_R^2)^{1/2} \quad (3.4)$$

If the systematic uncertainty s_R in the measurement of individual variable is independent of the systemic limit in each of the other measured variables, then:

$$s_R^2 = \sum_{i=1}^N \left(\frac{\partial R}{\partial X_i} s_{X_i} \right)^2 \quad (3.5)$$

$$r_R^2 = \sum_{i=1}^N \left(\frac{\partial R}{\partial X_i} r_{X_i} \right)^2 \quad (3.6)$$

The sample standard deviation (R_{X_i}) is used as the basis for computing the random error:

$$R_{X_i} = \left\{ \sum_{i=1}^N \frac{(X_i - \bar{X}_i)^2}{N-1} \right\}^{1/2} \quad (3.7)$$

The elemental random error (standard error), r_{X_i} , for certain level of confidence (Moffat, 1988; Dieck et al., 2005) can be written as:

$$r_{X_i} = \frac{R_{X_i}}{\sqrt{N}} \quad (3.8)$$

By 95% confidence level, the interval $\bar{X} \pm 2r$ is recommended by (Rood and Telionis, 1991; Kim et. al 1993; Coleman and Steele, 2009). The random error is evaluated for accuracy and repeatability of parameter measurements. To reduce precision error, the data acquisition system took several readings for each data and averaged them out; for example, 8000 data points were collected for temperature over one second, and the mean value are used for the calculation.

Systematic uncertainty – estimation of elemental systematic uncertainty may be derived from instrument specifications, calibration certificate and information from the literature. Literature/calibration certificates/specification mostly gives the limit of error at a specific confidence level. Following Dieck et al. (2005), the elemental systematic error can be estimated as:

$$s_x = \frac{B_l}{2} \quad (3.9)$$

where B_l is the limit of error and 2 is the statistical number according to a 95% confidence level. The limit of error above 0° for Type K thermocouple is $\pm 1.1^\circ\text{C}$ or 0.4% (whichever is greater) by Omega (2016). The systematic error is minimised through calibration of measurement equipment. The combined uncertainty at 95% confidence level is $\bar{X} \pm 2\delta X_i$.

For the Nusselt number, using equations (3.5), (3.6) and (2.38), the error propagation can be determined in dimensionless form as:

$$\left(\frac{s_{Nu}}{Nu}\right)^2 = \sum_{i=1}^N \left(\frac{\partial Nu}{\partial X_i}\right)^2 = \left(\frac{s_h}{h}\right)^2 + \left(\frac{s_{D_h}}{D_h}\right)^2 + \left(\frac{s_k}{k}\right)^2 \quad (3.10)$$

$$\left(\frac{r_{Nu}}{Nu}\right)^2 = \sum_{i=1}^N \left(\frac{\partial Nu}{\partial X_i}\right)^2 = \left(\frac{r_h}{h}\right)^2 + \left(\frac{r_{D_h}}{D_h}\right)^2 + \left(\frac{b_k}{k}\right)^2 \quad (3.11)$$

The heat transfer coefficient is further defined in a similar way as the equations (3.10) and (3.11), using the definition of heat transfer coefficient in equation (2.39). The error bars on Nusselt number calculations as will be discussed in the later chapters are determined based on the described method. The combined uncertainty in the heat transfer rates is in the range of 1.38 – 12.5% at 95% confidence interval and that of Nusselt number is in the range of 1.41 – 12.6%. The uncertainties from the geometric tolerance of heat exchanger fabrication and thermal conductivity of helium are assumed negligible for the uncertainty on the Nusselt number. The lower

bound in the uncertainty is achieved at a temperature of 70°C on HHX and mean pressure of 10bar. The upper bound resulted from a 30°C temperature on HHX at a mean pressure of 1.0bar. The uncertainty gets lower as the temperature and the mean pressure increase.

3.7 Summary

The design, development and testing of the experimental set-up that will facilitate the study of heat transfer and acoustic pressure drop on T-HEX and F-HEX in oscillatory have been discussed in this chapter. The design of test objects, mainly the heat exchanger and edge shapes, has been described in detailed. The design considerations include the selection of heat exchanger type, fabrication method, health and safety checks, and the symmetrical arrangement of the heat exchangers. The geometrical design has been validated and found to reflect the targeted capabilities such as the maximum design mean pressure in the resonator and the excursion limit of the driver piston. The measurement techniques and capabilities have been established. The calibration of transducers and the determination of resonance frequency and its dependency on the mean pressure and edge shape have also been discussed. The pressure amplitude distribution and the method of estimating the measurement uncertainty as relevant to the later chapters have been discussed.

Chapter 4

Experimental Analysis of the Tube and Finned Heat Exchangers

This chapter describes the heat transfer analysis on the T-HEX and F-HEX configurations, including the edge shapes. Measurement data from the experimental set-up and the measurement techniques, as described in Chapter 3, are used for the heat transfer analysis. Section 4.1 provides details of experimental conditions, including operating conditions under which the heat exchangers are tested. Section 4.2 gives the description of relevant expressions and methodology that are used in the analysis. Section 4.3 discusses the heat transfer results. The comparison between the heat transfer results in this study and other models from the literature are presented in section 4.4. Section 4.5 gives the concluding summary for the chapter.

4.1 Experimental conditions

Heat transfer performance of heat exchanger in oscillatory flow is critical to the overall efficiency of the thermoacoustic engines and coolers. Maximising heat transfer and minimising acoustic pressure losses are essential and both effects depend on flow conditions and suggest that the geometry or design of the heat exchanger impacts its performance. To test the effects of geometric design on heat transfer, two sets of heat exchangers (T-HEX and F-HEX), and the plate attachments (ogive edge shapes) were made, as described in the previous chapter. In addition, three lengths of heat exchangers were achievable in both sets, with the use of blank plate attachments – 20.0 mm, 24.0 mm, and 28.0 mm. The heat transfer as measured on T-HEX and F-HEX as a function of the drive ratio and the mean pressure in the experimental set-up are discussed here.

The operating conditions are given in Table 4.1. Some of the experiments on T-HEX (ogive) are conducted up to 30bar mean pressure as can be seen in the plot of resonance frequency (cf. Figure 3.20). Table 4.1 indicated the experimental conditions with the mean pressure that are common to all the heat exchanger geometries and edge shapes. To achieve the experimental conditions, the test rig was set-up and allowed to be at thermal and acoustic equilibrium conditions. During operation, the two water loops created heating and cooling loads in a typical set of

heat exchangers in the test section. When the acoustic driver is excited, the helium gas within the set-up oscillated through the heat exchangers in the test section, thereby generating transfer of heat between the hot and cold heat exchangers.

Table 4.1: Geometric and operating conditions

T-HEX (Flat edge)					
Mean pressure (bar)	1.0	3.0	5.0	7.5	10.0
Resonance frequency (Hz)	53.3	52.3	53.6	54.5	54.6
Drive ratio, <i>DR</i> (%)	0.1 – 3.0				
T-HEX (Ogive edge)					
Resonance frequency (Hz)	52.8	53.7	54.3	54.5	55.0
Drive ratio, <i>DR</i> (%)	0.1 – 3.0				
F-HEX (Flat edge)					
Resonance frequency (Hz)	52.3	53.6	54.5	54.6	53.3
Drive ratio, <i>DR</i> (%)	0.08 – 1.0				
F-HEX (Ogive edge)					
Resonance frequency (Hz)	53.1	53.9	54.2	54.4	55.2
Drive ratio, <i>DR</i> (%)	0.1 – 0.9				
Water temperature (°C)					
CHX1	10				
HHX	30, 50, 70				
CHX2	10				
Flow rates (L/min)	0.44				

The heat load delivered to the HHX at temperatures of 30, 50 and 70°C is removed by the two CHX's at a constant temperature of 10°C. The constant flow rate of 0.44lpm is used for both hot and cold heat exchangers. Simultaneously, oscillating pressures were produced as the helium gas moved through the heat exchangers. By measuring these pressure amplitudes in various locations within test rig (cf. Figure 3.2), the volumetric velocity of helium gas through the heat exchangers, their associated acoustic impedances, and resulting acoustic power losses could be calculated, in addition to the acoustic pressure drop across each of the heat exchanger that can be calculated from the pressure amplitudes measured at location 1, 2, 3, and 4. (cf. Figure 3.4). At every location within the test section, temperature

and pressure amplitude measurements from thermocouples and pressure transducer are recorded. Similarly, for the water side, water temperatures and flow meter data are recorded. Eight thousand readings are obtained over the duration of one second, and continuous data reading over the duration of a typical experimental condition are also recorded. At each experimental condition, desired drive ratio is achieved by changing the excitation voltage supplied to the acoustic driver, through driver controller's keypad. This, in turn, changes the displacement amplitude of the driver piston accordingly, resulting in the desired drive ratio. A similar procedure is involved for completing experiments on each set of heat exchangers and edge shapes. It should be noted that in all cases, only mean temperatures were measured. Thus, only the time-averaged heat transfer was calculated. Some oscillation components of heat transfer will be present in the experiment, in addition to the mean value; however, the oscillating component is assumed negligible in the current work.

4.2 Data reduction

The data collected from the experiments was used to evaluate heat transfer performance, which is represented in the forms of heat transfer rate (\dot{Q}), heat transfer coefficient (h), and Nusselt number (Nu).

4.2.1 Heat transfer rates (\dot{Q})

As helium gas oscillates in the HHX, heat transfer between the helium gas and the exchanger caused the temperature of water within it to decrease. Similarly, for the CHX1 and CHX2, heat transfer between the helium gas and the heat exchangers resulted in the temperature of water within them to increase in this case. By measuring the difference between the temperatures of water at the inlet and outlet of each heat exchanger, the heat transfer within each heat exchanger could be calculated by using the water volume flow-rate, the specific heat capacity, the density and the following equations:

$$\dot{Q}_h = \dot{m}_h \cdot c_{p,h} (T_{w,i} - T_{w,o})_h = \rho_w q_v c_{p,h} (T_{w,i} - T_{w,o})_h \quad (4.1)$$

$$\dot{Q}_{c1,c2} = \dot{m}_{c1,c2} c_{p,(c1,c2)} (T_{w,o} - T_{w,i})_{c1,c2} = \rho_w q_v c_{p,(c1,c2)} (T_{w,o} - T_{w,i})_{c1,c2}$$

The subscripts w , i , and o denote water, the location of inlet and outlet of fluid stream on the water side of the heat exchangers. Subscripts h , $c1$, and $c2$ denote heat transfer rates for the hot and cold heat exchangers. A constant flow rate of 0.44 litres per minute (lpm) was used on CHX1, HHX and CHX2 in all experiments. Using equation (2.34) the Reynolds number on the water side is in the range of 827 – 2659. This range is due to the change in temperature of the thermal reservoir for the HHX. The density and specific heat capacity are evaluated at average inlet and outlet water temperatures as follows:

$$\frac{(T_{w,i} + T_{w,o})_h}{2}, \text{ and } \frac{(T_{w,o} + T_{w,i})_{c1,c2}}{2} \quad (4.2)$$

The water density is calculated from (Maidment, 1993)

$$\rho_{water} = 1000 \times \left\{ 1 - \left(\frac{T_{\circ C} + 288.9414}{(508,929.2 \times (T_{\circ C} + 68.12963))} \times (T_{\circ C} - 3.9863)^2 \right) \right\} \quad (4.3)$$

The specific heat capacity of water is estimated at mean temperature using empirical equation (4.4). The specific value of water at temperature $T^{\circ C}$ with reference to its specific value at $15^{\circ C}$ (4.1855 kJ/kgK) is given by (Richardson, 2005):

$$\frac{c_p(T^{\circ C})}{c_p(15^{\circ C})} = \left(0.996185 + 0.0002874 \left(\frac{T + 100}{100} \right)^{5.26} + 0.011160 \times 10^{-0.036T} \right) \quad (4.4)$$

The empirical equation (4.4) is applicable for $0 \leq T (^{\circ C}) \leq 90^{\circ C}$ and $P = P$ (atm).

The heat balance measurement on the heat exchangers can be considered in two ways: the heat balance across the symmetric arrangement of the heat exchangers and heat balance across a single heat exchanger. The heat balance resulting from the symmetry can be written as:

$$\dot{Q}_h = \dot{Q}_{c1} + \dot{Q}_{c2} \quad (4.5)$$

where \dot{Q}_h is the heat input through the HHX. \dot{Q}_{c1} and \dot{Q}_{c2} are the heat removed by the two CHX1 and CHX2. The heat balance on a single heat exchanger can be described as:

$$\dot{Q} = \dot{Q}_{measured} - \dot{Q}_{loss} \quad (4.6)$$

The heat transfer rates in equation (4.1) include heat leaks as expressed in equation (4.6). The major advantage of the symmetric arrangement of heat exchangers in this study is mainly to facilitate heat measurement on the HHX and allow accurate estimation for the heat leak. Also, an enormous volume of silicate wool in the test section (cf. Figure 3.5) provided lots of insulation for the heat exchangers and prevented heat loss to and from the environment. In other words, the HHX is well insulated against heat loss through unaccountable means, which was evident during the experiments as well as in the results that will be discussed in the sections below. Despite the high-level heat leak prevention, it is still inevitable that some form of heat leak would be present. Therefore, heat leaks are accounted for to ensure accurate heat transfer calculation. ‘Static’ measurements were carried out at the beginning of every experiment, that is, data were recorded when the system is at thermal equilibrium condition and before the acoustic driver is switched on (i.e. no flow excitation). The heat transfer by conduction through helium gas is evaluated using the temperature difference between the inlet and the outlet of the heat exchangers as described in equation (4.1). The maximum of these are 15.59, 29.19 and 17.17 W for CHX1, HHX, and CHX2, respectively, at $P_m = 10$ bars and $T_h = 70^\circ\text{C}$ on HHX. Also, heat transfer by conduction through insulation material as well helium gas at 202 mm away from the CHX2 are evaluated using the Fourier equation, defined as:

$$\dot{Q}_{loss} = k_{ins} A_{hx} \frac{\Delta T_{ins}}{\Delta x} \quad (4.7)$$

where k_{ins} , A_{hx} , ΔT_{ins} and Δx are the thermal conductivity of insulation, the outer surface area of HEX in contact with the insulation, temperature difference across the insulation and distance from the outer wall of HHX to the location of the thermocouple (T17). At static condition (no-flow excitation), $P_m = 10$ bar and temperature of 70°C on HHX, the heat transfer by conduction in the insulation material is 102.4 mW, and that of helium gas is 14 mW. These values are obtained using thermocouples T16 and T17. The estimated heat leaks are subtracted from the heat transfer rates in equation (4.6) during heat transfer analysis. Other sources of heat leak include heat conduction through the fittings. However, this is difficult to account for and considered negligible in this study. As mentioned earlier, the significance of heat loss analysis is to correction heat transfer data from the heat

exchanger, thereby ensuring the reliability of the correlation that will be proposed from the analysis.

4.2.2 Surface temperature (T_s)

In the current study, the surface temperatures of the heat exchangers on the helium side are measured directly from the experiments using thermocouples T13, T14, and T15 (cf. Figure 3.4). This is done to account for the heat conduction of the aluminium material of the heat exchanger (Tang et al., 2013; Al-Damook et al., 2015). The surface temperature is required for the calculation of heat transfer coefficient and as boundary conditions for the 3D numerical model, as will be discussed in Chapter 5.

Another possibility, though not used in the current study, for obtaining the surface temperature of the heat exchanger is by using logarithmic mean temperature difference (LMTD) method, where the measured temperatures on the water side of the heat exchanger are utilized in the calculation (Incorpera et al., 2007 (pg.711 – 739); Brady, 2011). The LMTD surface temperatures can be written for CHX1, HHX and CHX2 as:

$$T_{s(c1,c2)} = \frac{(T_{w,o} - T_{w,i})}{\ln\left(\frac{T_{w,o}}{T_{w,i}}\right)}, \quad T_{s,h} = \frac{(T_{w,i} - T_{w,o})}{\ln\left(\frac{T_{w,i}}{T_{w,o}}\right)} \quad (4.8)$$

Equation (4.8) assumes that the heated surface in contact with oscillating helium is held at a constant temperature. Also, considering the thin wall of the heat exchanger (0.5 mm) that separates the helium gas from the water side, this approximation would provide an alternative method of estimating the gas side surface temperature if it was not measured directly. However, the surface temperatures that are measured directly on the gas side of the heat exchangers are used in the calculation of heat transfer coefficient, as previously remarked, to improve the measurement uncertainty.

4.2.3 Nusselt number (Nu)

In the current study, heat transfer performance of the current heat exchangers in oscillating flow would be presented in terms of the gas side Nusselt number to allow comparison with the 3D numerical model and other models from the literature. The Nusselt number is the ratio of the convective to conductive heat transfer normal to

the wall. The Nusselt number is related to the heat transfer coefficient (h) in the following expression as:

$$Nu = \frac{hD_h}{k} \quad (4.9)$$

In the current study, the heat transfer coefficient is defined as (Holman, 2001; Al-Damook et al., 2015):

$$h = \frac{\dot{Q}}{A_s \Delta T} = \frac{q}{\Delta T} \quad (4.10)$$

Where \dot{Q} is the heat transfer rate defined in equation (4.1) A_s is the wall area of the heat exchangers in contact with the helium gas and q is the heat flux. As previously remarked, ΔT is the temperature difference between the solid medium and the fluid temperature, being referred to as the thermal potential for the heat transfer coefficient. In oscillatory flow, the fluid temperature changes in time and location due to the forward and backwards movement of the gas particles. Heat transfer coefficients, as typically defined for steady flow, may not strictly be appropriate for oscillating flow. Until now, it appears that there is no general guideline for articulating the way that the heat transfer coefficient can best represent the oscillatory nature of the reciprocating flow. The thermal potential can be mathematically represented as $\Delta T = T_s - T_i$. T_i is defined as the mean of gas temperatures at the inlet and outlet of the heat exchangers (cf. Figure 3.12). The subscript i indicates locations 1, 2, 3 and 4 (cf. Figure 3.4), i.e.

$$T_i = \left(\frac{T_{inlet} + T_{outlet}}{2} \right) \quad (4.11)$$

The symmetric arrangement of the thermocouples at locations around the heat exchangers allows the averaging of temperatures at inlet and outlet of each heat exchanger. This definition is chosen to reflect the contribution of the gas temperatures (i.e. gas temperatures at the inlet and outlet of the heat exchangers) to the heat transfer performance of heat exchanger. From equations (4.10) and (4.11), the heat transfer coefficient for CHX1_t, HHX_t and CHX2_t can be written as (Tang et al., 2013):

$$h_{h,c1,c2,(T-HEX)} = \frac{\dot{Q}}{A_s \left[T_s - \left(\frac{T_{inlet} + T_{outlet}}{2} \right) \right]} \quad (4.12)$$

As previously described, the F-HEX consists of aluminium fins brazed to the base surface of the heat exchanger. The symmetric arrangement of the heat exchangers in the current study involves the heat transfer to and from oscillating gas. For an identical set of heat exchangers, it is logical that the heat transfer performance would be the same as will be seen in the later chapters.

Also, from equations (4.10) and (4.11), the heat transfer coefficient for CHX1_f, HHX_f and CHX2_f can be formulated as:

$$h_{h,c1,c2,(F-HEX)} = \frac{\dot{Q}}{\left(A_s + \sum_{i=1}^n A_{f,i} \eta_{f,i} \right) \left[T_s - \left(\frac{T_{inlet} + T_{outlet}}{2} \right) \right]} \quad (4.13)$$

where A_s is an area of the base surface, $A_{f,i}$ and $\eta_{f,i}$ are the surface area and the fin efficiency of the i th fin, respectively. Ideally, the fins in F-HEX would conduct heat perfectly from the base surface and convectively transfer it to or from the gas while maintaining a surface temperature equivalent to its source of heat. Actual fins, however, experience a temperature gradient along their length. Thus, the performance of the fin is represented as fin efficiency, which is defined by a ratio of the actual convective heat transfer from the fin over the convective heat transfer as if the entire fin surface had the same temperature with its base temperature. In the case of a fin with the uniform cross section (cf. Figure 3.10) with convective heat transfer at the fin tip, the definition of fin efficiency is given as (McQuiston and Parker, 1994):

$$\eta_f = \frac{\tanh(mh_{cor})}{mh_{cor}} \quad (4.14)$$

where m and h_{cor} are expressed by:

$$m = \left(\frac{2h}{k_{al}f_t} \right)^{1/2} \quad (4.15)$$

where h , k_{al} and f_t are the convective heat transfer coefficient, the thermal conductivity of fin material (aluminium) and the fin thickness. When the fin is

considered having convective heat transfer at its tip, the corrected fin length (h_{cor}) which is half of the channel height can be found from:

$$h_{cor} = \frac{f_h}{2} - f_t \quad (4.16)$$

In the current study, fins were brazed to the base surfaces of the F-HEX. The efficiency of a single fin obtained from equation (4.14) will be used to evaluate the performance of the fins attached to each slot of F-HEX. The overall fin efficiency (η_s) characterises the heat transfer performance of all fins including the base area to which they are attached. The overall fin efficiency (η_s) is obtained from:

$$\eta_s = 1 - \frac{A_f}{A_o}(1 - \eta_f) \quad (4.17)$$

where, A_f and A_o denote the fin area and the total area associated with both the finned and the unfinned area. The unfinned area is the external surface of slots in F-HEX that is contact helium gas.

To take care of the heat transfer through the plate attachments, they are considered as an extended surface, and their fin efficiency was evaluated. This consideration holds for both T-HEX and F-HEX when the plate attachments are used. Otherwise, equation (4.12) is used in the calculation of heat transfer coefficient for the T-HEX.

The viscosity and thermal conductivity of helium gas obey the power law over a large temperature range (Swift, 2002) and they are assumed to be independent of pressure, so that:

$$k = 0.152 \cdot \left(\frac{T}{T_o}\right)^{0.72} \quad \mu = 1.99 \cdot 10^{-5} \cdot \left(\frac{T}{T_o}\right)^{0.68} \quad (4.18)$$

The mean temperature defined by equation (4.11) is used in the evaluation of equation (4.18). Again, the symmetric arrangement of the heat exchanger permits the use of this averaged temperature.

The mean density of helium gas within the experiment is calculated using the mean operating pressure and the ideal gas law as:

$$\rho_m = \frac{P_m}{\gamma R_{sp} T_i} \quad (4.19)$$

where T_i is the mean gas temperature (cf. equation (4.11)).

The hydraulic diameter in terms of geometric dimensions of flat crest fins for the F-HEX can be formulated from equation (2.35), following Kern and Kraus (1972) and Kutz (2006):

$$D_h = \frac{4A_c}{\Pi} = \frac{4(f_h - f_t) \left(\frac{1}{N_f} - f_t \right)}{2 \left(f_h + \frac{1}{N_f} - 2f_t \right)} \quad (4.20)$$

Equation (4.20) represents hydraulic diameter for a single cell in the fin. Total hydraulic diameter can be evaluated from the number cells in each of the slots that make up the F-HEX gas channel.

Porosity is an important geometrical parameter especially when pressure drop consideration is involved. From equation (2.36), the porosity of T-HEX can be defined as:

$$\sigma_{T-HEX} = \frac{nd_t^2}{d_f^2} \quad (4.21)$$

where d_t , n and d_f are the tube diameter, total number of tubes and frontal core diameter, respectively. Similarly, from equation (2.36), the porosity of F-HEX with plain flat crest fins can be formulated as:

$$\sigma_{F-HEX} = \frac{\sum_{i=1}^n (W_i \times N_f \times A_c) + \pi r_e^2}{\pi \left(\frac{d_f}{2} \right)^2} \quad (4.22)$$

where W_i , A_c , and r_e are the width of n th slot (i.e. cut-off length), the cross-sectional area for flow of a single cell in the fin, and the radius of the slot edge.

4.2.4 Acoustic Reynolds number (Re_1)

The Reynolds number as defined in equation (2.34) is based on the hydraulic diameter of the flow channel. For the gas side, the acoustic Reynolds number is defined as:

$$Re_1 = \frac{\rho u_{m,h} D_h}{\mu} \quad (4.23)$$

The acoustic Reynolds number is based on hydraulic diameter. $u_{m,h}$ is the velocity amplitude at the centre of HHX. The velocity amplitude is related to the displacement amplitude by $\xi_1 \omega = u_1$ according to equation (2.32), with the velocity leading the displacement by 90° in phase. The velocity amplitudes at the centre of HHX are obtained from Wakeland and Keolian (2004):

$$u_{m,h} = \frac{u_1}{\sigma} \quad (4.24)$$

The acoustic Reynolds number for all the experimental results is in the range of 45 – 7900. According to Merkli and Thomann (1975), the flow regime in oscillatory flow is considered laminar as long as the critical Stokes Reynolds number is less than 400. The Stokes Reynolds number is defined as $Re_c = 2u_{m,h}/(\nu\omega)^{1/2}$ with ν and ω denoting the kinematic viscosity and angular velocity, respectively. The Stokes Reynolds number for all the drive ratios investigated in the experiment is in the range of $15 \leq Re_c \leq 1000$ with 70% of this range falling in the laminar oscillatory flow regime.

4.3 Heat transfer conditions

The results of heat transfer on the heat exchangers (T-HEX and F-HEX) are discussed in this section. The results cover the effect of operating parameters on the heat transfer performance of the heat exchanger. The operating parameters as investigated include the effect of gas mean pressure, drive ratio and the gas mean temperature on the heat exchangers' performance. Measurements are taken at the same locations in all the configurations of the heat exchangers tested. The measurement uncertainties in the experiments are evaluated for all heat transfer results as discussed in Chapter 3 (section 3.6). However, the error bars are only shown on the Nusselt number results at 30°C temperature setting. The error bars at

other temperatures (50°C and 70°C) appear too small and make the symbols on the plots difficult to interpret. Hence, they are left out to aid the clarity of the results.

4.3.1 Temperature measurements

The gas temperature profiles as measured from different locations in the test section and for selected operating conditions are plotted against the drive ratio, as shown in Figure 4.1 for the T-HEX (flat) and T-HEX (ogive). The plot shows the temperatures at the inlet and outlet of the heat exchanger on the water side for CHX1, HHX and CHX2. On the helium side, the plot shows the measured temperature on the surface of the gas channel, middle of the gas channel and inlet and outlet of the heat exchangers. The hot water temperature is at 50°C, and three mean pressures are at 3, 5 and 10 bar. These are represented in Figure 4.1(a - c) for T-HEX (flat) and Figure 4.1(d-f) for T-HEX (ogive). Temperatures at the inlet of the CHX1 ($T_{c1,i}$), CHX2 ($T_{c2,i}$), are denoted by the bottom lines while the top line represents the inlet temperature of HHX ($T_{h,i}$). These three lines are virtually stable as they are maintained at given temperatures. When the gas parcels begin to oscillate, the transported heat between the hot and the two cold heat exchangers can be seen from the span of the temperature difference between the inlet and the outlet of CHX1, HHX and CHX2, which becomes increasingly large. This behaviour can be seen for the three mean pressures represented in the plot. The gas oscillation also causes a gradual difference in the surface temperatures ($T_{s,c1}$, $T_{s,h}$ and $T_{s,c2}$) as the drive ratio increases. Temperatures T-1, T-2, T-3 and T-4 in the legend of Figure 4.1 are the average temperature from three thermocouples at locations 1, 2, 3, and 4 in the test section (cf. 3.4). $T_{c1,mid}$, $T_{h,mid}$ and $T_{c2,mid}$ are temperatures in the middle of the gas channel of CHX1, HHX and CHX2, respectively. The gas temperatures T-2 and T-3 measured at the gaps between CHX1/HHX and HHX/CHX2 gradually decrease as the drive ratio (DR) increases.

The decrease in the temperature T-2 and T-3 with respect to DR is because the cold gas from the cold heat exchangers penetrates the hot heat exchanger absorbing and carrying heat on its returning cycle. Simultaneously, the gas parcels at location T-1 and T-4, located just behind the CHX1 and CHX2, are warmer because the two cold heat exchangers receive more heat from HHX as the gas oscillates back and forth.

The temperature profiles of oscillating gas T-1, T-2, T-3 and T-4 are closer to each other and almost stable where the $DR > 0.6\%$.

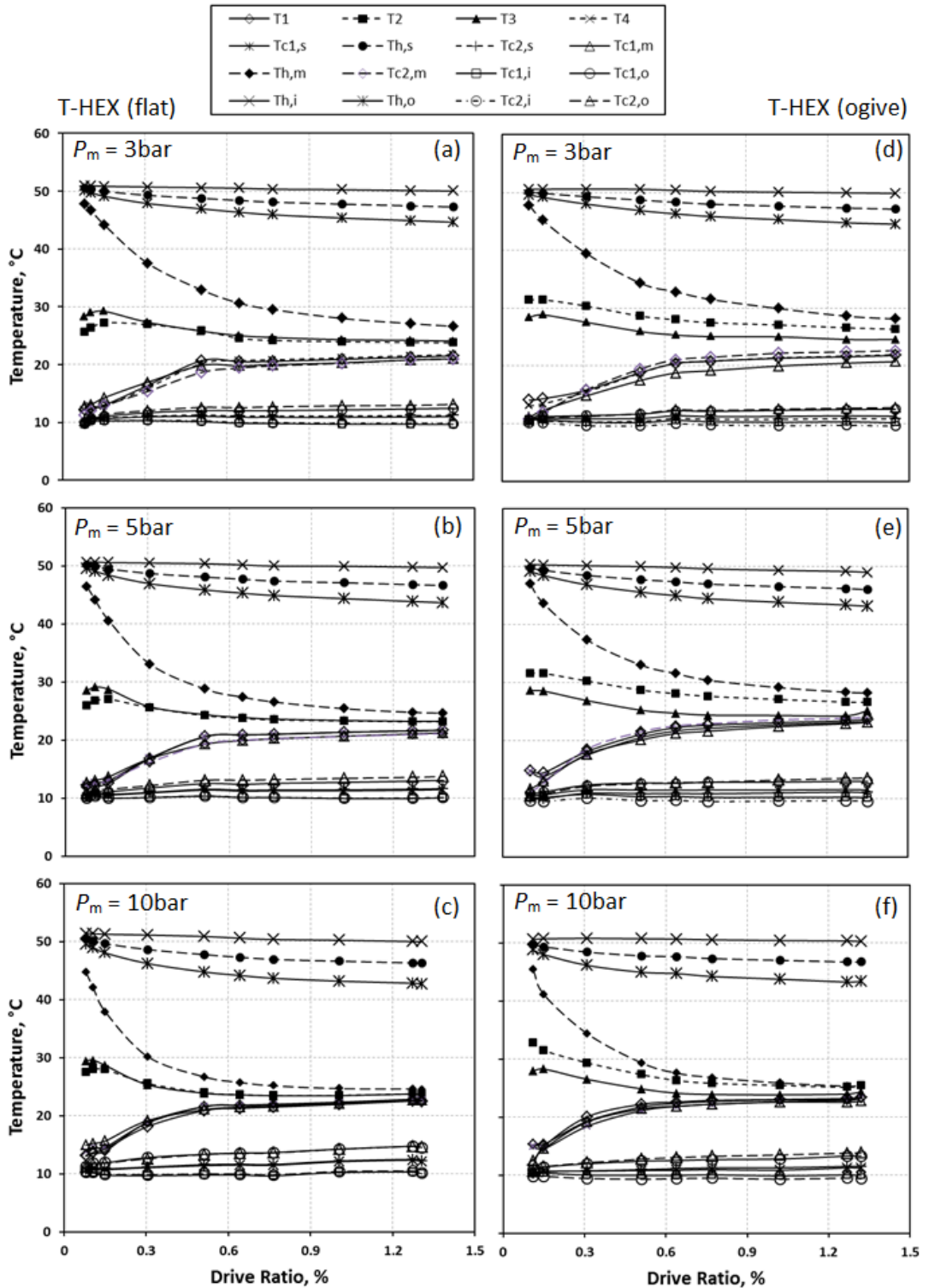


Figure 4.1: Measured temperature at various locations versus DR at $T_h = 50^\circ\text{C}$, at $P_m = 3\text{bar}$, 5bar and 10bar (a) – (c) T-HEX (flat) (d) – (f) T-HEX (ogive).

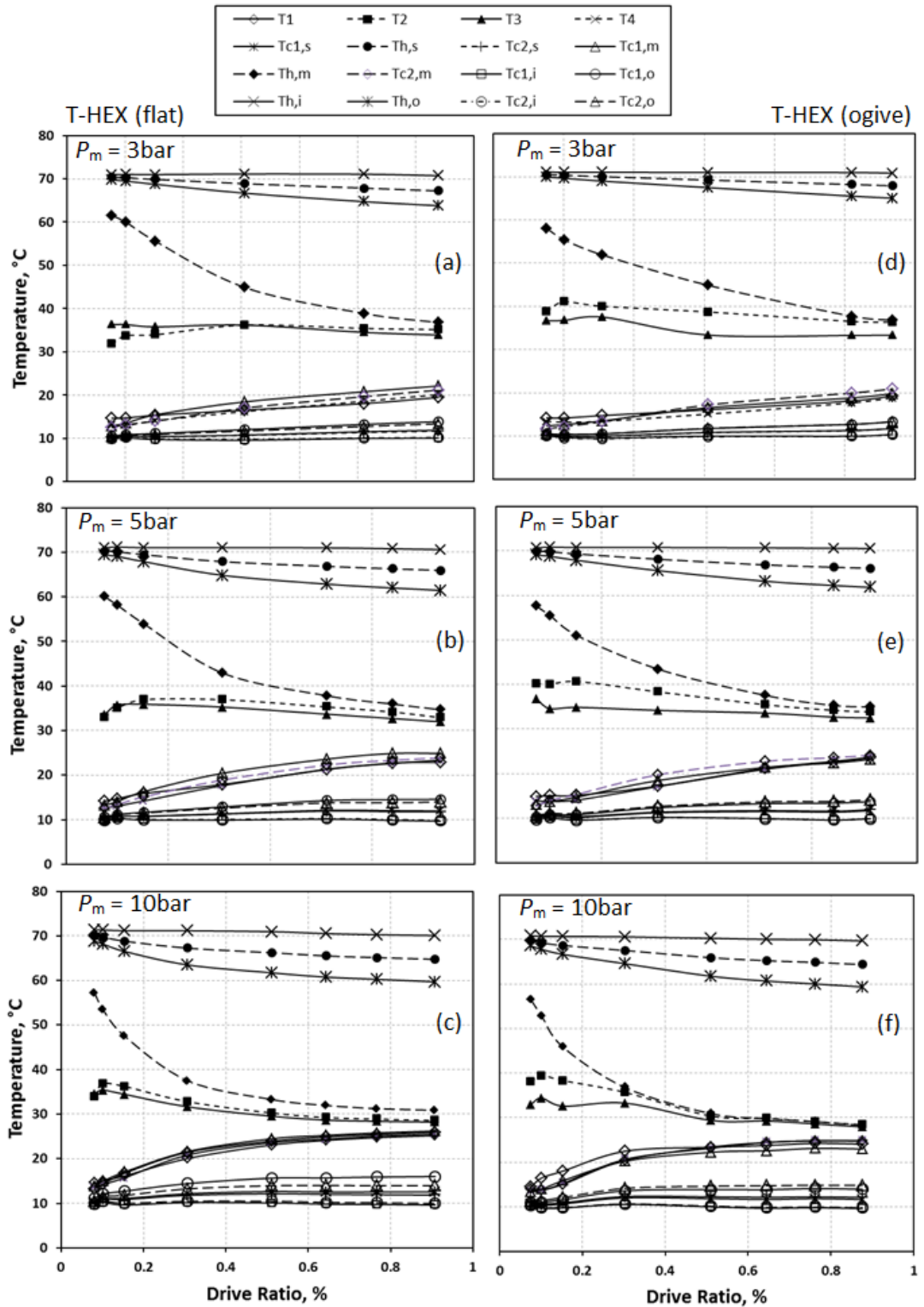


Figure 4.2: Measured temperature at various locations versus DR at $T_h = 50^\circ\text{C}$, $P_m = 3\text{bar}$, 5bar and 10bar (a) – (c) F-HEX (flat) and (d) – (f) F-HEX (ogive).

The temperature profile from $T_{c1,m}$, $T_{h,m}$ and $T_{c2,m}$ in the middle of the heat exchangers also exhibits a somewhat similar trend to that just described but with more rapid decrease for the HHX. This behaviour of temperature profiles may

indicate that the heat transfer between CHX1, HHX and CHX2 is reaching its maximum performance and DR is more likely to be less influential on the heat transfer performance. Generally, from Figure 4.1 (a-c) more heat is transported at a given DR as the mean pressure is increasing. The temperature profiles for T-1, T-2, T-3 and T-4 as well as $T_{c1,m}$, $T_{h,m}$ and $T_{c2,m}$ are closer to each other at high mean pressure (10bar) than at low (3bar). This can be attributed to the decrease in the penetration depths (cf. Figure 3.23), because of an increase in the mean pressure.

Figure 4.1 (d – f) shows the measured temperature at different locations for the T-HEX (ogive), for a similar mean pressure range as just described. The observed phenomenon is akin to that of T-HEX (flat) in Figure 4.1 (a-c), but the slope of oscillating gas temperatures T-1, T-2, T-3 and T-4, as well as $T_{c1,m}$, $T_{h,m}$ and $T_{c2,m}$ are generally more gentle, indicating less rapid temperature change of the oscillating gas. The plot of water temperatures at the exit points on cold and hot streams also becomes more gradual for $DR > 0.5\%$ and nearly constant after $DR > 0.8\%$. Figure 4.2 (a – c) and (d – f) represent the measured temperatures for the F-HEX (flat) and F-HEX (ogive) configurations. The maximum drive ratio attainable for this heat exchanger sets is 0.88% at a mean pressure above 5bar. This reduction in the DR was not expected because F-HEX has a high porosity (32.5%) in comparison with the T-HEX (24.3%). The behaviour of measured temperatures for both edge shapes, F-HEX (flat) and F-HEX (ogive), is like that of T-HEX (flat) and T-HEX (ogive) in Figure 4.1. The similarity in measured temperature behaviour is for both the gas side and the water side.

4.3.2 Effect of drive ratio (DR) on heat transfer rates (\dot{Q})

The effect of DR on heat transfer rate (\dot{Q}) is discussed in this section. The heat transfer rate is considered for T-HEX (flat), T-HEX (ogive), F-HEX (flat) and F-HEX (ogive) configurations. The results on CHX1, HHX and CHX2, are presented for HHX operating temperature (T_h) range of 30, 50, and 70°C. The two cold heat exchangers are maintained at constant temperature ($T_{c1,c2}$) of 10°C. The negative values of \dot{Q} from the two cold heat exchangers represent heat withdrawn from the oscillating helium gas. The results are presented according to different temperature settings on HHX.

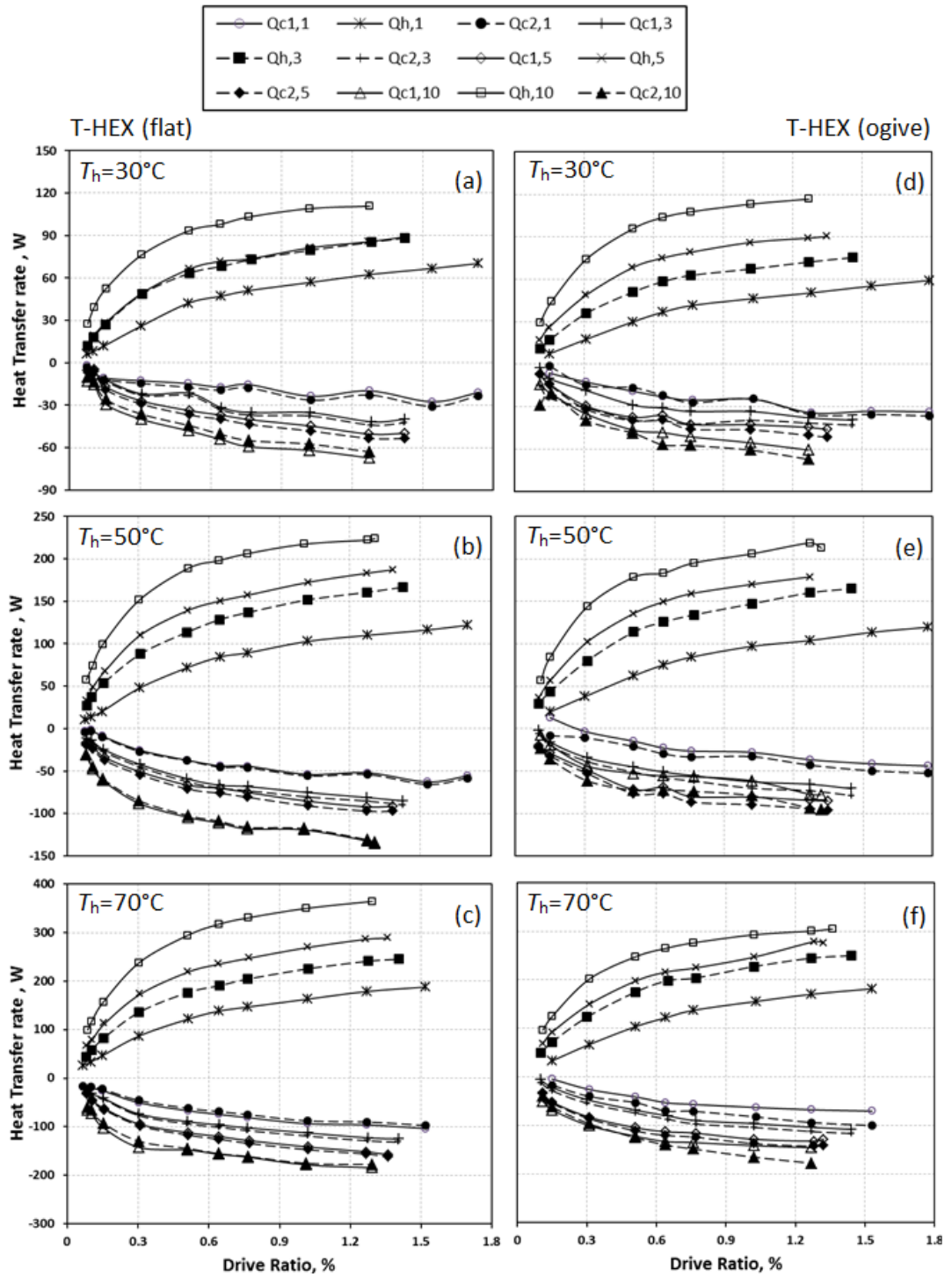


Figure 4.3: Effect of DR on \dot{Q} for the CHX1, HHX and CHX2 at various P_m , $T_h = 30^\circ\text{C} - 70^\circ\text{C}$ and $0.08 < DR < 1.8\%$ (a) – (c) T-HEX (flat) (d) – (f) T-HEX (ogive).

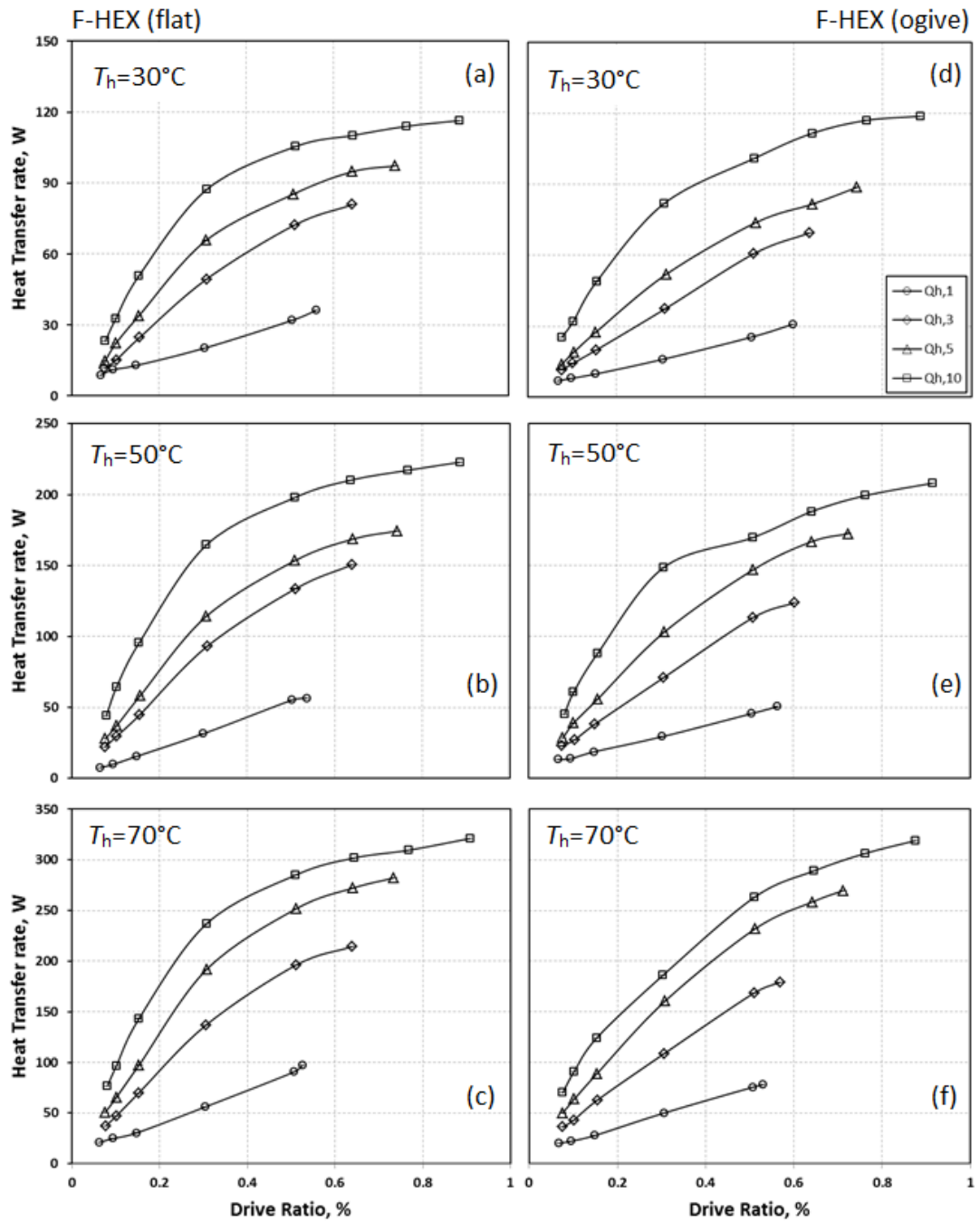


Figure 4.4: Effect of DR on \dot{Q} for the HHX at various P_m , $T_h = 30^\circ\text{C} - 70^\circ\text{C}$ and $0.08 < DR < 0.9\%$ (a) – (c) F-HEX (flat) (d) – (f) F-HEX (ogive).

In Figure 4.3 (a-c) and (d-f) show the effect of drive ratio ($0.08 < DR < 1.8\%$) on heat transfer rates for T-HEX (flat) and T-HEX (ogive), respectively. The \dot{Q} is presented on each plot for CHX1, HHX and CHX2. Generally, the \dot{Q} increases with the drive ratio. The rate of increase is rapid for $DR < 0.6\%$ for both configuration of heat exchangers and at all temperatures and mean pressures. Beyond this drive ratio, the increase becomes gradual. The rate of increase appears less rapid on CHX1 and

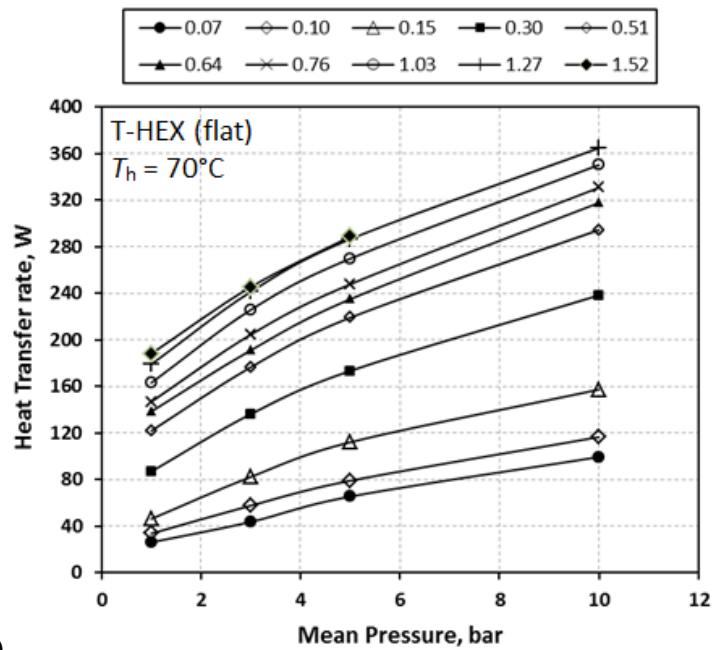
CHX2 because each of the two heat exchangers would ideally remove half of the heat input from the HHX according to the symmetric arrangement. The rapid increase in the heat transfer rates occur when the gas displacement amplitude is less than the total heat exchanger length, i.e. 28 mm ($DR < 0.6\%$) and gradually becomes less rapid as the displacement amplitude becomes larger and larger in comparison with the exchanger length. The increase/decrease of DR reflects the increase/decrease of displacement amplitude. This similar effect of DR on heat transfer was observed by Piccolo (2011), where the author reported the variation of heat flux (heat load per unit area) with the DR through a numerical computation. The effect of ogive edge shape is less pronounced at 30°C (Figure 4.3d). As the mean pressure and temperature of HHX increase (Figures 4.3e), the heat transfer rate of T-HEX (ogive) becomes gradually less in magnitude than the T-HEX (flat) configuration, especially for the CHX1 and CHX2 curves. This is more noticeable at 70°C and $P_m = 10\text{bar}$ (Figure 4.3f). The results of \dot{Q} for F-HEX (flat) and F-HEX (ogive) are described in Figure 4.4 (a-c) and (d-f), respectively, only on the HHX for the temperature of $30 - 70^\circ\text{C}$. The trends are like those observed for T-HEX (flat) and T-HEX (ogive) as described in Figure 4.3.

The heat balance for the symmetric arrangement of heat exchangers is evaluated using equation (4.5). In Figure 4.3, the deviation or heat imbalance can be seen at all drive ratios, mean pressures and HHX temperatures. The heat imbalance, when evaluated for every single experimental condition, does not follow a specific pattern of distribution, i.e. it varies differently across the experimental conditions at random patterns. The range of deviation in the heat balance for T-HEX (flat) across all experimental conditions is $0.089 - 45\text{ W}$. The lower bound occurred at $DR = 0.31\%$, $P_m = 10\text{ bar}$ and $T_h = 30^\circ\text{C}$, while the upper bound occurred at $DR = 1.29\%$, $P_m = 10\text{ bar}$ and $T_h = 50^\circ\text{C}$. Generally, the heat balance assumptions hold well for conditions at $T_h = 70$ on HHX for all mean pressure and DR 's for T-HEX (flat) configuration. For the T-HEX (ogive), the deviation range for all experimental conditions is $0.22 - 65\text{ W}$. The lower bound occurred at $DR = 1.27\%$, $P_m = 5\text{ bar}$ and $T_h = 50^\circ\text{C}$, while the upper bound occurred at $DR = 1.02\%$, $P_m = 10\text{ bar}$ and $T_h = 50^\circ\text{C}$. The imbalance in the heat transfer rates between HHX and CHXs can be attributed to heat losses

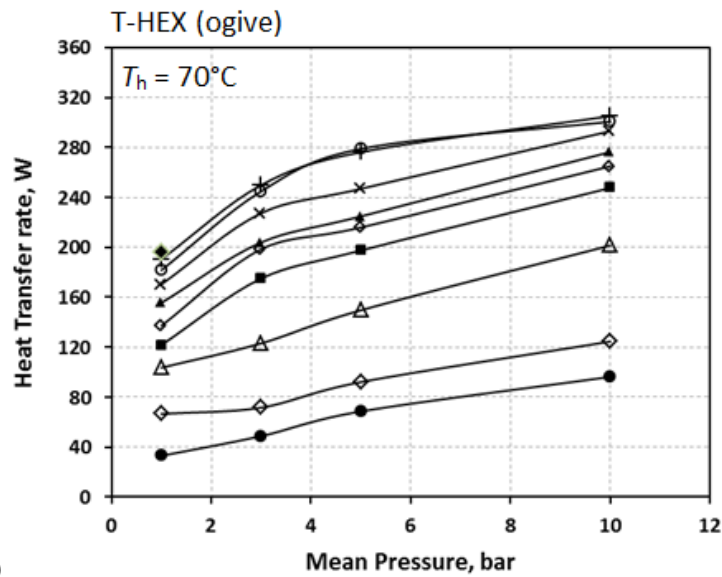
from the sources that are difficult to account for, such as heat loss through the fittings, etc.

4.3.3 Effect of mean pressure (P_m) on heat transfer rates (\dot{Q})

The effect of mean pressure on heat transfer rate is shown in Figure 4.5, for all drive ratios. Experimental results from the same measurements as those shown in the previous sections can be re-arranged to show the dependence of heat transfer rate on mean pressure. The \dot{Q} results are presented for 70°C on HHX for both T-HEX and F-HEX configurations over the range of investigated drive ratios.

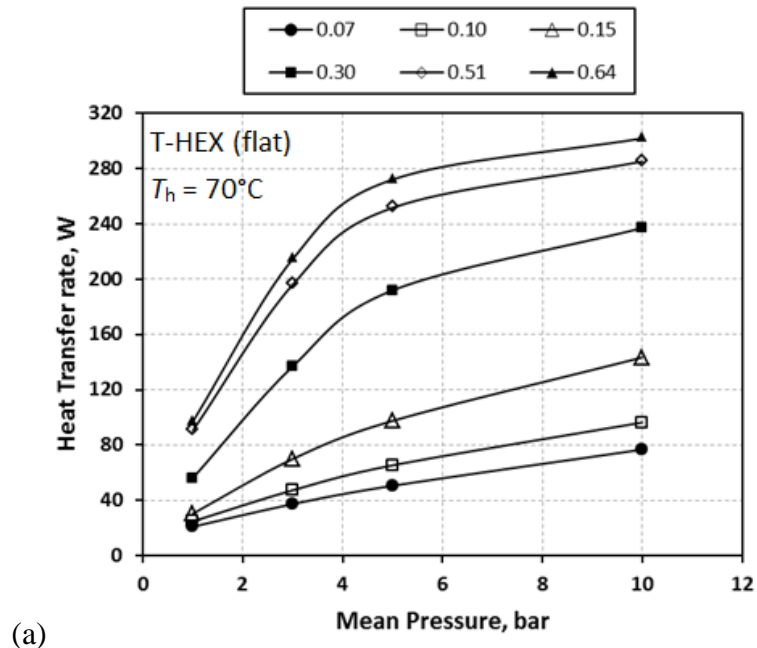


(a)

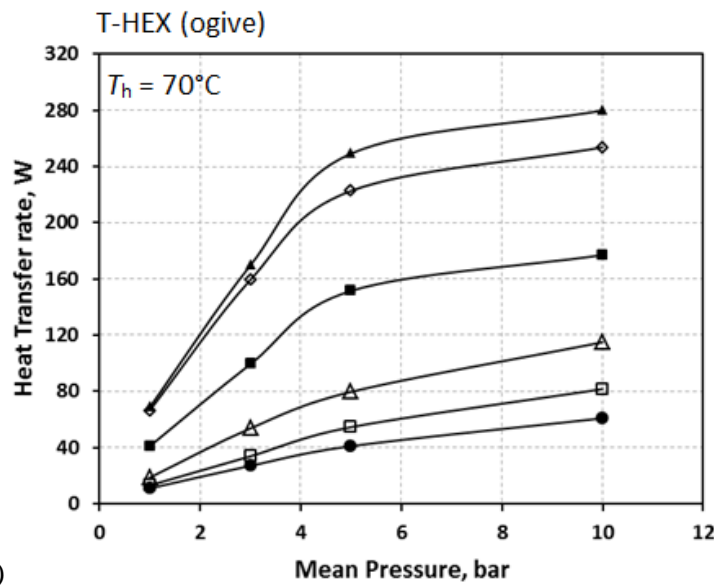


(b)

Figure 4.5: Effect of P_m on \dot{Q} for the HHX at $0.08 < DR < 1.52\%$ and $T_h = 70^\circ\text{C}$ (a) T-HEX (flat) (b) T-HEX (ogive).



(a)



(b)

Figure 4.6: Effect of P_m on \dot{Q} for the HHX at $0.08 < DR < 0.64\%$ and $T_h = 70^\circ\text{C}$ (a) F-HEX (flat) (b) F-HEX (ogive).

The connecting lines between the symbols are only for visual guidance. Figure 4.5(a) shows the \dot{Q} results for the T-HEX (flat). As can be seen from the plot, the \dot{Q} increases with increase in mean pressure for all values of drive ratios ($0.07 < DR < 1.52\%$). Figure 4.5b shows the effect of mean pressure on heat transfer rate for T-

HEX (ogive). The \dot{Q} increases as the mean pressure increases. The increase is rapid between 1 to 3bar after which it starts to become less pronounced, noticeably at the drive ratio higher than 0.3%. Figure 4.6(a) shows the results for F-HEX (flat). The trend is generally like that seen in T-HEX (ogive) results at higher drive ratio above 0.3%. Below this drive ratio, the \dot{Q} increases continuously for all the mean pressures. A similar overall trend can be observed in Figure 4.6(b) for F-HEX (ogive). The peak of \dot{Q} seems to occur at a mean pressure above 3 bar for the $DR > 0.15\%$. The heat transfer rate results discussed in this section will allow the presentation of heat transfer performance in the form of a Nusselt number, in the following sections. The effect of drive ratio on the Nusselt number will be discussed.

4.3.4 Effect of drive ratio (DR) on Nusselt number (Nu)

This section shows the variation of the gas side Nusselt number in oscillatory flow (Nu) against drive ratio and mean pressure. The Nusselt number, as presented in this section, is obtained using equation (4.9). The results from the two sets of the heat exchanger and the edge shapes are described at the condition of 30 – 70°C of HHX temperature. Figure 4.7 a-c shows the results as presented for hot exchanger for T-HEX (flat). In the plot (Figure 4.7 a-c), the variation of the Nusselt number against the drive ratio can be observed. Nu increases rapidly from the smallest drive ratio (0.08%) until 0.6% where the gas peak-to-peak displacement amplitude is still in the range of heat exchanger length. For $DR > 0.6\%$, Nu number still shows an increasing trend at a lower rate and is less pronounced at $DR > 0.9\%$. The overall trend is like the one observed for the heat transfer rates (cf. Figure 4.3). The Nusselt number at 30°C on HHX is comparable to that of 50°C on HHX at all drive ratios for the mean pressure of 10 bar. A higher Nusselt number can be observed at 70°C, and 10.0bar mean pressure. The higher Nusselt number at 70°C and 10.0bar mean pressure can be attributed to the change in the fluid properties because of an increase in temperature. The results of the Nusselt number on T-HEX (ogive) are presented in Figure 4.7 (d-f). Generally, a similar trend to that of T-HEX (flat) can be observed from the plots. The Nusselt number on CHX1 and CHX2 at 70°C temperature on HHX is given in Figures 4.8 – 4.9 for both T-HEX (flat) and T-HEX (ogive). The Nusselt number results show a similar trend to that of hot exchanger given in Figure 4.7. This is quite reasonable considering each set of symmetrically arranged heat

exchangers are of the identical type for a typical experiment. The Nusselt number of T-HEX (ogive) in Figures 4.8b and 4.9b is lower than that of T-HEX (flat), which indicates that the profiled edge may have adversely influenced the heat transfer performance of the cold heat exchangers.

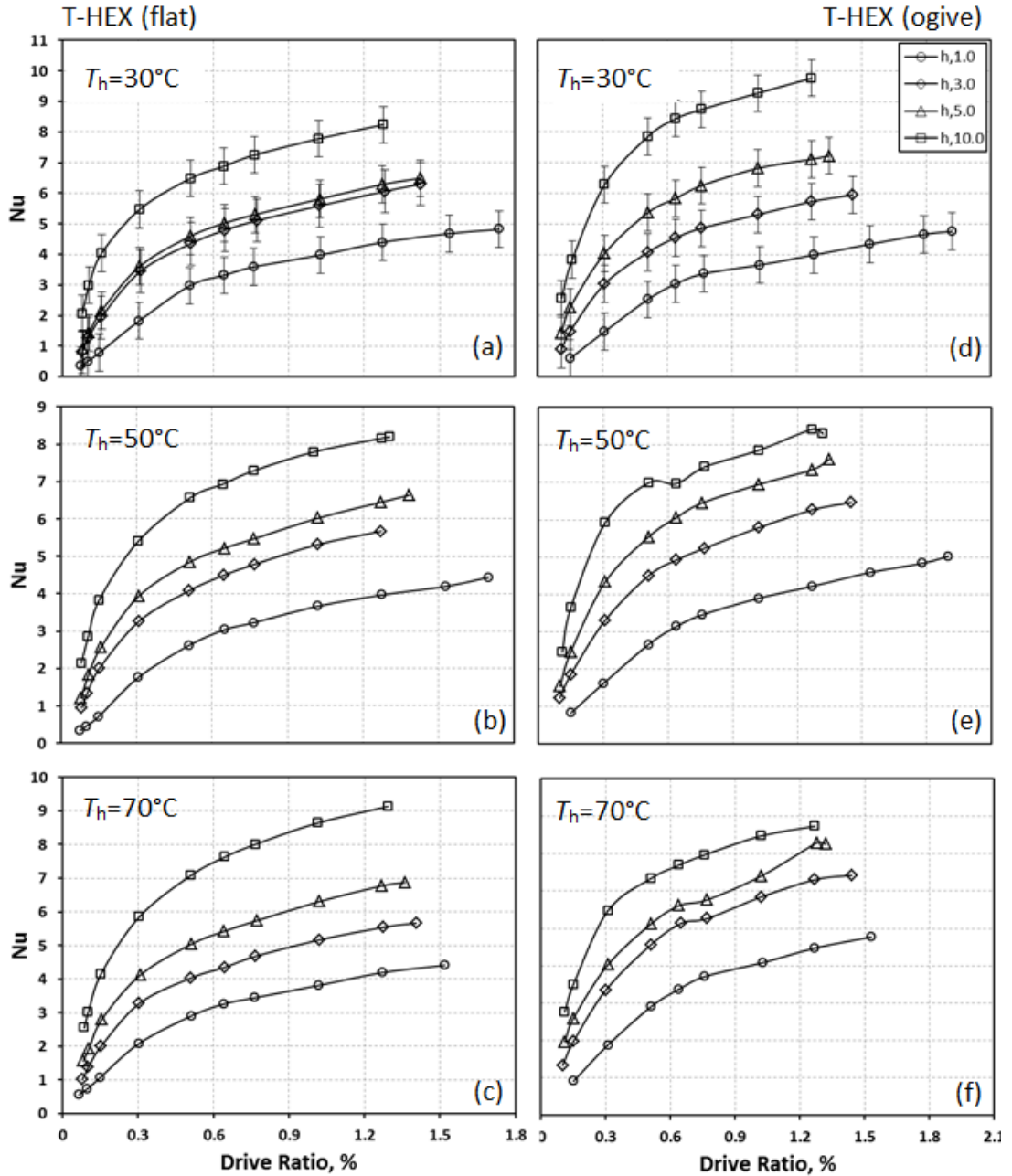


Figure 4.7: Effect of DR on Nu for the HHX at various P_m and $T_h = 30 - 70^\circ\text{C}$ (a) – (c) T-HEX (flat) and (d) – (f) T-HEX (ogive).

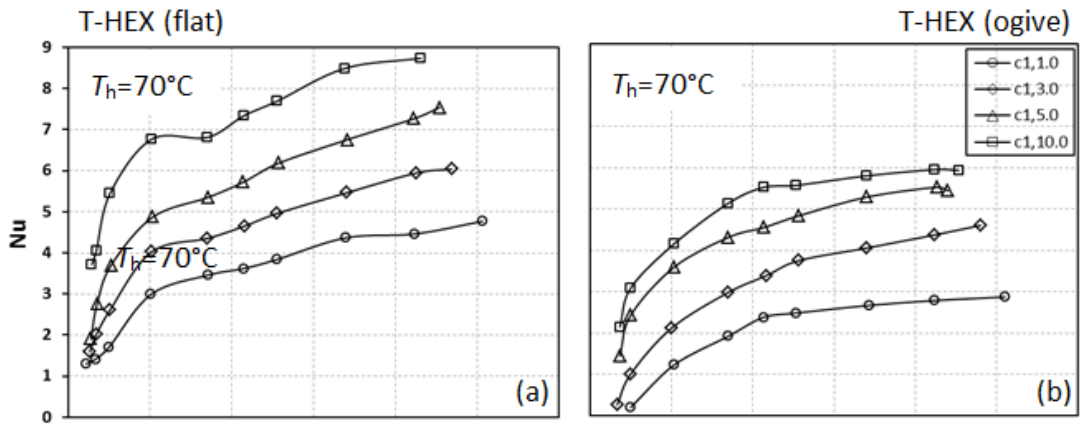


Figure 4.8: Effect of DR on Nu for the CHX1 at various P_m and $T_h = 70^\circ\text{C}$ (a) T-HEX (flat) (b) T-HEX (ogive)

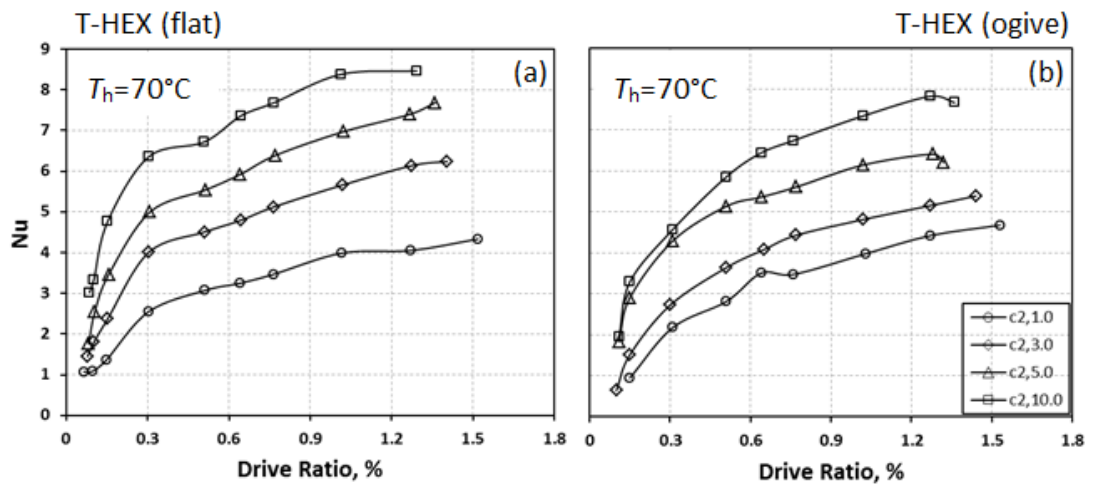


Figure 4.9: Effect of DR on Nu for the CHX2 at various P_m and $T_h = 70^\circ\text{C}$ (a) T-HEX (flat) (b) T-HEX (ogive)

Figure 4.10 shows the variation of Nusselt number with drive ratio on HHX for F-HEX (flat) and F-HEX (ogive) at $T_h = 70^\circ\text{C}$ temperature. The results show a similar trend to that of T-HEX in relation to Figure 4.7. There is a significant increase in the Nusselt number at lower drive ($< 0.6\%$) which gradually becomes less pronounced as the drive ratio increases above this point. Generally, the Nu number shows upward increase as the mean pressure increases for the configuration of the heat exchangers that are considered in the current study. The comparison of the Nusselt number from this study will be compared with the existing models from the literature in the next section.

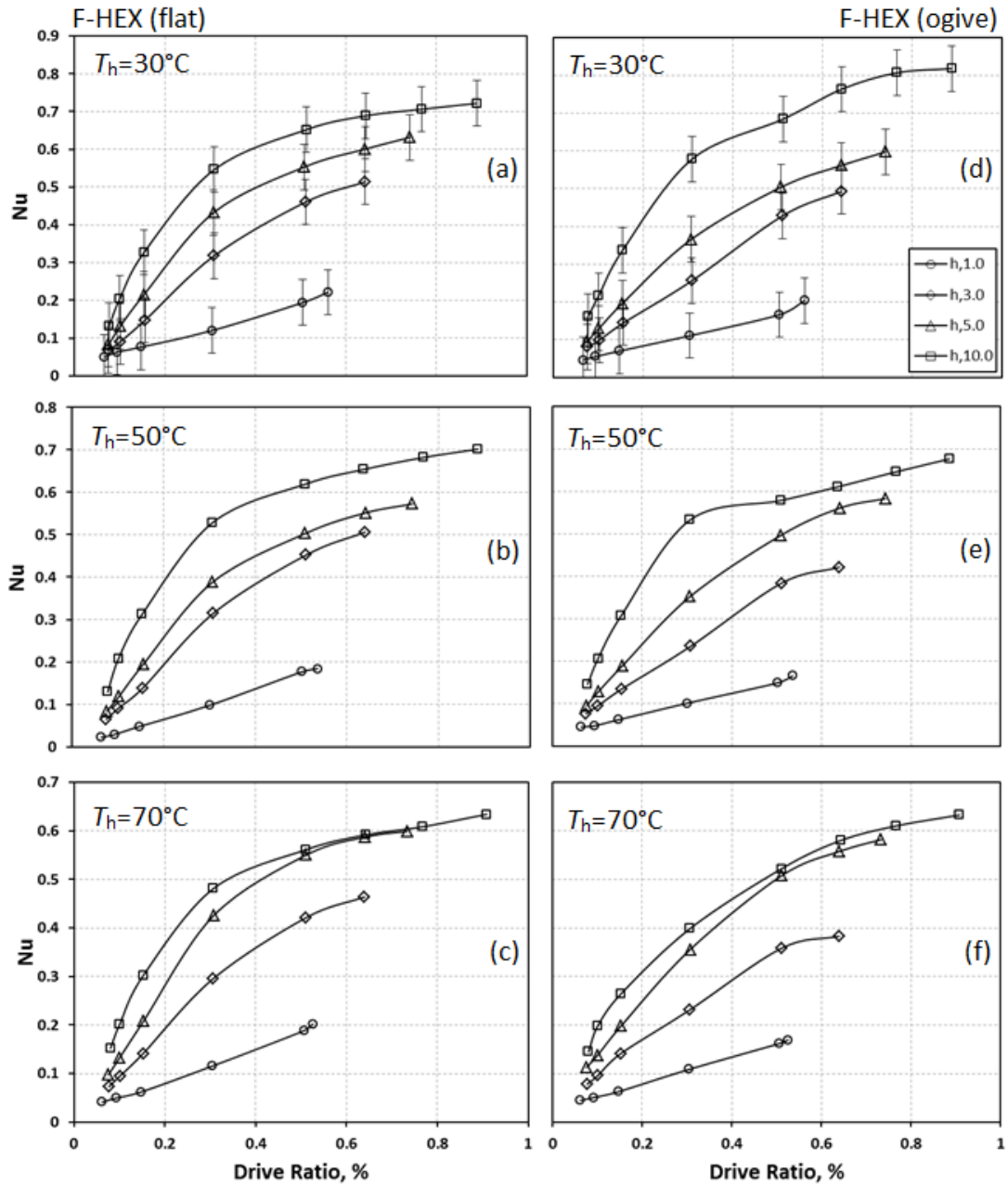


Figure 4.10: Effect of DR on Nu for the HHX at $0.08 < DR < 0.9\%$ and $T_h = 30 - 70^\circ\text{C}$ (a) – (c) F-HEX (flat) (d) – (f) F-HEX (ogive).

4.4 Comparisons of heat transfer results to other models from the literature

The experimental heat transfer coefficient in terms of Nusselt number is compared with the results estimated from other existing correlations in the literature, in this section. The results of $P_m = 5$ and 10bar are selected for T-HEX (flat) and T-HEX (ogive) at 70°C . The comparison is made against the acoustic Reynolds number.

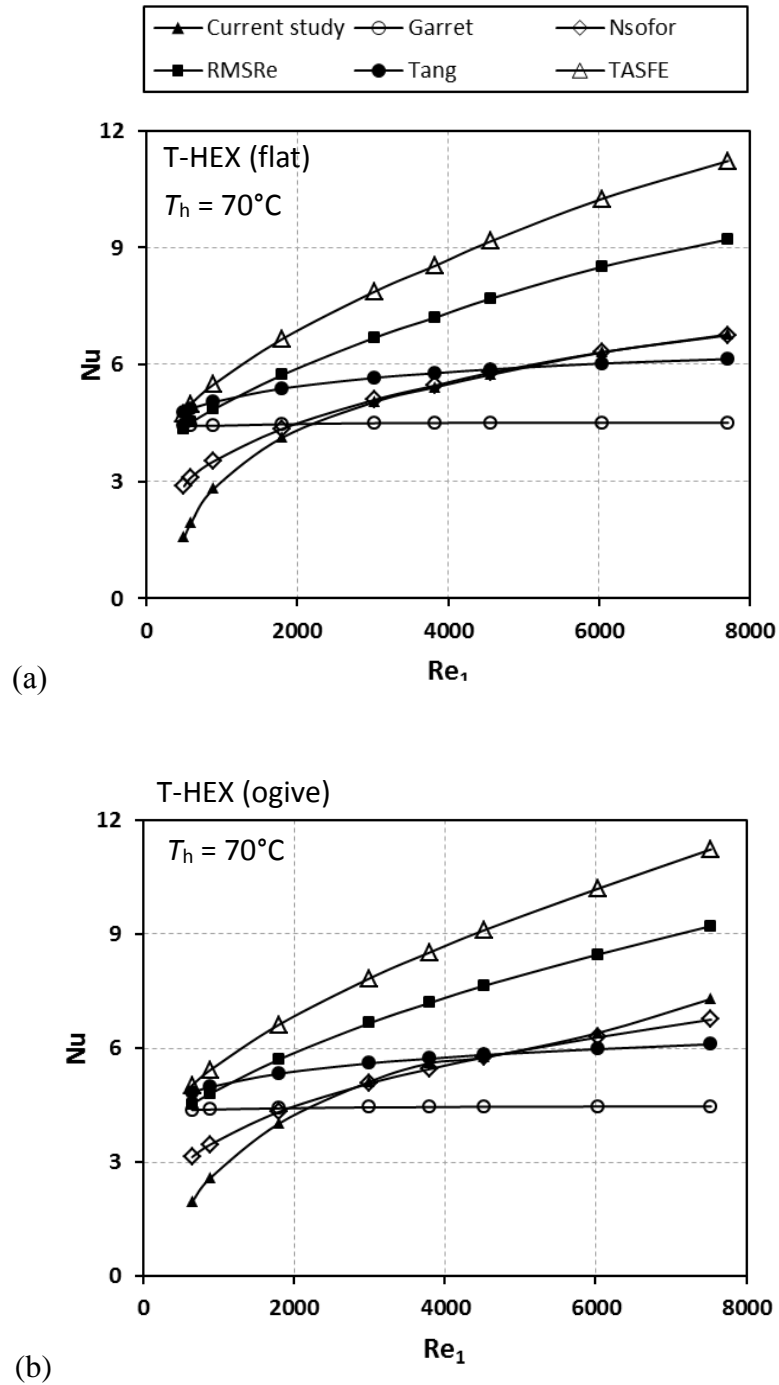


Figure 4.11: Nu versus Re_1 for HHX at $P_m = 5\text{bar}$ and $T_h = 70^\circ\text{C}$ (a) T-HEX (flat), (b) T-HEX (ogive).

The existing correlations that are considered include the Time-Average Steady-Flow Equivalent (TASFE) and Root Mean Square Reynolds Number (RMSRe) approximations, the correlation proposed by Nsofor et al. (2007), Tang et al. (2014) and the ‘boundary layer’ approach by Garrett et al. (1994). The Nusselt number and

acoustic Reynolds number (cf. equation (4.23)) from the studies are calculated based on the same length scale (D_h) as defined in equation (4.20).

The TASFE and RMSRe approximations are considered here for the comparison of Nusselt number following the approach used by Piccolo and Pistone (2006). The TASFE and RMSRe are described by expressions (4.25) and (2.27) as:

$$Nu = \frac{\varpi}{\pi} \int_0^{\varpi} \left\{ 3.66 + \frac{0.0668(D_h / L) \text{Pr} \text{Re}_1 \sin \omega t}{1 + 0.04[(D_h / L) \text{Pr} \text{Re}_1 \sin \omega t]^{2/3}} \right\} dt \quad (4.25)$$

Integrating expression (4.25) leads to the TASFE approximation in the following form (Piccolo and Pistone, 2006):

$$Nu = 2.8731 + 0.11432(\text{Re}_1)^{1/2} + 0.00035(\text{Re}_1) \quad (4.26)$$

$$Nu = 3.66 + \frac{0.0668(D_h / L) \text{Pr}(\text{Re}_1 / \sqrt{2})}{1 + 0.04[(D_h / L) \text{Pr}(\text{Re}_1 / \sqrt{2})]^{2/3}} \quad (4.27)$$

$$\text{Re}_{rms} = \text{Re}_1 / \sqrt{2} \quad (4.28)$$

The root mean square Reynolds number relates to acoustic Reynolds number as given in equation (4.28), and it has been utilised in equation (4.27). L is the length of the heat exchanger. The acoustic Reynolds number (Re_1) and the Prandtl number (Pr) are calculated based on equations (4.23) and (2.31). Nsofor et al. (2007) proposed a correlation in the form of Nu based on their experimental results. Their results are correlated in terms of root mean square Reynolds number. By using equation (4.28), their correlation can be written as:

$$Nu = 0.61(\text{Re}_1 / \sqrt{2})^{0.31} \text{Pr}^{0.11} \quad (4.29)$$

Tang et al. (2014) correlated the results of their experiments based on maximum Reynolds number and Valensi number. This can be written as:

$$Nu = 0.43 \text{Re}_1^{0.0876} \text{Va}^{0.405} \quad (4.30)$$

The Valensi number in equation (4.30) is defined in terms of hydraulic diameter and the viscous penetration depth as:

$$\text{Va} = 2(d_h / \delta_v)^2 \quad (4.31)$$

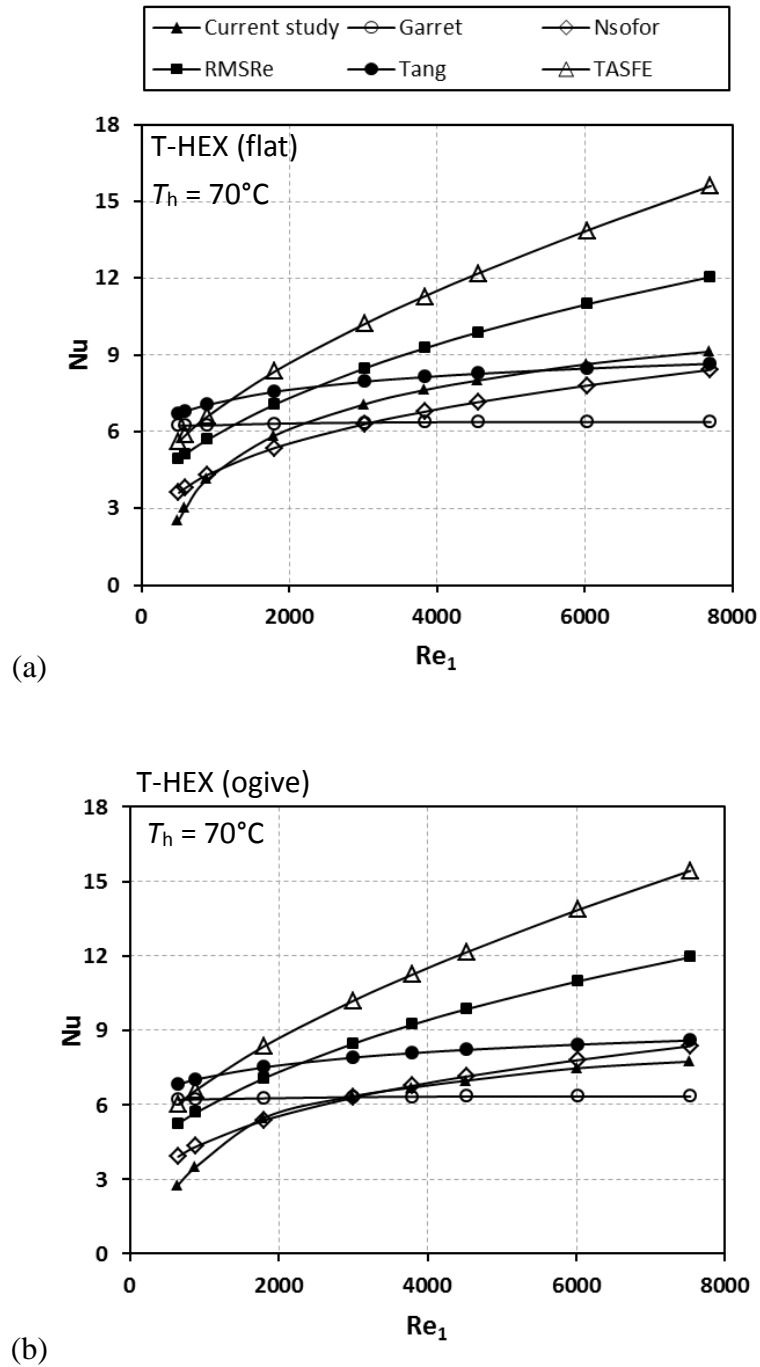


Figure 4.12: Nu versus acoustic Reynolds number (Re_1) for HHX at $P_m = 10$ bar and $T_h = 70^\circ\text{C}$ (a) T-HEX (flat), (b) T-HEX (ogive).

Garrett et al. (1994) proposed an approach in terms of RMS heat transfer coefficient for characterising the performance of heat exchangers in oscillatory flow, based on the original ‘boundary layer conduction’ approximation from Swift (1992). This can be written as:

$$h_{rms} = \frac{h}{\sqrt{2}} = \frac{1}{\sqrt{2}} \frac{k}{\delta_k} \quad (4.32)$$

The thermal conductivity of the fluid (k) and the thermal penetration depth (δ_k) are used in the expression (4.32). By using equation (4.9), the Nusselt number can be written as:

$$Nu = \frac{1}{\sqrt{2}} \frac{d_h}{\delta_k} \quad (4.33)$$

Expressions (4.26), (4.27), (4.29), (4.30) and (4.33) are compared with the Nusselt number from the current study and shown in Figures (4.11) and (4.12). As earlier remarked, the result is presented for the HHX within the set of T-HEX (flat) and T-HEX (ogive) configurations.

Table 4.2: Average deviation (%) of the Nusselt number from different models

Models	T-HEX (flat)	T-HEX (ogive)
	5bar mean pressure	
Garrett et al. 1994	33.66	36.10
Nsofor et al. 2007	7.37	6.54
RMSRe	31.27	26.57
Tang et al. 2014	19.26	16.17
TASFE	41.83	38.19
	10bar mean pressure	
Garrett et al. 1994	31.93	17.56
Nsofor et al. 2007	11.22	5.28
RMSRe	23.04	30.50
Tang et al. 2014	18.43	19.62
TASFE	36.58	43.46

The comparison made in Figures (4.11) and (4.12) reveals that the Nusselt number from the current study have a good match with the prediction from the correlation of Nsofor et al. (2007) at both low and high acoustic Reynolds number. The TASFE and RMSRe over predicted the Nusselt number. Similar prediction by TASFE and RMSRe are observed by Piccolo and Pistone (2006) and Kamsanam et al. (2014). The average deviation (%) from different models are summarised in Table 4.2.

Considering the comparison of the results from a current study with the experimental data by Tang et al. (2014), and Garret et al. (1994), the discrepancies between results at the same acoustic Reynolds number (Re_1) are observed. This could be due to the difference in both operating and geometrical conditions of heat exchangers used in their studies.

4.5 Summary

The experimental results of heat transfer performance in oscillatory flow have been discussed in this chapter. The investigations conducted on T-HEX and F-HEX and their edge shapes were presented. The temperature profiles of helium gas and water at different relevant locations in the test rig were presented to facilitate heat transfer analysis. The effect of operating parameters – drive ratio (DR) and mean pressure (P_m), on the heat transfer rates (\dot{Q}) and Nusselt number (Nu) was described, with respect to the operating temperature of the hot heat exchanger (HHX). Heat transfer performance in terms of the Nu is obtained for the two heat exchanger configurations that are considered in this study. T-HEX (flat) and T-HEX (ogive) configurations were used for the comparison of heat transfer in oscillatory flow with other relevant models in the literature. Good agreement is obtained from the comparison.

Chapter 5

3D Simulation Model for Tube Heat Exchangers

This chapter describes the development and experimental validation of 3D simulation model of T-HEX. The 3D model is developed to investigate the thermal and acoustic pressure drop performance of T-HEX in oscillatory flow. In section 5.1, the description of the 3D simulation model is given. Section 5.2 describes the details of the general methodology adopted for the simulation study, including the solution procedure, the geometrical and computational domain, and the boundary conditions obtained directly from the experiments. Section 5.3 discusses the investigated operating conditions. The discussion about validation of the model with experimental results is given in section 5.4. In section 5.5, the heat transfer results are discussed for the investigated T-HEX over the range of operating conditions in the experiment and the simulation. Section 5.6 deals with the acoustic pressure conditions in the simulation. The results are discussed in some detail, and the summary is given in section 5.7 to end the chapter.

5.1 Three-dimensional model description

A heat exchanger is one of the key components of the thermoacoustic system. Its performance regarding heat transfer and acoustic pressure drop contributes largely to the overall efficiency of thermoacoustic engines and coolers. As reviewed under the literature survey, the bulk of numerical study on the heat exchanger of thermoacoustic systems in the literature has been based on 1D or 2D models with simple geometry mostly, parallel plate structures, and sets of simplifying assumptions or the use of porous media to account for the presence of heat exchangers. The heat transfer and the fluid flow phenomena in thermoacoustic devices are quite complex and nonlinear with three-dimensional effects. These nonlinear phenomena which the existing linear theory cannot capture like turbulence, streaming flows and vortices formation can be visualised and studied by CFD. Another advantage of CFD codes is that more complicated geometries can be generated more easily. For example, Zink et al. (2010) looked at the influence of resonator curvature on the thermoacoustic effect and showed that presence of

curvature influences both the amplitude and the frequency of acoustic waves. Therefore, a three-dimensional simulation model was developed in this study based on the actual geometric dimensions of the T-HEX and the edge shapes described in Chapter 3.

It can be recalled that two different configurations of heat exchangers (T-HEX and F-HEX) were designed, fabricated and tested in the experiments. However, only the T-HEX has been modelled in the current simulation study. The reason why F-HEX was not modelled in the numerical study was that it has a high aspect ratio between its geometric dimensions and the fin thickness. This caused enormous problems for the ANSYS-Meshing solver leading to poor mesh quality that was far below what the Fluent solver could handle.

The T-HEX (flat) and T-HEX (ogive) were modelled in three-dimensions using ANSYS Fluent 17.0 (2015). The simulation model is a direct replica of the part of the experimental set-up that is chosen as the computational domain. The 3D model utilises experimental results as thermal and acoustic boundary conditions and later for validation. The models here involve solving of the unsteady flow field (transient). Therefore, time-dependent Navier-Stokes equations (2.41 – 2.43) are used in the simulation. The effect of drive ratio in the range of 0.3 – 1.25%, on the heat transfer and acoustic pressure drop are investigated. The effect of edge shape at the entrance and exit of the T-HEX was considered. Buoyancy effect was taken into consideration in the simulation. The results are presented for pressure and temperature profiles, heat fluxes, Nusselt number (Nu), and the acoustic pressure drop created by the heat exchangers.

5.2 Methodology

Before going into the details of the developed 3D model, it is worth mentioning that the numerical modelling phase of this study began with the development of a 2D preliminary simulation model based on data estimation from the literature. The results of the 2D model will be discussed in Chapter 6. Figure 5.1 shows the approach that was adopted for the simulation study. Based on the knowledge gained from the 2D simulation model – such as the appropriate length of computational domain that will ensure the flow structures in the vicinity of heat exchangers are not influenced by flow conditions from the upstream or downstream regions, the

experimental set-up was designed to allow the required data to be obtained for the 3D model. The location of inlet and outlet of the computational domain was incorporated in the test rig during the design stage following the knowledge gained from the 2D simulation. After the experiment was performed and the required data collected, the 3D simulations were developed, and the real data from experiments was used as thermal and acoustic boundary conditions and for validation of the developed 3D model.

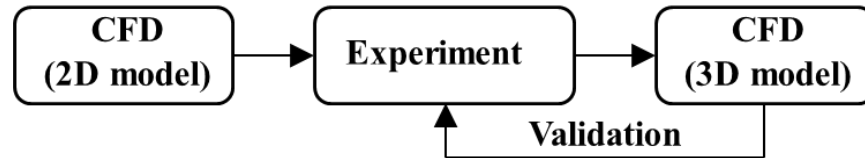


Figure 5.1: Adopted approach to integrating experiments with the CFD model

5.2.1 Geometrical model and computational domain

The experimental set-up has been described in the previous chapter, including the heat exchangers and the edge shapes; therefore, such details will not be repeated here.

Table 5.1: Operating parameters and gas properties

Operating parameter	Values
Mean pressure (P_m), bar	5
Frequency of oscillation (f), Hz	53.6
Drive ratio, %	$0.16 \leq DR \leq 1.27$
Helium properties	
Molar mass, kg/mol	0.04
Specific gas constant, J/kgK	2078.5
Specific heat, J/kg.K	5193
Speed of sound, m/s	1019.4

The computational domain is defined based on the test rig as shown in Figure 5.2a.

In the 3D geometry, three identical tube heat exchangers are arranged in series (CHX1, HHX and CHX2) in an oscillating helium gas environment, as shown in Figure 5.2b. The symmetric arrangement of the heat exchangers will simply be

referred to as the ‘core’ henceforth. The schematic representation of the edge shape is shown in Figure 5.2c. The 3D CAD model of the heat exchangers and the mesh configuration are shown in Figure 5.2d. The inlet (x1) and outlet (x2) of the domain are located at distance 3.842 and 4.742 m from the close end of the test rig.

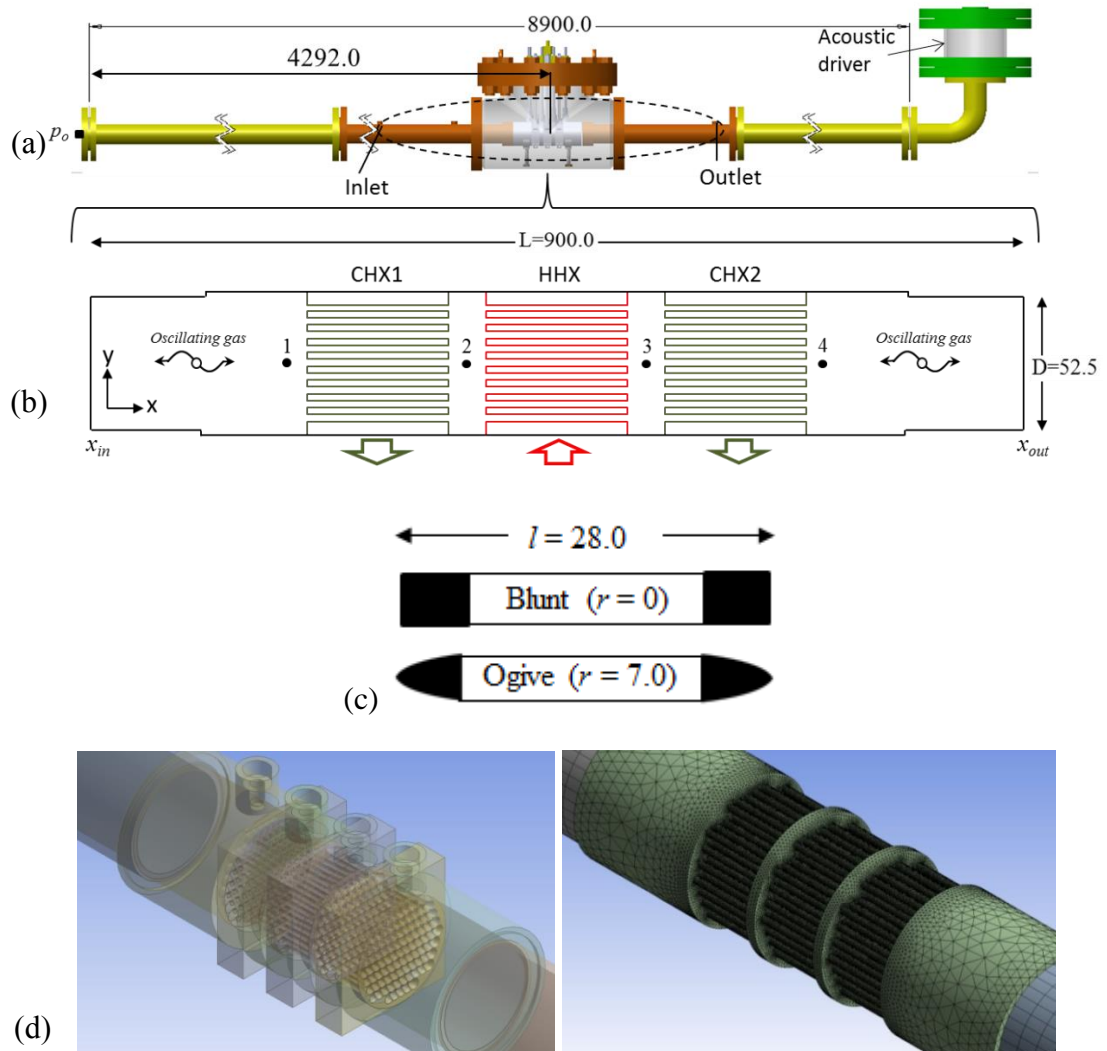


Figure 5.2: (a) Sketch of experimental set-up (b) computational domain (c) 3D model of T-HEX showing the mesh.

Locations 1 ($x = 4.244$ m), 2 ($x = 4.276$ m), 3 ($x = 4.308$ m), 4 ($x = 4.340$ m), are used for data sampling, and oscillating variables at each location are identified with a number from the location (e.g. location 1 has temperature T-1). All dimensions are in mm.

The operating parameters and properties of helium are shown in Table 5.1. The temperature dependent properties of helium, that is, the thermal conductivity and

viscosity are defined by equation (4.18). The density is defined as per the ideal gas law in equation (4.19).

5.2.2 Numerical solution procedure

The procedure for obtaining the solution of numerical modelling work is represented in Figure 5.3. The same principle is applied for investigations reported in Chapter 6 although the detailed modelling will differ in the dimensionality of the model. The ovals and boxes on the right side of the flow chart represent the main workflow that is carried out within ANSYS Fluent 17.0 (2015).

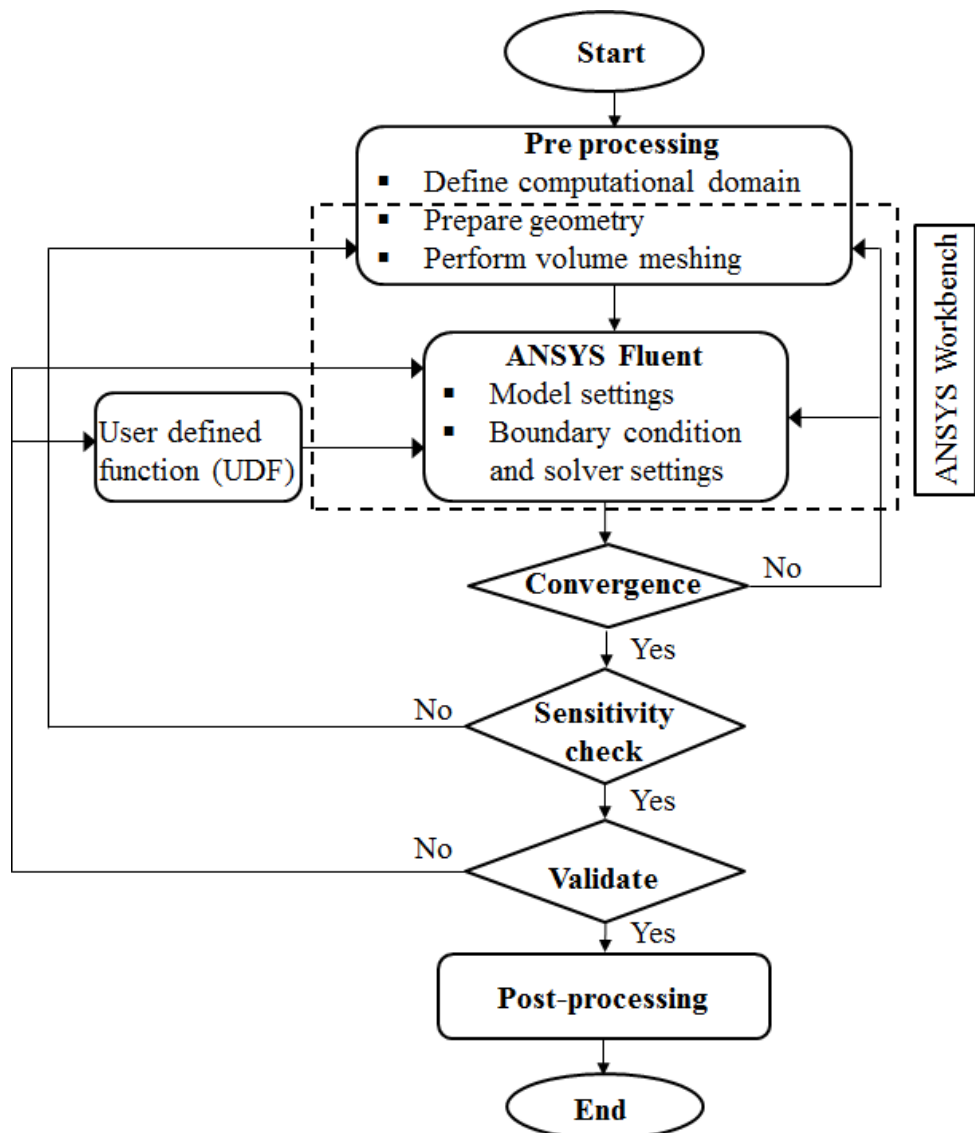


Figure 5.3: Numerical solution procedure for the 3D model

Having defined the appropriate computational domain as shown in Figure 5.2, the 3D CAD model of the heat exchangers, as used for fabrication, are imported into the

Design Modeller to create the fluid domain that forms the computational domain. The domain is meshed and tested for error in the ANSYS meshing which was then imported into the ANSYS Fluent for setting up and calculation. The box represented by a dashed line covered the workflow executed in the ANSYS Workbench 17.0 (2015). The single box on the left side represents the step where the User-Defined-Function (UDF) code is developed using C programming language. These UDF codes were hooked into ANSYS Fluent and then compiled within the ANSYS Fluent. The codes were developed for use in several stages during the setting up and running of the model. Appendix-C shows all the codes written in C language.

In ANSYS Fluent, an appropriate transport equation is then assigned to the domain for heat transfer and acoustic pressure drop investigations. The boundary conditions are set up with suitable equations developed via user-defined-code (UDF). An appropriate solver is set, and the ANSYS Fluent case and data files are exported for submission to the HPC for simulation, using journal file. Calculations start at an assigned size of a time step. The time step must be chosen small enough to achieve the desired accuracy and avoid numerical diffusion and divergence. In this work the time step was determined as follows:

$$\Delta t = \frac{1}{Nf} \quad (5.1)$$

where N is the number of time steps over one cycles, which was set at 600 in the 3D model and 500 in the 2D model, after the sensitivity check for time discretization has been performed. If divergence was reported, the model would be revised based on the type of divergence. The correction may involve a change in the boundary condition or solver setting or re-meshing of the mesh. If the solution converges, then the sensitivity check will be carried out, which involves a gradual increase of the mesh density until the solution is not sensitive to the increase in the mesh density. The converged mesh is then used to obtain the solution which was validated by comparing the results obtained with the experiment. The validated mesh is then ready for post-processing, and thorough analysis is conducted. A set of user-defined-code was written at this stage to get the relevant data for the flow and heat transfer analysis. Data processing involved software such as MATLAB 2013b, CFD-Post 17.0 (2015) and Microsoft Excel Office 2010.

5.2.3 Physical model

Time-dependent Navier-Stokes (N-S) equations, as described in Chapter 2, are solved in ANSYS Fluent using a finite volume method (ANSYS Fluent 17.0, 2015; Versteeg and Malalasekera, 2007). The Reynolds-Averaged Navier-Stokes (RANS) equation is used for the turbulence model. Previous relevant studies (Mohd Saat, 2013) have used Reynolds Averaged Navier-Stokes (RANS) equations to model turbulence flow through heat exchangers under oscillatory flow conditions. Time averaging the continuity, momentum and energy equations in Navier-Stokes equations with variables decomposed into mean and fluctuating components as written in equation (5.2), leads to RANS equations:

$$\varphi = \bar{\varphi} + \varphi' \quad (5.2)$$

where $\bar{\varphi}$ and φ' are the mean and fluctuating components of the scalar variable.

The scalar variable can be velocity, pressure or any other scalar transport quantities.

The RANS equations are written in conservative form as:

Continuity equation

$$\frac{\partial \rho}{\partial t} + \frac{\partial}{\partial x_j} (\rho u_j) = 0 \quad (5.3)$$

Momentum equation

$$\begin{aligned} \frac{\partial (\rho u_i)}{\partial t} + \frac{\partial}{\partial x_j} (\rho u_i u_j) = & -\frac{\partial p}{\partial x_i} + F_i + \frac{\partial}{\partial x_j} (\tau_{ij})_{eff} + \frac{\partial}{\partial x_j} (-\overline{\rho u'_i u'_j}) \\ & + \frac{\partial}{\partial x_i} (-\overline{\rho u'^2}) + S_m \end{aligned} \quad (5.4)$$

Energy equation

$$\frac{\partial}{\partial t} (\rho E) + \frac{\partial}{\partial x_i} [u_i (\rho E + p)] = \frac{\partial}{\partial x_j} \left((k)_{eff} \frac{\partial T}{\partial x_j} + u_i (\tau_{ij})_{eff} \right) + S_h \quad (5.5)$$

Here,

$$(\tau_{ij})_{eff} = \mu \left(\frac{\partial u_j}{\partial x_i} + \frac{\partial u_i}{\partial x_j} \right) - \frac{2}{3} \mu_{eff} \frac{\partial u_k}{\partial x_k} \delta_{ij} \quad (5.6)$$

$$-\overline{\rho u'_i u'_j} = \mu_t \left(\frac{\partial u_j}{\partial x_i} + \frac{\partial u_i}{\partial x_j} \right) - \frac{2}{3} \left(\rho \kappa + \mu_t \frac{\partial u_k}{\partial x_k} \right) \delta_{ij} \quad (5.7)$$

Equations (5.5) and (5.6) are the effective stress tensor, and the Reynolds Stresses term used to model momentum equation for the turbulence affected flow. F , S_m and

S_h are the external force and the source terms in Fluent. RANS has an advantage of being computationally efficient compared to other algorithm models such as full Reynolds Stress Model (RSM) and Large Eddy Simulation (LES); of which the details can be found in ANSYS Fluent 17.0 (2015) manual.

SST k- ω turbulence model (Menter, 1994) is used for turbulence closure in this study. SST k- ω is a two-equation turbulence model that has the advantage of resolving the flow phenomena within the boundary layer using the standard k- ω turbulence model and then switching to the k-epsilon in the region outside the boundary layer (free stream). This helps to accurately predict the onset and the size of separation under adverse pressure gradient and captures the possible transition or turbulence in the flow. Also, it has been shown (Mohd Saat, 2013) that SST k- ω predicts oscillating velocity profiles near the wall and the core, better than other turbulence models when compared with experimental data. Pressure-based solver, Pressure Implicit Splitting Operators (PISO), and second-order discretization are used for the time, the transport equations, and the turbulent equations in all simulation cases.

5.2.4 Boundary and initial conditions

In the current study, the pressure amplitude and the phase information as directly measured from the experiments at the locations indicated as inlet and outlet (cf. Figure 5.2) are used as boundary conditions in the computational model. The acoustic conditions (pressure wave) assigned at inlet and outlet locations of the domain are defined as:

$$p_{in} = p_{1,in} \cdot \cos(\omega t + \phi_{in}) \quad (5.9)$$

$$p_{out} = p_{1,out} \cdot \cos(\omega t + \phi_{out}) \quad (5.10)$$

where $p_{1,in}$, $p_{1,out}$, ϕ_{in} and ϕ_{out} are the measured pressure amplitudes and their corresponding phases from the inlet and outlet in the test rig (cf. Figure 5.2a). It should be noted that the use of measured phases from the experiments eliminates the common argument about selecting the correct phasing when oscillating variables are introduced at each end of a computational domain with open two ends.

Turbulence boundary conditions are specified in terms of intensity and length scale as:

$$I = 0.16 \left(\text{Re}_{1(in,out)} \right)^{-1/8} \quad \ell = 0.07D \quad (5.11)$$

The acoustic Reynolds number (cf. equation 4.23) in the turbulent intensity definition is defined as $\text{Re}_{1(in,out)} = \rho_o u_{1(in,out)} D / \mu_o$ for the inlet and outlet locations of the domain. The velocity amplitudes used in $\text{Re}_{1(in,out)}$ is calculated from:

$$u_{1,in}(x) = \frac{p_o}{\rho_m a} \sin(k' x_{in}) \quad (5.12)$$

$$u_{1,out}(x) = \frac{p_o}{\rho_m a} \sin(k' x_{out}) \quad (5.13)$$

where p_o is the pressure amplitude at the pressure antinode (closed end of the resonator). The values of density and a dynamic viscosity at the reference temperature (300 K) are used in equations (5.12) and (5.13). Default values are retained for all other constants in the SST k- ω turbulence model. (ANSYS Fluent 17.0, 2015).

The thermal boundary conditions on walls of CHX1, HHX and CHX2 are specified using the measured wall temperature from the experiment. At the inlet and outlet of the domain, additional temperature conditions are specified as:

$$\left. \frac{\partial T}{\partial x} \right|_{x_{in}, x_{out}} = 0 \quad (5.14)$$

Equation (5.14) is the temperature condition defined such that the temperature of the cells next to the boundaries (cf. Figure 5.2b) is equal to that of the reversing flow.

The resonator wall is modelled as adiabatic and non-slip boundary conditions are applied to all walls. The convergence criteria used for the transport and energy equations are 10^{-5} , 10^{-5} , and 10^{-8} .

5.3 Computational conditions

5.3.1 Mesh convergence study

The mesh convergence study was done using T-HEX (flat), based on the knowledge of refinement gained from the 2D model as will be described in Chapter 6 (Rochie, 1994; Ilori et al., 2014). A very small mesh size (0.25mm) was required in the ‘core’ formed by the T-HEX before the simulation can be run successfully, which yielded the total mesh count of 4,192,248. The mesh refinement in the region of interest did

not lead to a significant improvement in the results. The maximum improvement between the ‘coarse’ and ‘fine’ mesh size was less than 1.3%, at the refinement ratio of 1.8.

Table 5.2: Operating parameters based on the experimental results

Drive Ratio (%)	Displacement Amplitude (mm)	Reynolds Number (-)	Stokes Reynolds Number, Re_s (-)
0.16	8.64	82,37.47	85.22
0.31	17.43	16,254.14	168.15
0.64	35.97	33,726.57	348.91
1.02	57.24	53,756.19	556.12
1.27	72.46	66,650.74	689.52

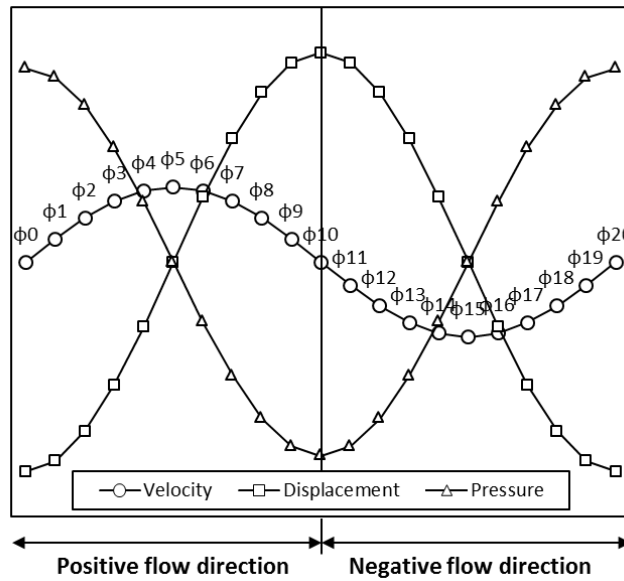


Figure 5.4: Definition of flow direction in a flow cycle and the relationship between the velocity, gas displacement and pressure amplitudes

5.3.2 Investigated conditions

The investigated numerical conditions are given in Table 5.2 at a mean pressure of 5 bar and resonance frequency of 53.6 Hz. The displacement amplitudes are calculated from equation (2.32) for the midpoint (centreline) of HHX. The porosity as calculated from equation (2.36) is 24.31% for T-HEX. As previously remarked, Merkli and Thomann (1975) considered the flow regime in an oscillatory flow to be

laminar if the critical Stokes Reynolds number is less than 400. The Stokes Reynolds number for all the drive ratios investigated in the experiments used for this current study is calculated based on T-HEX (flat) configuration and shown in Table 5.2. The Stokes Reynolds number involved here is lower than the transition point suggested by Merkli and Thomann (1975) at $DR \leq 0.64\%$ while at $DR > 0.64\%$ the Stokes number exceeded the suggested point. It was observed (Mohd Saat, 2013) that at low drive ratio of 0.3% (with a Stokes Reynold number of 58.76 based on parallel plate heat exchanger configuration) the numerical study with turbulence model yielded results closer to the experimental data (Shi et al., 2010) in comparison with the predicted result from laminar model. Based on this, the turbulence model that is described in section 5.2.2 was used in all the simulations and at all drive ratios investigated in the current work.

The definition of flow direction in a cycle is shown in Figure 5.4. A complete flow cycle consists of twenty phases with $\phi 1$ - $\phi 10$ constituting the positive flow direction (suction), and $\phi 11$ to $\phi 20$ for negative flow direction (ejection) when the flow reverses. The choice of 20 phases here is arbitrary; the flow cycle can be discretised into a convenient number of phases, e.g. Aben et.al. (2009) in line with the requirement of analysis.

5.4 Comparison between experimental and simulation results

The comparisons between the simulation and experimental results are presented for T-HEX (flat edge) and T-HEX (ogive edge) in this section. Pressure distribution, temperature profile flow structure, heat transfer and acoustic pressure drop are discussed.

5.4.1 Pressure amplitude profile

Figure 5.5 shows the pressure amplitude distribution along the test section (marked with a black dashed line in Figure 5.2a). The comparison is made for T-HEX (flat edge). The region between $4.2 < x < 4.4$ m on the plot denotes the pressure amplitudes at locations 1, 2, 3, and 4 within the heat exchanger core (cf. Figure 5.2b) in the acoustic environment. There is good agreement between the measured (symbols) and simulated pressure amplitudes along the system. The predicted results show the same trend to the measured results at all drive ratios ($0.64 \leq DR \leq 1.27\%$). A typical averaged discrepancy between the measured and predicted results is lower

than 10%. The agreement between the measured and simulated results was needed to yield confidence in the 3D numerical model results.

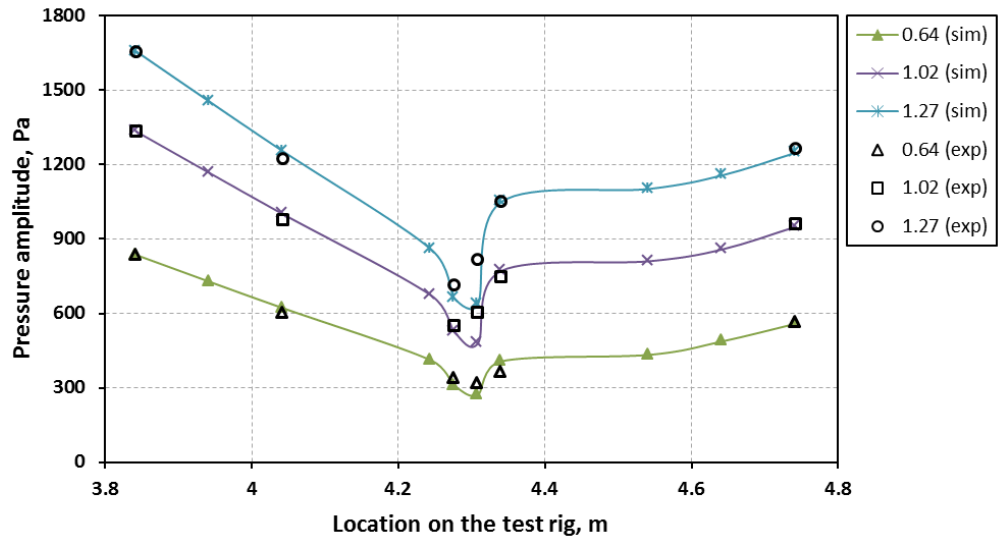


Figure 5.5: Comparison between the experimental and the numerical pressure amplitudes in the test section (T-HEX (flat)) at $0.64 < DR < 1.29\%$, $P_m = 5\text{bar}$ and $T_h = 70^\circ\text{C}$

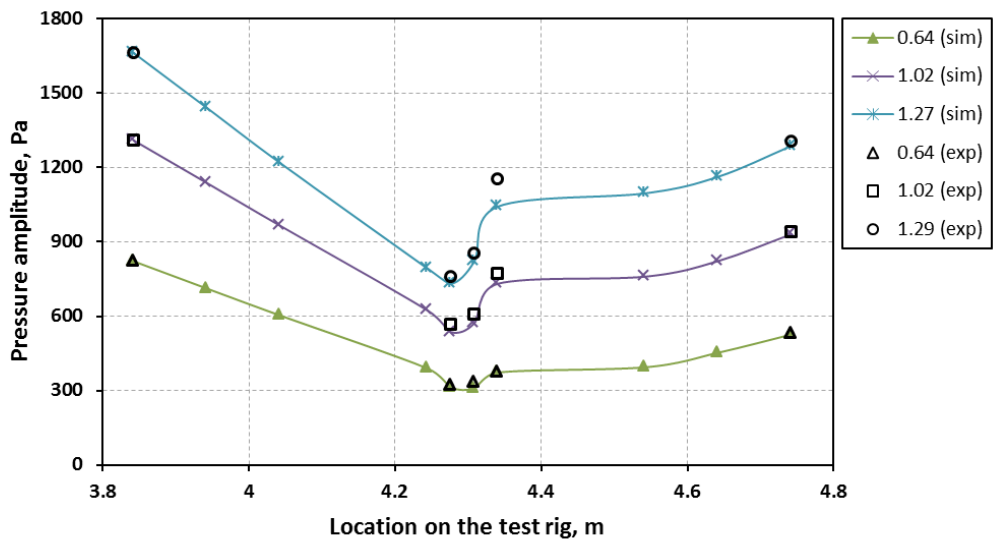


Figure 5.6: Comparison between the experimental and the numerical pressure amplitudes in the test section (T-HEX (ogive)), at $0.64 < DR < 1.29\%$, $P_m = 5\text{bar}$ and $T_h = 70^\circ\text{C}$

The comparison between the measured and simulated pressure amplitudes for T-HEX (ogive) is shown in Figure 5.6. Again, there is good agreement between the measured (symbols) and the simulated results. The predicted pressure profile shows

the same trend to that of experiments at all drive ratios ($0.64 \leq DR \leq 1.29\%$). The presence of the heat exchanger core modified the pressure distribution within the test section, where the pressure transducers are submerged in the acoustic environment. The predicted pressure amplitude results for T-HEX (flat) and T-HEX (ogive) are compared as shown in Figure 5.7, to show the influence that the edge shape has on the pressure profile. The pressure amplitude profile is distorted at the location of the heat exchanger core due to the flow resistance caused by the presence of the heat exchangers. The effect of edge shape is pronounced at this location. The drop in the pressure amplitude is highest at locations 2 and 3, which corresponds to the gaps between CHX1/HHX and HHX/CHX2. The ogive edge minimised the pressure drop at this location in comparison with the flat edge shape, noticeable at high drive ratio.

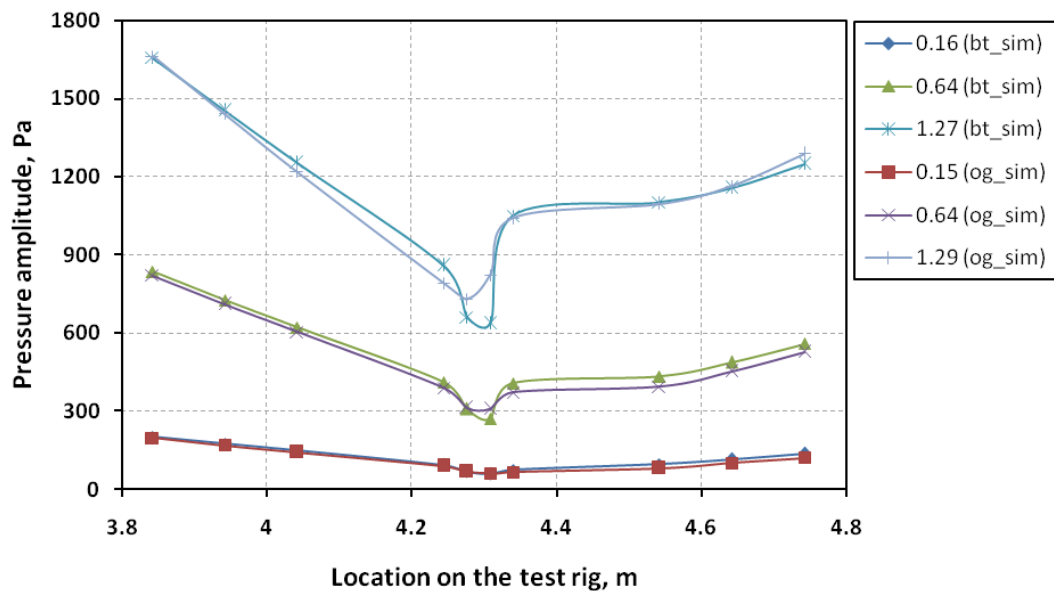


Figure 5.7: Effect of edge shape of heat exchanger on pressure amplitude distribution along the test rig, at $0.15 < DR < 1.29\%$, $P_m = 5\text{bar}$ and $T_h = 70^\circ\text{C}$

5.4.2 Velocity amplitude profile

Figure 5.8 shows the maximum velocity amplitudes in the positive flow direction along the system for the T-HEX (flat) and T-HEX (ogive). The sudden change in the cross-sectional area caused a sharp rise in the velocity amplitude across the transition between the resonator and the heat exchangers. The maximum velocity amplitudes as a function of drive ratio $0.15 < DR < 1.29\%$ for T-HEX (flat) and T-HEX (ogive) is shown in Figure 5.9. The comparison is made at location 3 (Figure 5.2b). This location is chosen to demonstrate the influence of edge shape on the flow

condition as near as possible to the velocity antinode in the test rig (0.2472λ). As can be seen in the plot, the effect of edge shape on the peak velocity amplitude is clearly visible at all drive ratios.

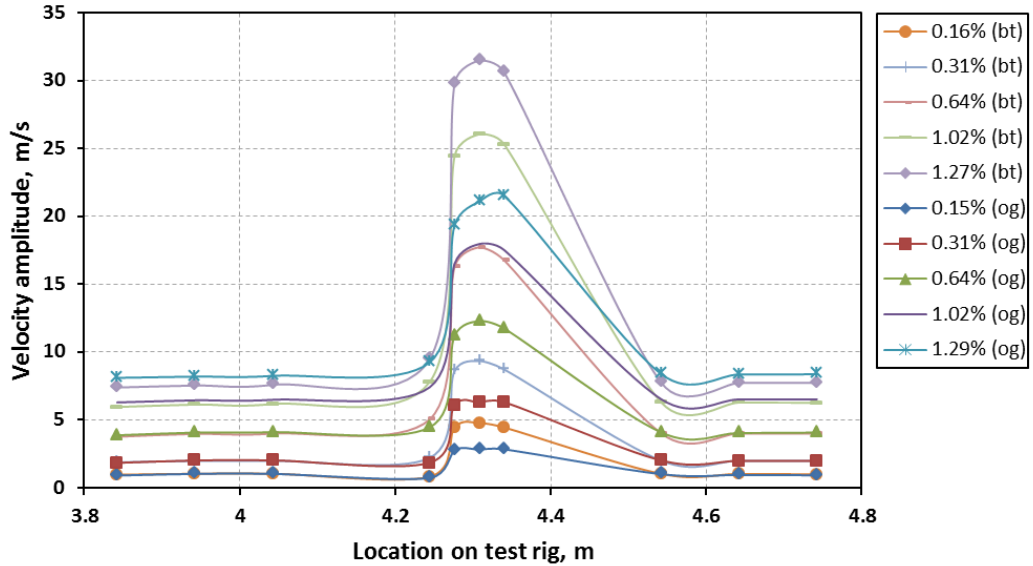


Figure 5.8: Comparison between the predicted velocity amplitude along the test section for the T-HEX (flat) and the T-HEX (ogive), at $0.15 < DR < 1.29\%$, $P_m = 5\text{bar}$ and $T_h = 70^\circ\text{C}$

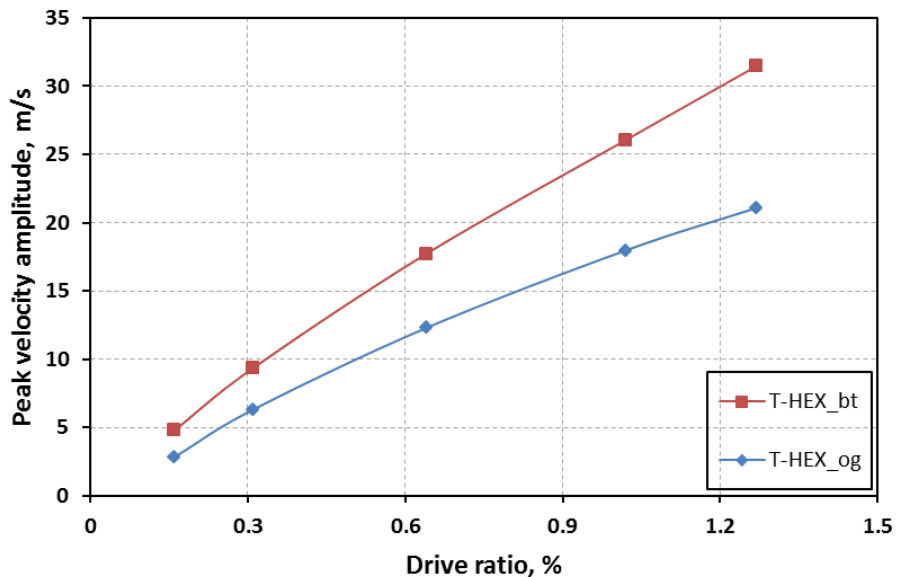


Figure 5.9: Comparison between the predicted velocity amplitudes for the T-HEX (flat) and the T-HEX (ogive), at $0.15 < DR < 1.29\%$, $P_m = 5\text{bar}$ and $T_h = 70^\circ\text{C}$. The peak velocity amplitude is the maximum velocity amplitude within the flow cycle in a positive direction.

The higher velocity amplitude in the case T-HEX (flat) can be attributed to the fact that the velocity flow transition over the 90° edge will be more sudden at the change in cross section, which will cause an increase in the gas velocity. Also, the available flow area will be smaller than the streamlined edge causing an increase in the velocity according to the law of mass conservation. The transition of flow over the streamlined body will be more gradual and lead to smaller increases in velocities relative to the squared-edge shapes. The effect of this velocity condition on acoustic pressure drop and heat transfer will be further discussed in the sections below. The velocity amplitude and the displacement amplitude are related as can be seen in equation (2.32). The equation is stated here for convenience as:

$$\xi_1 = \frac{|u_1|}{\omega} = \frac{P_o}{\omega \rho_m a} \sin(k' x) \quad (5.15)$$

The displacement amplitude that corresponds to the velocity amplitudes as plotted in Figure 5.9 is presented in Table 5.3 for T-HEX (flat) and T-HEX (ogive). The summary gives the displacement amplitudes in the range of 14.17 – 93.50 mm, and 8.37 – 62.63 mm for T-HEX (flat) and T-HEX (ogive), respectively. The effective length of the heat exchanger is 28 mm which corresponds to the drive ratio of 0.31% and 0.48% for T-HEX (flat) and T-HEX (ogive), respectively.

Table 5.3: Comparison of the simulation results for all edge shapes

D_r (%)	Flat edge		Ogive edge	
	$u_{i,ft}$ (m/s)	ξ_{ft} (mm)	$u_{i,og}$ (m/s)	ξ_{og} (mm)
0.16/0.15	4.77	14.17	2.82	8.37
0.31	9.34	27.74	6.30	18.72
0.64	17.72	52.62	12.29	36.49
1.02	26.06	77.37	17.97	53.35
1.27/1.29	31.49	93.50	21.09	62.63

5.4.3 Temperature profile

In Figure 5.10, the difference between the experimental and simulation gas temperatures are presented for various locations near the heat exchangers ($x = 4.244, 4.276, 4.308$ m and 4.340 m), i.e. T-1, T-2, T-3 and T-4 (cf. Figure 5.2b).

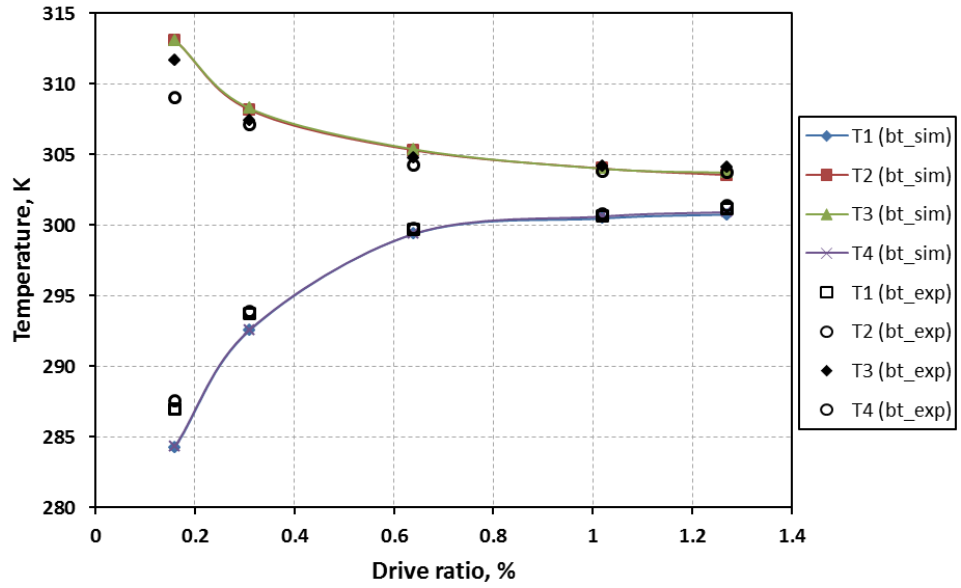


Figure 5.10: Comparison between the experimental and the numerical time-averaged temperatures (T-1, T-2, T-3 and T-4) for the T-HEX (flat), at $0.16 < DR < 1.27\%$, $P_m = 5\text{bar}$ and $T_h = 70^\circ\text{C}$

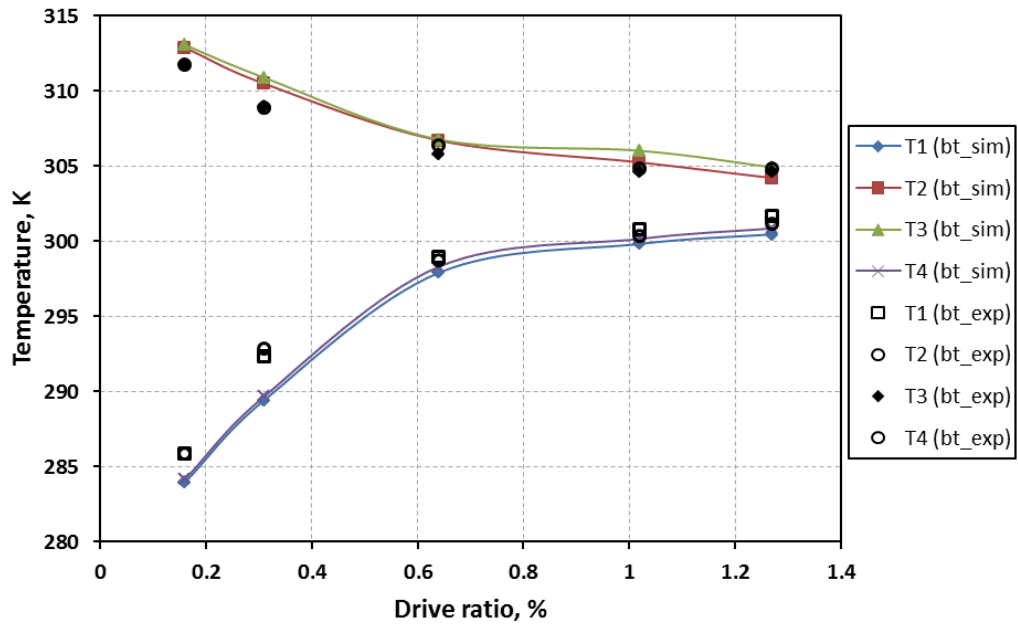


Figure 5.11: Comparison between the experimental and the numerical time-averaged temperature (T-1, T-2, T-3 and T-4) for the T-HEX (ogive), at $0.16 < DR < 1.27\%$, $P_m = 5\text{bar}$ and $T_h = 70^\circ\text{C}$.

There exists a good agreement between both results with maximum discrepancies of 6.7% and 5.3% for T-HEX (flat) and T-HEX (ogive), respectively. The difference occurs at the low $DR (< 0.31\%)$, where the gas displacement and the imposed

temperature gradient are low. It should be noted that the difference between T_h and $T_{c1,c2}$ (i.e. $T_h - T_{c1,c2}$) is used as a reference in the evaluation of the deviation. The predicted temperature profile shows a similar trend to that of experiments. The comparison between the measured and predicted temperatures is shown in Figure 5.11 for T-HEX (ogive). There is a good agreement between the measured (symbol) and the predicted values. At low drive ratio ($DR \leq 0.64\%$) the gas temperature values from the HHX decreased rapidly, CHX1 and CHX2 experience rapid increase in the gas temperature at the same time. This indicates rapid movement of the hot gas from the hot heat exchanger into the cold region of the cold heat exchangers. The measured temperatures are higher than the predicted values for CHX1 and CHX2. However, the experimental gas temperature values are lower for HHX than the predicted values at drive ratio $DR < 0.65\%$. Above this drive ratio, both predicted and measured values are almost the same in magnitude for CHX1 and CHX2, as well as for the HHX.

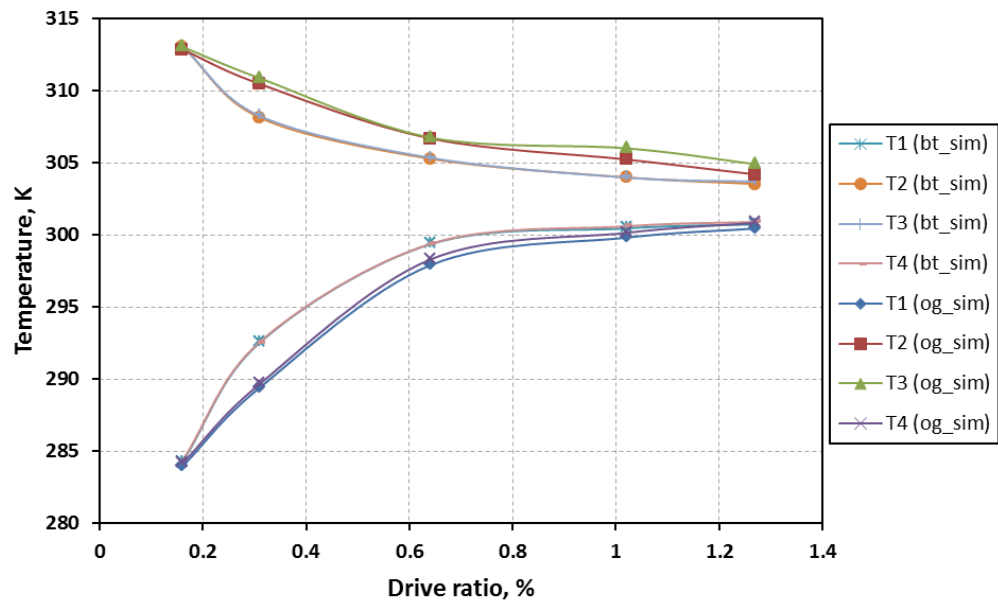


Figure 5.12: Comparison between the numerical time-averaged temperatures (T-1, T-2, T-3 and T-4) for the T-HEX (flat) and the T-HEX (ogive), at $0.15 < DR < 1.29\%$, $P_m = 5\text{bar}$ and $T_h = 70^\circ\text{C}$.

The comparison between the predicted gas temperatures for T-HEX (flat) and T-HEX (ogive) are shown in Figure 5.12. As can be seen in the plot, the predicted gas temperatures for T-HEX (ogive) are higher for HHX and lower for CHX1 and CHX2 at the investigated drive ratios, in comparison with the T-HEX (flat). The

maximum of this difference is about 3°C (i.e. 4% at a reference temperature of $T_h - T_{c1,c2}$). This influences the magnitude of heat transfer to the gas at the hot heat exchanger and heat rejected at the cold heat exchangers as will be discussed in the next section. The temperature profile shows dependency on the drive ratio.

5.5 Heat transfer

The heat transfer results from experiments and simulation are compared and presented in terms of the heat flux and Nu in this section. Space-cycle averaged heat flux, cycle-averaged and space-cycle Nu are presented for the T-HEX (flat) and T-HEX (ogive).

5.5.1 Heat flux

The heat flux is obtained as a function of both space and cycle (Zhao and Cheng, 1995; Shi et al., 2010; ANSYS Fluent 17.0, 2015). The space-cycle averaged heat flux is as follows:

$$q_{h,c1,c2} = \frac{1}{2\pi A_s} \int_0^{2\pi} \int_{A_x} q(x, \phi) \Big|_{wall} dA d\phi \quad (5.16)$$

The local instantaneous heat flux, $q(x, \phi)$, as a function of area and phase are obtained directly from ANSYS Fluent 17.0 (2015), which is then averaged over one flow cycle. The heat flux as calculated using equation (5.16) is shown in Figure 5.13 for T-HEX (flat) as a function of drive ratio ($0.16 \leq DR \leq 1.27\%$), while that of T-HEX (ogive) is illustrated in Figure 5.14, at $0.15 \leq DR \leq 1.29\%$. The positive heat fluxes reflect heat being transferred from hot wall to the gas while the opposite is for the cold heat exchanger where heat is transferred from fluid to the wall. As evident in the plot, there is good agreement between measured (symbols) and predicted heat flux. The agreement is, however, better at $DR < 0.64\%$ than higher drive ratios. Both results show a similar trend over the investigated drive ratios (CHX1, HHX, and CHX2). The heat fluxes increase with the increase in drive ratios for the three heat exchangers. The heat flux increases gradually over the drive ratios $0.15 \leq DR \leq 1.27\%$ for both experimental and predicted results. The magnitude of heat absorbed by the cold heat exchangers is equivalent to the magnitude of heat given to the oscillating gas by the hot heat exchanger. The comparison between the predicted heat fluxes for T-HEX (flat) and T-HEX (ogive) are presented in Figure 5.15.

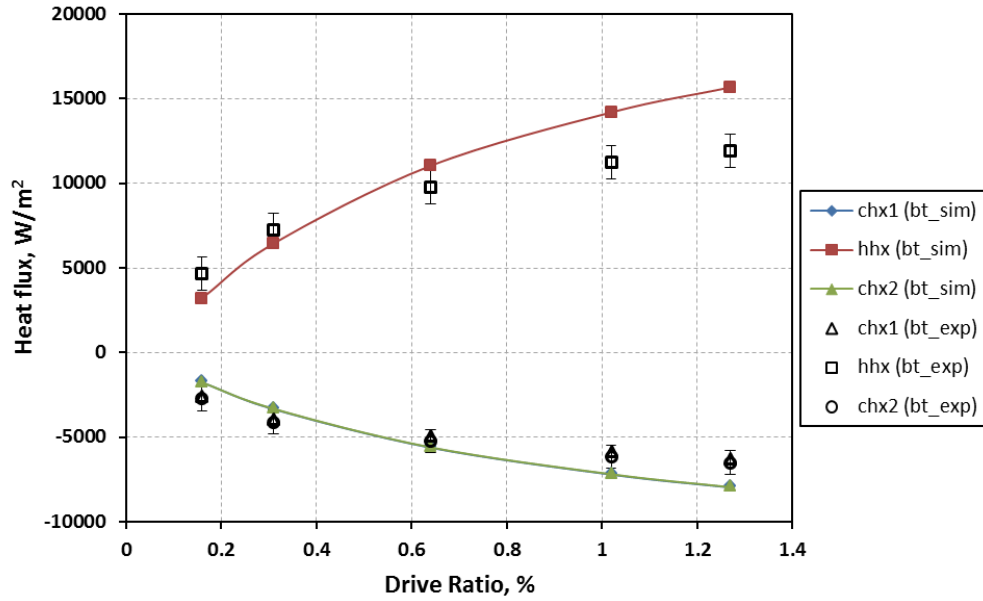


Figure 5.13: Comparison between the simulation and the experimental heat fluxes for the T-HEX (flat), at $0.16 \leq DR \leq 1.27\%$, $P_m = 5\text{bar}$ and $T_h = 70^\circ\text{C}$.

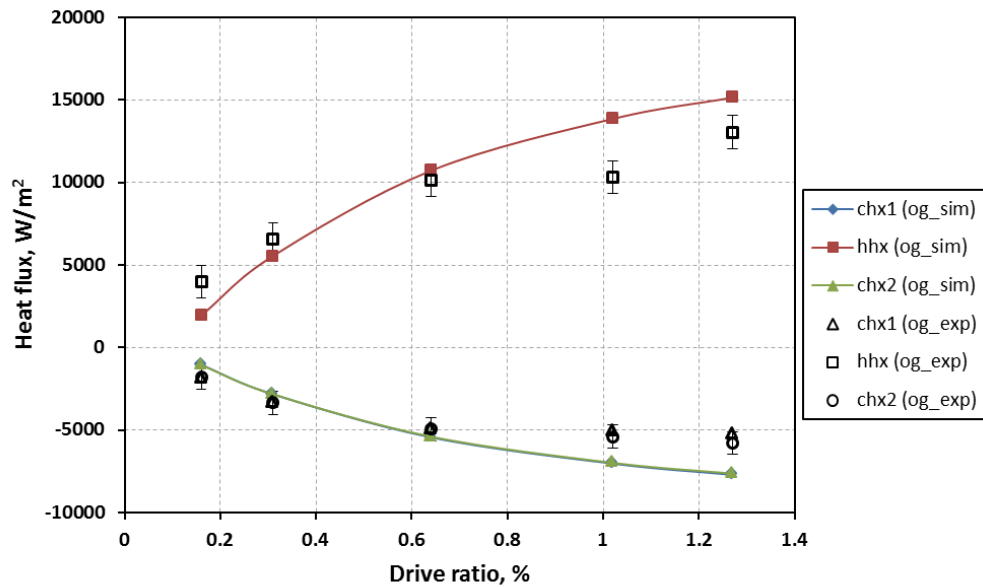


Figure 5.14: Comparison between the simulation and the experimental heat fluxes for the T-HEX (ogive), at $0.15 \leq DR \leq 1.29\%$, $P_m = 5\text{bar}$ and $T_h = 70^\circ\text{C}$.

The heat fluxes have a similar increasing trend for the two edge shapes. T-HEX (ogive) yielded lower heat fluxes noticeably at the lower drive ratios ($DR < 0.8\%$). As the drive ratio increases, the difference between the heat fluxes for the edge shapes becomes less and less. As earlier remarked, the minimisation of acoustic pressure drop is desirable to the overall efficiency of thermoacoustic devices. On the

other hand, reduction in heat transfer will adversely affect the overall efficiency of the system.

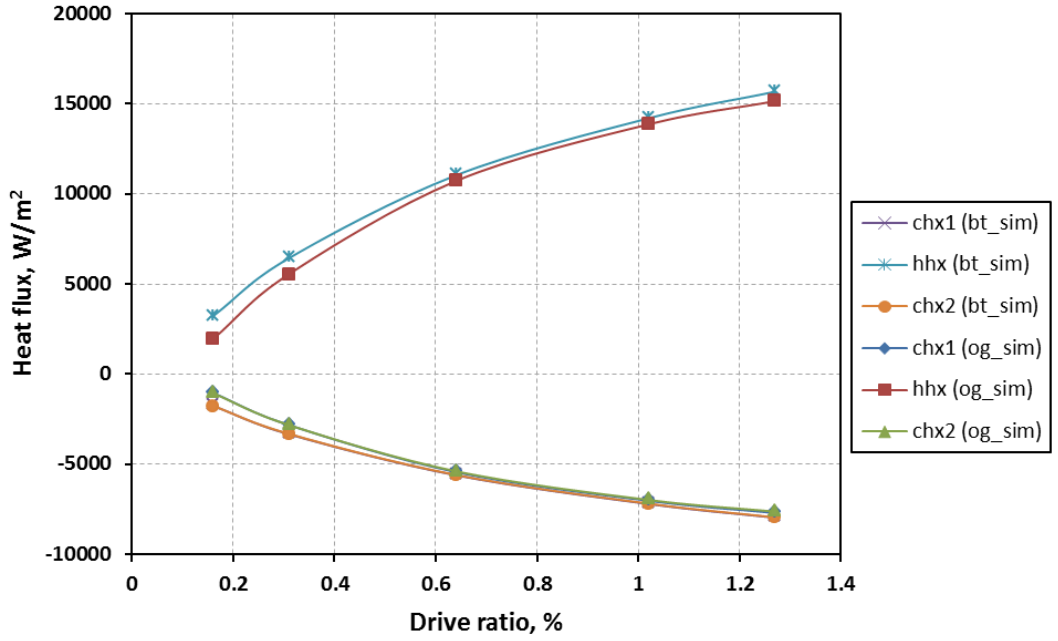


Figure 5.15: Comparison between the numerical heat fluxes for the T-HEX (flat) and the T-HEX (ogive), at $0.15 \leq DR \leq 1.29\%$, $P_m = 5\text{bar}$ and $T_h = 70^\circ\text{C}$.

5.5.2 Nusselt number (Nu)

The Nu can be estimated from the definition given in equation (4.9). Here, it is defined with respect to flow cycle and area of the heat exchanger as:

$$Nu_{h,c1,c2} = \frac{1}{2\pi A_s} \int_0^{2\pi} \int_{A_s} Nu(x, \phi) dA d\phi \quad (5.17)$$

where $Nu(x, \phi)$ is the local instantaneous Nu defined as:

$$Nu(x, \phi) = \frac{h_c(x, \phi) d_h}{k} \quad (5.18)$$

h_c is the local instantaneous heat transfer coefficient defined as:

$$h_c(x, \phi) = \frac{q(x, \phi)}{\Delta T(x, \phi)} \quad (5.19)$$

As previously remarked, the thermal conductivity is evaluated using the average gas temperature at the inlet and outlet of the heat exchangers. The thermal potential for the heat transfer coefficient is obtained as $\Delta T(x, \phi) = T_w(x) - T_i(\phi)$. $T_i(\phi)$ is defined as the mean of gas temperatures at locations 1, 2, 3 and 4 (c.f. Figure 5.2). That is:

$$T_i(\phi) = \frac{T_{inlet}(\phi) + T_{outlet}(\phi)}{2} \quad (5.20)$$

The definition of thermal potential is application dependent (Zhao and Cheng, 1995; Shi et al., 2010). It is defined here to reflect the contribution of the temperature near the heat exchanger's inlet and outlet.

Figure 5.16 shows the comparison of the experimental and numerical Nu for T-HEX (flat). The numerical values are obtained from equation (5.17) while the experimental values are calculated from equations (4.9 – 4.11). Both measured values (symbols) and predicted have a similar increasing trend over the range of drive ratio $0.16 < DR < 1.28\%$. A good agreement between the two results can be observed from the plot. It should be noted that having a similar trend in the Nu for CHX1, HHX and CHX2 in both experimental and numerical results is entirely reasonable because the heat exchangers are identical. The comparison between experimental and predicted Nu for T-HEX (ogive) are shown in Figure 5.17. A good agreement exists between the measured (symbols) and the numerical results at low drive ratio. There is a noticeable difference between the two results at high drive ratio ($DR > 0.6\%$). This difference was not expected, given the fact that good agreements between the experimental and numerical results have been observed as discussed in the earlier sections.

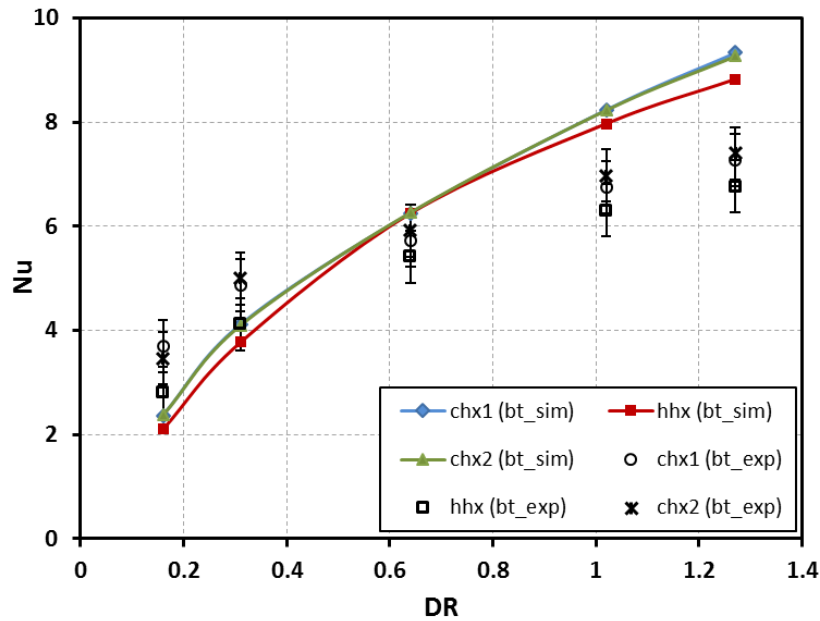


Figure 5.16: Comparison of the experimental and the simulation Nu for the T-HEX (flat), at $0.16 \leq DR \leq 1.27\%$, $P_m = 5\text{bar}$ and $T_h = 70^\circ\text{C}$.

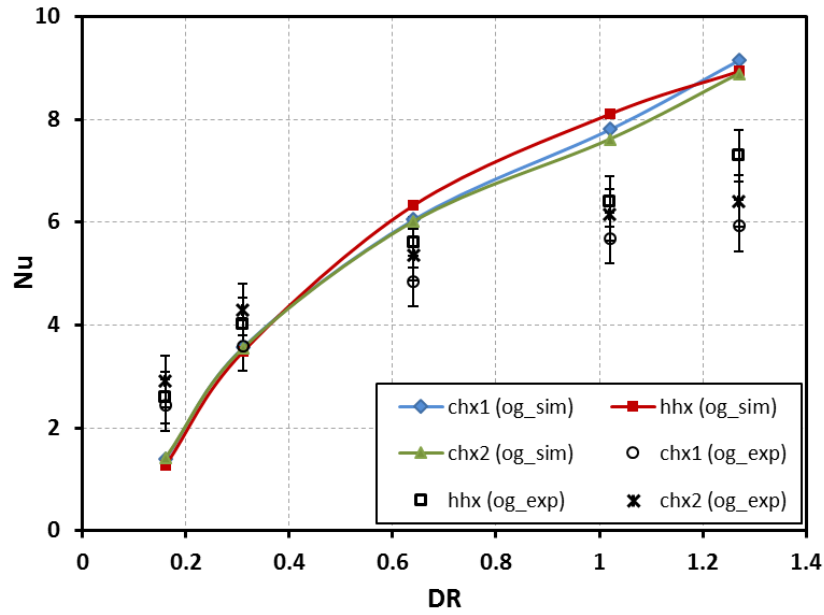


Figure 5.17: Comparison of the experimental and the simulation Nu for the T-HEX (ogive), at $0.16 \leq DR \leq 1.29\%$, $P_m = 5\text{bar}$ and $T_h = 70^\circ\text{C}$.

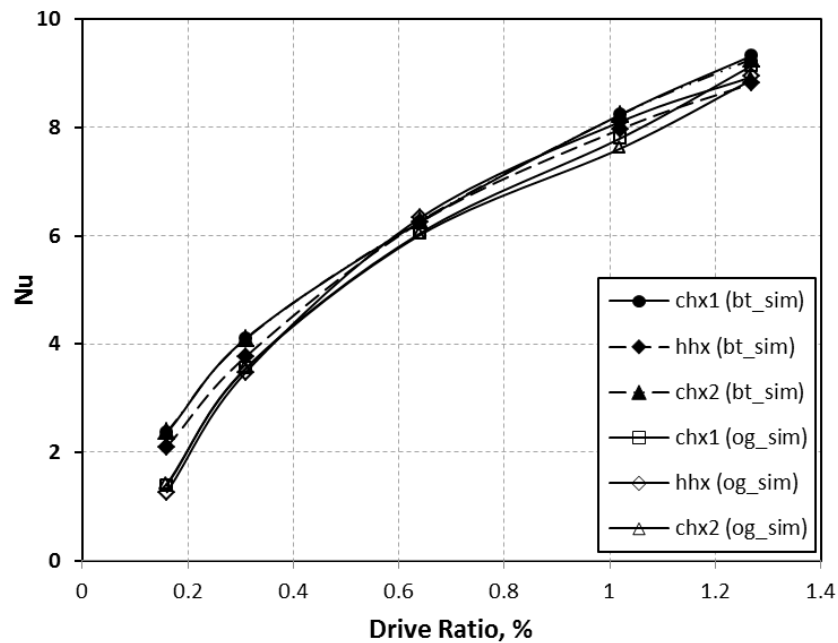


Figure 5.18: Comparison between the numerical Nu for the T-HEX (flat) and the T-HEX (ogive), at $0.15 \leq DR \leq 1.29\%$, $P_m = 5\text{bar}$ and $T_h = 70^\circ\text{C}$.

The average discrepancy between the CFD prediction and the measured Nusselt number in Figures 5.16 and 5.17 are 21% and 25% for T-HEX (flat) and T-HEX (ogive), respectively. Figure 5.18 shows the comparison between numerical results for T-HEX (flat) and T-HEX (ogive) at $0.15 \leq DR \leq 1.29\%$. The results for both

edge shapes have a similar increasing trend as the drive ratio increases. The ogive edge shape, however, causes a slight unwanted reduction in the Nu in comparison with the flat edge. As described earlier, an increase in the heat transfer would be desirable from the viewpoint of overall efficiency, not the opposite.

5.6 Acoustic pressure drop

Figure 5.19a-c represents the acoustic pressure drop across CHX1, HHX, CHX2, respectively for the T-HEX (flat) while Figure 5.19e-f, shows the acoustic pressure drop across CHX1, HHX, CHX2 for the T-HEX (ogive) configuration. Data is sampled at locations 1, 2, 3, and 4 (cf. Figure 5.2a). Δp_{12} , Δp_{23} and Δp_{34} refer to the acoustic pressure drop across CHX1, HHX and CHX2, respectively, measured as a function of time. The time (t) is normalised by the period of oscillation i.e. $T_p = 1/f$. The comparison is made between the numerical results for T-HEX (flat) and T-HEX (ogive). The acoustic pressure amplitudes are the static oscillating pressure in the fluid domain. Generally, from the plots (Fig. 5.19), the acoustic pressure drop shows a strong dependency on the drive ratio. As the drive ratio is increasing, the pressure drop increases significantly due to the increasing effect of minor losses created by a sudden change in the cross section at the entry and exit of the heat exchangers.

Table 5.4: Reduction in the acoustic pressure drop on the CHX1

Drive ratio, %	Reduction (suction stage), %	Reduction (ejection stage), %
0.16	17.29	19.88
0.31	21.39	21.38
0.64	16.74	38.75
1.02	4.44	47.61
1.29	2.26	51.35

The acoustic pressure drop also shows dependency on the flow direction for the CHX1 and CHX2. This can be observed for both edge shapes (flat and ogive) that are considered in the 3D model. Due to the symmetric arrangement of the exchangers, the pressure drop across HHX shows no dependence on the flow

direction. Distortion can be observed in the pressure profile at the entry and exit of the CHX1 and CHX2 for both edge shapes, especially at higher drive ratios.

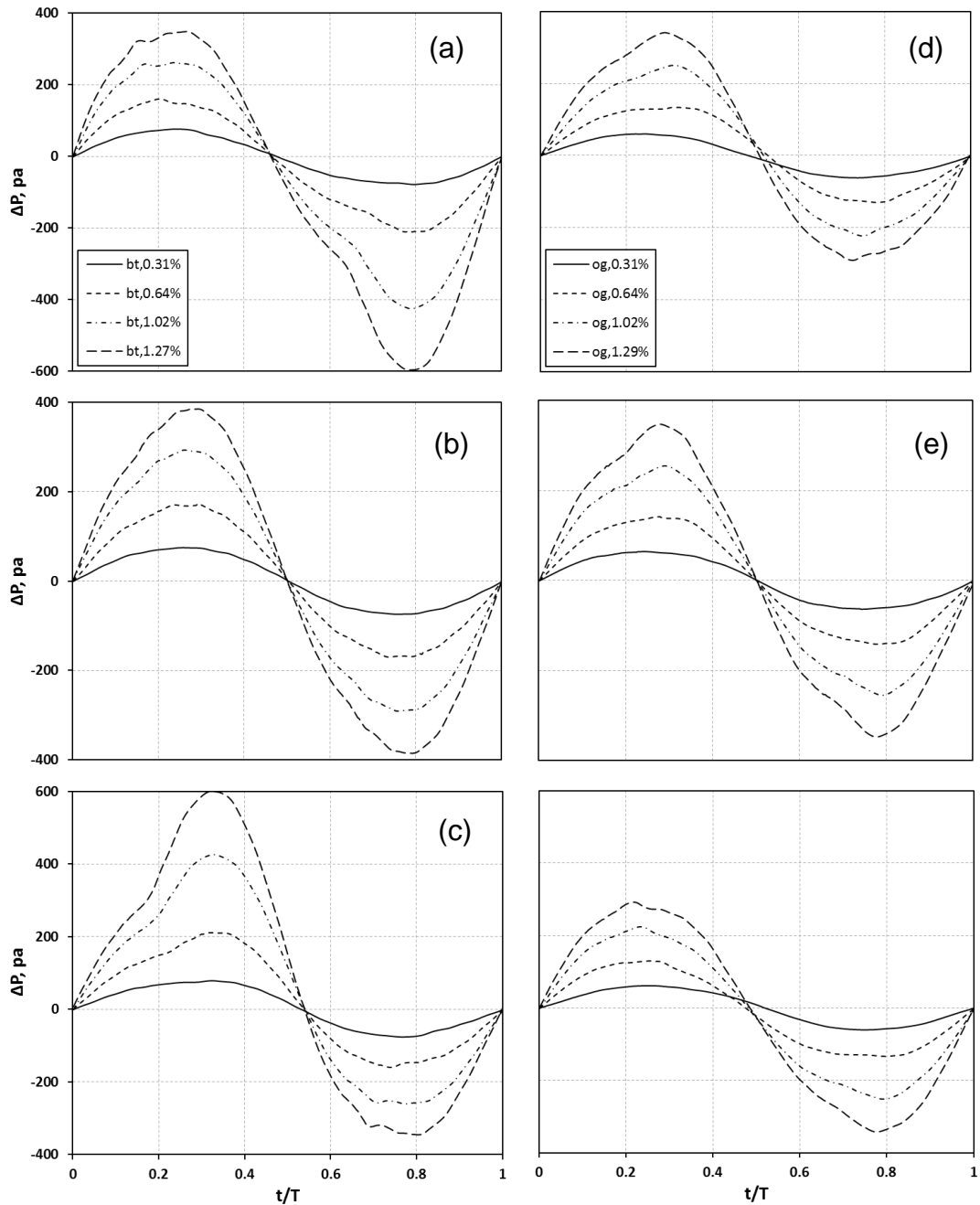
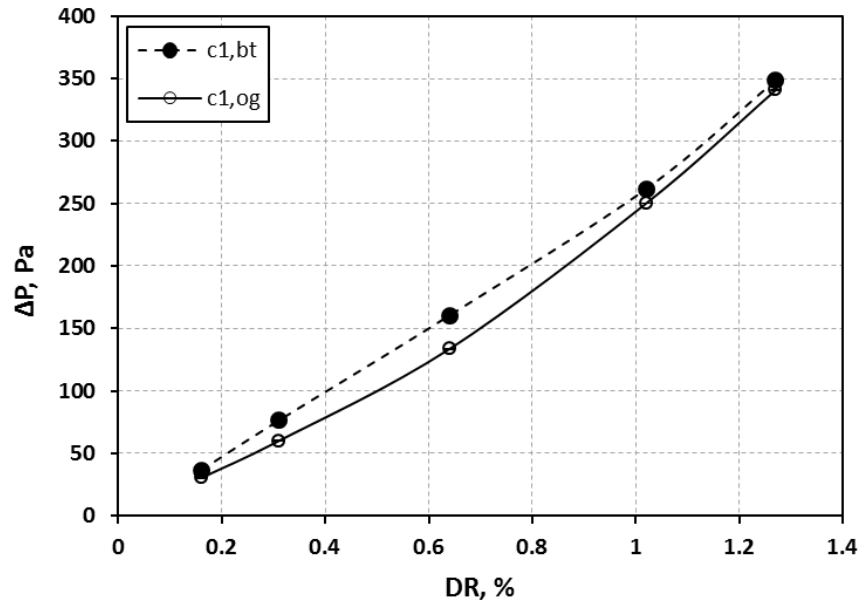


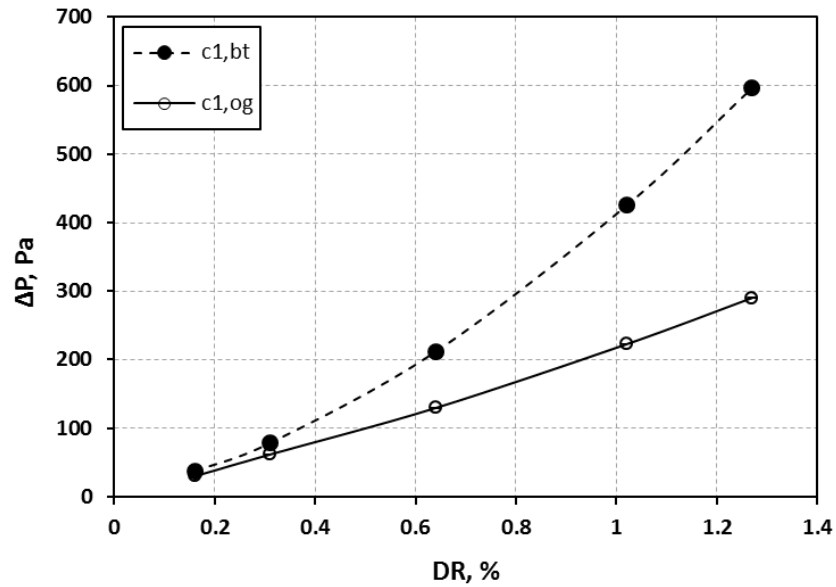
Figure 5.19: Acoustic pressure drop as a function of t/T across the T-HEX (flat) and the T-HEX (ogive), at $0.3 \leq DR \leq 1.29\%$, $P_m = 5\text{bar}$ and $T_h = 70^\circ\text{C}$ (a) – (c) CHX1-HHX-CHX2 (flat) (d) – (f) CHX1-HHX-CHX2 (ogive).

Clearly, from the plots (Fig. 5.19a-c), T-HEX (ogive) has an acoustic pressure drop magnitude lower than T-HEX (flat) at all drive ratios ($0.31 \leq DR \leq 1.29.0\%$). The presence of the profile edge minimised the pressure drop across the three symmetrically arranged set of heat exchangers. As previously explained, this would

be desirable for the thermoacoustic devices if the heat transfer performance of the heat exchanger is not adversely affected.



(a)



(b)

Figure 5.20: Comparison of the acoustic pressure drop across CHX1 (a) suction stage (b) ejection stage

At lower drive ratios of 0.31%, the effect of edge shape on acoustic pressure drop is less pronounced. The extent of reduction in the acoustic pressure drop when the ogive edge is present is shown in Table 5.4 for CHX1. Due to symmetry, the results on the CHX2 are the inter-switch between the suction and ejection results shown in Table 5.4 for CHX1. The extent of reduction in the pressure drop across HHX is 16% and 10% at drive ratio of 0.16% and 1.29%, respectively, for both suction and

ejection stages, which is again due to the symmetry in the arrangement of the heat exchangers. At the suction stage, the reduction gradually decreases as the drive ratio is increasing while the opposite applies to the ejection stage of the flow. Figure 5.20 shows the graphical representation of the minimisation of acoustic pressure drop across CHX1 because of the profiled edge shape (ogive). The peak of pressure drop generally falls at $0.2 < t/T < 0.4$ and $0.6 < t/T < 0.8$ in the suction and ejection stage of the flow cycle.

5.7 Summary

A 3D computational model has been developed. The simulation results have been validated with the experimental results for the T-HEX (flat) and T-HEX (ogive). Good agreements between the numerical and experimental results are achieved. The effect of edge shape has been tested by comparing the performance of T-HEX (ogive) with that of T-HEX (flat) configuration. It is observed that the presence of aerodynamic edge shape causes a slight adverse reduction in the heat transfer performance of the T-HEX configuration as represented in terms of Nu . However, the adverse effect of ogive shape on heat transfer tends to diminish gradually as the drive ratio is increasing.

The ogive edge, however, minimised the acoustic pressure drop by about 51% at the highest drive ratio considered in the study. The favourable reduction of acoustic pressure drop increases as the drive ratio increases is desirable to the overall efficiency of the system. The use of edge shape could be beneficial to thermoacoustic technologies because the systems operate at high drive ratios in practice.

Chapter 6

2D Simulation Model for Parallel Plate Heat Exchanger

This chapter describes the work on heat transfer and oscillatory flow behaviour in three identical heat exchangers, one ‘heat source’ centrally positioned between two ‘heat sinks’, The investigation is based on a 2D numerical model that was carried out as part of the design activities for the experimental set-up described in Chapter 3. The 2D simulation model results are validated with the measurement results obtained from the experimental set-up as described in Chapter 3 and the results from the analytical solution. In section 6.1, the background to the current study is given. Section 6.2 discusses the methodology adopted in the study, including the chosen geometrical and computational domain, physical model and the initial and boundary conditions. Section 6.3 described the mesh sensitivity. In section 6.4, the model validation against analytical results is discussed. Section 6.5 described the validation of computational results against the experimental data. The effects of edge shape on flow velocity and temperature profiles are discussed in sections 6.6 and 6.7, respectively. In sections 6.8 the edge shape effects on heat transfer are discussed while the edge shape effects on acoustic pressure drop are given in section 6.9. The summary of the findings from the study is outlined in section 6.10.

6.1 Background

Heat exchangers are critical components of energy systems such as thermoacoustic heat engines and coolers. Their appropriate design and development are essential for achieving high-performance efficiency by these energy technologies. For this reason, the work here focuses on the investigation of the effect of edge shape on heat transfer, flow behaviour and acoustic pressure losses in the heat exchangers under oscillatory flow conditions, using experimentally and analytically validated 2D CFD simulation methods. It is worth mentioning that the current 2D CFD model was developed at the initial phase of the experimental set-up described in Chapter 3 and it provided the necessary insight that led to the development of the 3D model described in Chapter 5.

The heat transfer and acoustic pressure drop study are done through the examination of time-dependent velocity, pressure and temperature fields, heat fluxes and heat transfer coefficient correlation in terms of Nusselt number, and the acoustic pressure drop created by the heat exchangers in an oscillatory flow. The heat exchanger configuration is modelled as parallel plate type and the edge shapes – blunt, cone, ogive, and round-edge – are considered at the entrance and exit of the heat exchangers. The investigation is carried out with respect to the drive ratio in the system, for the range of $0.3 \leq DR \leq 2.0$ for a flow cycle ($0 < t/T < 1.0$). The significance of the study here includes the benefit of determining the relationship between changes in the heat transfer and acoustic pressure drop conditions and specific flow behaviour, such as vortex shedding or turbulence. It also offers insight into the ways by which the non-linearity associated with the geometrical discontinuity in the internal core of thermoacoustic device can be minimised using edge shape, thereby contributing to the improvement of overall system efficiency.

6.2 Methodology

Figure 6.1 shows the schematic of the standing wave experimental apparatus (cf. Figure 3.1 and 3.2) which was used to obtain the experimental data for comparisons with the current numerical investigations. Its geometry also served to define the computational domain. The methodology for obtaining the numerical results here is like the one described in Chapter 5 (section 5.2). Hence only the details that are specific to the 2D model are given. This section aims to discuss the geometrical model and computational domain, physical model and underlying equations as well as initial and boundary conditions. The simulation is carried out using ANSYS Fluent 15.0 (2013), and the post processing was done in the ANSYS CFD-Post 15.0 (2013).

6.2.1 Geometrical model and Computational Domain

The geometry consists of a half-wavelength thermoacoustic experimental set-up, as previously described and shown in Figure 6.1a. The computational domain (Figure 6.1b) is a 2D replica of the test section and has a total length (L) of 900 mm. The geometric and operating parameters as used in the simulation are given in Table 6.1. In the 2D geometry, three identical parallel plate heat exchangers are arranged in series with a gap of 4 mm between two adjacent heat exchangers. A hot heat

exchanger (HHX) is placed between two cold heat exchangers (CHX1 and CHX2). As stated earlier, this heat exchanger arrangement enables an improved heat balance estimation on the HHX.

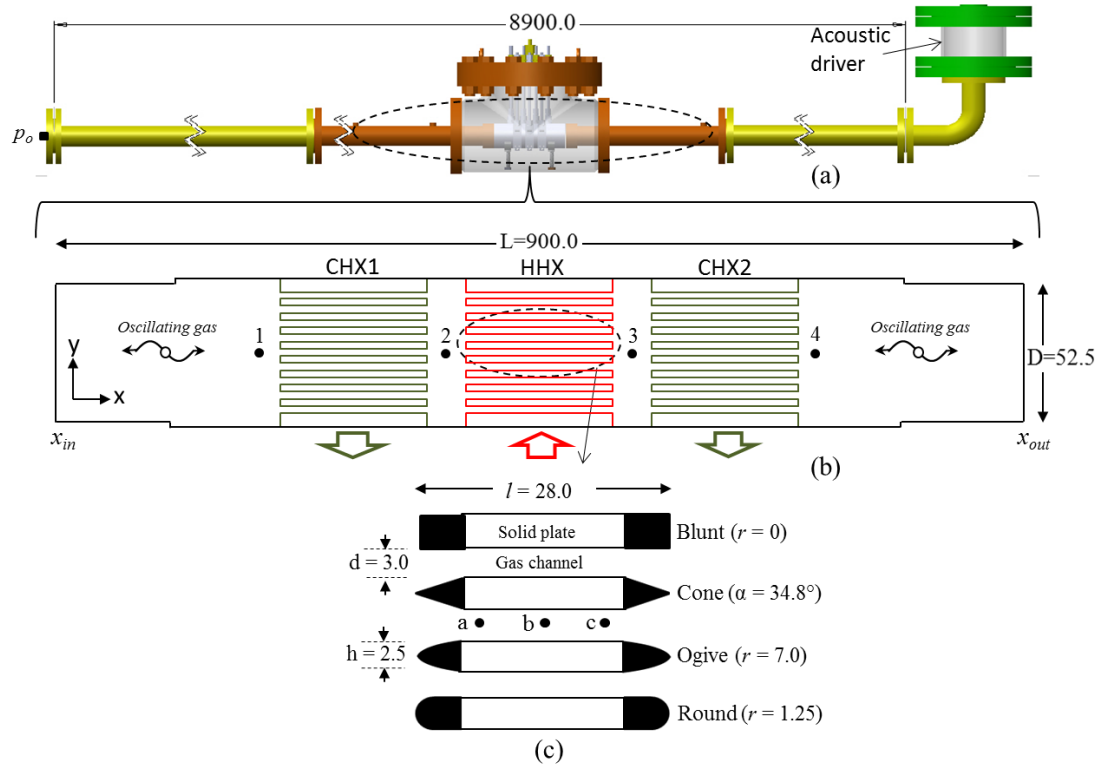


Figure 6.1: Sketch of experimental set-up (b) computational domain (c) aerodynamic edge shapes. Locations 1 ($x = 4244$ mm), 2 ($x = 4276$ mm), 3 ($x = 4308$ mm), 4 ($x = 4340$ mm), a ($x = 4315$ mm), b ($x = 4324$ mm) and c ($x = 4333$ mm) are used for data sampling.

The axial location (x) is in the direction of acoustic propagation. The variables at each location are identified with a number from the location (e.g. location 1 has a temperature $T-1$ and a pressure amplitude $P1$). Location ‘a’ is at 5mm into the gas channel (measuring inward from the stagnation point on the edge shapes)

In the computational domain, the oscillatory flow is induced by imposing a standing-wave through the inlet and outlet of the domain ($x = 3842$ mm and $x = 4742$ mm from the pressure antinode (P_0)). The edge shapes in this study are named as ‘blunt’, ‘cone’, ‘ogive’ and ‘round’ as shown in Figure 6.1c. The ‘blunt-edge’ is the basic edge shape with 90° sharp corners (radius $r = 0$ mm). The ‘cone-edge’ has an angle of divergence of $\alpha = 34.8^\circ$. The ‘ogive-edge’ has an ogive-like shape with curvature radius $r = 7$ mm while the round-edge has a radius of $r = 1.25$ mm

forming a half circle at the entrance and exit of the heat exchangers' channels. Each of the shapes has a similar vertical height that is equal to the plate thickness (h). For every individual simulation case, the three heat exchangers (Figure 6.1b) are used as a set, with the same type of edge shape. The separation distance between two adjacent heat exchangers is 4mm, irrespective of the edge shape type. The heat exchanger length is defined as $l = 28$ mm. There are nine flow channels in each of the three heat exchangers. The computational domain is chosen such that the flow is not disturbed near the boundaries of the domain. This is to ensure that any unsteadiness from the upstream or downstream regions does not influence the flow structures in the vicinity of heat exchangers in the oscillatory flow.

Table 6.1: Geometric and operating parameters for the simulation

Parameters	Values/descriptions
Medium	Helium
Mean pressure (P_m), MPa	0.1
Frequency (f), Hz	57.0
Drive ratio, %	$0.3 \leq DR \leq 2.0$
CHX1 surface temperature (T_{c1}), °C	15.0
HHX surface temperature (T_h), °C	50.0
CHX2 surface temperature (T_{c2}), °C	15.0
Inlet boundary location, mm	3493
Outlet boundary location, mm	4393

Inlet and outlet of computational domain are defined with respect to the pressure antinode (P_o) in the experimental set-up as indicated in Figure 6.1a. The thermal and viscous penetration depths are defined as $\delta_k = \sqrt{2k/\omega\rho_m c_p} = 0.99\text{--}1.05$ mm and $\delta_v = \sqrt{2\mu/\omega\rho_m} = 0.82\text{--}0.86$ mm for the range of temperature in this study. Again, the drive ratio is the ratio of maximum pressure amplitude to the mean pressure in the system, i.e. $DR = (|p_o|/P_m) \times 100\%$. Figure 6.1b shows the locations where data are sampled. Locations 1, 2, 3, and 4 correspond to the positions of thermocouples and pressure transducers in the experimental set-up at axial locations (x) = 4244 mm, 4276 mm, 4308 mm, and 4340 mm. Locations a, b and c are in the central flow

channel of CHX2. Location ‘a’ is at the inlet of the channel (5 mm inward) corresponding to $x = 4315$ mm, location ‘b’ is at the centre line midpoint ($x = 4324$ mm), and location ‘c’ is at the outlet of the channel (5 mm inward) ($x = 4333$ mm).

6.2.2 Physical model

Full time-dependent Navier-stokes (N-S) equations are solved in Fluent using a finite volume method (ANSYS Fluent 15.0.1, 2013; Versteeg and Malalasekera, 2007). In modelling heat transfer and turbulence flow through parallel, previous relevant studies (Mohd Saat, 2013) have used Reynolds Averaged Navier-Stokes (RANS) equations as previously remarked. SST $k-\omega$ model is utilised for the turbulence closure in the RANS equations. Both details of Navier-stokes and RANS equations have been given in Chapter 5.

6.2.3 Initial and boundary conditions

Temperature-dependent thermo-physical properties, viscosity and thermal conductivity of helium is considered using the definition given in equation (4.18) and repeated here for convenience:

$$\mu = 1.99 \cdot 10^{-5} \cdot \left(\frac{T}{T_o}\right)^{0.68} \quad k = 0.152 \cdot \left(\frac{T}{T_o}\right)^{0.72} \quad (6.1)$$

where subscript ‘o’ denotes the reference temperature ($T_o = 300\text{K}$). Pressure inlet and outlet (reversing flow) boundary conditions are specified as functions of the axial locations at distances given in Table 6.1. This corresponds to the inlet and outlet location of the computational domain (cf. Figure 6.1b). The acoustic boundary (pressure wave) conditions are defined by the linear acoustic approximation (Swift, 2001).

$$p_{in} = p_o \cos(k'x_{in}) \cdot \cos(\omega t) \quad (6.2)$$

$$p_{out} = p_o \cos(k'x_{out}) \cdot \cos(\omega t) \quad (6.3)$$

Turbulence boundary conditions are specified in terms of intensity and length scale as:

$$I = 0.16 \left(\text{Re}_{1(in,out)}\right)^{-1/8} \quad \ell = 0.07D \quad (6.4)$$

The acoustic Reynolds number is defined as $\text{Re}_{1(in,out)} = \rho_o u_{1(in,out)} D / \mu_o$ for the inlet and outlet locations of the domain. The velocity amplitude used in the acoustic Reynolds number is calculated as:

$$u_{1,in} = \frac{P_o}{\rho_m a} \sin(k' x_{in}) \quad (6.5)$$

$$u_{1,out} = \frac{P_o}{\rho_m a} \sin(k' x_{out}) \quad (6.6)$$

where p_o is the pressure amplitude at the close end of the resonator. The values of density and a dynamic viscosity at the reference temperature (300 K) are used in equations (6.5) and (6.6). Default values are retained for all other constants in the SST k- ω turbulence model.

The thermal boundary conditions on the walls of CHX1, HHX and CHX2 are specified in terms of constant wall temperatures. CHX1 and CHX2 walls are maintained at a constant temperature of 15°C and HHX wall is kept at 50°C. These temperature settings are like the experimental condition that is used for the validation. At the inlet and outlet of the domain, additional temperature conditions are specified as:

$$\left. \frac{\partial T}{\partial x} \right|_{x_1, x_2} = 0 \quad (6.7)$$

Condition (6.7) is set at the inlet and outlet boundaries to keep the temperature of the cells next to the boundaries equal to that of the reversing flow.

The resonator wall is modelled as adiabatic and non-slip boundary conditions are applied to all walls (CHX1, HHX, CHX2 and resonator). The time step is defined as in equation (5.1). Sensitivity check for time discretization was carried out and a time step of $\pi/250\omega$ was found to be sufficient for the convergence criteria used for the transport and energy equations (10^{-5} , 10^{-5} , and 10^{-8}).

The normalised half plate distance (δ), velocity amplitude (U) and fluid temperature (θ) are introduced as:

$$\delta = \frac{y_o}{d} \quad (6.8)$$

$$U = \frac{u_1}{u_{1,max}} \quad (6.9)$$

$$\theta = \frac{T_f - T_w}{T_h - T_c} \quad (6.10)$$

In expression (6.8), the half plate distance in the flow channel (y_o) is normalised by the plate separation distance. The velocity amplitude in equation (6.9) is normalised

by the $u_{1,max}$ which is the maximum velocity amplitude in the positive oscillatory flow direction (cf. Figure 5.4). As mentioned earlier, a complete flow cycle consists of 20 phases with $\phi 1$ - $\phi 10$ constituting the positive flow direction (suction), and $\phi 11$ to $\phi 20$ for negative flow direction (ejection) when the flow reverses. In equation (6.10), the normalised fluid temperature utilises the local fluid temperature, wall temperature, and reference hot (here 50°C) and cold (here 15°C) temperatures (Zhao and Cheng, 1998).

6.3 Mesh sensitivity

A systematic mesh convergence study was carried out before the detailed study to characterise the required spatial discretisation and ascertain the independence of simulation results on mesh refinement (Roache, 1994). Heat exchangers with ogive-edge were used for the convergence study. During the mesh dependence studies, the number of elements was increased until the changes in the solution were negligible.

Table 6.2: Parameters for the convergence study

Case	Mesh count	Refinement ratio
C1	43348	-
C2	70376	1.62
C3	113979	1.62
C4	179140	1.60

In the presented example, the mesh count that were used are given in Table 6.2. A total of 113,979 cells was employed in the simulation study with y^+ below one everywhere in the wall region, having the maximum value of 0.327 i.e. $y^+ < 1$. Figure 6.2 shows the sensitivity of the solution to the mesh refinement in terms of the centreline velocity amplitude sampled at location 'b' (Figure 6.1c). From the plot, mesh count C2 (70,376 cells) was sufficient for the simulation run, increase in number cells leads to an improvement less than 1% in the variables of interest. As remarked earlier, mesh count C3 (113,979 cells) was used for the ogive shape, and approximate mesh count was subsequently used for the other three edge shapes (blunt, cone and round) to obtain all the simulation results reported below.

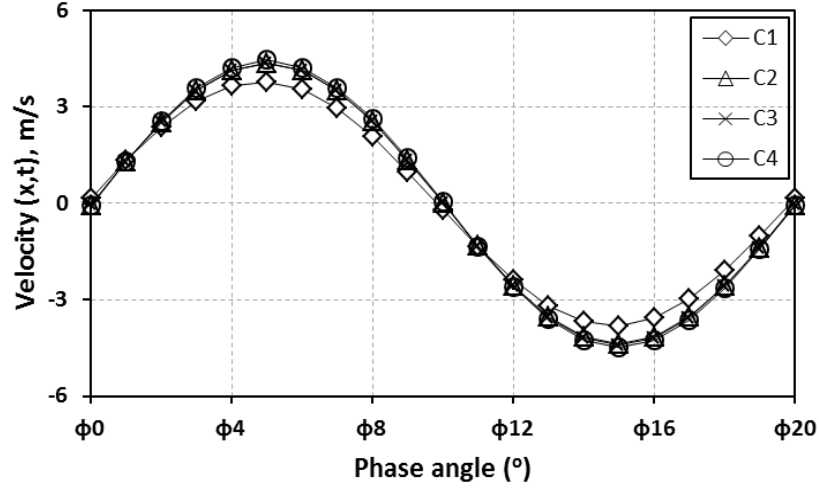


Figure 6.2: Comparison of axial velocity amplitudes as a function of phase angle for various mesh sizes, at $DR = 0.3\%$ ($x = 4324$ mm).

The chosen number of mesh size allows the fine mesh to be present everywhere in the domain including the vicinity of the core, to ensure that heat transfer and flow conditions within the thermal and viscous penetration depths in the channel are captured for all edge shapes and drive ratios.

6.4 Model validation against analytical result

The numerical results are validated in two different ways, which consists of analytical and experimental validation. Figure 6.3 shows the comparison between the centreline velocity amplitude in the CHX2 and the analytical solution for laminar flow in a channel formed by parallel plates.

The analytical expression is defined as (Swift, 2001):

$$u(y,t) = \text{Re} \left(\frac{u_b}{\sigma} \left\{ 1 - \frac{\cosh[(1+i)(y-y_o)/\delta_v]}{\cosh[(1+i)y_o/\delta_v]} \right\} e^{i\omega t} \right) \quad (6.11)$$

$y = 0$ at the central channel of HHX in Figure 6.1a and $y_o = d/2$.

The porosity of the heat exchanger is considered in equation (6.11) because of the comparable flow channel height and the plate thickness, i.e. 3mm and 2.5mm, respectively. The simulation result for blunt edge shape at 0.3% drive ratio was used for the comparison. As evident from the plot, the simulation and analytical results

showed a good agreement. The maximum discrepancy in the predicted velocity amplitudes in all phases within the flow cycle is 3%.

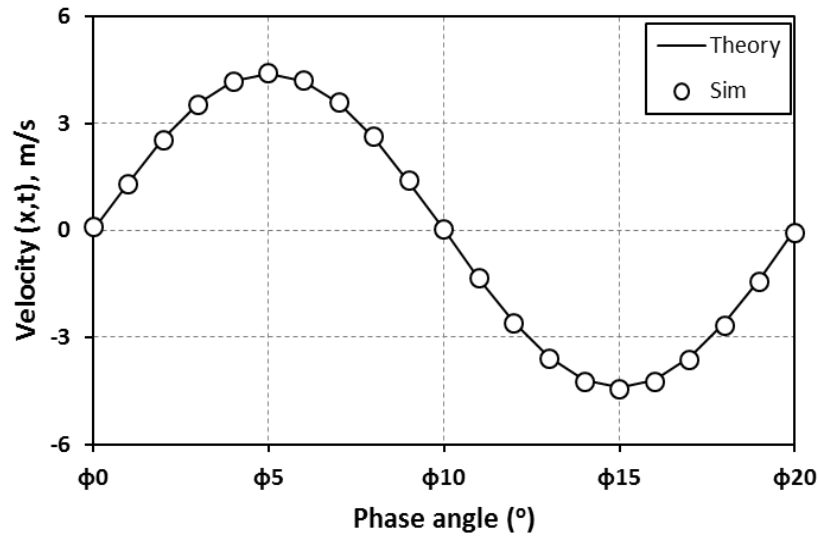


Figure 6.3: Comparison between the analytical and the simulation results for the axial velocity amplitude as a function of phase angle at $DR = 0.3\%$ ($x = 4324$ mm).

6.5 Validation against experimental results

In this section, the numerical results are compared with the experimental values of pressure amplitude and time-averaged gas temperature. The experimental data are obtained from the experimental set-up described in Chapter 3. The results from T-HEX (flat) are used for the comparison. Figure 6.3 compares the pressure amplitude from experiments against the predicted pressure amplitude at $x = 4.34$ m (Figure 6.1b). The results represent the data at drive ratio of 0.3% for the blunt edge-shape ($r = 0$). Pressure amplitude from the experiment is phase averaged over forty flow cycles (Smith and Swift, 2003), while the pressure amplitude from the simulation is phase averaged over 20 cycles after the solution has converged. There is a good agreement between both results. The maximum discrepancy between the experimental and simulation results is about 6.8%. This discrepancy may be due to three-dimensional effects present in the experimental setup which is represented by a 2D model in the simulation. In Figure 6.5, the time-averaged gas temperature from experiments is compared to the predicted values at the axial locations 1 to 4 (i.e. $x = 4.244$ m, 4.276 m, 4.308 m, and 4.340 m). There is a good agreement between both results. The predicted temperature profile shows a similar trend to that of

experiments. At $DR \leq 0.7\%$ when the gas displacement amplitude $\xi \leq 27.98\text{mm}$ is comparable to the heat exchanger length ($l = 28\text{mm}$), the gas temperature values from the experiment are higher than the predicted values for CHX1 and CHX2.

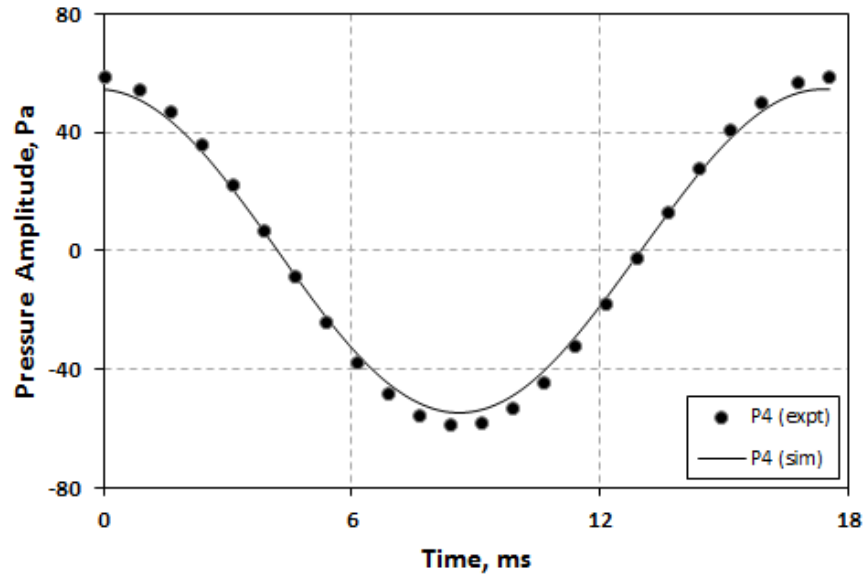


Figure 6.4: Comparison between the experimental and the numerical pressure amplitudes blunt edge-shape ($r = 0$) at $DR = 0.3\%$ ($x = 4308$ mm)

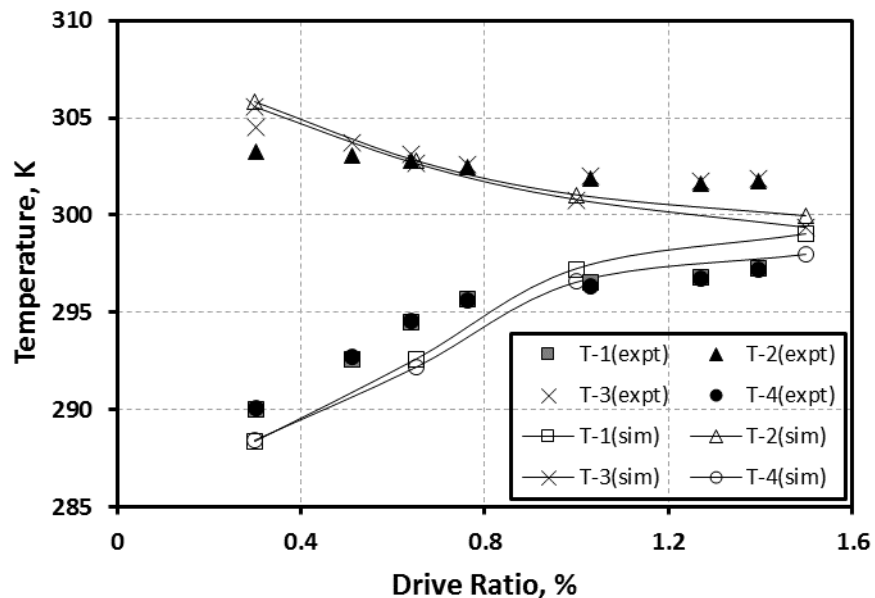


Figure 6.5: Comparison between the experimental and the numerical time-averaged temperatures (T-1, T-2, T-3 and T-4), at $0.3 \leq DR \leq 1.5\%$

However, the experimental gas temperature values are lower for HHX than the predicted values at $DR < 0.65\%$, which indicates that the model under predicts the cold temperature, but overpredict the hot temperature when the gas displacement

amplitude is below or comparable to the heat exchanger length ($DR < 0.65\%$). At $DR > 0.7\%$, there is a reverse switch in the temperature profile. The predicted values are higher than the experiment for CHX1 and CHX2 while the experimental values are greater than the predicted value for HHX. The maximum discrepancy between the two results is below 7%. It should be noted that the difference between T_h and $T_{c1,c2}$ (i.e. $T_h - T_{c1,c2}$) is used as a reference in the evaluation of the deviation. The result is consistent with the findings by Piccolo and Piston (2006). The uncertainties associated with the experimental gas temperature and pressure amplitude measurements are evaluated using the method described in the literature (Dieck et al., 2005; Moffat, 1988; Kim et al., 1993). Also, the variation in the data over three runs (repetitions) of experiments at the same experimental conditions for gas temperature and pressure amplitude are both less than 1.5%. These variations are too small to clearly appear if indicated on the plots (Figures 6.4 and 6.5).

6.6 Effect of edge shape on velocity profile

The initial numerical work focused on investigating such aspects as mesh independence and validation against both analytical solutions and available experimental results for sharp-edged heat exchanger plates. Having sufficient confidence in the numerical methods permitted further studies related to the performance of heat exchangers with arbitrary shapes in terms of velocity and temperature fields, the heat transfer processes as well as acoustic pressure drop (pressure drop) across the heat exchangers.

The summary of simulation results for all the edge shapes (blunt, cone, ogive, and round) is given in Table 6.3. The corresponding displacement amplitudes ($\xi = u/\omega$) at different drive ratios range from 12–76.56 mm, 10.89–73.66 mm, 11.37–75.21 mm and 11.84–76.45 mm for the blunt, cone, ogive and round edge shapes, respectively. The closest heat exchanger to the velocity antinode in the experimental rig is the CHX2. Therefore, locations around it are chosen for data sampling to obtain parameter as close as possible to the velocity antinode. The results shown in Figure 6.6 for time-dependent velocity are taken from the inlet of the CHX2 ($x = 4315$ mm) (cf. Figure 6.1c). Data is sampled at this location to determine the extent of influence of the edge shape on fluid flow and heat transfer by examining the velocity and temperature fields.

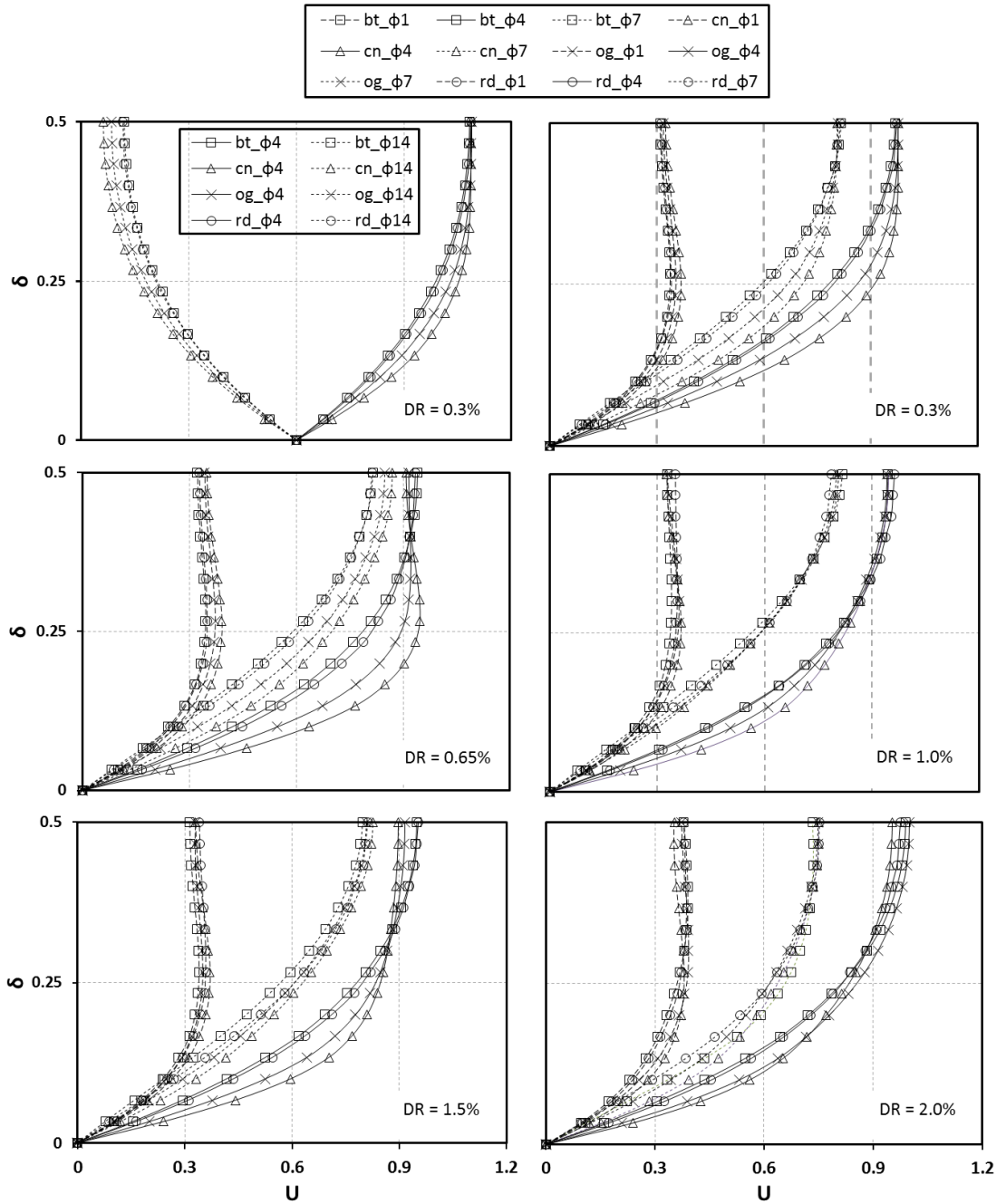


Figure 6.6: Phase-dependent velocity profiles as a function of y at $0.3 \leq DR \leq 2.0\%$ ($x = 4315$ mm).

In the legend, $bt_ \phi 1$, $bt_ \phi 4$, and $bt_ \phi 7$ represents the flow at phase 1, 4 and 7 for blunt edge shape, $cn_ \phi 1$, $cn_ \phi 4$, and $cn_ \phi 7$ denotes flow phases for the cone edge shape, $og_ \phi 1$, $og_ \phi 4$, and $og_ \phi 7$ represents the flow at phase 1, 4 and 7 for ogive edge shape, while $rd_ \phi 1$, $rd_ \phi 4$, and $rd_ \phi 7$ represent the flow at phase 1, 4 and 7 for round-edge shape.

The velocity profiles are plotted for half of the channel separation height (i.e. $d/2$). For clarity, the effect of edge-shape on velocity field is compared at three different

phases, ϕ_4 , ϕ_7 , and ϕ_{10} within the first half of the flow cycle, i.e. positive flow direction (cf. Figure 5.4), for all edge shapes and $0.3 \leq DR \leq 2.0\%$. From the plots, the edge shapes influence the flow structure at the entrance and exit of the channels. At all drive ratios, the effect of cone edge shape appears to be most noticeable on the velocity profile compared to the other edge shapes. The maximum velocity amplitudes during the positive flow direction are given in Table 6.3.

Table 6.3: Comparison of the simulation results for all the edge shapes at $T_{c1,c2} = 15^\circ\text{C}$, $T_h = 50^\circ\text{C}$, $P_m = 1$ bar and $Re_1 = 96 - 672$

DR (%)	Blunt		Cone		Ogive		Round	
	$u_{i,bl}$ (m/s)	T (K)	$u_{i,cn}$ (m/s)	T (K)	$u_{i,og}$ (m/s)	T (K)	$u_{i,rd}$ (m/s)	T (K)
0.3	4.33	313.71	3.90	307.54	4.07	310.85	4.24	313.09
0.65	9.32	314.92	8.19	317.87	8.60	317.26	9.18	316.29
1.0	14.22	313.52	13.46	313.37	13.69	314.01	14.15	313.72
1.5	21.69	310.77	19.89	311.07	20.69	311.40	20.96	312.30
2.0	27.42	310.48	26.38	311.24	26.93	310.51	27.38	311.92

The corresponding acoustic Reynolds number range for these velocity amplitudes is $96 - 672$ for all edge shapes. The influence is more pronounced near the wall for all the three phases (ϕ_4 , ϕ_7 , and ϕ_{10}), i.e. within the viscous penetration depth ($\delta_v = 0.84$ mm (average value)), at $DR = 0.3\%$ and 0.65% where the gas displacement amplitude is smaller than the heat exchanger length. Additionally, the flow symmetry is not present at all DR 's (e.g. 0.3%) for all edge shapes. The lack of symmetry indicates that the fluid moves at a higher velocity, causing significant gas displacement amplitudes during the ejection stage, which influences the heat transfer rates and the pressure drop for the heat exchangers as will be discussed in the next sections. To further establish the influence of the edge shapes on the flow behaviour, the velocity profiles are monitored at the centre line location in the CHX2 ($x = 4324$ mm), and the results are shown in Figure 6.7 for velocity fields at $DR = 0.65\%$ and 1.0% . At this location, the effect of edge shape on fluid flow has diminished considerably. In Figure 6.8, the maximum velocity amplitudes for all edge shapes

and drive ratios are shown for positive flow direction. By taking blunt edge shape as the baseline, the cone edge case has velocity amplitude that is about 10%, 12% and 4% lower at $DR=0.3\%$, 0.65% and 2.0% , respectively. The ogive edge case has velocity amplitudes that are about 6%, 7% and 1.8% lower at $DR=0.3\%$, 0.65% and 2.0% , respectively. Finally, the round edge case has velocity amplitude that is about 2%, 1.4% and 0.2% lower at drive ratios 0.3% , 0.65% and 2.0% , respectively.

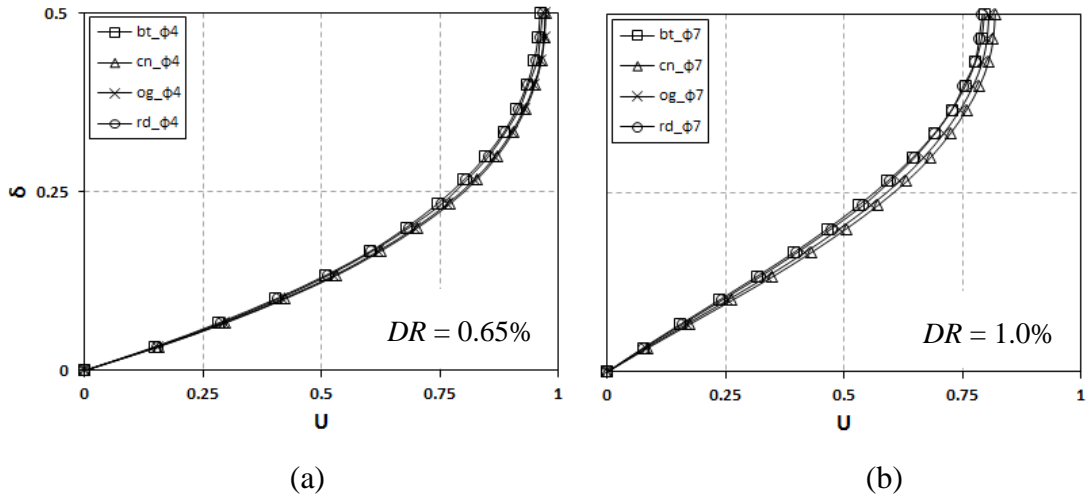


Figure 6.7: Centreline velocity profile at the middle of CHX2 ($x = 4324$ mm) for blunt, cone, ogive and round edge shapes (a) $DR = 0.65\%$ ($\phi 4$) (b) $DR = 1.0\%$ ($\phi 7$).

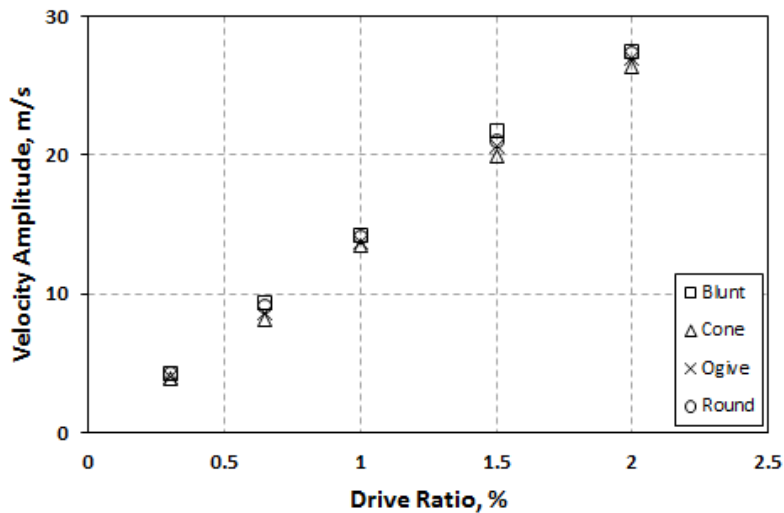


Figure 6.8: Maximum velocity amplitudes as a function of DR for blunt, cone, ogive and round edge shapes ($x = 4315$ mm)

The velocity amplitude for the blunt-edge shape was expected to be greater than the other edge shapes because of the flow disturbance caused by the sharp edge, which

is likely to result in flow separation at the edge of the flow channel. In addition, flow transition over the 90° edge will be more sudden at this change in cross section, which will cause an increase in the gas velocity. The transition of flow over the streamlined body will be more gradual and lead to smaller increases in velocities relative to the shapes.

The effect of edge shape on the flow conditions in and around the heat exchangers can also be described using the vorticity contour. In Figure 6.9, the comparisons between flow patterns for all edge shapes at two different drive ratios (0.3 and 1.0%) are shown. The vorticity contour is plotted to show the vortex structure within the flow channels and at the edges of the three symmetrically arranged heat exchangers. The vorticity is calculated as:

$$\omega = \frac{\partial v}{\partial x} - \frac{\partial u}{\partial y} \quad (6.12)$$

where u and v are the velocity components in the x and y flow direction. Vorticity at $\phi 7$ is used in the comparison for clarity. In Figure 6.9a, at drive ratio 0.3% a pair of vortex structures can be seen in the flow channel and at the end of the channel (right side of CHX2). They are symmetrical relative to the centre line of the channel in the x - y plane. They both have equal but opposite strengths. A recirculation region is formed at the end of the channel, where the pair of vortices remains attached and symmetrical. This phenomenon is similar for all the edge shapes at this drive ratio, which indicates that they have a similar effect due to low acoustic displacement. A symmetrical fill up of the gap between HHX and CHX2 can also be seen on the left end of CHX2. At $DR = 1.0\%$ (Figure 6.9b), the flow velocity has increased, and the gas displacement amplitude has increased accordingly. For all edges, a pair of vortex structure can be seen within the channel, with symmetrical fill up, including the gap between two adjacent plates. For the blunt edge shape, vortex shedding starts immediately after the flow exits the flow channel at the ejection stage in the flow cycle. The formation appears with much turbulence as the vortices do not seem to shed off with the uniform alternating pattern. The vortex strength for the wake appearing at the end of plates for 1.0% drive ratio can create a strong disturbance when it is pushed back into the channel. This could be an explanation for the distortion that is observed in the pressure drop profile (Figure 6.13), which will be discussed later. The influence of cone-edge shape is shown next in Figure 6.9b. At the channel end, cone-edge shape produces an elongated pair of vortices but nearly

symmetrical about the centre line and less distorted when compared with the other edge shapes. A pair of separated vortices with weak strength can be seen in the contour, after the elongated pair, which is the remnant from the breakup. The vortex structures that are formed from the plate with ogive edge shape exhibit a similar pattern that is like that of the cone edge, but slight more ‘wavy’.

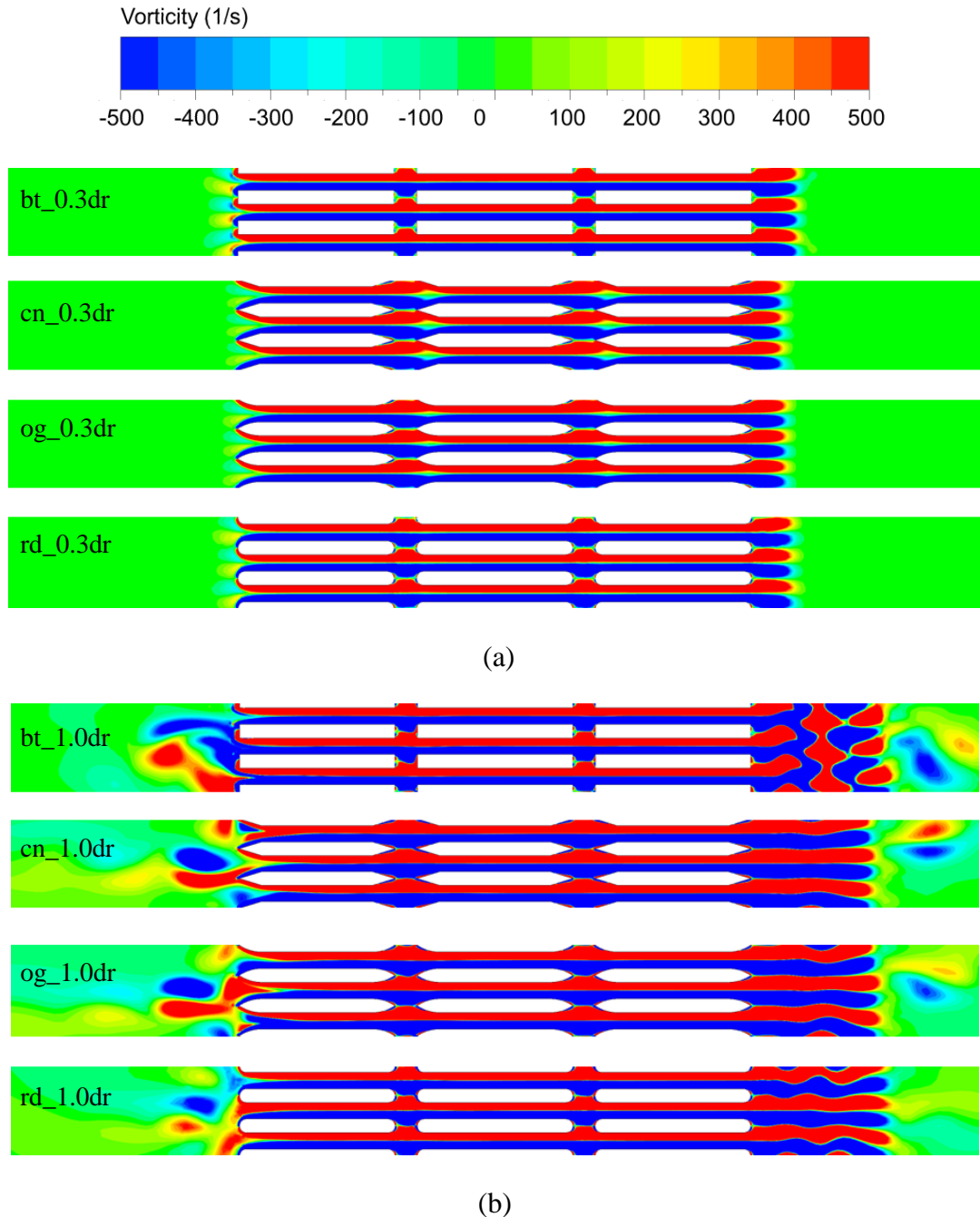


Figure 6.9: Vorticity (1/s) contours for blunt, cone, ogive and round edge shapes, respectively, at $\phi 7$ (a) $DR = 0.3\%$ (b) $DR = 1.0\%$.

For the round edge, at the right end of CHX2, the flow pattern has changed a bit. The pair of vortices has become further elongated and more 'wavy'. It is worth noting that at higher drive ratios, cone edge shape tends to produce the most uniform pattern of vortices in comparison with other edge shapes. It should also be noted that there are vortex structures on the left side of the geometry (i.e. inlet to the CHX1), which vary in pattern and strength from one edge shape to another. This would probably be remnants of the vortex structures that was formed and been pushed back into the plate channel during the ejection and suction stage of the previous flow cycles.

6.7 Effect of edge shape on temperature profile

The edge shape effect on gas temperature is examined through the temperature profiles presented in Figure 6.10. The instantaneous temperature is shown as a function of three phases in the first half of the acoustic cycle, normalised by the wall and reference hot and cold temperatures. Like the velocity fields, the results at CHX2 inlet ($x = 4315$ mm) are discussed first. At $DR = 0.3\%$, the edge shapes cause a slight reduction in the gas temperature at the inlet into the CHX2 with cone edge shape having the lowest temperature value of 307.54 K, followed by ogive, round and blunt (i.e. $T_{cn} < T_{og} < T_{rn} < T_{bt}$), as given in Table 6.3. The values for round and blunt edge shapes are very close (310.85, 313.09 and 313.71 K, respectively). At $DR = 0.65\%$ when the displacement amplitude is almost the same as the heat exchanger length, the cone edge shape gave the highest fluid temperature followed by ogive, round and blunt edge shapes. The temperature fields at $DR = 0.65\%$ gave maximum values for all edge shapes in comparison with other temperature fields from the remaining drive ratios (i.e. 0.3%, and 1.0 - 2.0%), which indicates that the DR could be favourable for heat transfer consideration. At $DR > 0.65\%$, the ogive edge consistently gives a higher temperature than other edge shapes. Also, an annular effect (Yu et al., 2014; Zhao and Cheng, 1995) can be observed at $\phi 7$ for all the edge shapes at $DR = 1.0\%$. At DR of 1.5 – 2.0%, a similar effect is present at $\phi 10$ and $\phi 7$. Figure 6.11 shows the time-averaged temperature at the flow channel inlet, the midpoint in the centreline and the outlet locations of CHX1, HHX and CHX2, for example, as indicated on CHX2 in Figure 6.1c (i.e. locations a, b and c). For these three locations, the temperature shows a strong dependency on the DR . The

combined temperature gains from both CHX1 and CHX2 for each of the edge shapes gradually equate the temperature drop in HHX at $DR > 1.0\%$.

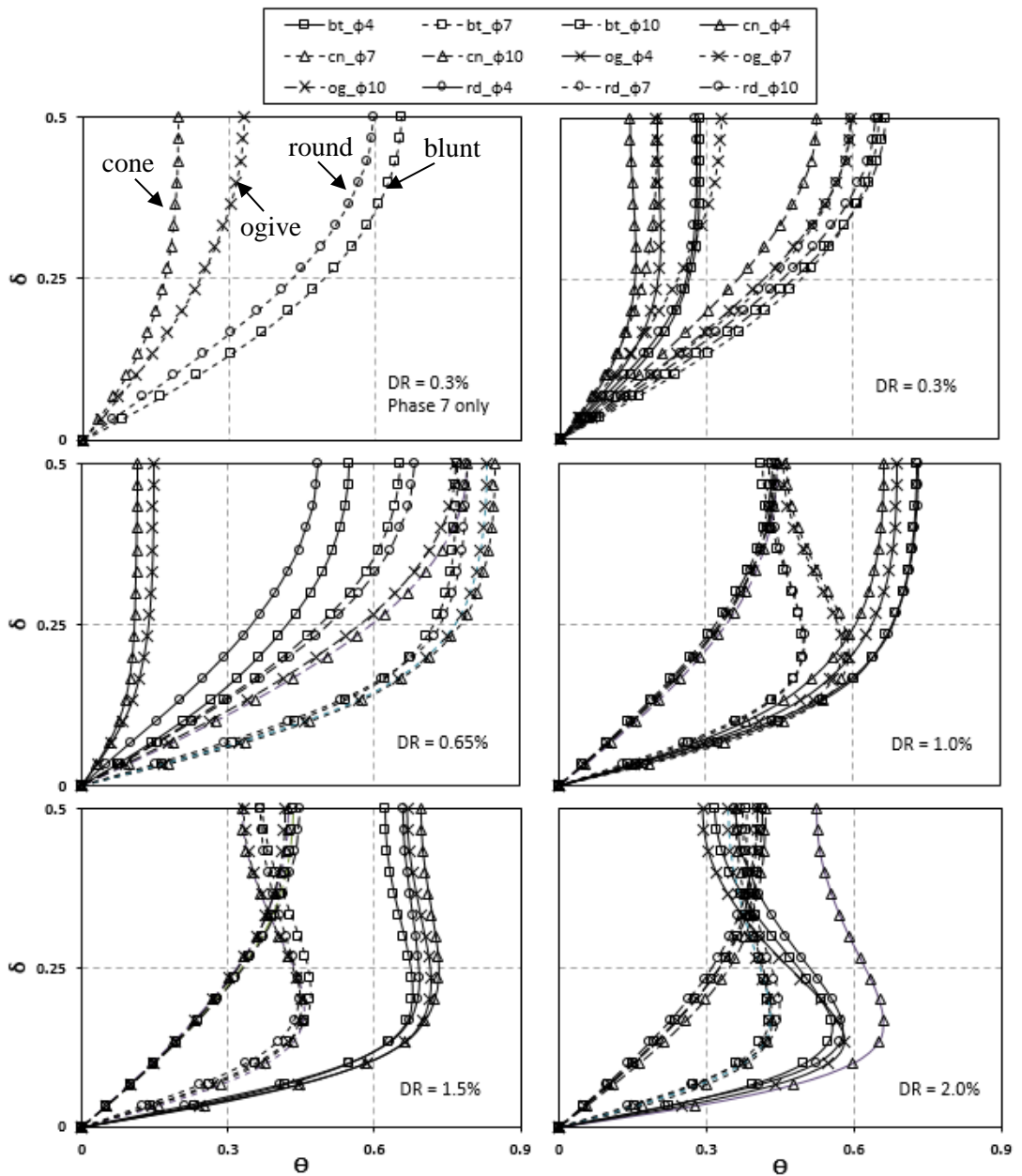


Figure 6.10: Cross-sectional temperature profiles at $0.3 \leq DR \leq 2.0\%$ ($x = 4315$ mm).

In the legend, bt_φ1, bt_φ4, and bt_φ7 represents the flow at phase 1, 4 and 7 for blunt edge shape, cn_φ1, cn_φ4, and cn_φ7 denotes flow phases for the cone edge shape, og_φ1, og_φ4, and og_φ7 represents the flow at phase 1, 4 and 7 for ogive edge shape, while rd_φ1, rd_φ4, and rd_φ7 represent the flow at phase 1, 4 and 7 for round-edge shape.

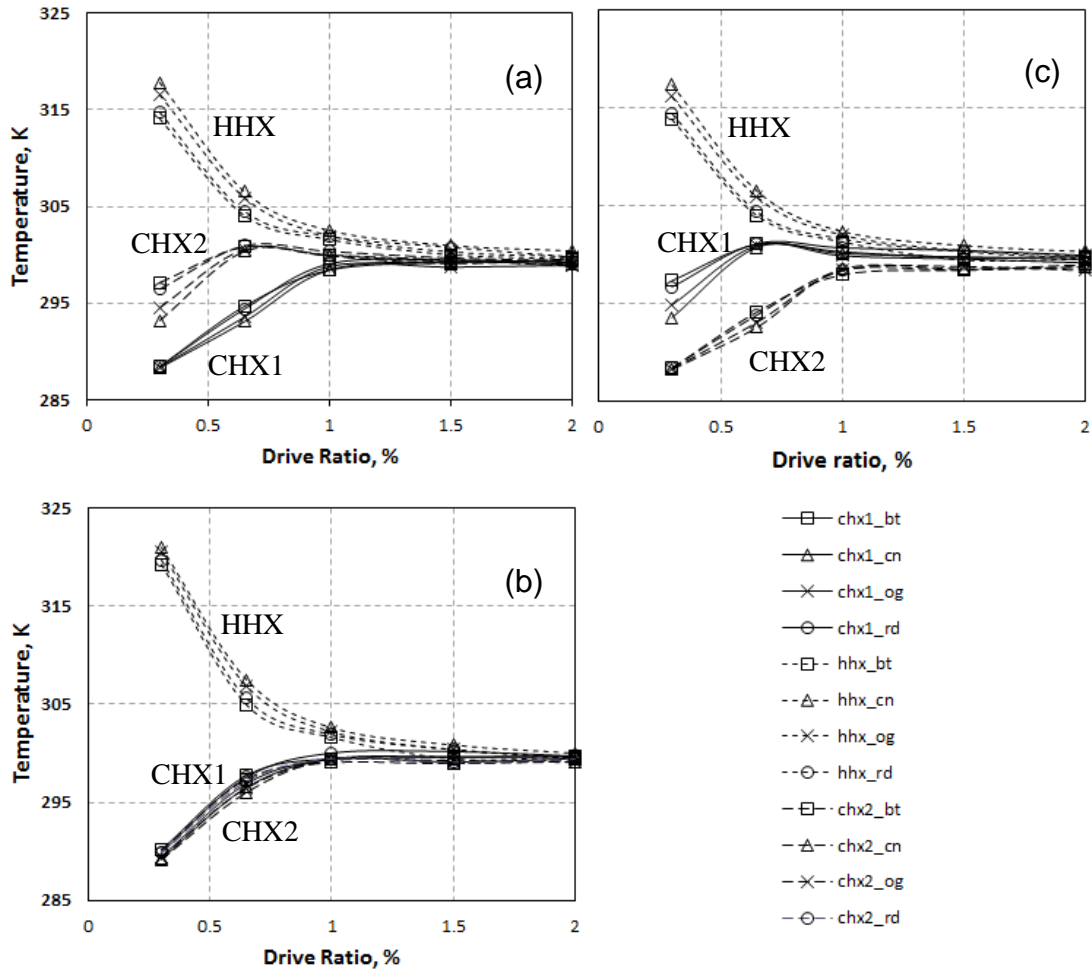


Figure 6.11: Time-averaged temperature profile of CHX1, CHX2 and HHX for the blunt, cone, ogive and round edge shapes (a) inlet (b) centreline and (c) outlet. Locations are about a, b, and c (i.e. $x = 4315$ mm, $x = 4324$ mm, and $x = 4333$ mm) in Figure 6.1c. Similar locations are used for the three heat exchangers.

As evident in the plot, the rate of decrease within the HHX channel is very rapid at $0.3 \leq DR \leq 0.7\%$. Likewise, the rate of increase in temperature in the CHX1 and CHX2 is equally sudden at the same range of DR . This is the situation where the displacement amplitude is below or comparable to the heat exchanger length. At $DR > 0.7\%$, only slight decreases (HHX)/ increases (CHX1 and CHX2) can be observed in the temperature profile, which indicates a lower heat transfer rate that can be attributed to the displacement amplitude larger than the heat exchanger length. However, at the inlet location of CHX2, the fluid temperature is warmer than that of the midpoint in the centreline at $DR \leq 0.65\%$. This increase in temperature is influenced by the temperature of the warmer fluid exiting the HHX. The gas displacement amplitude was not large enough to rapidly move the fluid to the heat

exchange area of the CHX2 where it can reject heat at the temperature of the heat sink (CHX2), which causes an imbalance between heat gained and heat rejected. A similar effect can be observed at the outlet of CHX1 (Figure 6.11c). In all the cases, the cone edge shape consistently gave the highest temperature within the HHX, followed by ogive, round and blunt edge shape. Within the CHX1 and CHX2, the order of influence was opposite.

From the temperature profiles in Figures 6.10 and 6.11, it can therefore be seen that the edge shapes slightly influenced the heat transfer in the heat exchanger channel and the linkage between the velocity and temperature amplitudes can be easily inferred from Figures 6.6 - 6.11. However, as previously observed by Mozurkewich (1998), the gas temperature within the exchanger can be quite non-uniform, rather than being anchored to the wall temperature when observed at an individual phase within the acoustic cycle. Therefore, the effect of edge shape on the global heat transfer rate will be examined in the next section.

6.8 Effect of edge shape on heat transfer

The effect of edge shapes on the heat transfer behaviour of the heat exchangers is considered in this section. From the temperature profiles in Figure 6.10, the heat flux on the wall of each of the heat exchangers can be estimated to gain an insight into the heat transfer within the flow channels.

6.8.1 Heat flux calculation

The local instantaneous heat flux as a function of axial location and phase is defined as:

$$q(x, \phi) = -k \left. \frac{dT(x, y, \phi)}{dy} \right|_{wall} \quad (6.13)$$

Following the standard convention, the negative sign indicates heat transfer from the solid wall to the fluid and the opposite would mean heat transfer from gas to a solid wall. A combination of the space-averaged and cycle-averaged local heat fluxes would yield the space-cycle averaged heat flux for the heat exchangers which is given by (Zhao and Cheng, 1995; Shi et al., 2010; ANSYS Fluent 17.0, 2015):

$$q_{h,c1,c2} = \frac{1}{2\pi l} \int_0^{2\pi} \int_0^l q(x, \phi) \Big|_{wall} dx d\phi \approx \frac{1}{2\pi} \sum_{i=0}^{2\pi} \left(\sum_{j=0}^l -k \left. \frac{\Delta T}{\Delta y} \right|_{wall} \cdot \Delta x_j \right) \cdot \Delta \phi_i \quad (6.14)$$

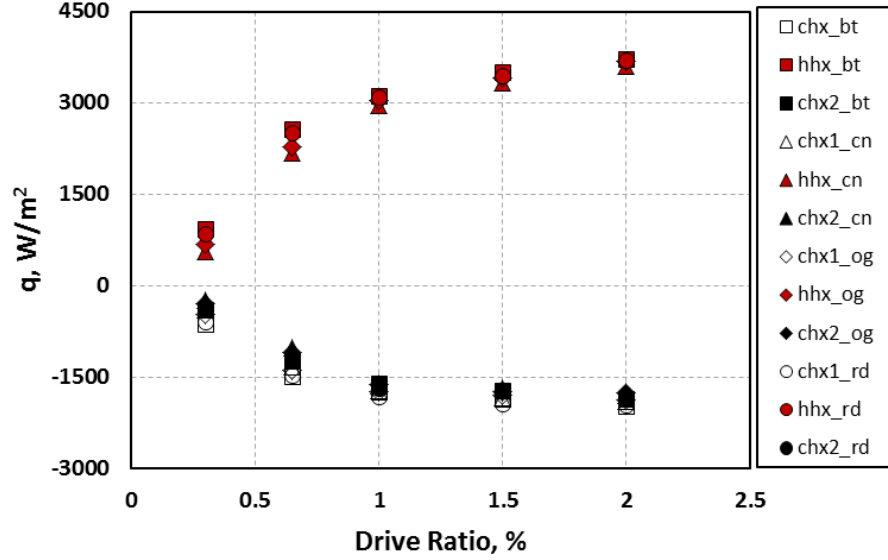


Figure 6.12: Space-cycle averaged heat flux as a function of DR for the CHX1, HHX and CHX2.

The local instantaneous heat flux, $q(x, \phi)$, as a function of space and phase are obtained directly from ANSYS Fluent 15.0 (2013), which is then averaged over one flow cycle as represented in equation (6.14). One flow cycle consists of 20 phases (cf. Figure 5.4). The heat flux is shown in Figure 6.12 for $0.3 \leq DR \leq 2.0\%$. For the three heat exchangers, the heat fluxes increase with the increase in DR . The positive heat fluxes represent heat transfer from the hot wall to the gas while the opposite is for cold heat exchanger where heat is transferred from fluid to the wall. Heat flux increases rapidly between drive ratios $0.3 \leq DR \leq 1.0\%$ after which there is a gradual increase in the remaining drive ratios. Again, the rapid increase in the heat flux occurs when the gas displacement amplitude is less than the heat exchanger length, i.e. 12 mm ($DR = 0.3\%$) and 26 mm ($DR = 0.65\%$) against 28mm heat exchanger length. It is observed that the net heat fluxes from both CHX1 and CHX2 are slightly higher than that of heat flux from HHX at each DR . For instance, the combination of heat flux from CHX1 and CHX2 at $DR = 0.3\%$ (for blunt-edge shape) is 8.2% higher than the heat flux from HHX at the same DR . According to the symmetric heat exchanger arrangement, the heat balance in terms of heat flux can be written as:

$$q_h = q_{c1} + q_{c2} \quad (6.15)$$

The heat flux from HHX should be equal to the combined heat fluxes from CHX1 and CHX2 as can be seen in equation (6.15). The imbalance in the heat flux result is not accounted for in the numerical model since the resonator walls are set to the adiabatic condition. In the actual experiments, this would mean a heat leak to the surrounding (insulation material). In the plot (Figure 6.12), the heat fluxes have a similar trend against the DR for all edge shapes. For the three heat exchangers, the blunt edge shape gave highest heat fluxes at all drive ratios compared to other edge shapes. Cone-edge shape consistently gives the lowest heat fluxes at all drive ratios. The blunt edge gave the highest heat fluxes at all drive ratios – this may be attributed to the effect of flow disturbances associated with its edge shape (c.f. Figure 6.9) The maximum and minimum heat fluxes for blunt and cone edge shapes occurred at $DR = 2.0\%$ in the HHX with values 3728 W/m^2 (blunt edge) and 3596 W/m^2 (cone edge). As remarked at the beginning, the consideration here is twofold: on the one hand, the minimisation of acoustic pressure drop is desirable from the point view of overall efficiency of the thermoacoustic system. On the other hand, the reduction in the heat transfer performance of heat exchanger is undesirable as this will impinge on the overall efficiency of the system. The edge shapes introduce a different degree of unwanted reduction in the heat flux, and this is most severely felt at the lowest drive ratio ($DR = 0.3\%$). Using blunt shape as the baseline, the cone-edge shape caused about 40% reduction in the heat flux at $DR = 0.3\%$ and about 4% at $DR = 2.0\%$. The ogive-edge caused about 27% reduction at $DR = 0.3\%$ and less than 1% at $DR = 2.0\%$. That of the round edge shape is about 8% lower and less than 0.5% at the DR of 0.3% and 2.0% respectively. From this analysis, the unwanted reduction in the heat flux is significantly reduced as the DR increases.

6.8.2 Nusselt number calculation

The local instantaneous Number, $Nu(x, \phi)$ and $h_c(x, \phi)$ are defined as given in equations (5.18) and (5.19), respectively. As observed earlier, the thermal potential, $\Delta T(x, \phi)$, for $h_c(x, \phi)$ is defined here based on the symmetric heat exchanger arrangement here. The space-cycle Nusselt number (Nu) is defined for CHX1, HHX and CHX2 as:

$$Nu_{h,c1,c2} = \frac{1}{2\pi l} \int_0^{2\pi} \int_0^l Nu(x, \phi) dx d\phi \approx \frac{1}{2\pi l} \sum_{i=0}^{2\pi} \left(\sum_{j=0}^l Nu(x, \phi)_{wall} \cdot \Delta x_j \right) \cdot \Delta \phi_i \quad (6.16)$$

where subscripts h , $c1$, and $c2$ denote the Nu for HHX, CHX1, and CHX2, respectively. Figure 6.13 shows the space-cycle Nu from the simulation against the experimental Nu . Overall, the numerical Nu has a similar trend with the experimental values for the three heat exchangers. However, the magnitude of Nusselt number differs noticeably, especially at $DR > 0.3\%$. The experimental results are obtained for the flat-edge tube-heat exchanger, T-HEX (flat), configuration (Ilori et al., 2013), which has a considerable geometrical difference with the parallel configuration in the current study. Therefore, the difference in the predicted and experimental values of Nu could be attributed to the difference in the geometry and of course, the 3-dimensional effect as previously mentioned. The difference in the calculation method of the heat transfer coefficient could also contribute to the discrepancy.

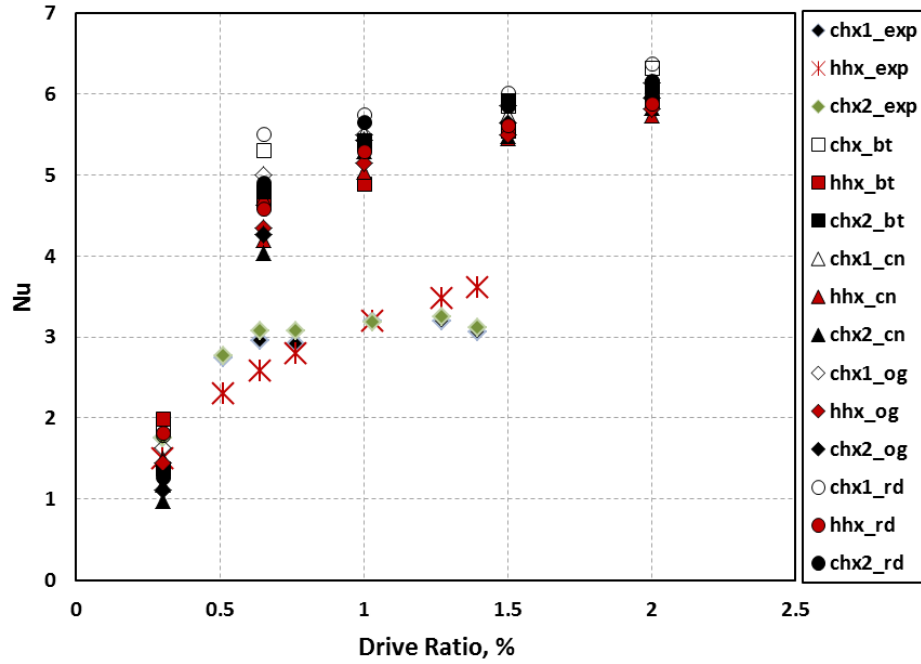


Figure 6.13: Comparison of Nu from the experiments and space-cycle averaged Nu from the simulation.

In the experiment heat transfer coefficient was calculated from equation (4.10), which is represented in equation (6.17) for convenience:

$$h = \frac{q}{\Delta T} \quad (6.17)$$

The Nusselt number in terms of heat exchanger length is defined as:

$$Nu = \frac{hL}{k} \quad (6.18)$$

It should be noted that having a similar trend in the Nusselt number for CHX1, HHX and CHX2, and for all edge shapes (Figure 6.13) is entirely reasonable given that the heat exchangers are of the same configuration, i.e. the plate thickness, spacing and length, and edge shape. The Nu largely reflects the physics correctly. The Nu increases with drive ratio for all edge shapes, and again, the blunt edge shape has the highest Nu . The increase in the Nu is rapid for all edge shapes at drive ratio below 0.65% and becomes weak and gradual at $DR > 0.7\%$. This behaviour agrees well with the description available in the literature and the thermoacoustics design guidelines (c.f. Swift, 2001).

6.9 Effect of edge shape on acoustic pressure drop

Figure 6.14a-c shows the pressure drop due to minor losses across CHX1, HHX, and CHX2. Data is sampled at locations $x = 4244$ mm, $x = 4276$ mm, $x = 4308$ mm, and $x = 4340$ mm, as indicated by points 1, 2, 3, and 4 in Figure 6.1b. Δp_{12} , Δp_{23} and Δp_{34} refer to the pressure drop across CHX1, HHX and CHX2, respectively, and are measured as a function of time, normalised by the period of oscillation, i.e. $T_p = 1/f$. Clearly, from the plots (Fig. 6.14a-c), the cone-edge shape minimised the pressure drop better than the other edge shapes. As previously explained, this would be desirable for the thermoacoustic devices as long as the heat transfer performance of the heat exchanger is not adversely affected. At $0.3 < DR < 0.65\%$, the effect of edge shape on the pressure drop is less pronounced, which is like what was observed in the vorticity plots at $DR = 0.3\%$ in the previous section. In Figure 6.14(a), the peaks of the pressure drop are present at $0 < t/T < 0.3$ in the suction phase of the acoustic cycle for drive ratio higher than 0.3%. As the DR increases, the distortion in the pressure drop profile becomes increasingly significant due to the increasing effect of minor losses created by a sudden decrease in the cross section. Under this condition, the cone-edge shape consistently exhibits a lower pressure drop than other edge shapes. The influence of the edge shape on the pressure drop shows a strong dependency on the drive ratio and flow direction. Also, the influence of symmetrical arrangement of the heat exchangers can easily be inferred (Figure 6.14a-c). At $0.3 < t/T < 0.5$, the acoustic pressure drop has reduced, and the cone-edge still has the lowest pressure drop. When the flow enters the ejection phase ($0.5 < t/T < 1$) the pressure drop is at its lowest for all edge shapes.

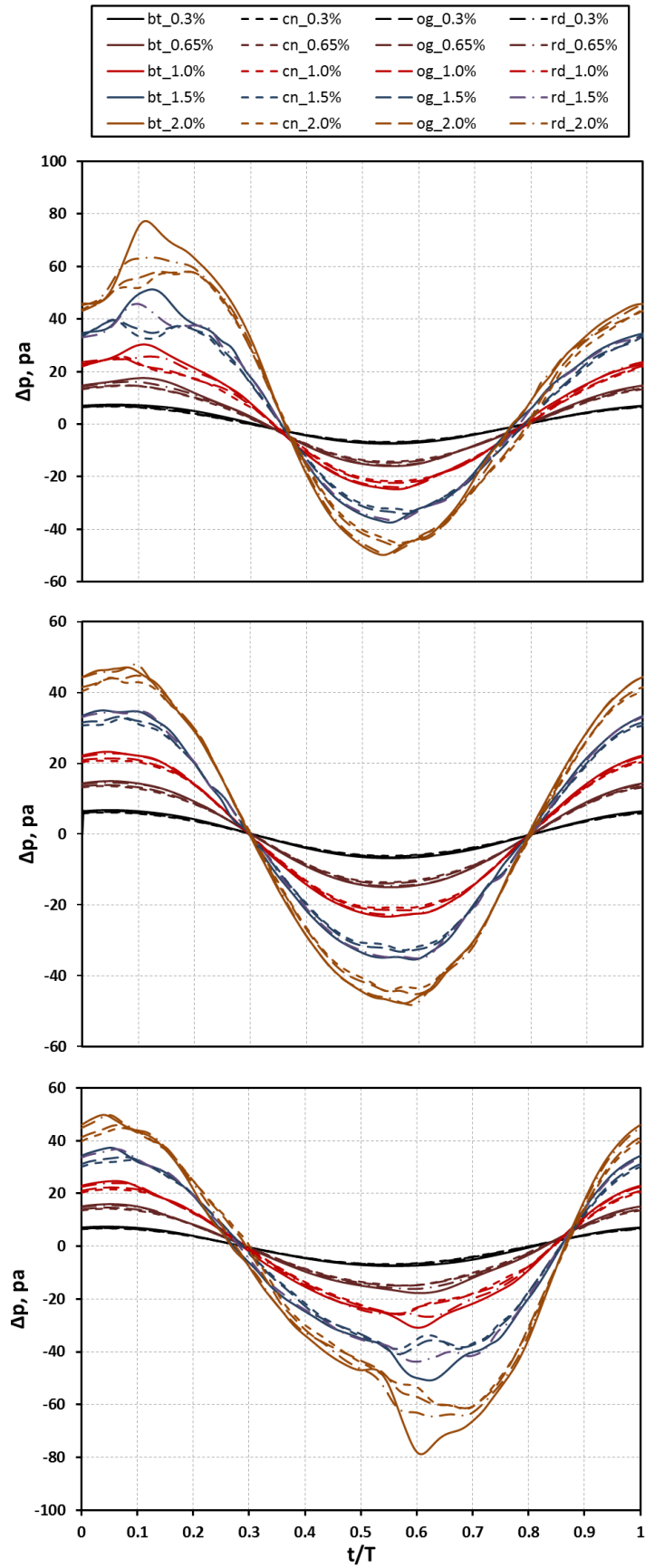


Figure 6.14: Acoustic pressure drop versus t/T for all the edge shapes (blunt, cone, ogive, and round) at $0.3 \leq DR \leq 2.0\%$ (a) CHX1, (b) HHX, (c) CHX2.

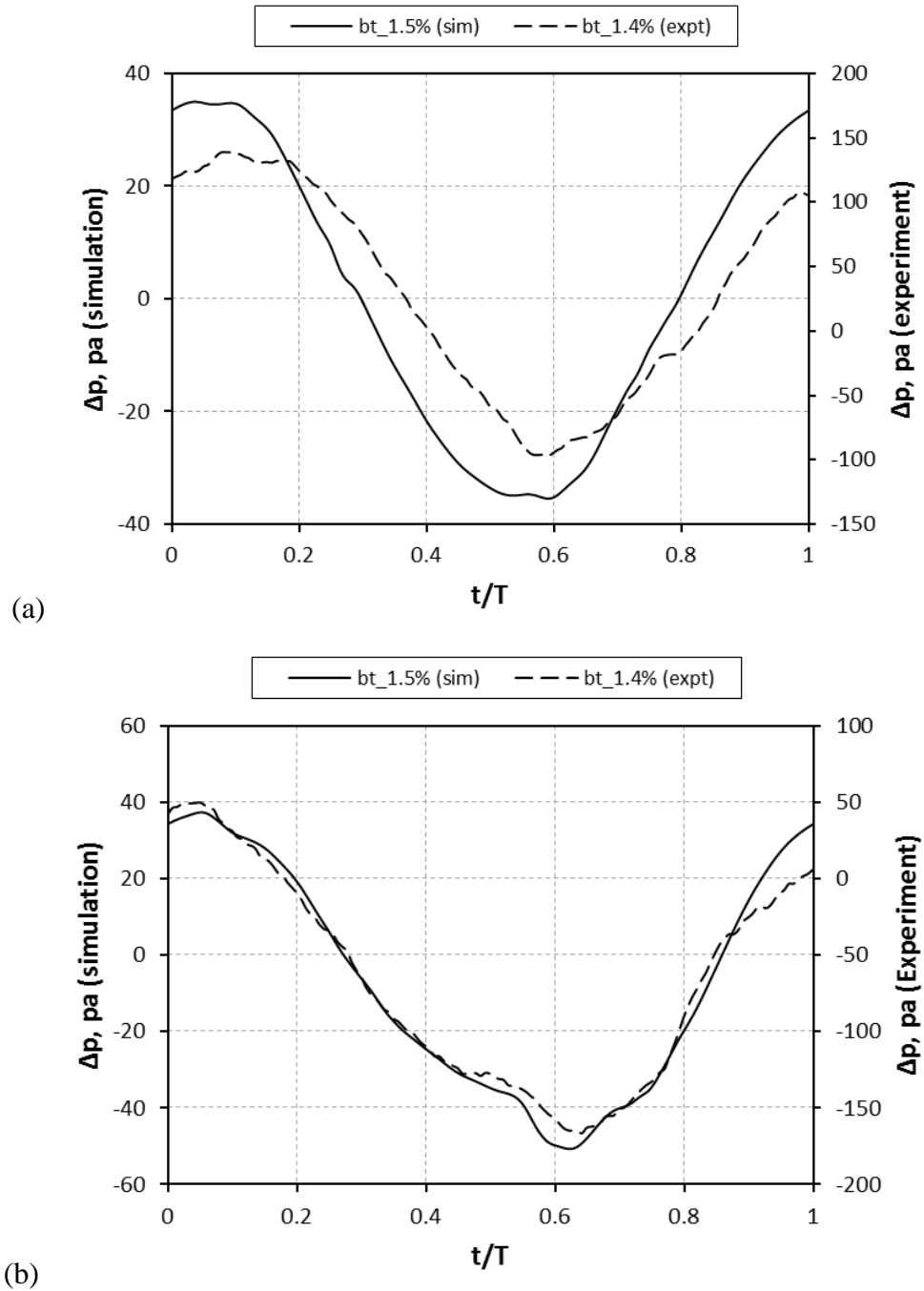


Figure 6.15: Comparison of experimental and numerical acoustic pressure drop versus of t/T for blunt edge shape at $P_m = 1$ bar, $DR = 1.4\%$ (Experiment) and $DR = 1.4\%$ (simulation) across (a) HHX (b) CHX2.

Figure 14b shows the pressure drop across HHX. In the suction stage ($0 < t/T < 0.5$), the distortion in the pressure drop is less pronounced compared to that of CHX1 in a similar stage. The magnitude of pressure drop remains almost the same between the ejection stage of CHX1 and suction stage of HHX. Similar behaviour is observed when the flow exits HHX and enters CHX2 as shown in the Figure 6.14c. However,

during the ejection stage in CHX2 at $0.5 < t/T < 1$, the sudden increase in the cross section significantly increases the acoustic pressure drop as previously observed during the suction stage of CHX1.

The cone-edge minimised the pressure drop across the heat exchangers compared to the other edge shapes. It is noteworthy that the acoustic pressure drop may depend on the sampling location; however, since the same locations are used for the comparison of the edge shape effect, the plots thus reflect the real contribution of individual edge shape to the minimisation of pressure drop across the three heat exchangers.

In Figure 6.15, the comparison between the experimental and simulation results are shown for the acoustic pressure drop across the HHX and CHX heat exchangers. The blunt edge shape is used for the comparison in both experiment and simulation. There is a qualitative agreement between the pressure drops across HHX and CHX for the two results. The trends in both plots (Figure 6.15a and b) are similar, and the distortions caused by the sudden change in the cross-section and edge profile are present in both cases. However, the magnitude of the pressure drop from the experiment is considerably higher than that of the simulation. This difference is as high as more than a factor of two at both the suction and ejection stage ($0 < t/T < 0.5 < 1$), for the maximum pressure drop in the flow cycle for HHX and CHX. As remarked in the previous section, this significant discrepancy in the measured and predicted values of acoustic pressure drop may be attributed to the difference in geometry and the presence of a three-dimensional effect in the flow.

6.10 Summary

The effect of edge shape on the heat transfer and acoustic pressure drop in the heat exchanger under oscillatory flow conditions has been investigated numerically, and the results have been validated experimentally and analytically. The investigation was carried out with respect to the drive ratio in the system over the range of $0.3 \leq DR \leq 2.0\%$ within a flow cycle of $0 \leq t/T \leq 1$ for four different edge shapes – blunt, cone, ogive and round. It was found that heat transfer and acoustic pressure drop of the heat exchangers show a strong dependency on the drive ratio for the edge shapes that are studied. Each edge shape shows a different level of influence on the heat transfer conditions and the acoustic pressure drop across the heat exchangers.

Chapter 7

Conclusions and Future Work

7.1 Conclusions

This study has investigated the heat transfer and acoustic pressure drop performance of T-HEX, F-HEX and parallel plate heat exchanger, in oscillating flow under different operating conditions. The investigation covers both experimental and numerical approaches. The geometric consideration includes the effects of edge shape on the heat exchanger performance.

In consideration of the objectives highlighted in section 1.3, objectives (1) - (3) have been achieved through the study presented in Chapter 3 and Chapter 4. An experimental setup and measurement technique has been developed for the characterisation of heat exchanger performance in oscillatory flow. The developed technique allowed simultaneous collection of temperature and pressure amplitude data for further analysis of heat transfer and pressure drop on symmetrically arranged compact heat exchangers, as anticipated at the design phase. Experiments were carried on Tube-Heat-Exchangers (T-HEX) with squared-edge ($r = 0$) and ogive edge shape ($r = 7$). Similarly, experiments were also carried out on Finned-Heat-Exchangers (F-HEX) with a flat edge ($r = 0$) and ogive edge ($r = 2$). The effect of drive ratio and mean pressure was tested on the heat transfer performance of the two heat exchanger configurations. The geometric design of F-HEX, however, limits the maximum obtainable drive ratio (within the safe zone for the acoustic driver) to 0.9% against that of T-HEX that reached 1.8%.

The heat transfer rates on the heat exchanger set were obtained on CHX1, HHX and CHX2 for the two configurations of heat exchangers and the edge shapes. The DR and mean pressure was found to influence the heat transfer rates, which shows rapid increases at $DR < 0.6\%$ and gradually become less rapid as the displacement amplitude becomes larger in comparison with the exchanger length. The increase/decrease of drive ratio reflects the increase/decrease of displacement amplitude. For effect of the mean pressure of the system, the heat transfer rates show an increasing trend at ($0.07 < DR < 1.52\%$) for T-HEX (flat). For the T-HEX

(ogive), the increase is rapid between 1 to 3bar after which it starts to become less pronounced noticeably at a drive ratio higher than 0.3%. F-HEX (flat) and F-HEX (ogive) was found to show similar behaviour to that of T-HEX (ogive).

Based on the heat transfer rates, the heat transfer performance of the heat exchanger was presented in terms of the Nusselt number. The Nusselt number shows dependency on the drive ratio for T-HEX (flat), T-HEX (ogive), F-HEX (flat), and F-HEX (ogive). The Nusselt number increases rapidly at $0.08 < DR < 0.6\%$, after which there was a steady rise for the remaining range of DR . Additionally, the Nusselt number shows dependency on the mean pressure of the system. The comparison of Nusselt number values on T-HEX (flat) and T-HEX (ogive) at different mean pressures, with other models and correlations, reveals that the current heat transfer performance of heat exchangers is within the range of heat transfer reported elsewhere.

Objective (4) has been met through the study presented in Chapter 5. A 3D numerical model has been developed to evaluate the heat transfer and acoustic pressure drop on heat exchanger in oscillatory flow. The developed 3D model on T-HEX (flat and ogive) utilised the experimental data as the thermal and acoustic initial and boundary conditions and for validation of the simulation result. Good agreement between the numerical and experimental results was achieved.

The effect of edge shape on the performance of heat exchanger was studied with respect to the drive ratio. The effect of edge shape was determined by comparing the performance of T-HEX (ogive) with that of T-HEX (flat) configuration. Acoustic pressure drop and heat transfer results reveal that both the Nusselt number and pressure drop depend strongly on drive ratio. Furthermore, the pressure drop shows dependency on the acoustic flow direction.

It was observed that the presence of profile edge shape causes a slight adverse reduction in the heat transfer performance of T-HEX as represented in terms of Nu . However, this adverse reduction tends to diminish gradually as the drive ratio is increasing.

The increase in the drive ratio resulted in an increase in acoustic pressure drop. This increase in pressure drop, however, was minimised by as high as 51% at the highest drive ratio in this study (1.29%). The favourable minimisation of acoustic pressure

drop increases as the drive ratio increases, which is quite encouraging considering that the practical thermoacoustic device operates at high amplitudes.

Objective (5) was achieved through the results presented in Chapter 6. A 2D numerical model was developed based on a parallel plate heat exchanger. The effect of four different edge shapes (blunt, cone, ogive and round) on the heat transfer and acoustic pressure drop in oscillatory flow was investigated numerically, and the results have been validated experimentally and analytically.

The investigation was carried out with respect to the drive over the range of $0.3 \leq DR \leq 2.0\%$ within a flow cycle of $0 \leq t/T \leq 1$ for the edge shapes. It was found that heat transfer and acoustic pressure drop of the heat exchangers shows a strong dependency on the drive ratio for all the edge shapes that are studied. Each edge shape shows a different level of influence on the heat transfer conditions and the acoustic pressure drop across the heat exchangers.

For the heat transfer, it was found that blunt edge and round edge shapes behave very similarly. They both have Nusselt number values that are higher than those of cone-edge and ogive edge. The wall heat fluxes and the Nusselt number increases with the increase in drive ratio for all edge shapes. The increase is rapid until $DR = 0.7\%$ and slows down after that. Furthermore, it was found that the thermal potential for the heat transfer coefficient can be defined to reflect the contribution of the gas temperatures near the channel inlet and exit, to the overall heat transfer performance of heat exchangers.

In terms of acoustic pressure drop Δp , cone-edge consistently gives a lowest acoustic pressure at all drive ratios, but more noticeably at the higher drive ratios $1.0 \leq DR \leq 2.0$ in the region of $0 < t/T < 0.3$ for CHX1 and $0.5 < t/T < 0.8$ for CHX2. Again, this is kind of interesting, since thermoacoustic devices operate at high drive ratio.

Objective (6) has been achieved through the entire chapters in this thesis. The sequential connection has been made between each chapter of the thesis to provide an understanding of the heat transfer and acoustic pressure drop in oscillatory flow based on experimental and numerical considerations.

7.2 Findings of the study

In summary, the key findings in this work include:

1. That the symmetrical arrangement facilitated accurate heat transfer estimation, which further led to the ‘discovery’ that the thermal potential for the heat transfer coefficient will be correctly defined in oscillatory flow if the average of temperature measurement between the gas channel inlet and outlet of the heat exchanger is taken into consideration.
2. That the use of profile edge shape can be explored to favourably minimise the acoustic pressure drop, to improve the overall efficiency of the thermoacoustic system. This is quite encouraging considering that the practical thermoacoustic device operates at high amplitudes.

7.3 Future works

7.3.1 Experimental study

1. The effect of spacing between two adjacent heat exchangers can be explored to determine the influence on the heat transfer and acoustic pressure drop performance of different configuration of heat exchangers. The gap between two heat exchangers is an important parameter that may affect the heat transfer performance. The current experimental set-up could be easily adjusted to allow this study.
2. In the current study, pure helium gas was used as the working gas due to its low viscosity and low Prandtl number compared to other noble gases. It has been reported elsewhere that the performance of thermoacoustic devices increases with the decrease of the Prandtl number. Gas mixtures such as helium-argon, helium-krypton, and helium-xenon can be used to achieve a lower Prandtl number. It would be useful to conduct experimental studies to determine the effect of such gas mixtures on the heat transfer and acoustic pressure drop performance in oscillatory flow.
3. The work of this thesis can be extended by implementing the PIV and PLIF techniques to gain insights into the temperature distribution and fluid flow velocity field under oscillatory flow conditions. Also, velocity measurement

in the test rig can be achieved using hot-wire anemometry which can be easily introduced in the existing set-up.

4. As the results of the current study suggest, heat transfer in oscillatory flow is influenced by the operating parameters such as drive ratio and mean pressure. To further investigate the heat transfer phenomena in oscillatory flow conditions, additional work should be conducted for the operating conditions that cover the range of the current experiment, such as the effect of different water flow rates on heat transfer performance.

7.3.2 Numerical study

The 3D dimensional simulation model developed in the current study represents a very useful attempt of modelling the heat exchanger in oscillatory flow. The 3D simulation models were based on actual heat exchanger geometry, which somewhat comes with the requirement of huge computational time and effort.

1. To facilitate the investigation of a wide range of operating and geometric parameters on heat transfer and acoustic pressure drop in oscillatory flow, the geometry in the 3D simulation needs not be modelled in full. The use of symmetry can be explored where it can give an adequate representation of the desired heat transfer and fluid flow phenomenon. This would allow the coverage of a large range of operating conditions that could not be covered in the current study.
2. An attempt to model the Finned-Heat Exchanger using symmetry approach should be considered. Furthermore, only the ogive-edge shape is investigated experimentally and in the 3D simulation. The edge shapes that are seen in the 2D models can be explored in the 3D model to establish further the possibility of using edge shapes for the improvement of the overall efficiency of the thermoacoustic system. Furthermore, the optimal curvature of the ogive-edge shape needs to be determined through optimisation study.
3. Only one turbulent model has been considered in the current study for the 3D simulation. To bring the magnitude of heat flux closer to the experiment or achieve better agreement between predicted and experimental results, different turbulent models should be employed in the 3D simulation study.

List of References

- Aben, P.C.H., P.R. Bloemen, and J.C.H. Zeegers, 2-D PIV measurements of oscillatory flow around parallel plates. *Experiments in Fluids*, 2008. 46(4): p. 631-641.
- Adams, T. M. 2002. *Guide for Estimation of Measurement Uncertainty in Testing (G104-A2LA)*: Maryland, USA: American Association of Laboratory Accreditation.
- Adeff Jay A., H.T.J., Design and construction of a solar powered, thermoacoustically driven, thermoacoustic refrigerator. *J. Acoust. Soc. Am.*, 2000. 107(6).
- ANSYS Fluent 14.5.7, 2013, "User Manual," ANSYS Inc.
- Arnott W. P., Belcher J. R., Raspet R., Bass H. E., 1994. Stability analysis of a helium-filled thermoacoustic engine. *Journal of Acoustical Society of America*, 96(1).
- Backhaus, S. and G.W. Swift, 2000. A thermoacoustic-Stirling heat engine: Detailed study. *Journal of Acoustical Society of America*, 107(6): p. 3148-3166.
- Belcher, J.R., et al., 1999. Working gases in thermoacoustic engines. *Journal of Acoustical Society of America*, 105(5): p. 2677-2684.
- Bell S., 2001. *Measurement good practice guide: A Beginner's Guide to Uncertainty of Measurement*. Middlesex, United Kingdom: National Physical Laboratory
- Berson A., Poignand G., Blanc-Benon P., Comte-Bellot G., 2011. Nonlinear temperature field near the stack ends of a standing wave thermoacoustic refrigerator. *International Journal of Heat and Mass Transfer* 54 (2011) 4730–4735
- Besnoin, E. and O.M. Knio, 2004. Numerical Study of Thermoacoustic Heat Exchangers. *Acta Acustica United with Acustica*, 90(3): p. 432-444.

Brady J. F, The effects of Geometry and Adjacent Regenerators on Shell-And-Tube Heat Exchangers in Oscillatory Flows. PhD thesis, The Pennsylvania State University, 2011

Brewster J. R., Raspet R., and Bass H. E., 1997. Temperature discontinuities between elements of thermoacoustic devices. *J. Acoust. Soc. Am.* Vol 102, (6), pp. 3355-3360.

Ceperley P.H, 1979. A pistonless Stirling engine – The traveling wave heat engine. *J. Acoust. Soc. Am.* 66(5), p. 1508-1513

Dieck, R. H., Steele, W. G. and Osolsobe, G. 2005: Test Uncertainty. ASME PTC 19.1-2005. New York: The American Society of Mechanical Engineers.

Al-Damook, A., Kapur, N., Summers, J.L., Thompson, H.M. 2015. An experimental and computational investigation of thermal air flows through perforated pin heat sinks. *Applied thermal engineering* 89,365 – 376

Fu, H.L., et al., 2001. An Experimental Study of Heat Transfer of a Porous Channel Subjected to Oscillating Flow. *Journal of Heat Transfer*, 123(1): pp. 162.

Fusco Andrew M., Ward William C., and S.G. W., 1992. Two-sensor power measurements in lossy ducts. *Acoustical Society of America*, 91(4).

Gardner, D.L. and G.W. Swift, 2003. A cascade thermoacoustic engine. *The Journal of the Acoustical Society of America*, 114(4): p. 1905

Garrett, S.L., 2004. Resource Letter: TA-1: Thermoacoustic engines and refrigerators. *American Journal of Physics*, 72(1): p. 11.

Garrett. S.L., Perkins D.K., and G. A., 1994. Thermoacoustic Refrigerator Heat Exchanger- Design, Analysis and Fabrication. *Proc. of the Tenth International Heat Transfer Conference*, Brighton, UK

Gopinath Ashok and H.D. R., 2000. An experimental study of heat transfer from a cylinder in low amplitude zero-mean oscillatory flows. *International Journal of Heat and Mass Transfer*, 43: p. 505-520.

Gu C., Zhou Y., Wang J., Ji W., Zhou Q., 2012. CFD analysis of nonlinear processes in pulse tube refrigerators: Streaming induced by vortices. *International Journal of Heat and Mass Transfer* 55. 7410–7418

Herman, C. and Y. Chen, 2006. A Simplified Model of Heat Transfer in Heat Exchangers and Stack Plates of Thermoacoustic Refrigerators, *Heat Mass Transfer* 42, 901-917

Incropera, F. P., DeWitt, D. P., Bergman, T. L., and Lavine, A. S., 2007, *Fundamentals of Heat and Mass Transfer*, 6th ed., John Wiley and Sons, New York

Ilori, O.M., Mao X., Jaworski A.J. CFD-Simulation of Oscillatory Flow Around the Heat Exchangers of Thermoacoustic Devices. *Proceedings of the 2014 International Mechanical Engineering Congress & Exposition, IMECE2014*, November 14-20, 2014, Montreal, Quebec, Canada

Jaworski A. J., Mao X., Yu Z., 2009. Entrance effects in the channels of the parallel plate stack in oscillatory flow conditions. *Experimental Thermal and Fluid Science*, 33(3): p. 495-502.

Jaworski A. J., Piccolo A., 2012. Heat transfer processes in parallel-plate heat exchangers of thermoacoustic devices-numerical and experimental approaches. *Applied Thermal Engineering*. Vol. 42, pp. 145-153

Kamsanam W, Mao X., and Jaworski A. J., 2015, Development of experimental techniques for measurement of heat transfer rates in heat exchangers in oscillatory flows. *Experimental Thermal and Fluid Science* 62, 202–215

Kamsanam W, Mao X., and Jaworski A. J., 2016. Thermal performance of finned-tube thermoacoustic heat exchangers in oscillatory flow conditions. *International Journal of Thermal Sciences* 101, 169-180

Maidment, D. R., 1993. *Handbook of Hydrology*. New York: McGraw-Hill.

Marx David, Bailliet Helene, and V. Jean-Christophe, 2008. Analysis of acoustic flow at abrupt change in section of waveguide using Particle Image Velocimetry and Proper Orthogonal Decomposition. *Acta Acustica United with Acustica*, 94: p. 54-65.

McQuiston, F. C., and Parker, J. D., 1994, Heating, Ventilating, and Air-Conditioning Analysis and Design, John Wiley and Sons, New York.

Menter, F. R., 1994, "Two-Equation Eddy-Viscosity Turbulence Models for Engineering Applications," AIAA Journal, 32(8), pp. 1598-1605.

Merlki P., and Thomann, H., 1975, "Transition in Oscillating Pipe Flow," Fluid Mech., 68(3), pp. 567-575.

Moffat, R. J. 1988. Describing the Uncertainties in Experimental Results. Experimental Thermal and Fluid Science, 1(1), pp. 3-17

Mohd Saat F. A., 2013. Numerical Investigations of Fluid Flow and Heat Transfer Processes in the Internal Structures of Thermoacoustic Devices, PhD Thesis, University of Leicester.

Mohd Saat, F.A.Z. and A.J. Jaworski, CFD Modelling of Flow and Heat Transfer within the Parallel Plate Heat Exchanger in Standing wave Thermoacoustic System. 19th International Conference of Sound and Vibration, 08-12, Lithuania, Vilnius, 2012.

Morris, P. J., Boluriaan, S., and Shieh, C. M., 2004, "Numerical Simulation of Minor Losses Due to a Sudden Contraction and expansion in High Amplitude Acoustic Resonators," ACTA Acustica United with Acustica, 90, pp. 393-409

Mozurkewich G., 1998. A model for transverse heat transfer in thermoacoustics. Journal of the Acoustical Society of America 103 (6), pp. 3318-3326

Mozurkewich G., 2001. Heat transfer from transverse tubes adjacent to a thermoacoustic stack. Journal of Acoustical Society of America. Vol. 110 (2), pp. 841-847.

Myer Kutz, 2006, Heat transfer calculations, McGraw-Hill Pvt Limited, India

Nijeholt J.A., Tijani M.E.H., Spoelstra S., 2005. Simulation of a traveling-wave thermoacoustic engine using computational fluid dynamics. Journal of Acoust. Soc. Am. 118 (4), pp. 2265 - 2270

Nsofor, E.C., S. Celik, and X. Wang, 2007. Experimental study on the heat transfer at the heat exchanger of the thermoacoustic refrigerating system. *Applied Thermal Engineering*, 27(14-15): p. 2435-2442.

Olson J.R. and S. G.W., 1997. Acoustic streaming in pulse tube refrigerators-tapered pulse tubes. *Cryogenics* 37 (12).

Omega Engineering (2016) Type-K thermocouple reference table. Accessed 06/09/2016 <http://www.omega.com/temperature/Z/pdf/z204-206.pdf>

Paek I., Braun J. E., and Mongeau L., 2005. Characterizing heat transfer coefficients for heat exchangers in standing wave thermoacoustic coolers. *Journal of Acoustical Society of America*. Vol. 118, iss. 4, pp. 2271-2280.

Petculescu, G. and Wilen, L. A., 2002. Traveling-wave amplification in a variable standing wave ratio device *Acoustics Research Letters Online*, 3, 71-76

Piccolo, A. 2011: Numerical computation for parallel plate thermoacoustic heat exchangers in standing wave oscillatory flow. *International Journal of Heat and Mass Transfer*, 54(21-22), pp. 4518-4530.

Piccolo, A. and G. Pistone, 2006. Estimation of heat transfer coefficients in oscillating flows: The thermoacoustic case. *International Journal of Heat and Mass Transfer*, 49(9-10): p. 1631-1642.

Qiu L.M., Lai B.H., Li Y.F., Sun D.M., 2012. Numerical simulation of the onset characteristics in a standing wave thermoacoustic engine based on thermodynamic analysis. *International Journal of Heat and Mass Transfer* 55 (2012) 2200–2203

Richardson, M.J. Specific heat capacities. Accessed 05/07/2016 http://www.kayelaby.npl.co.uk/general_physics/2_3/2_3_6.html

Roache, P. J., 1994. Perspective: A Method for Uniform Reporting of Grid Refinement Studies. *Transactions-American Society of Mechanical Engineers, Journal of Fluids Engineering*, 16, pp. 405-405.

Rott N., 1980. Thermoacoustics, *Advances in Applied Mechanics*. Vol. 20, pp. 135-175.

Shi, L., X. Mao, and A.J. Jaworski, 2010. Application of planar laser-induced fluorescence measurement techniques to study the heat transfer characteristics of parallel-plate heat exchangers in thermoacoustic devices. *Measurement Science and Technology*, 21(11): p. 115405.

Spoor, P.S. and G.W. Swift, 2000. Thermoacoustic Separation of a He-Ar Mixture. *Physical Review Letters*, 85(8): p. 1646-1649.

Swift G. W., Keolian R. M., 1993. Thermoacoustics in pin-array stacks. *J. Acoust. Soc. Am.* 94 (2), pp. 941-943

Swift, G.W., Thermoacoustic engines *Journal of Acoustical Society of America*, 1988. 84(4).

Swift, G.W., Thermoacoustics: A unifying perspective for some engines and refrigerators. Los Alamos National Laboratory, 2001(Fifth draft, LA-UR 99-895).

Tang K., Yu J., Jin T., Wang Y.P., Tang W.T., Gan Z.H., 2014. Heat transfer of laminar oscillating flow in finned heat exchanger of pulse tube refrigerator, *International Journal of Heat and Mass Transfer* 70 (2014) 811–818

Tang, K., Yu, J., Jin, T. and Gan, Z. H. 2013. Influence of compression expansion effect on oscillating-flow heat transfer in a finned heat exchanger. *Journal of Zhejiang University-SCIENCE A (Applied Physics and Engineering)*, 14(6), pp. 427-434.

Tijani M.E.H., Z.J.C.H., de Waele A.T.A.M., 2002. Design of thermoacoustic refrigerators. *Cryogenics* 42 p. 49–57.

Tijani, M.E.H. and S. Spoelstra, 2011. A high performance thermoacoustic engine. *Journal of Applied Physics*, 110(9): p. 093519.

Versteeg, K. and Malalasekera,W., 2007. *An Introduction to Computational Fluid Dynamics. The Finite Volume Method*, 2nd edition, England: Pearson Education Limited, Chap. 3.

Wagner, W. and Pru, A. The IAPWS Formulation 1995 for the Thermodynamic Properties of Ordinary Water Substance for General and Scientific Use, *Journal of Physical and Chemical Reference Data*, 31, 387-535 (2002)

Wakeland, R.S. and R.M. Keolian, 2002. Influence of velocity profile non-uniformity on minor losses for flow exiting thermoacoustic heat exchangers (L), *The Journal of the Acoustical Society of America*, 112(4): pp. 1249 – 1252.

Wakeland, R.S. and R.M. Keolian, 2004. Measurements of the resistance of parallel-plate heat exchangers to oscillating flow at high amplitudes. *The Journal of the Acoustical Society of America*, 115(5), pp. 2071.

Wakeland R. S., and Keolian R. M., 2004. Calculated effects of pressure-driven temperature oscillations on heat exchangers in thermoacoustic devices with and without a stack. *J. Acoust. Soc. Am.* Vol. 116, iss. 1, pp. 294-302.

Worlikar A. S., and Knio O. M., 1996. Numerical simulation of a thermoacoustic refrigerator I. Unsteady adiabatic flow around the stack. *Journal of Computational Physics*. Vol. 127, pp. 424-451.

Worlikar A. S., Knio O. M, and Klein R., 1998. Numerical simulation of thermoacoustic refrigerator II. Stratified flow around the stack. *Journal of Computational Physics*. Vol. 144, pp. 299-324.

Yazaki, T., Iwata, A., Maekawa, T. and Tominaga, A., 1998. Traveling Wave Thermoacoustic Engine in a Looped Tube. *Physical Review Letters* 81(15), 3128-3131.

Yazaki, T., Tominaga, A. and Narahara, Y., 1980. Experiments on thermally driven acoustic-oscillations of gaseous helium. *Journal of Low Temperature Physics*, 41(1-2), pp. 45-60.

Yu, Z. and Jaworski A.J., 2010. Impact of acoustic impedance and flow resistance on the power output capacity of the regenerators in travelling wave thermoacoustic engines. *Energy Conversion and Management*, 51(2): p. 350-359.

Zhao T., and Cheng P., 1995. A Numerical Solution of Laminar Forced Convection in a Heated Pipe Subjected to a Reciprocating Flow, *International Journal of Heat and Mass Transfer* 38(16), 3011-3022

Zhao T. S. and Cheng P., 1996. Oscillatory heat transfer in a pipe subjected to a laminar reciprocating flow. *Journal of Heat Transfer-Transactions of the ASME*, 118(3), pp. 592-597.

Zhao T.S., and Cheng P, Heat transfer in oscillatory flows, in: C.-L. Tien (Ed.), *Annual Review of Heat Transfer*, vol. IX, 1998 (Chapter 7).

Zink F., Viperman J.S., Schaefer L. A. Advancing Thermoacoustics through CFD Simulation Using Fluent, *Proceedings of ASME International Mechanical Engineering Congress and Exposition, USA (2008)*

Zoontjens L., Howard C.Q., Zander A.C., Cazzolato B.S., 2009. Numerical study of flow and energy fields in thermoacoustic couples of non-zero thickness. *International Journal of Thermal Sciences* 48 (2009) 733–746

Zukauskas, A. 1972. Heat transfer from tubes in crossflow. *Advances Heat Transfer*, 8, Academic Press, New York.

Nomenclatures

A	Area	$[\text{m}^2]$
a	Speed of sound	$[\text{m/s}]$
C	Compliance	$[\text{m}^3/\text{Pa}]$
COP	Carnot coefficient of performance $(T_C/T_H - T_C)$	$[-]$
c_p	Specific heat capacity	$[\text{J/kg}\cdot\text{K}]$
DR	Drive ratio (p_o/p_m)	$[-]$
D	Diameter	$[\text{m}]$
d, y	Plate spacing	$[\text{m}]$
f	Frequency	$[\text{Hz}]$
$f_{k,v}$	Spatially averaged thermo-viscous function	$[-]$
h	Heat transfer coefficient	$[-]$
$h_{k,v}$	Thermo-viscous function	$[-]$
i	$\sqrt{-1}$	$[-]$
	i th	$[-]$
j_c	Colburn-j factor $(j_c = Nu/RePr^{1/3})$	$[-]$
K	Minor loss coefficient	$[-]$
k	Thermal conductivity	$[\text{W/m}\cdot\text{K}]$
k'	Wave number	$[\text{rad/m}]$
L, l	Length	$[\text{m}]$
\dot{M}_2	Second-order time averaged mass flux	$[\text{kg/s}\cdot\text{m}^2]$
\dot{m}	Mass flow rate	$[\text{kg/s}]$
N, n	Sample number	$[-]$

Nu	Nusselt number ($Nu = hD_h / k$)	[-]
P	Pressure	[Pa]
p	Oscillating pressure	[Pa]
Pr	Prandtl number ($Pr = \mu c_p / k$)	[-]
\dot{Q}	Heat transfer rate	[W]
q	Heat flux	[W/m ²]
R	Gas constant	[J/kg·K]
Re	Reynolds number, ($Re = \rho u D_h / \mu$)	[-]
r	Radius	[m]
r_h	Hydraulic radius	[m]
T	Temperature	[K, °C]
T_p	Acoustic period	[s]
t	Time	[s]
t_p	Plate thickness	[m]
U	Volumetric flow rate	[m ³ /s]
u	Acoustic velocity in x direction	[m/s]
V	Volume	[m ³]
	Voltage	[V]
\mathbf{v}	Velocity vector	[m/s]
Va	Valensi number ($Va = \rho_m \omega D_h^2 / \mu$)	[-]
\dot{W}	Acoustic power	[W]
x	Distance in x -direction (axial location)	[m]
y_0	Half of the plate spacing	[m]

Greek letters

β	Thermal expansion coefficient	[K ⁻¹]
γ	Ratio of isobaric to isochoric specific heats	[-]
Δ	Difference	[-]
	Distance	[m]
δ	Penetration depth	[m]
ε	Heat transfer effectiveness	[-]
κ	Thermal diffusivity	[m ² /s]
η	Efficiency	[%]
λ	Wavelength	[m]
μ	Dynamic viscosity	[kg/m·s]
ν	Kinematic viscosity	[m ² /s]
ξ	Gas displacement amplitude	[m]
Π	Perimeter	[m]
π	3.14159	[-]
ρ	Density	[kg/m ³]
σ	Porosity	[-]
σ'	Viscous stress tensor	[Pa]
ϕ	Phase angle	[°]
θ	Normalised temperature	[-]
φ	Scalar variable	[-]
φ'	Fluctuating component of scalar variable	[-]
ω	Angular frequency	[rad/s]

Subscripts

A	Location A
B	Location B

<i>a</i>	Ambient
<i>al</i>	Aluminium
<i>C</i>	Cold
	Cross-sectional area
<i>c1,c2</i>	Cold heat exchangers 1 and 2
<i>crit</i>	Critical
<i>e</i>	Engine
<i>eff</i>	Effective
<i>f</i>	Fin
	Flow
<i>fr</i>	Frontal
<i>g</i>	Gas
<i>H,h</i>	Hot
<i>hx</i>	Heat exchanger
<i>i,in,inlet</i>	Inlet
<i>in</i>	Insulation
<i>l</i>	Length
<i>loss</i>	Loss
<i>m</i>	Mean value
<i>mid</i>	Middle point
<i>max</i>	Maximum condition
<i>o,out,outlet</i>	Outlet
<i>perfect</i>	Perfect condition
<i>RES</i>	Resonator
<i>room</i>	Room
<i>s</i>	Surface

<i>sp</i>	Specific
<i>tot</i>	Total
<i>w</i>	Water
	Wall condition
κ	Thermal
<i>v</i>	Viscous
	Volume
<i>0</i>	Reference condition
<i>1</i>	First order of acoustic variable, Count
<i>2</i>	Second order of acoustic variable, Count
<i>2mic</i>	Two-microphone method

Special symbols

Im []	Imaginary part of
Re []	Real part of
$\langle \rangle$	Spatial average perpendicular to x
	Magnitude of complex number
∇	Spatial gradient, the vector differential operator
∂	Partial derivative
Overdot	Time derivative
Overbar	Time average
Tilde	Complex conjugate

Abbreviation

<i>bt</i>	Blunt
<i>CAD</i>	Computer Aided Design
<i>CFD</i>	Computational Fluid Dynamics

<i>CHX</i>	Cold Heat exchanger
<i>cn</i>	Cone
<i>DeltaEC</i>	Design Environment for Low-amplitude Thermoacoustic Energy Conversion
<i>F-HEX</i>	Finned-Heat Exchanger
<i>HHX</i>	Hot Heat exchanger
<i>HPC</i>	High Performing Computing
<i>LDS</i>	Laser Displacement Sensor
<i>LES</i>	Large Eddy Simulation
<i>LMTD</i>	Log-Mean Temperature Difference
<i>og</i>	Ogive
<i>PISO</i>	Pressure-Implicit with Splitting of Operators
<i>PIV</i>	Particle Image Velocimetry
<i>PLIF</i>	Planar Laser-Induced Fluorescence
<i>RANS</i>	Reynolds-averaged Navier-Stokes
<i>RC</i>	Curvature Radius
<i>RMS</i>	Random Mean Square
<i>RMSRe</i>	Random Mean Square Reynolds number
<i>RSM</i>	Reynolds Stress Model
<i>m</i>	Round
<i>SST</i>	Shear Stress Transport
<i>STD</i>	Standard deviation
<i>SWTE</i>	Standing wave thermoacoustic engine
<i>TASFE</i>	Time Averaged Steady Flow Equivalent
<i>T-HEX</i>	Tube Heat Exchanger
<i>TWTC</i>	Travelling wave thermoacoustic cooler
<i>UDF</i>	User-Defined Function

Appendix A

List of Publications

Olusegun M. ILORI, Xiaoan MAO, Artur J. JAWORSKI: Numerical Simulation of Oscillatory Flow and Heat transfer in the Heat Exchangers of Thermoacoustic Devices. *Proceedings of the 24th IIR International Congress of Refrigeration, ICR2015, August 16-22, 2015, Yokohama, Japan*

Olusegun M. ILORI, Xiaoan MAO, Artur J. JAWORSKI: CFD Study of Oscillatory Flow through 90 Degree Bends of Thermoacoustic Devices. *Proceedings of the 24th IIR International Congress of Refrigeration, ICR2015, August 16-22, 2015, Yokohama, Japan*

Olusegun M. ILORI, Xiaoan MAO, Artur J. JAWORSKI: CFD-Simulation of Oscillatory Flow around the Heat Exchangers of Thermoacoustic Devices. *Proceedings of the 2014 International Mechanical Engineering Congress & Exposition, IMECE2014, November 14-20, 2014, Montreal, Quebec, Canada*

Olusegun M. ILORI, Artur J. JAWORSKI, Xiaoan MAO: Numerical Analysis of the Heat Transfer in an Oscillatory Flow around the Heat Exchangers of Thermoacoustic Systems. *Proceedings of CHT-15 International Symposium on Advances in Computational Heat Transfer, May 25-29, 2015, Rutgers University, Piscataway, USA*

Ilori O.M., Mao X., Jaworski A.J.: Design of Thermoacoustic Rig for the Analysis of Thermal and Hydraulic Performance of Heat Exchangers in Oscillatory Flow. *Proceedings of the World Congress on Engineering 2013 Vol III, WCE 2013, July 3 - 5, 2013, London, U.K (Nominated for best paper award in the student category)*

Appendix B

First version of the test section

The description of first version of test rig as designed and fabricated is shown in this section. The design concept is a 'side entry' type for the heat exchanger installation and instrumentation connection on the process side. It was discarded on the order of Health and Safety office of the University of Leeds.

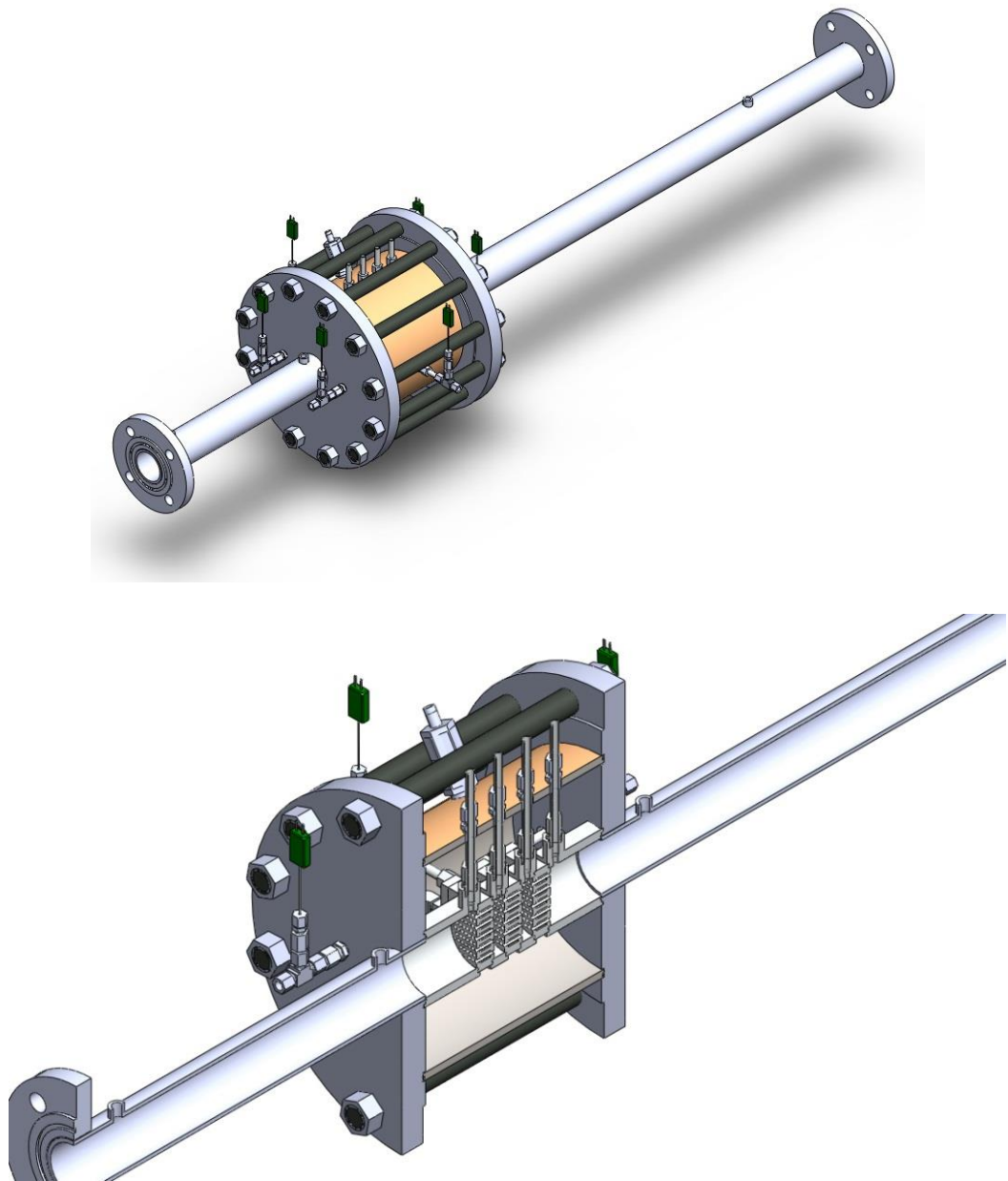


Figure A1: CAD-image of the first version of test section of the experimental set-up.

Appendix C

User-Defined-Function (UDF) code

The details of UDF code written in C language for use in ANSYS Fluent 17.0 are presented in here.

```
/***/Pressure boundary condition for the x1 and x2 in Figure 5.2***/
DEFINE_PROFILE (pressure_profile, thread, position)
{
    real x[ND_ND];
    real time;
    face_t f;
    time = RP_Get_Real("flow-time");

    begin_f_loop (f, thread)
    {
        F_CENTROID (x, f, thread);
        if (x [0]<0)
            F_PROFILE (f, thread, position) = 202.95*cos(336.778*time-0.65);
        else
            F_PROFILE (f, thread, position) = 138.41*cos(336.778*time+1.82);
    }
    end_f_loop (f, thread)
}

/***/ Gas property for Helium in equation (4.17) ***/
DEFINE_PROPERTY (mu1, c, t)
{
    real mu;
    real temp1=C_T (c, t);
    real t0=293.15;
    real b0=1.99e-05;
    real b_mu=0.68;
    mu=b0*pow (temp1/t0, b_mu);
    return mu;
}
/* following Swift, 2002 */

DEFINE_PROPERTY(k1,c,t)
{
    real k_1;
    real temp2=C_T(c,t);
    real t0=293.15;
    real b0=0.152;
    real bk=0.72;
    k_1=b0*pow(temp2/t0,bk);
}
```

```
        return k_1;                                /* following Swift, 2002 */
    }

/**** Vorticity, and variable gradients ****/

DEFINE_ON_DEMAND (vrt_diss_strg)
{
    Domain *d;
    Thread *t;
    cell_t c;
    real dpdx,dpdy,dTdx,dTdy;
    real a1,a2,a3,a4,b1,b2,b3,b4,vort,dissip;
    d=Get_Domain(1);
    thread_loop_c(t,d)
    {
        begin_c_loop(c,t)
        {
            dpdx=C_P_G(c,t)[0];
            dpdy=C_P_G(c,t)[1];
            dTdx=C_T_G(c,t)[0];
            dTdy=C_T_G(c,t)[1];
            a1=C_U_G(c,t)[0];          /* du/dx */
            a2=C_V_G(c,t)[1];          /* dv/dy */
            a3=C_V_G(c,t)[0];          /* dv/dx */
            a4=C_U_G(c,t)[1];          /* du/dy */
            b1=a1*a1;
            b2=a2*a2;
            b3=(a3+a4)*(a3+a4);
            b4=(a1+a2)*(a1+a2);
            vort=a3-a4;
            dissip=(2*(b1+b2))+b3-(2/3*b4);
            C_UDMI(c,t,0)=vort;
            C_UDMI(c,t,2)=dTdy;
            C_UDMI(c,t,3)=dTdx;
            C_UDMI(c,t,4)=dpdy;
            C_UDMI(c,t,5)=dpdx;
        }
        end_c_loop(c,thread)
    }
}
```

Appendix D

Calibration of PCB pressure transducers

In this appendix, the calibration of pressure transducers as discussed in Chapter 3 is presented. The serial number of each transducer is shown on the plot. The locations of pressure sensors are referenced as per the numbering in Figure 3.4.

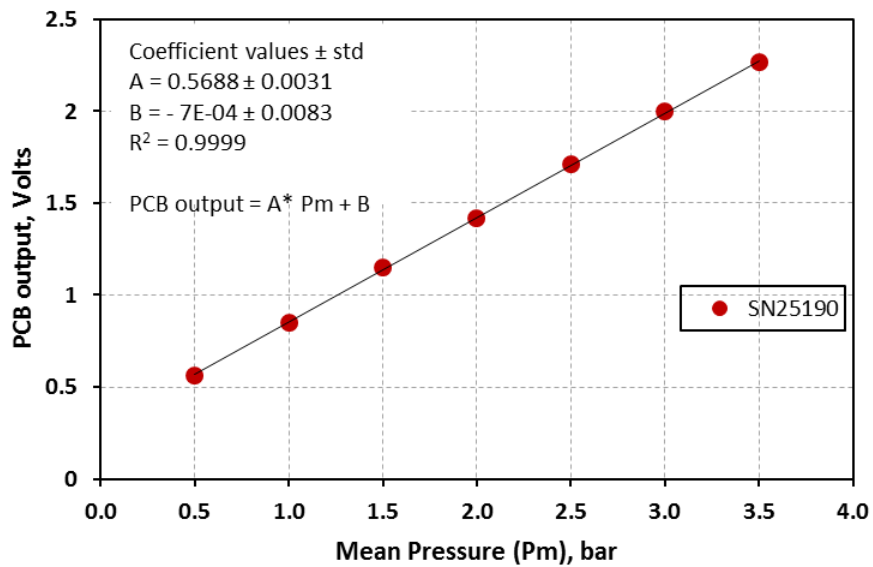


Figure D1: Calibration of pressure sensor P1. The coefficients are the slope and intercept of the least-squares fit.

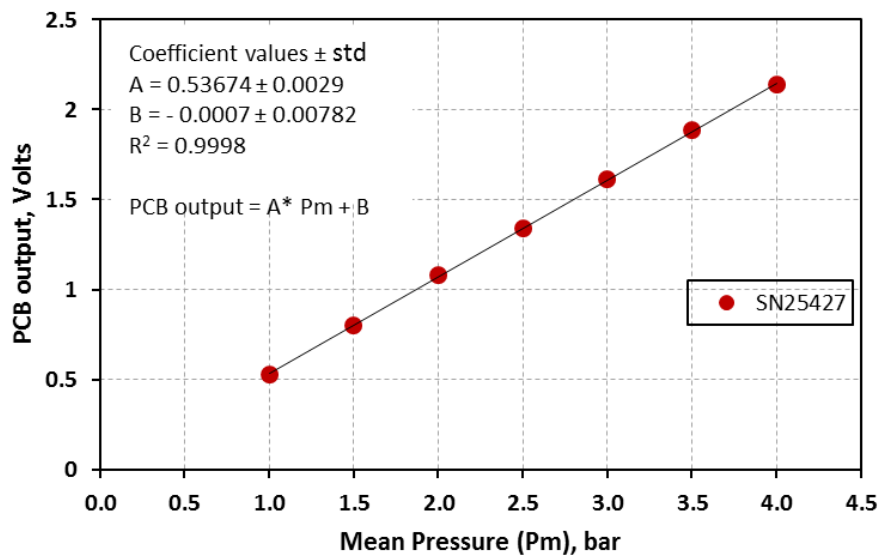


Figure D2: Calibration of pressure sensor P2.

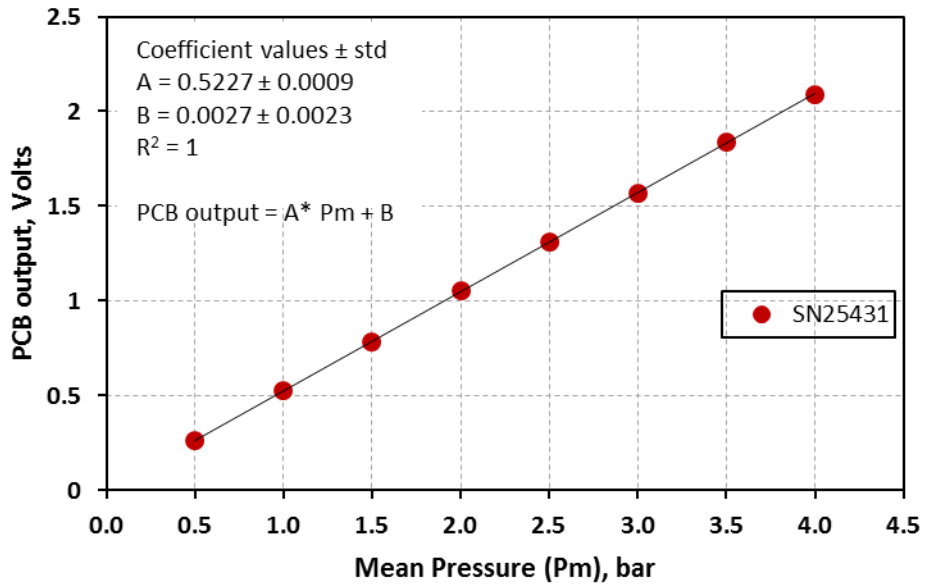


Figure D3: Calibration of pressure sensor (P5) at location 3

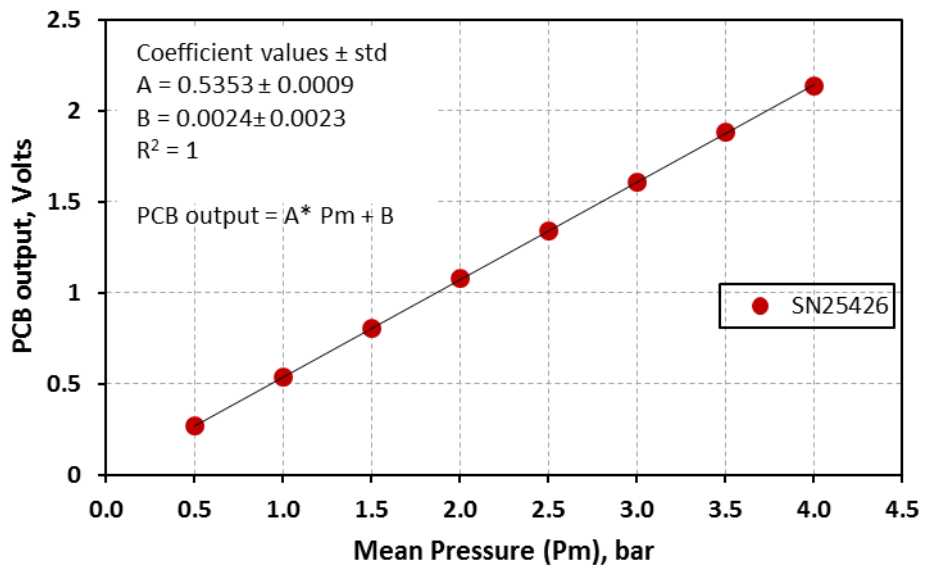


Figure D4: Calibration of pressure sensor (P6) at location 4

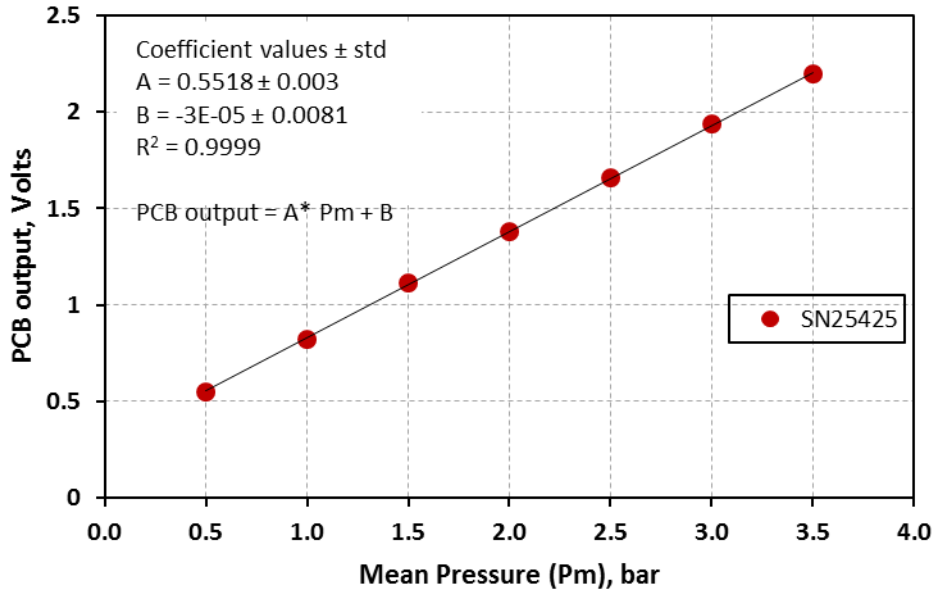


Figure D5: Calibration of pressure sensor P7.

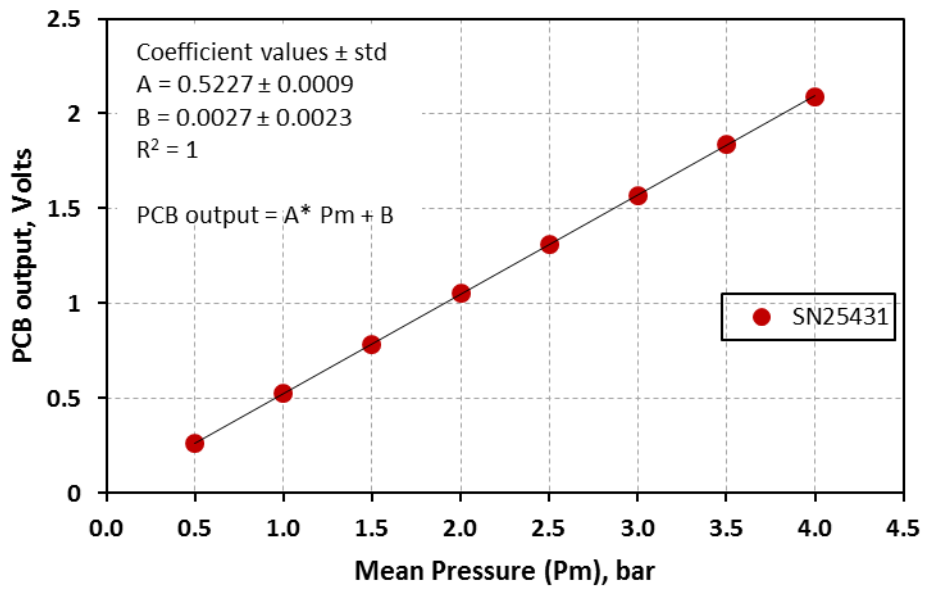


Figure D6: Calibration of pressure sensor P8 at the back of linear alternator

Appendix E

Drawing of the experimental set up

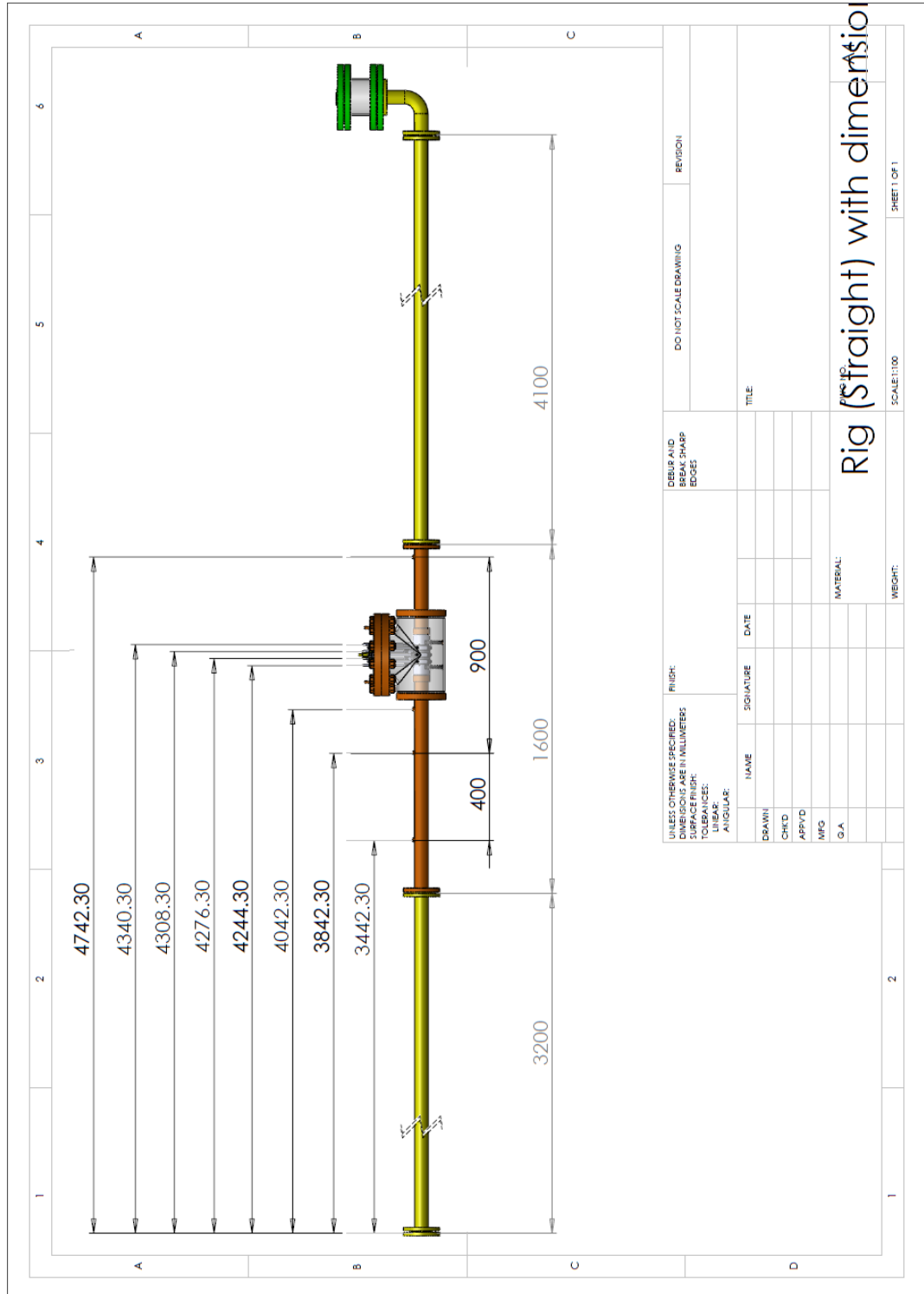


Figure E1: Overview of the dimensioned drawing of the experimental set up

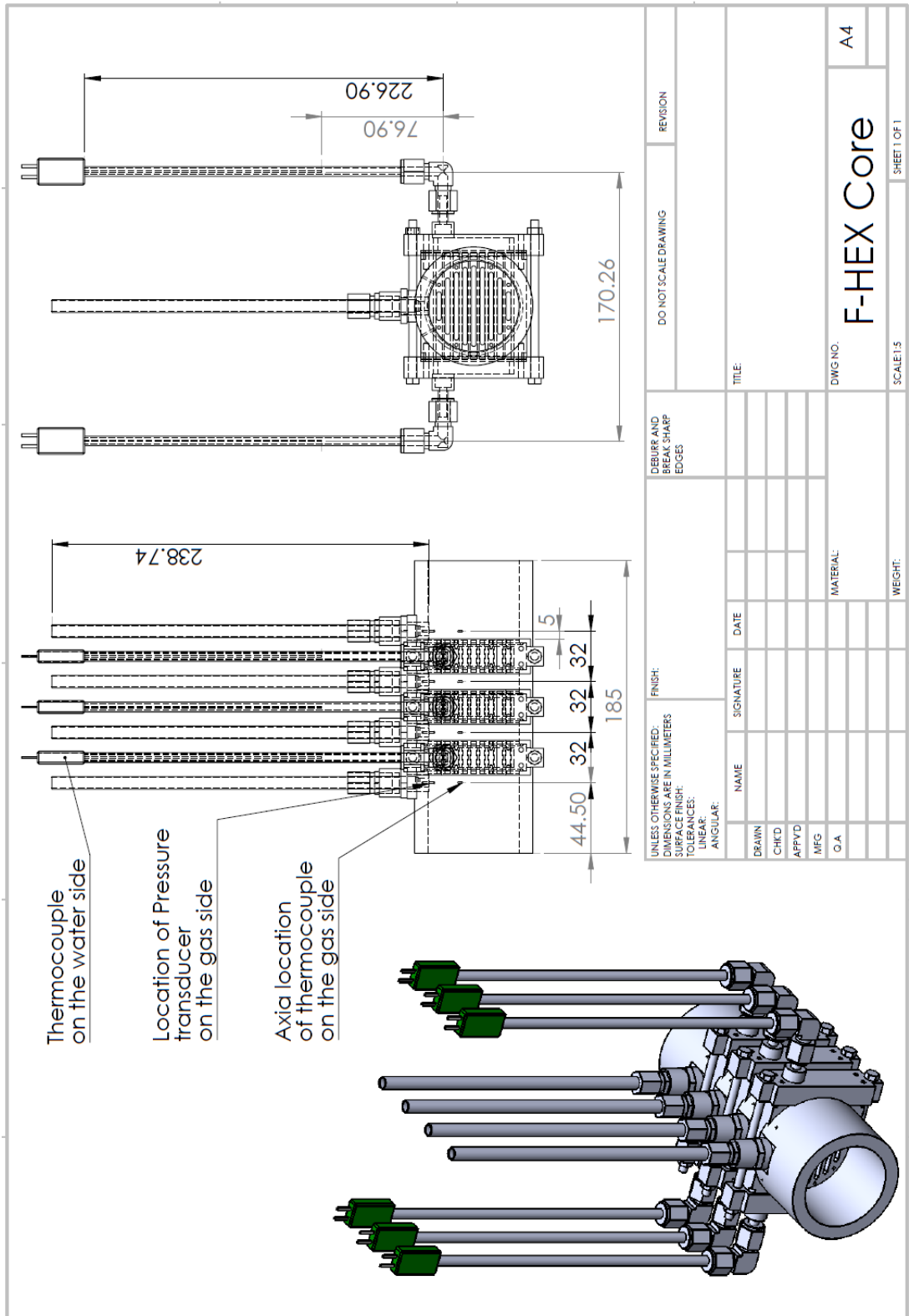


Figure E2: Drawing of the heat exchanger core showing position of the thermocouples (water and gas sides) and pressure transducers

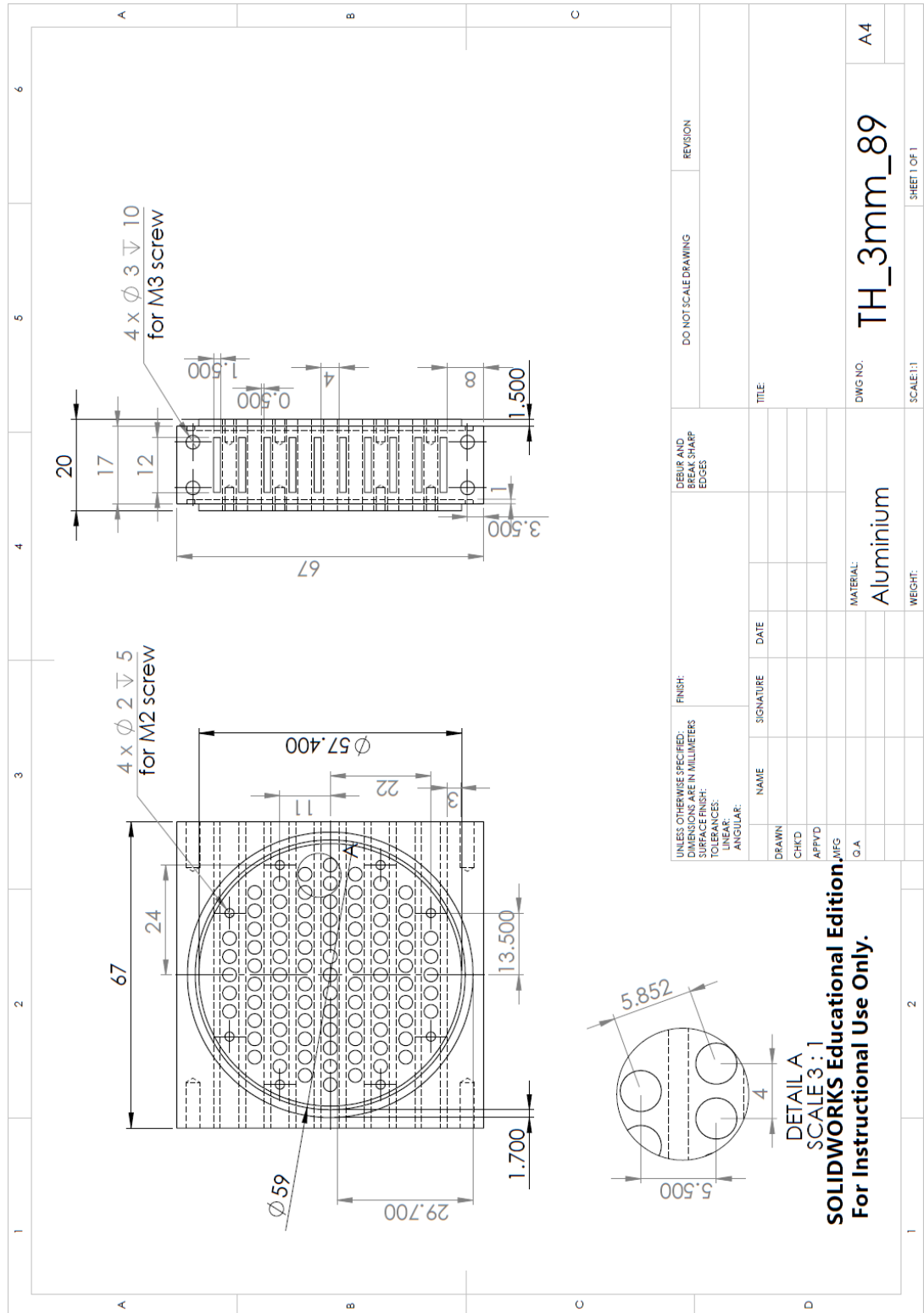


Figure E3: Drawing of the T-HEX configuration

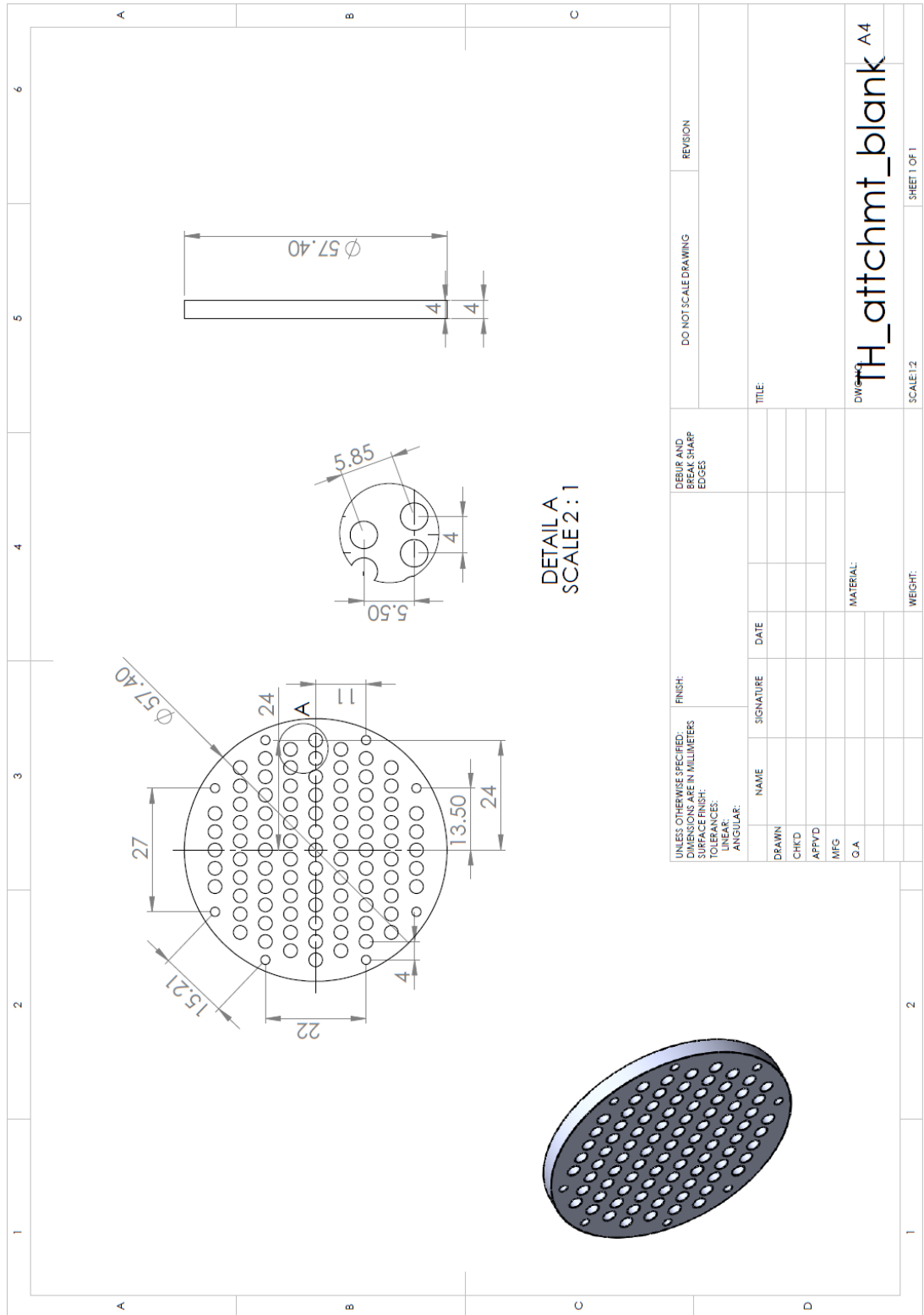


Figure E4: Drawing of a typical edge shape for T-HEX

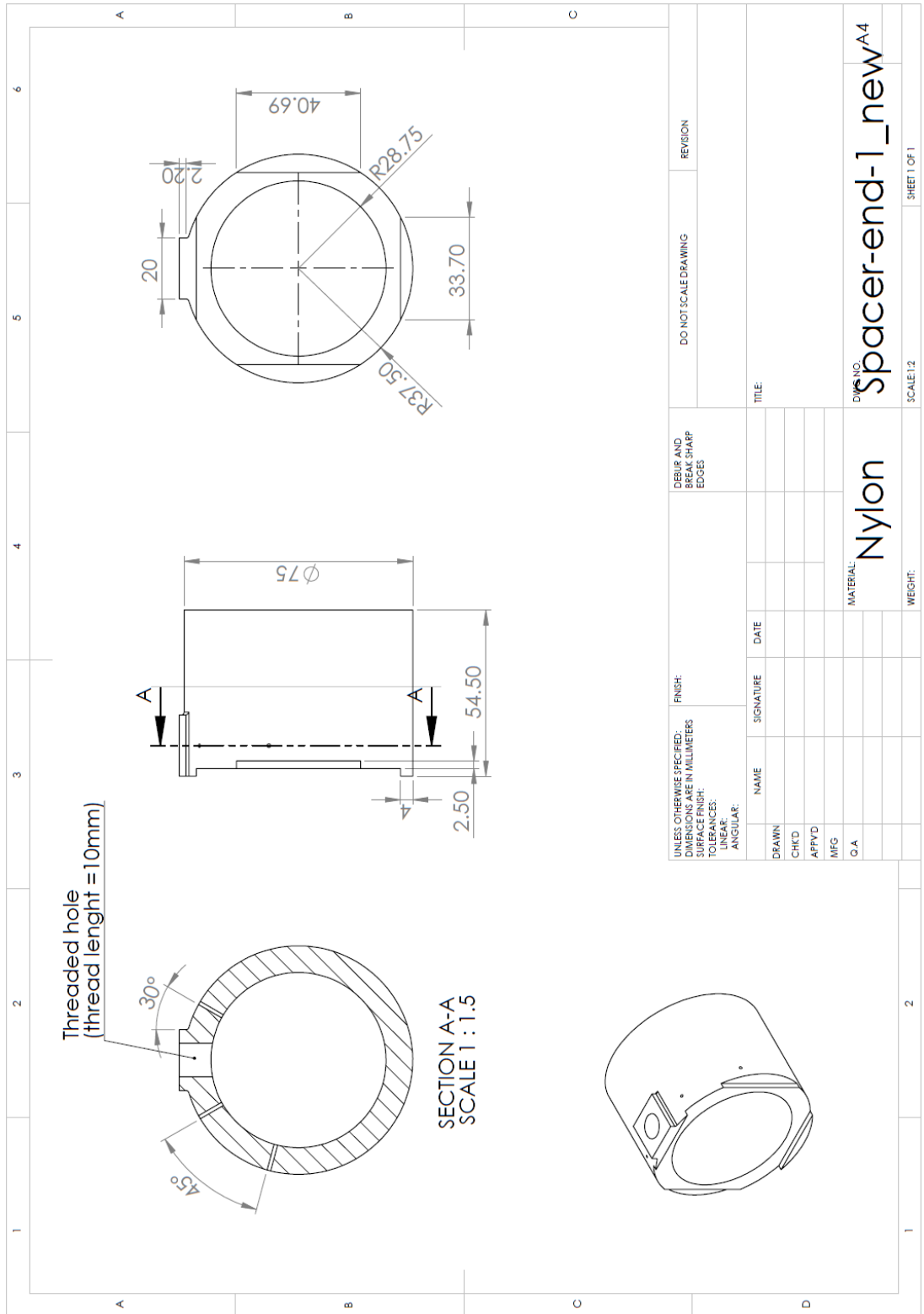


Figure E6: Drawing of a typical spacer (end)

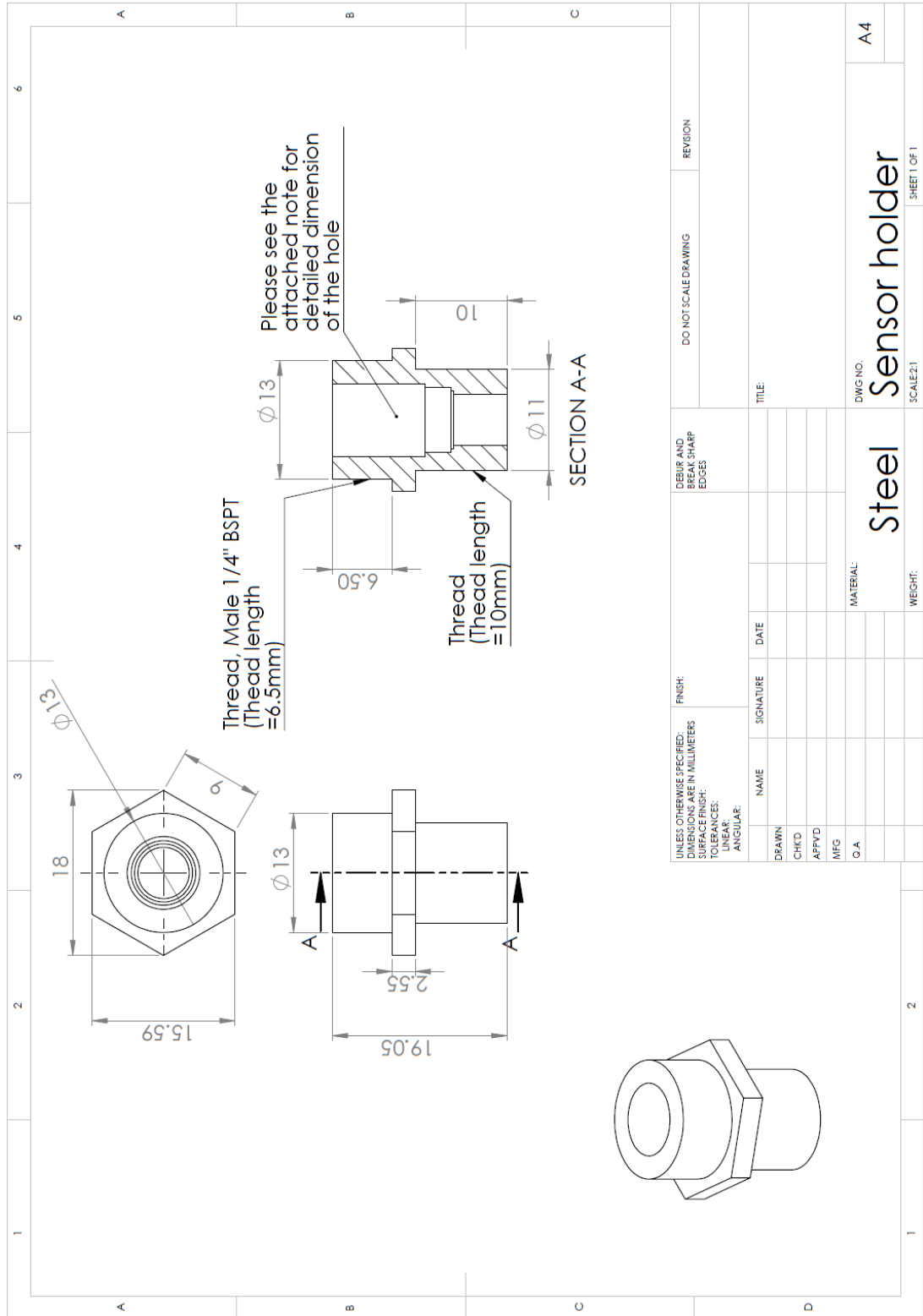


Figure E7: Drawing of a pressure sensor holder

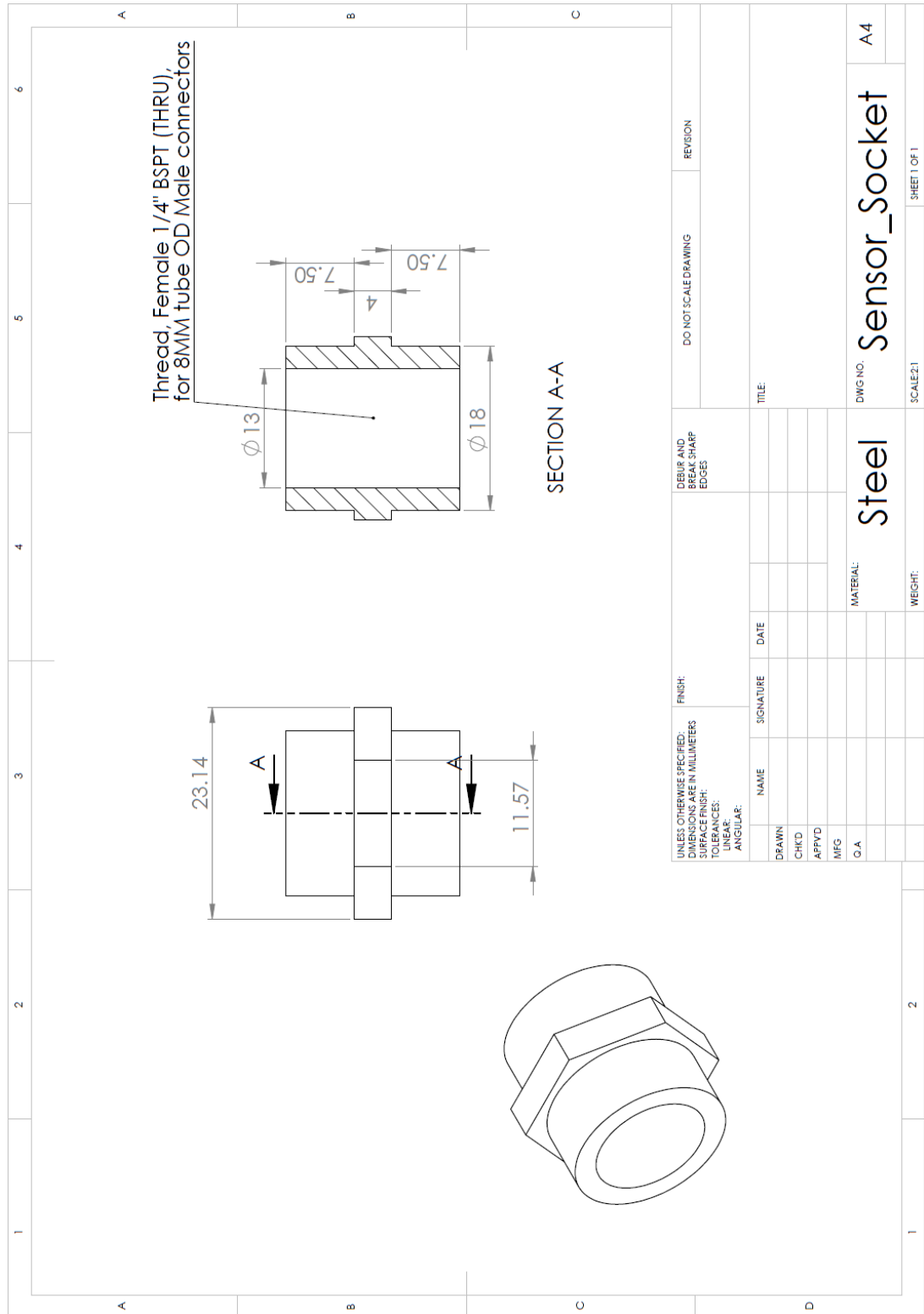


Figure E8: Drawing of a protection-socket for pressure sensor